Submesoscale dynamics in the open ocean

Liam Brannigan

Linacre College

Department of Physics

University of Oxford

A thesis submitted for the degree of

Doctor of Philosophy

Submesoscale dynamics in the open ocean

Abstract

The seasonal cycle of submesoscale flows in the upper ocean is investigated through a series of numerical simulations in an idealised model domain. Submesoscale processes become stronger as the resolution is increased from 4 km to 0.5 km. There is a seasonal cycle in the magnitude of horizontal buoyancy gradients and horizontal wavenumber spectra consistent with stronger mixed layer instabilities developing as the mixed layer deepens and energising the submesoscale. Up to 30% of the mixed layer volume in winter has negative potential vorticity and this negative potential vorticity is found in both mesoscale vortices and filaments. Further investigation of the filaments that arise in anticyclonic eddies show that they are generated in regions of negative potential vorticity and lead to the upwelling of fluid from the thermocline. Symmetric instability is found to be the most likely mechanism. The role of flow curvature is considered and it is shown that the angular velocity of mesoscale eddies, as well as relative vorticity, contributes to their stability. A numerical tracer release experiment shows that the filament generation process leads to downwelling of surface layer flows and a simplified biogeochemical experiment shows that the instability gives rise to much higher primary productivity in mesoscale anticyclones. Observations of a mixed layer front observed in the North Atlantic are presented which has a more diffuse cross-front buoyancy gradient at the surface than lower in the mixed layer and a strong ageostrophic cross-front velocity. The observations are used to motivate two dimensional simulations of Rossby adjustment. These simulations show that as the frontal strength increases the Rossby adjustment phase accounts for an increasing proportion of the restratification. The simulations become much more turbulent over the parameter range for frontal strength. The vertical profile in the observations can be re-produced when the adjustment is simulated with a thermocline, though definitive conclusions are difficult to draw.

Acknowledgements

I would like to thank my wonderful team of supervisors David Marshall, George Nurser and Alberto Naveira-Garabato. Their guidance has been instrumental in bringing this project to fruition. Above all, I have learned from them the power of curiosity when harnessed to the scientific method.

I have been fortunate to work in AOPP where I have had the chance to work alongside some innovative thinkers from many branches of climate research. I would like to thank Dave Munday, Ed Doddridge, Geoff Stanley, Ben Bronselear, Adam Levy, Graeme MacGilchrist, Richard Millar, Pete Davis, Talia Tamarin, James Maddison and Helen Pillar for their help and encouragement. Indeed, without the advice of Dave Munday, I would most likely still be trying to install the model on my computer. I thank Laure Zanna and Myles Allen for their feedback and encouragement in reviewing my transfer and confirmation reports. I am very grateful to Peter Read and John Taylor for their detailed examination of this thesis and their many helpful suggestions.

My project existed thanks to the efforts of Stephen Belcher in setting up the OSMOSIS consortium and I would like to thank all of my colleagues in the consortium, particularly Adrian Martin, Anna Rumyantseva, Brodie Pearson, Christian Buckingham, Andy Thompson, Ayah Lazar and Stephanie Waterman for their advice.

My opportunity to interact with some of the leading researchers in oceanography has not been limited to those within the OSMOSIS consortium. In particular, Baylor Fox-Kemper has been crucial in bringing this research to fruition both as a patient reviewer and a colleague. I learned from Carl Wunsch that textbooks exist to be questioned rather than believed. Carsten Eden, Sergey Danilov, Nils Brüggemann, Sören Thomsen and Jörn Callies have all given me new perspectives on this field for which I am grateful.

My family has supported me in this adventure as in many before. I hope they see their own tireless efforts reflected in this work. Finally, I will treasure Lucy for her love and support through this journey.

Contents

List of Figures

CHAPTER 1

Introduction

Submesoscale oceanic fronts have come to be recognised as a key component of the climate system, connecting the surface ocean to its interior and large scales to small. This thesis is an effort to expand our understanding of the dynamics of fronts in the surface mixed layer of the open ocean. It reflects an increasing interest in frontal processes in recent years as our ability to observe and model these processes has improved.

This work forms part of the Ocean Surface Mixing - Ocean Submesoscale Interaction Study (OSMOSIS) project, a combined observational and theoretical effort to advance understanding of the processes that set the properties of the near-surface mixed layer of the ocean. The project includes a large moored array of instruments at the Porcupine Abyssal Plain observation site in the northeast Atlantic and two research cruises to carry out a wide variety of other measurements of the upper ocean. The observation site chosen for OSMOSIS represents something of a departure from previous study of mixed layer fronts as it is an open ocean region where fronts are thought to be created by the stirring of large-scale buoyancy gradients by mesoscale eddies rather than fronts created by large-scale convergence of Ekman transport as at the sub-tropical front [e.g. Pollard and Regier, 1992] or a boundary current region [e.g. D'Asaro et al., 2011].

1.1 Background and motivation

1.1.1 Definition of key terms

Great effort has been made over the years in efforts to provide definitions for a front in the ocean or atmosphere [e.g. Fedorov, 1986; Schultz, 2015]. In this thesis a front will be taken simply to mean a location with a strong horizontal buoyancy gradient. Following, Hoskins [1982], no particular threshold of buoyancy gradient is set for a region to be considered a front.

Fronts in the ocean occur over a range of length and time scales. The fronts of primary interest here are those found in open ocean regions that arise due to the straining of the weak planetary buoyancy gradient by mesoscale eddies and Rossby waves. These fronts have cross-front widths of order 1 km, along-front lengths of order 100 km and are found mainly in the mixed layer. The time scale for the evolution of such fronts is thought to be of order f^{-1} [Thomas et al., 2008].

These mixed layer fronts are taken to be distinct from fronts in the ocean associated with major current systems that extend for thousands of kilometres along the front, tens of kilometres across the front, thousands of metres vertically and are quasi-permanent, albeit subject to meandering and occasional mesoscale wave-breaking. While these large fronts are not the subject of this thesis, they have many dynamical similarities with open ocean mixed layer fronts and a great deal of progress has been made understanding them to date. This they provide the starting point for this research. There are other oceanic fronts found principally in shallow boundary regions such as tidal fronts [Simpson and Hunter, 1974] or fronts that arise due to the input of buoyant water from rivers [e.g. Barth, 1994] to which occasional reference will also be made.

The sharp fronts of interest are more likely to form in the mixed layer of the ocean than in the interior because the free surface and the strong stratification at the base of the mixed layer inhibit vertical velocities and so allow frontogenesis to occur. In the interior of the ocean, on the other hand, increasing isopycnal slopes associated with frontogenesis lead to overturning eddy fluxes that weaken the fronts [Hoskins, 1982; Lévy et al., 2012].

The fronts of interest in this thesis are found in the mixed layer of the ocean. The mixed layer is a region of low potential vorticity (PV) that immediately overlies a region of much high potential vorticity in the thermocline. The potential

vorticity throughout this thesis is the Ertel potential vorticity [Ertel, 1942]:

$$q = (f + \nabla \times \mathbf{u}) \cdot \nabla b; \tag{1.1}$$

where ∇ is the gradient operator, $\mathbf{u} = (u, v, w)$ is the velocity vector and b is the buoyancy which is the negative of the potential density anomaly $b = -g\rho/\rho_0$, ρ is potential density and ρ_0 is the reference potential density. This definition of the Ertel potential vorticity suppresses the division by a constant reference potential density. References to the vertical component of potential vorticity in this thesis mean the product of the vertical absolute vorticity vector and the vertical buoyancy gradient $(f + \zeta_z)db/dz$, where $\zeta_z = \partial v/\partial x - \partial u/\partial y$ and $N^2 = \partial b/\partial z$ is the stratification. References to the baroclinic component of potential vorticity in this thesis mean the product of horizontal vorticity and the corresponding horizontal buoyancy gradients.

The study of fronts in the ocean is often thought to be equivalent to the study of submesoscale dynamics. Submesoscale refers to processes which have a smaller length scale than the mesoscale deformation length radius $R_d = NH/f$ where H is the vertical scale depth, which in this case is the mixed layer depth. This length scale is referred to as the Rossby radius in this thesis and is generally greater than 20 km in the mid-latitudes [Boccaletti et al., 2007]. As such, flows that have a length scale less than this are taken to be submesoscale. Flows that have a length scale less than R_d can be expected to have different behaviour than flows with a length scale greater than R_d, as the rotational constraint should be less important. This condition can be expressed theoretically as a flow where the quasi-geostrophic (QG) assumption that the Rossby number $Ro = U/fL \ll 1$ breaks down, where U is a characteristic velocity and L is a characteristic length scale. However, a mixed layer Rossby radius can also be defined as $R_{ML} = N_{ML}H_{ML}/f$ where the buoyancy frequency is calculated over the mixed layer and H_{ML} is the mixed layer depth. This length scale is generally smaller than the mesoscale baroclinic Rossby radius as it is typically of order 1 km [Thomas et al., 2008]. It is shown by Boccaletti et al. [2007] that there are modes of baroclinic instability in the mixed layer that scale with the mixed layer Rossby radius. Therefore, these modes can be thought of as a shallow quasi-geostrophic regime that exists alongside the deep quasi-geostrophic regime [Callies and Ferrari, 2013]. Despite this potential source of confusion, the practice in the literature is followed in this thesis and submesoscale is used to refer to flows that have a smaller length scale than the mesoscale Rossby radius, but it is not assumed *a priori* that these are

flows with $Ro \approx 1$. Therefore 'submesoscale fronts' in this thesis refer to fronts in the mixed layer of the ocean that have a width of order 1 kilometre, that extend through the mixed layer and have Rossby and Richardson numbers of order 1.

Reference is made through this thesis to 'balanced' and 'unbalanced' flow. Balanced flow is defined as a flow "in which the three-dimensional velocity field is functionally related to the mass field" [McIntyre, 2015a]. At ocean fronts balance is typically taken to mean geostrophic balance [e.g. Thomas et al., 2013], though as noted by McIntyre [2015a], this is the simplest but least accurate balance. Unbalanced refers to a flow for which the particular balance relation breaks down.

The related concepts of restratification, subduction and upwelling (or downwelling) occur throughout this thesis. Restratification refers to a process that leads to an increase in stratification of a water column and requires a positive vertucal buoyancy flux. Such a buoyancy flux can occur due to heating at the surface or a freshwater input at the surface. It can also occur dynamically where there is a thermally direct circulation that leads to lighter water being transported upwards while heavier water is transported downwards. Subduction is the generic name for the exchange of fluid between the mixed layer and thermocline [Marshall et al., 1993, e.g.]. In the presence of a horizontal buoyancy gradient, a restratification can occur where the lighter waters flow over the heavier waters. As the heavier waters are no longer in the surface mixed layer, they are said to be subducted. Therefore, restratification can induce subduction. Upwelling (downwelling) refers to any upwards (downwards) vertical transport of the fluid. The vertical velocities associated with upwelling can form part of a restratification. However, if the vertical velocities are aligned along isopycnal surfaces, then a vertical transport can occur without any restratification.

1.1.2 Fronts in the climate system

The requirement that fronts be regions of horizontal buoyancy gradients means that they are places where isopycnals outcrop from the largely adiabatic interior to the ocean surface. As such fronts are locations where the subduction of water masses from the surface layer can occur and so play a role in setting the dynamical properties of the interior in terms of tracers such as potential vorticity, heat, fresh water and so on [e.g. Luyten et al., 1983; Pollard and Regier, 1992; Spall, 1995]. Water subducted from the surface layer can also carry dissolved materials such as CFCs [Haine and Richards, 1995], carbon and other nutrients [e.g. Haine and Richards, 1995; Williams and Follows, 2003]. Karleskind et al. [2011] show

that the subduction of nutrients in the north-eastern Atlantic prior to the spring bloom affects ecosystems in remote locations and Lévy et al. [2012] suggest that submesoscale flows may be responsible for pulses of CO2 into the oceanic interior.

Subduction is said to be 'temporary' if the fluid parcels are re-entrained into the deepening mixed layer over the following winter and 'permanent' if the fluid parcel remains in the thermocline for at least a year. Both forms of subduction are of interest here, as temporary subduction can be associated with corresponding upwelling of nutrient-rich water into the euphotic zone – defined to be the near-surface layer that receives sufficient light for photosynthesis to occur – with important consequences for marine ecosystems.

Subduction in this thesis refers primarily to the exchange of water between the mixed layer and upper thermocline in the mid-latitude open ocean, rather than deep and bottom water formation associated with deep convection in the high latitudes and marginal seas [e.g. Danabasoglu and McWilliams, 1995]. The heat transport and dissolved greenhouse gas fluxes associated with shallow subduction may, however, be of importance for decadal-scale climate predictability [Deser et al., 1996; Schneider et al., 1999; Bates et al., 2002].

1.1.3 Fronts in oceanic energy cascades

Conservation laws for energy and enstrophy in homogeneous geostrophic turbulence models show that the net energy flux is predominately to larger spatial scales while the net enstrophy flux is to smaller spatial scales [Charney, 1971; Rhines, 1979; Salmon, 1980]. The energetic pathways of the ocean have been a focus of recent study in oceanography with the debate framed in a series of review papers [Wunsch and Ferrari, 2004; Ferrari and Wunsch, 2009, 2010]. The current picture is that energy is input to the ocean by frictional and buoyancy fluxes at the surface at scales much larger than the mesoscale Rossby radius of deformation. Such motion is baroclinically unstable and so leads to a cascade of energy towards the first Rossby radius. At this length scale the motions are stable and can barotropize in the vertical and grow again in horizontal scale [Salmon, 1980; Fu and Flierl, 1980; Scott and Wang, 2005]. This growth may be arrested at the Rhines scale [Rhines, 1979] or by some other process. However, these relatively large-scale barotropic flows are relatively inefficient at dissipating energy and so the question as to how the energy can eventually be dissipated as Joule heating remains open [Wunsch and Ferrari, 2004]. Note that this theory of geostrophic

turbulence is subject to an assumption that geostrophic turbulence is homogeneous in a manner that is not consistent with observed features of the oceanic or atmospheric circulation such as strong jets [McIntyre, 2015b].

One immediate suggestion is that a large part of the eddy kinetic energy is dissipated by bottom drag, particularly in the presence of topography [e.g. Polzin et al., 1997; Marshall and Garabato, 2008; Ferrari and Nikurashin, 2010]. Other avenues include the dissipation of kinetic energy at western boundaries in 'Rossby graveyards' [Zhai et al., 2010] or mixing induced by non-linearities in the equation of state [Huang, 2004]. Frontal processes in the mixed layer can also be a route to dissipation of kinetic energy. This dissipation can occur because the potentially higher Rossby number of frontal flows means that quasi-geostrophic constraints of inverse cascades may not hold, thus allowing a route to down-scale energy fluxes [Molemaker et al., 2005, 2010; Thomas and Taylor, 2010; Brüggemann and Eden, 2014].

The pathways that this loss of geostrophic balance could take have been the subject of intense research. One route is for submesoscale flows to directly generate fine-scale turbulence. This kind of process has been shown to occur in large eddy simulations by Skyllingstad and Samelson [2012] who find that weak turbulence develops due to the shear associated with baroclinic waves. The authors report that this is a route to dissipation which goes directly from the submesoscale length scale to the turbulent length scale without 'cascading' through intermediate wavelengths. Hamlington et al. [2014] perform a similar large eddy simulation of baroclinic waves but including surface wind forcing and an imposed Stokes drift. They focus on the potential interactions between mixed layer instabilities and Langmuir turbulence [Thorpe, 2004; Grant and Belcher, 2009; Belcher et al., 2012] and find that the small-scale turbulent fluxes are amplified in the presence of Stokes forcing.

A second branch of research has focused on paths to dissipation which involve a cascade through wavenumber space to small-scales. Molemaker et al. [2010] compare simulations of an Eady-type flow [Eady, 1949] in quasi-geostrophic and non-hydrostatic Boussinesq models. They show that as the resolution is increased the quasi-geostrophic model is increasingly inefficient at dissipating kinetic energy while the Boussinesq model can equilibrate across a range of Rossby numbers. Brüggemann and Eden [2014] show that the downscale flux is only associated with the divergent component of the flow and that this flux decreases as the Rossby number grows.

The dissipation of the kinetic energy of balanced motion via the equilibration of symmetric instability is another branch of research. Taylor and Ferrari [2009] show that in a large eddy simulation of a symmetrically unstable front the strong vertical shear leads to the generation of Kelvin-Helmholtz instabilities that are efficient at dissipating turbulent kinetic energy. Thomas and Taylor [2010] show in consequence that when the dissipation of kinetic energy by symmetric instability is taken into account, the wind work done on the geostrophic flow is reduced close to the surface. Thomas et al. [2013] consider the potential role of energy dissipation via symmetric instability for the Gulf Stream, but do not conclude that it may be a significant term in the energy budget.

A fourth branch of research looks at the emission of inertia-gravity waves due to spontaneous generation or Rossby adjustment of a flow, as defined in Section 1.2.2 [Ford, 1994a,b; O'Sullivan and Dunkerton, 1995; Dunkerton, 1995; Ford et al., 2000; McIntyre, 2009; Danioux et al., 2012; Vanneste, 2013; Alford et al., 2013; Borchert et al., 2014; Tsang and Dritschel, 2015]. Rossby adjustment is the ageostrophic flow that Note that spontaneous emission in this thesis is taken to mean the generation of inertia-gravity waves due to the loss of balance of the flow, without demanding that the wave emission is related to the thinness or otherwise of quasi-manifolds [McIntyre, 2015a]. There are a range of processes which can lead to such spontaneous emission including convection or the adjustment of a vortex to a more stable shape [Tsang and Dritschel, 2015]. The parameter space in which the wave emission occurs, particularly the degree to which the flow must depart from the quasi-geostrophic approximation is a matter of debate [Tsang and Dritschel, 2015; McIntyre, 2015a]. The parameter space to understand the emission process must include the aspect ratio of the region where balance is lost, gravitational-rotational effects characterised by the Burger number and inertial effects characterised by the Rossby and Froude numbers. Spontaneous emission is not thought to be a dominant source of internal wave energy for the ocean compared to tides and wind-forcing [Danioux et al., 2012; Callies and Ferrari, 2013], but it may be of importance for frontal dynamics. In an analytical study of frontogenesis, Shakespeare and Taylor [2013] find that if the emitted inertia-gravity waves are unable to propagate away due to the strain of the flow, they may prevent a front from reaching a state of geostrophic balance.

In summary, the energetic pathways of the ocean remains one of the major open questions of the field and the role of submesoscale processes within the ocean's energy budget is likely to remain of interest for quite some time.

1.1.4 Effect of frontal processes on biological productivity

Ocean fronts can be regions of high biological productivity [Uda, 1938; Knauss, 1957; Owen, 1981; Sournia, 1994; Long et al., 2012; Clayton et al., 2014]. As noted by Sournia [1994]; Margalef [1997], fronts in the ocean are themselves habitats, as well as being boundaries between different communities. The open ocean mixed layer fronts that are the main focus of this thesis may have relevance for biological processes in two ways.

The first of these is the effect of frontal dynamics on the timing of the spring bloom in the mid- to high-latitudes. In a combined observational and numerical study of spring bloom onset in the Icelandic Basin, Mahadevan et al. [2012] find that the restratifying effect of mixed layer eddies leads to shallowing of the mixed layer above the critical depth faster than is expected based on surface buoyancy fluxes alone. In the Ross Sea restratification induced by the Ekman buoyancy flux led to the development of biological hotspots [Long et al., 2012]. They note that primary production is light-limited in the Ross Sea and so is particularly sensitive to the mixed layer depth. Alternatively, Huisman et al. [1999] and Taylor and Ferrari [2011] propose that spring blooms develop when vertical turbulent mixing is reduced below a critical value. In effect, the near-surface restratification by symmetric and baroclinic instabilities inhibits vertical velocities and thus the vertical displacements of phytoplankton away from the light-rich euphotic zone. Behrenfeld [2010] proposes an additional theory for phytoplankton bloom timing that is related to the rates of grazing by zooplankton, a factor that is largely independent of frontal dynamics.

The second way in which frontal processes may be of relevance for marine ecosystems is as a nutrient supply mechanism in oligotrophic conditions – defined here to be conditions where the growth of phytoplankton is limited by nutrient availability – that are often found in summertime in the mid-latitudes [e.g. Morel et al., 2010]. An outstanding issue over the last 30 years is that estimates of the rates at which biogeochemical processes occur based on methods that intrinsically integrate over large space and time scales are up to an order of magnitude larger than can be explained by numerical models or estimates of nutrient upwelling [Shulenberger and Reid, 1981; Jenkins, 1982; Platt and Harrison, 1985; Jenkins and Goldman, 1985; Emerson et al., 1997; Oschlies, 2002b,a; Michaels, 2007; Ledwell et al., 2008; Eden and Dietze, 2009]. The uncertainty surrounding this point

is such that there is an on-going debate as to whether the oligotrophic ocean is autotrophic – defined to be a region with more primary production than respiration and so a region that produces more carbon than it releases – or heterotrophic – defined to be a region with less primary production than respiration and so a region that consumes more carbon than it releases [Ducklow and Doney, 2013; Williams et al., 2013; Duarte et al., 2013]. This question as to whether the oligotrophic ocean is autotrophic or heterotrophic is largely a test of our understanding of the biological and advective pathways that nutrients take in the ocean. The question needs to be resolved if we are to understand the sign of net vertical carbon fluxes from the mixed layer of the oligotrophic ocean that covers much of the Earth's surface. If this flux is negative, then we need to ensure that global climate models can capture this net sequestration of carbon away from the atmosphere.

Satellite observations suggest that mesoscales eddies play host to large amounts primary productivity in the oligotrophic ocean [McGillicuddy et al., 1998; Williams and Follows, 2003; Crawford et al., 2007; McGillicuddy et al., 2007; Hansen et al., 2010; Lehahn et al., 2011, 2014] and so mesoscale vortex dynamics may be important for understanding higher productivity in eddies. Existing ideas for this include the doming and slumping of isopycnals into and out of the euphotic zone [e.g. Benitez-Nelson et al., 2007; Crawford et al., 2007], Ekman pumping in eddies [Martin and Richards, 2001; McGillicuddy et al., 2007; Gaube et al., 2013, 2014a] or the divergence of Ekman transports due to gradients in geostrophic vorticity [Mahadevan et al., 2008]. It is also proposed that the larger vertical fluxes found at ocean fronts could generate the vertical nutrient transport required [Lévy et al., 2001; Mahadevan and Archer, 2000; Klein and Lapeyre, 2009; Taylor and Ferrari, 2011], though this does not explain the elevated productivity found inside mesoscale vortices [Ledwell et al., 2008; McGillicuddy et al., 2007; Lehahn et al., 2011; Gaube et al., 2014b].

1.1.5 Scientific challenge

In addition to the practical reasons for wanting to study ocean fronts detailed above, frontal dynamics are also of pure scientific interest. The large shear found at fronts means they are an area where the quasi-geostrophic approximation should begin to break down. Examining the extent to which this surprisingly robust model holds and whether it can be replaced by an alternative simplification of the equations of motion is one of the main challenges in the field [Hoskins and Bretherton, 1972; Lapeyre and Klein, 2006; Callies and Ferrari, 2013]. Mixed

layer frontal dynamics relates to geostrophic turbulence in the planetary boundary layer and means that a full theory would have to take into account a diverse range of effects from intense turbulence, the presence of buoyant bubbles formed by wave breaking, or the modulation of incoming radiation due to bubbles [Zhang et al., 1998] among a large range of other possible processes.

The study of mixed layer fronts is also an observational challenge for scientists as these transient fronts grow and dissipate over the course of days at locations in the open ocean that are difficult to predict. In addition, the velocities associated with many frontal flows are often of similar magnitude to those generated by surface waves, geostrophic flows and the internal wave field. The order 1 km width of these fronts means they are at the edge of or beyond the resolution for many satellite products such as sea surface temperature, sea surface height or sea surface salinity. This challenge in remote sensing is particularly the case in cloudy locations such as the Porcupine Abyssal Plain. The highly non-linear response of marine organisms to small changes in physical conditions creates a tracer field for smaller-scale processes that is more apparent in remotely-sensed fields. An example of this is shown in a SeaWiFS ocean quasi-true colour image in Figure 1.1, where a mesoscale anticyclonic vortex is host to submesoscale filaments of chlorophyll. The role of biological processes must be taken in careful consideration when interpreting such images.

While observing mixed layer fronts is difficult, modelling them is only slightly more tractable. The mixed layer fronts of interest in this thesis are in many respects a down-scale extension of the mesoscale eddy field. This means that the numerical domain must simultaneously resolve both mesoscale and the submesoscale features. Increases in computing power in recent years have allowed such numerical simulations to be attempted. However, a compromise of some sort must always be made to resolve the range of length scales required. The large-scale circulation of a region can be included at the expense of limited submesoscale resolution [e.g. Lévy et al., 2010]. Alternatively a series of nested models (e.g. Capet et al. [2008b]; Mensa et al. [2013]; Gula et al. [2014]) or an idealised channel domain [Mahadevan, 2006; Fox-Kemper et al., 2008; Brüggemann and Eden, 2014] can allow higher resolution to be obtained. The interaction of submesoscale flows with finescale turbulence can be modelled using large eddy simulations in a channel figuration which is large enough to allow for baroclinic waves to develop [e.g. Skyllingstad and Samelson, 2012; Hamlington et al., 2014].

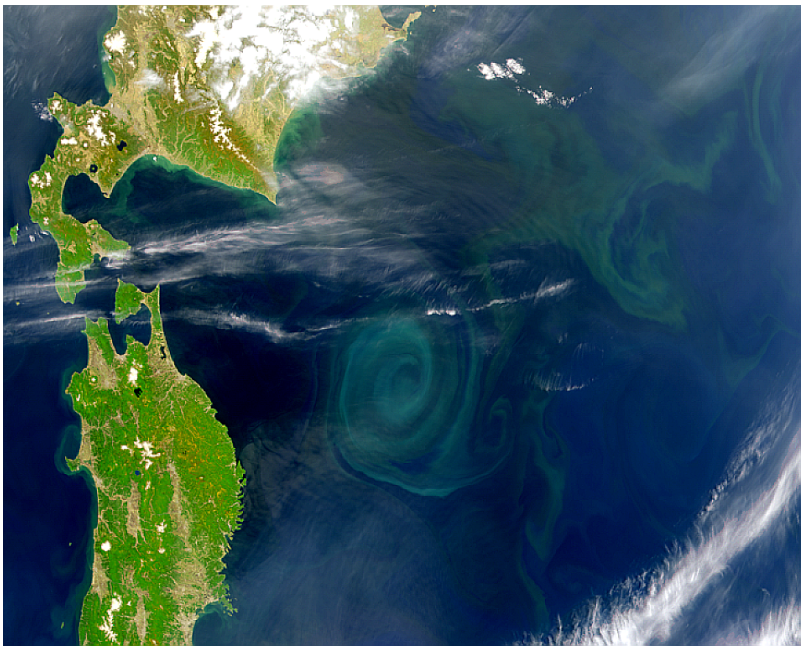

Figure 1.1: Ocean colour data from SeaWiFS off the coast of Japan on 22nd May 1999. The image shows high primary productivity in a mesoscale anticyclonic vortex. Image provided by the SeaWiFS Project, NASA/Goddard Space Flight Center, and ORBIMAGE.

All simulations remain regional at best and the simulations are of short duration compared to many climate signals [Wunsch, 1999].

1.2 Past work and present state of knowledge

1.2.1 Early developments

While mariners and scientists have been aware for centuries of the existence of regions in the ocean where properties change rapidly [Fedorov, 1986], the systematic study of ocean fronts is a relatively recent phenomenon, with few significant results before World War II. Cromwell and Reid [1956] remark that the main exception is the work of Japanese researchers [e.g. Uda, 1938], who were motivated by the frequent presence of fish and whales – important sources of protein in Japan – at ocean fronts [Sournia, 1994]. Fronts could often be identified from a ship by surface wave breaking, convergences of buoyant material and sharp changes in colour – it is this latter property that gives rise to the name of the Kuroshio which translates as 'the black stream'. However, these developments were not well understood outside Japan, to the extent that Professor Uda was apparently still impressing attendees with his results at a meeting in Europe

some 50 years later [Fedorov, 1986]. In Europe and North America at the time, fronts were often still treated as simply the boundary between different water masses [Iselin, 1936]. The landmark work by Sverdrup et al. [1942], for example, makes little mention of fronts and states that discontinuities in water masses do not occur.

Progress in the study of frontal dynamics was (and is) hindered observationally by the requirement to measure temperature, salinity and currents at spatial resolutions of order 100 m and temporal resolution of minutes to days. Conducting such observations was particularly demanding for early workers where even ascertaining the position of the ship was challenging. The development of the thermograph in the 1950's allowed continuous measurement of the near-surface temperature for the first time. Cromwell and Reid [1956] exploited this technology to examine fronts in the equatorial Pacific. In doing so they appropriated the term 'front' from meteorology instead of the 'current-rip' term that had been used previously [Uda, 1938]. They propose a definition of a front similar to that employed in this thesis in that it refers to a "band along the sea surface where the density changes abruptly". They also then became the first to face the issue of deciding just how abrupt the density change must be in order to be considered a front. Based on the observed temperature profiles, they conjectured that the front they observed had a convergent downwelling flow on both sides of the front. Knauss [1957] also observed a tropical front sharpened by a down-front Ekman transport actively generating convective instability.

Work on these fronts continued to be sporadic over the 1960's with the next significant observation made by Voorhis and Hersey [1964] following the invention of the towed thermistor chain that allowed observations on the order 100 m scale necessary for progress. Voorhis and Hersey [1964] observed a front in the Sargasso Sea, now known as the sub-tropical front, and found that it was continuous and meandering over more than 150 km. Observations with an electromagnetic current meter showed that there was a strong current of almost 0.6 m s^{-1} in a direction consistent with geostrophic balance with cyclostrophic effects present in the meanders and order one Rossby numbers. No dynamical theory is presented for the formation or destruction of the front, though the authors state their belief that it is of importance for the circulation in the Sargasso Sea. In a further observation of the sub-tropical front in the Sargasso Sea, Katz [1969] sums up the understanding of ocean fronts at that time. Observations had shown that near-discontinuities in water mass properties existed in the open ocean, that they

were likely generated by large-scale convergences of Ekman transport and associated with local convergences on both sides of the front. This local convergence "drained'' – or subducted – water that had come into contact with the other side of the front, preserving its sharp structure.

Over the same post-war period, a theory for the dynamics of western boundary currents was developed [Stommel, 1948; Munk, 1950], followed by increasing evidence for the existence of the mesoscale eddy field in the ocean [Williams, 1793; Iselin and Fuglister, 1948; Fuglister and Worthington, 1951][1] . From the 1970's it was clear that the open ocean is a turbulent environment with structure on a wide range of scales. New contributions would be made much more frequently, to the extent that Fedorov [1986] remarked that more than 500 research articles had been published on ocean fronts in the period from 1975-1980 alone. To get an overview of developments from this period, key processes are considered individually below.

1.2.2 Rossby adjustment

Rossby adjustment is the ageostrophic flow that develops for flows that are not in geostrophic balance. Geostrophic balance is at the heart of many theories of ocean dynamics. It arises when the pressure gradient force is balanced by the Coriolis force. Although it has long been understood that an initial state in geostrophic balance is not linearly stable [Eady, 1949], departures from geostrophic balance are generally thought to be relatively small at the mesoscale and larger scales.

Geostrophic balance is an attracting state for flows of sufficient scale as departures from balance lead to ageostrophic flows that tend to restore balance [Rossby, 1938]. The key insight of Rossby [1938] was that the conservation of potential vorticity in a homogeneous, frictionless flow means that the final balance state can be inferred from the initial potential vorticity distribution. The passage to this balanced state is marked by the emission of inertial waves that have no potential vorticity but which can extract energy from the flow. Following, McIntyre [2015a], the term 'geostrophic adjustment' is avoided in preference for 'Rossby adjustment', given that the adjustment itself is ageostrophic.

[1]Jonathon Williams was a grandnephew of Benjamin Franklin. Richardson [1983] writes that he measured surface temperatures by lowering a cooking pot from the end of a sounding line and found that "The evidence of this various current in so short a space, the heat of the water not being raised to the heat of the stream, and our situation to the Northward made me conclude that this to be the whirlpools of the eddy of the Gulf Stream just on the northern edge of it".

Tandon and Garrett [1994] consider the Rossby adjustment of the ocean mixed layer, where there is no initial flow to balance a horizontal buoyancy gradient. This unbalanced state is taken to occur after a diapycnal mixing event that leaves the mixed layer unstratified. They show that the adjustment process leads to a restratification of the mixed layer and an increase in the Richardson Ri $= N^2/(u_z^2 + v_z^2)$ where the subscripts denote differentiation. With time dependence, the final state has Ri$= 1/2$ averaged over an inertial period. They predict that the transitory state will be turbulent due to the low initial Richardson number. Tandon and Garrett [1995] followed this up with a model that included a variable mixed layer depth and found similar results.

Studies of Rossby adjustment in the ocean often assume the initial unbalanced state arises due to a diapycnal mixing event [e.g. Young, 1994]. A separate pathway to an unbalanced state is observed by Dale et al. [2008] in an upwelling region of the Oregon shelf with repeated towed observations. In this case a down-front wind had initially steepened isopycnals. The wind then weakened and reversed over about an inertial period when an extensive restratification occurred. Dale et al. [2008] find that the resultant Rossby adjustment was initially dominant in the restratification with Ekman transport playing a greater role eventually. It could be the case that Rossby adjustment is important for ocean fronts subject to time-varying winds.

1.2.3 Frontogenesis

The growth of frontal structures has long been a point of inquiry in atmospheric science as they are often associated with precipitation [Schultz, 2015], a matter close to the hearts of the Norwegian and British meteorologists that studied them. The 'Norwegian School' were the first to integrate a dynamic concept of fronts into synoptic meteorology. Previous efforts to understand fronts had failed, according to Bergeron [1959], due to a general lack of understanding of hydrodynamics, or an excessive focus on Eulerian over Lagrangian methods.

The concept of frontal formation due to a horizontally confluent flow was first proposed by Bergeron [1928]. It was recognised from this period that frontogenesis is accompanied by vertical motions and a tilting of isentropic surfaces [Bjerknes, 1919]. Sawyer [1956] introduced a diagnostic expression for the vorticity of the cross-front flow and time-dependent variations of this expression were developed by Stone [1966a]; Williams and Plotkin [1968]; Williams [1968] with the assumption of quasi-geostrophy.

Hoskins and Bretherton [1972] remark that these efforts failed to represent frontogenesis in a realistic manner because sharp frontal gradients lead to the breakdown of quasi-geostrophic assumptions. In essence, the cross-front ageostrophic flow becomes strong enough to affect the advection of potential vorticity and thus the subsequent development of the flow. Instead, Hoskins and Bretherton [1972] make a semi-geostrophic assumption whereby the along-front velocity is in geostrophic balance, but the cross-front velocity is not so constrained. This assumption allows a time-dependent model that describes realistic frontogenesis for the case where the time scale of straining is long compared to the inertial period. The physical mechanism is for a straining flow to increase the across-front buoyancy gradient. However, in doing so it also advects flow with weaker thermal wind shear into the frontal region thus moving the front away from thermal wind balance in both the mass and momentum distribution. Quasi-geostrophic theory then predicts the development of a frontal overturning circulation. However, as quasi-geostrophy only allows the advection of potential vorticity by the geostrophic velocity, the convergences that arise due to the ageostrophic overturning circulation are omitted. This limitation prevents the development of strong vortex stretching due to the ageostrophic flow. If the semi-geostrophic approximation is made and so the ageostrophic flow can advect potential vorticity and a solution that allows the generation of discontinuities at boundaries in finite time emerges.

Macvean and Woods [1977, 1980] apply the theory of Hoskins and Bretherton [1972] to an oceanic case and find that the degree of frontal intensification falls away rapidly from the surface, even in the presence of a mixed layer. They find that frontogenesis can affect the transport of tracers from the surface mixed layer into the thermocline, in analogy with the transport of low potential vorticity troposphere air across the tropopause [Sawyer, 1956; Hoskins and Bretherton, 1972].

Pollard and Regier [1992] observe the sub-tropical front in the Atlantic and find that vertical velocities – estimated using the semi-geostrophic omega equation [Hoskins and Draghici, 1977; Hoskins et al., 1978] – are large. Rudnick and Luyten [1996] find a similar result at the sub-tropical front in the North Atlantic and also shows the importance of the thermal wind contribution to potential vorticity at fronts. Despite its limitations, the frontogenesis model of Hoskins and Bretherton [1972] has proved remarkably successful in describing frontal growth.

The model is generalised by Shakespeare and Taylor [2013] to remove the restriction on the deformation rate being weak relative to the Coriolis frequency which leads to even larger vertical velocities as the feedbacks on the front become stronger.

A point of interest in recent decades are the factors that ultimately limit frontogenesis in the atmosphere or ocean. While molecular diffusion is an obvious candidate, the strong gradients found at fronts admit other faster-developing flows. A high resolution simulation of frontogenesis by Snyder et al. [1993] finds that the degree of geostrophic balance decreases as the front becomes increasingly sharp and so gravity wave emission occurs. This wave emission is excluded from a balanced model such as semi-geostrophy. Shakespeare and Taylor [2013] also find strong gravity wave emission associated with frontogenesis.

McWilliams et al. [2009] and McWilliams and Molemaker [2011] show that baroclinic instability can grow in the presence of a straining deformation field. This is in contrast to earlier results of Bishop [1993] and Spall [1997]. McWilliams and Molemaker [2011] show that the baroclinic wave growth increases with the increasing Rossby and Froude numbers at the front, while the deformation rate that acts to damp them does not. While the flow associated with an individual baroclinic meander can lead to frontogenesis or frontolysis [Spall, 1995], the net effect of baroclinic instability is frontolytic when averaged over many wave periods as baroclinic instability tends to reduce horizontal buoyancy gradients by overturning them into the horizontal [Boccaletti et al., 2007]. This point is considered further in Chapter 1.2.5 on baroclinic instability below.

Frontogenesis also plays an important role in theories of upper ocean dynamics. This is done by simplifying the equations of motion in a small Rossby number expansion. An inversion of the potential vorticity field to recover the flow then requires four factors: the mass under each stratification surface, the distribution of potential vorticity on each stratification surface, the distribution of buoyancy on boundaries and a balance condition [Hoskins et al., 1985; McIntyre, 2015b]. Bretherton [1966] shows that a good description of the interior flow can be obtained even if the surface buoyancy anomalies are neglected. The complementary approach is to investigate the flow that is arrived at by assuming interior potential vorticity is uniform and using only the boundary buoyancy anomalies. This model is known as surface quasi-geostrophy [Blumen, 1978; Held et al., 1995; Lapeyre et al., 2006], which can be thought of as an Eady model [Eady, 1949] with a single boundary. Therefore, upper and lower edge waves cannot become

phase-locked and so baroclinic instability does not occur. Instead, the edge waves are efficient at stirring the surface buoyancy field to create small-scale structures. In this way, the effect of surface quasi-geostrophic dynamics is thought to amount to frontogenesis.

A major attraction of surface quasi-geostrophic theory is that it would allow detailed inference of upper-ocean velocities based on remotely-sensed observations of the sea surface. A numerical analysis by Lapeyre et al. [2006] finds that the velocities inferred from surface buoyancy and interior potential vorticity inversions are anti-correlated with similar results found by LaCasce and Mahadevan [2006]; Klein et al. [2008]. Overall, however, the evidence in favour of surface quasi-geostrophic inversion to describe upper-ocean velocities is mixed. In an analysis of the velocity field in North Atlantic repeat transects Callies and Ferrari [2013] find that shallow horizontal wavenumber spectra of velocity are only found in the mixed layer, contrary to a surface quasi-geostrophic prediction that such shallow spectra would also be present to some depth in the thermocline. More promisingly, recent efforts have focused on employing both sea surface height and sea surface temperature signals to estimate the interior flow [Smith and Vanneste, 2013; Wang et al., 2013].

1.2.4 Ekman buoyancy flux

During the *Fram* expedition to the Arctic, F. Nansen observed that icebergs drifted at an angle to the wind and recognised that this could reflect a rotation of the current vector with depth. Upon his return he discussed this phenomenon with W. Bjerknes who asked W.E. Ekman to investigate it [Nierenberg, 1996]. Ekman did so and found that with the assumption of a turbulent vertical eddy viscosity, the so-called 'Ekman spiral' emerged [Ekman, 1905]. A key property of this spiral is that the net transport is to the right of the wind in the northern hemisphere. The properties of the Ekman solution remain a subject of active interest [e.g. Polton et al., 2013], particularly as observing the Ekman spiral has proved challenging [e.g. Price et al., 1987; Chereskin and Roemmich, 1991; Lenn and Chereskin, 2009; Polton et al., 2013].

The classical Ekman transport is $M_e = \tau/\rho f$ [Cushman-Roisin and Beckers, 2011] where τ is the surface stress. In an analysis of Ekman transport in the presence of geostrophic vorticity gradients at small Rossby number, Stern [1965] shows that the Ekman advection of geostrophic vorticity needs to be taken into

account. Vortex stretching is then generated at the base of the Ekman layer to balance the transport of geostrophic vorticity by the Ekman transport, even when the wind stress is horizontally uniform. In consequence, the modified Ekman transport depends on the effective Coriolis parameter, i.e. including the geostrophic vorticity and so is given by $M_e = \tau/\rho(f + \zeta_z)$. Niiler [1969] shows that the variation in lateral shear across the Gulf Stream means that this effect produces divergences in the Ekman transport. These divergences lead to ageostrophic secondary circulations at fronts even where there is no curl in the wind stress [Cushman-Roisin, 1981; Thomas and Rhines, 2002; Thomas, 2005; Thomas and Lee, 2005; Mahadevan, 2006; Mahadevan et al., 2008].

A wind stress aligned with the geostrophic shear tends to steepen isopycnals towards the vertical, as observed by Samelson and Paulson [1988] and perhaps Knauss [1957] as noted in Chapter 1.2.1. This is referred to as a 'down-front' wind throughout this thesis. On the other hand a wind stress that opposes the geostrophic shear flattens isopycnals and is referred to as an 'up-front' wind throughout this thesis. Thomas [2005] shows down-front winds lead to fluxes of potential vorticity substance out of the ocean at fronts and up-front winds lead to fluxes of potential vorticity substance into the ocean. Thomas and Lee [2005] shows that the ageostrophic secondary circulation associated with the divergences of the Ekman transport has a frontogenetic effect. In a numerical simulation of a wind-forced channel, Mahadevan [2006] conclude that the strongest vertical velocities arise due to the ageostrophic secondary circulations.

1.2.5 Baroclinic instability

The linear instability of baroclinic flow with positive potential vorticity was first established by Charney [1947] and Eady [1949]. The instability in this case arises due to the interaction of edge waves that extract potential energy from the mean baroclinic flow. Hoskins et al. [1985] show that baroclinic instability can be thought of as the interaction of two Rossby edge waves. The flow associated with the dominant instability in this case is found to be approximately in geostrophic balance.

Eady [1949] inferred the importance of the Richardson number for understanding the growth of these instabilities. The relationship with classic instability theory in fluid dynamics was established by Phillips [1951] as baroclinic instability was found to grow where there is a change in the sign of the potential vorticity gradient.

While baroclinic instability has been the subject of a vast number of papers in atmospheric and oceanic dynamics, its relevance for the oceanic mixed layer has been relatively slow to emerge. As noted in Chapter 1.2.1, the early observations of the sub-tropical front found that the front has a wave-like meandering structure, though the connection with baroclinic instability was not made at this point [Voorhis and Hersey, 1964]. However, the data gathered from the Mesoscale Ocean Dynamics Experiment (MODE) experiment showed conclusively that eddy fluxes with both deep and shallow modes are operative in setting sea surface temperature in the open ocean. Voorhis et al. [1976] note that the horizontal length scale associated with these near-surface variations is consistent with a deformation radius implied by the seasonal pycnocline depth –or the mixed layer Rossby radius as it is now called – rather than the main thermocline depth.

Further progress in understanding ocean fronts from the perspective of baroclinic instability came with the Frontal Air-Sea Interaction Experiment (FASINEX) experiment [Weller, 1991]. This experiment again focused on the Atlantic sub-tropical front with both ship surveys and moorings employed. Eriksen et al. [1991] show that the sub-tropical frontal jet has velocities of 0.5 m s^{-1} with horizontal variability that range from tens to hundreds of kilometres. Weller [1991] finds evidence of cold-core eddies in the vicinity of the jet with horizontal length scales of 15-25 km, similar to that of the frontal jet. Samelson [1993] summarises these findings and investigates whether these cold-core eddies can be generated by frontal baroclinic instabilities in a linear instability analysis. He finds that the maximum growth occurs for wavelengths of 70 km and timescales of 2.3 days. The relatively long length scale of 70 km here reflects a lower value of the Coriolis frequency in the sub-tropics and a deep vertical scale of 300 m assumed for the mixed layer depth. Samelson and Chapman [1995] follow this up with a primitive equation simulation of instability growth in a channel model. This simulation shows a preference for the development of cold-core cyclones as a response to baroclinic wave breaking, as predicted by Samelson [1993]. Samelson and Chapman [1995] do not demonstrate the dynamical cause of this preference, though refer to a theory of asymmetric baroclinic wave breaking of Pratt et al. [1991] based on the critical line theory of Nakamura and Plumb [1994]. This latter approach has become incorporated into a theory known as inhomogeneous potential vorticity mixing [e.g. Dritschel and McIntyre, 2008] that may provide insights into wave-breaking and up-gradient momentum fluxes at jets. Spall [1995] models a similar frontal con-

figuration, though in a three-layer isopycnal model. He also finds that cyclones are formed preferentially.

The energetics of these baroclinic frontal instabilities are investigated by Samelson and Chapman [1995] who find that there is an initial energy transfer from available potential energy to kinetic energy as the disturbance grows, followed by a transfer from eddy kinetic to mean kinetic energy as the eddies equilibrate. These energy fluxes could be a manifestation of inhomogeneous potential vorticity mixing and illustrate the role of up-gradient momentum fluxes in sharpening jets and fronts in the mixed layer. This may be in contrast to a general assumption that mixed layer fronts are sharp because of frontogenesis effects i.e. the presence of a boundary at the surface that constrains overturning motions [Lévy et al., 2012].

The focus on mixed layer baroclinic instabilities in recent years has been on their associated buoyancy fluxes and net restratification. Nurser and Zhang [2000] consider the effect of frontal eddy generation and find that it can lead to rapid restratification and shallowing of the mixed layer. Boccaletti et al. [2007] find that the low Richardson numbers found in the mixed layer increase the growth rate of baroclinic instability compared to the quasi-geostrophic growth rate [Stone, 1966b, 1971]. In addition, the linear instability analysis of Boccaletti et al. [2007] includes a deformable mixed layer base, though slopes in the mixed layer base turn out to have little effect on the overall result. The approach of Boccaletti et al. [2007] is followed by Fox-Kemper et al. [2008] who develop a parameterisation for the buoyancy fluxes associated with baroclinic instability in the mixed layer. This parameterisation is discussed in more detail in Chapter 1.3.

A further avenue of investigation has been subduction from the mixed layer due to baroclinic instabilities. The 3-layer simulation of Spall [1995] finds that particles can be subducted due to overturning frontal instabilities. If a particle is subducted from a deep mixed layer it tends to have a negative potential vorticity anomaly with an anticyclonic circulation once subducted in the pycnocline. Therefore, this subduction is a potential generation method for submesoscale coherent vortices [McWilliams, 1985]. Spall [1995] finds that the vortices that emerge from the subduction process can arrange themselves in dipoles of oppositly signed eddies, similar to the 'hetons' of Hogg and Stommel [1985].

As well as the classical mode of baroclinic instability [Eady, 1949; Stone, 1966b], a further mode is found by by Molemaker et al. [2005], who revisit the linear stability analysis of Stone [1966b]. They carry out a similar eigenvalue problem and,

with fifty additional years of progress in computing power and numerical algorithms, find additional higher wavenumber modes that can outcompete the Eady mode given certain initial conditions. Unlike the 'Eady problem' where the flow in the instability remains close to geostrophic balance, the new modes in Molemaker et al. [2005] are much more ageostrophic. The condition for the growth of these modes is that $A - |S| < 0$, where $A = f\mathbf{k} + \nabla \times \mathbf{u}$ is the absolute vorticity and $S = [(u_x - v_y)^2 + (v_x + u_y)^2)^{1/2}$ is the strain, where both are calculated along stratification surfaces. This condition corresponds to an initial condition where the basic state flow has anticyclonic relative vorticity (though still with positive potential vorticity). As such Molemaker et al. [2005] call this 'ageostrophic anticyclonic instability.

1.2.6 Symmetric instability

In a resting, stratified ocean, a perturbation to a water particle that moves it vertically will result in a buoyancy force that accelerates the particle back towards its original buoyancy surface. Upon reaching its original buoyancy surface it will overshoot and the overall result is a gravity wave. Similarly, a particle perturbed horizontally in a resting rotating fluid experiences a lateral acceleration due to the Coriolis effect. This can be thought of as an acceleration of the particle back towards its original momentum surface [Eliassen, 1962]. Upon reaching its original momentum surface it will overshoot and the overall result is an inertial oscillation. Typically in the ocean we consider scenarios where the slope of buoyancy surfaces is shallower than the slope of momentum surfaces. The perturbations then result in inertia-gravity waves [Munk, 1981].

At ocean fronts the diabatic effect of surface cooling and frictional Ekman buoyancy fluxes can result in a steepening of buoyancy surfaces [Thomas, 2005]. In thermal wind balance, this steepening of the buoyancy surfaces results in a strong vertical shear that tilts the momentum surfaces towards the horizontal. This tilting can result in the momentum surfaces becoming steeper than the buoyancy surfaces. In this case a perturbation of a particle along a buoyancy surface causes the particle to leave its momentum surface. The induced acceleration of the particle towards its momentum surface then causes it to leave its buoyancy surface and so induce a further acceleration back towards the buoyancy surface. When the momentum surfaces are shallower than the buoyancy surfaces perturbed particles are accelerated away from their original location. Hoskins [1974] shows that

this scenario of shallower momentum surfaces corresponds to the potential vorticity and f being of opposite sign, or $fq < 0$. Throughout this thesis $f > 0$ and so negative potential vorticity is taken to be equivalent to $fq < 0$. The acceleration of the particle away from its starting point is the essence of symmetric instability. An alternative derivation is made by Stone [1966b], who shows that for flows in thermal wind balance symmetric instability is expected to be dominant where $0.25 < \mathrm{Ri} < 0.95$. These limits are for fronts in thermal wind balance with no relative vorticity and no curvature. Bachman and Taylor [2014] show that for a front with relative vorticity but no curvature the upper bound on symmetric instability occuring is $\mathrm{Ri}_c = f/(f + \zeta_z)$.

This insight that the relative signs of f and q provides information about the stability of the flow comes from Hoskins [1974], following Ooyama [1966]. They show that for a stably-stratified and rotating fluid with $fq > 0$ and no vertical shear $fq = f(f + \zeta_z)N^2 = \sigma_{min}^2 \sigma_{max}^2$ where σ_{max} is the highest frequency gravity wave and σ_{min} is the frequency of inertial oscillations. This relation is of interest, as large-scale flows have a balanced component that is described by potential vorticity and a wave component with no potential vorticity. This relation shows that fq also carries important information about the fate of small perturbations to the balanced state.

The terminology surrounding symmetric instability is somewhat inconsistent in the literature. In this thesis symmetric instability is the instability that emerges for stable stratification with $fq < 0$ [Hoskins, 1974]. This is not the only instability permitted for this stage of course. Regarding terminology in this thesis, convective instability arises where $fq < 0$ due to unstable stratification, centrifugal instability arises where $fq < 0$ due to anticyclonic relative vorticity and symmetric instability arises where $fq < 0$ due to the baroclinic component of potential vorticity. Hybrid modes are said to arise when $fq < 0$ due to more than one of these factors. A schematic of this framework is given in Thomas et al. [2013]. These definitions have useful practical implications when considering the energetics of the flow, as convective instability sources its energy from vertical buoyancy fluxes, centrifugal instability sources its energy from lateral shear of the balanced flow and symmetric instability sources its energy from vertical shear of the balanced flow [Thomas et al., 2013]. Unfortunately, this division of processes by general is not quite general. As discussed below, Bachman and Taylor [2014] show that what would generally be considered as symmetric instability can both restratify and destratify the fluid or do neither. Frictional effects play a much larger role in these

instabilities than baroclinic instabilities [e.g. Marshall and Schott, 1999; Thomas and Taylor, 2010] and thus the dissipation of kinetic energy must be taken into account when considering the energetics of the instability. No *a priori* assumption is made about the corresponding energetics of any given mode in this thesis.

Until the 1990's, relatively little attention was paid to symmetric instability in the ocean, perhaps due to the (continuing) challenge in observing it. This lack of attention changed due to two emerging interests. On one hand, attention turned to the limits of balanced dynamics [Lorenz, 1960; Charney, 1971] and quasi-geostrophic theory [McWilliams et al., 1998] in particular. Quasi-geostrophy has proved very successful in describing large scale features of the flow in the ocean and in the atmosphere of Earth and other planets. However, it is weakly dissipative of kinetic energy [Molemaker et al., 2005] and so an understanding of ocean energetics requires an understanding of how and where quasi-geostrophy breaks down. As the flow associated with symmetric instability is unbalanced, it represents one pathway for the breakdown of quasi-geostrophy. Thomas and Taylor [2010] find that the strong shear of the flow leads to the generation of Kelvin-Helmholtz instabilities and then the viscous dissipation of the kinetic energy. They remark that this dissipation is of particular interest because the primary kinetic energy source for symmetric instability is the geostrophic flow and so this geostrophic energy is then not available to drive the large-scale circulation. They estimate this reduction in power input as 5% of the total wind power input based on the ECCO state estimate of Wunsch et al. [2009]. They note that the state estimate does not include baroclinic eddies and so forced symmetric instability there would increase the area over which the energy dissipation could occur.

The second reason for growing interest in symmetric instability is the dynamical response of the ocean to intense buoyancy loss in regions of deep convection such as the Labrador Sea. Thomsen et al. [2014] perform a linear stability analysis of the Labrador current and finds that symmetric instability is expected to occur throughout the year, but more frequently in winter. Haine and Marshall [1998] examine the stability of the mixed layer in large eddy simulations. They find that the conditions for symmetric instability, or a hybrid gravitational-symmetric instability are likely to be ubiquitous in the mixed layer when cooling is applied at the surface. Going beyond surface cooling, Thomas and Rhines [2002] investigate the stratified spin-up of a fluid in response to a wind stress at the surface and

show that effective buoyancy loss and negative potential vorticity can be generated by a down-front wind stress. They find the dominant instability that grows in response to this negative potential vorticity is a symmetric instability, rather than a hybrid gravitational-symmetric mode.

The results noted above show that symmetric instability is likely to occur in the mixed layer of the ocean. More attention has since been paid to its dynamical properties in this mixed layer regime. Taylor and Ferrari [2009] perform high resolution 2D simulations of symmetrically unstable fronts. They find that linear theory for symmetric instability accurately predicts the growth rate for the most unstable modes in regions of negative potential vorticity and that once these modes reach finite amplitude they generate secondary Kelvin-Helmholtz instabilities. These secondary instabilities rapidly mix positive potential vorticity fluid entrained from the thermocline and so lead to the equilibration of symmetric instability. These results are in broad agreement with previous work on symmetric instability in an atmospheric context by Thorpe and Rotunno [1989]. The interaction of symmetric instability and gravitational instability is investigated by Taylor and Ferrari [2010] in a similar configuration to that used by Haine and Marshall [1998]. They find that gravitational instabilities are dominant in a 'convective layer' near the surface at fronts, with the lateral motion by symmetric instability dominant below the convective layer. They develop an implicit scaling relationship for the convective layer depth.

Symmetric instability is challenging to observe directly that would only be observable with acoustic current profilers in particularly benign situations as the vertical wavelength is comparable to the vertical resolution of the acoustic profilers and other flows due to inertial oscillations or surface waves have similar magnitudes. The main exceptions to this have invoked a thermal wind balance approximation to infer the presence of negative potential vorticity where stratification is weak and horizontal buoyancy gradients are strong [D'Asaro et al., 2011; Thomas et al., 2013]. The thermal wind assumption does not take into account the effect of Stokes shear on potential vorticity. The Stokes shear is the vertical derivative of the mass transport associated with the wave-averaged Stokes drift and amounts to a vortex-stretching effect [McWilliams and Fox-Kemper, 2013]. Haney et al. [Subm. to JPO] show that the Stokes shear has dynamical importance as the Stokes shear offsets the negative potential vorticity flux due to down-front winds where wind and waves are in equilibrium.

1.2.7 Other processes

The author has heard the dynamics of mixed layer fronts referred to as 'the submesoscale zoo' due to the diversity of separate processes that have been proposed as being active there. Various constraints, including time, space and computational limits preclude the detailed analysis of all of these, though their potential effects are noted where relevant.

The interaction of mixed layer fronts with surface waves has been the subject of recent investigation. This effect arises as the shear due to the Stokes drift alters the thermal wind balance and the waves induce a vortex-stretching and Stokes-Coriolis force – which is the effect of planetary rotation acting on the vertically-sheared Lagrangian Stokes velocity – that affects the flow [McWilliams and Fox-Kemper, 2013]. Recent results show that for the typical scenario, where wind and waves are oriented in the same direction, the Stokes shear of the surface waves offsets the negative-definite baroclinic contribution to potential vorticity in thermal wind balance [Haney et al., Subm. to JPO]. The shear associated with Stokes drift also leads to Langmuir turbulence [Thorpe, 2004]. The large eddy simulations of Hamlington et al. [2014] that resolve both submesoscale instabilities and Langmuir turbulence show that symmetric instability is less prevalent when the Stokes shear is present and that Langmuir turbulence offsets some of the restratification by submesoscale instabilities.

The role of inertial oscillations at fronts has also come under increasing attention. Alford et al. [2013] observe strong near-inertial wave propagation from mixed layer fronts in the North Pacific. They attribute the wave generation to a Rossby adjustment process at the front. In an analytical and numerical study Thomas and Taylor [2014] find that parametric subharmonic instability may lead to the damping of inertial oscillations at ocean fronts. This instability arises due to the presence of inertia-gravity waves with a frequency of $f/2$. Waves with frequency less than f are, of course, precluded for the ocean at rest. However, for baroclinic flows the lowest permissible frequency is $\sigma_{min} = (fq/N^2)^{1/2}$ [Hoskins, 1974; Thomas and Taylor, 2014] and so lower frequency waves are permissible in the very baroclinic mixed layer. Such an instability is found to grow where $Ri > 1$ in a region of the parameter space that is generally thought to be dominated by baroclinic instabilities. The parametric subharmonic instability is similar to symmetric instability in that it is highly sheared and efficient at generating secondary instabilities that dissipate kinetic energy [Thomas and Taylor, 2014].

1.3 Parameterisation of frontal dynamics

With the increasing understanding of frontal dynamics in recent decades, the first efforts to parameterise the dynamics have been made. These parameterisations can be divided into two categories. In the first are schemes to parameterise multiple processes together, based on principles such as the release of potential energy from horizontal buoyancy gradients and the effect of friction on these flows. This class of parameterisations includes the sub-inertial mixed layer approximation of Young [1994], which acts as a quasi-geostrophy model for the mixed layer. This model allows for ageostrophic cross-front flows such as those associated with geostrophic adjustment and geostrophic flows associated with mixed layer instabilities. It includes a larger frictional effect than would be associated with typical quasi-geostrophic-turbulence to capture the effect of shear-driven turbulence. Subsequently, Ferrari and Young [1997] consider models where the eddy buoyancy flux is parameterised as a diffusive flux which is proportional to some power of the horizontal buoyancy gradient. Spall and Chapman [1998] follow a similar approach with a scaling proposed for the cross-front heat flux due to the generation and propagation of baroclinic eddy pairs. Overall, this diffusive approach has not been advanced in recent years, but could be useful for inclusion in simplified ocean models.

In the second category are parameterisations where specific processes are handled separately. Tandon and Garrett [1994] propose a parameterisation for Rossby adjustment based on theoretical and numerical arguments. The essence of this parameterisation is that the adjusted state should have $\mathrm{Ri} \sim 1/2$. The primary example of a parameterisation of mixed layer frontal dynamics is that developed and implemented in climate models in a series of papers by Fox-Kemper et al. [2008], Fox-Kemper and Ferrari [2008] and Fox-Kemper et al. [2011]. This parameterisation focuses on baroclinic instability in the mixed layer. The theoretical basis of this parameterisation is a Transformed Eulerian Mean approach [Green, 1970; Stone, 1972; Andrews et al., 1987; Gent and Mcwilliams, 1990; Visbeck et al., 1997] that specifies the buoyancy transports induced by finite amplitude mixed layer baroclinic instabilities. In practice the parameterisation leads to an overturning streamfunction that adiabatically re-arranges horizontal buoyancy gradients. As in Visbeck et al. [1997], along-isopycnal mixing in the manner of Redi [1982] is not included, as it is assumed that the transport by the deep mesoscale field dominates lateral mixing [Fox-Kemper et al., 2008].

These efforts to parameterise mixed layer eddy fluxes inherit many of the issues associated with extant mesoscale eddy parameterisations. Firstly, the schemes parameterise only the buoyancy flux associated with the instability. The up- or down-gradient momentum fluxes are not included [Visbeck et al., 1997]. Secondly, the energetic pathway induced by the parameterisation is effectively from available potential energy directly to dissipation. Alternative pathways, such as kinetic energy returning to the mean flow [Samelson and Chapman, 1995] or to the internal wave field are not considered. Addressing these issues will likely require a separate framework, such as a parameterisation for the eddy flux of potential vorticity Marshall et al. [2012].

There is no parameterisation yet available for the other important dynamical processes at ocean fronts such as symmetric instability or Langmuir turbulence interactions. Bachman and Taylor [2014] take a step towards a parameterisation of symmetric instability by examining the extent to which symmetric instability occurs at relatively coarse resolution, which means horizontal grid spacings of up to 4 km in this case. They show that the shallower modes of the instability can occur at these resolutions.

1.4 Thesis objectives and outline

The objectives of this thesis are to improve our understanding of mixed layer fronts in the open ocean from numerical and observational perspectives. This includes understanding the processes that lead to the formation and destruction of these fronts and the effect the frontal processes have on related factors such as vertical heat transport and biogeochemical processes.

The original question that drove the design of the OSMOSIS mooring array is how submesoscale flows vary over the course of a seasonal cycle. The numerical configuration for simulations to investigate the seasonal cycle are described in Chapter 2. The results of these simulations in terms of the seasonal cycle are set out in Chapter 3. A feature of these simulations is that submesoscale filaments are found inside mesoscale anticyclonic vortices. The question of the how these filaments are generated and the dynamical consequences of the filaments is considered in Chapter 4. High spatial resolution observations of mixed layer fronts made during the OSMOSIS cruises show strong ageostrophic velocities and suggest that cross-front diapycnal mixing is occurring at fronts. The observations are presented and possible dynamical causes are investigated numerically in Chapter

5. Chapter 6 includes a summary of the main contributions of this thesis to our understanding of submesoscale dynamics in the open ocean, the main implications of these findings and sets out future work to be carried out.

CHAPTER 2

Numerical set-up

2.1 Introduction

The main numerical component of this experiment is carried out in an idealised configuration intended to be analogous to the OSMOSIS observation site in the North Atlantic. The observation site is the Porcupine Abyssal Plain located near 16°W, 49°N, a region where mean flows are weak and mesoscale eddies dominate the kinetic energy budget [Painter et al., 2010]. This numerical experiment complements a moored array of instruments, sea glider deployments and two process cruises over 2012-2013 in the OSMOSIS project. Comparisons will be made to these observations as the results are presented in Chapter 3, though the model has not been 'tuned' to replicate the observations.

An important point of reference for the design of this numerical experiment is an insightful series of papers by Capet and co-authors [Capet et al., 2008b,c,d], that examine the transition from mesoscale to submesoscale dynamics in a model domain analogous to the California Current System. An advantage of the approach taken by Capet and co-workers of generating a geostrophic eddy field over using a spin-down model is that the submesoscale processes grow occur in the context of the strain induced by a larger scale eddy field. This strain is an important control on the growth rate of instabilities [Bishop, 1993; Spall, 1997; McWilliams and Molemaker, 2011; Thomas, 2012]. A comparable experimental methodology is employed in this work whereby simulations are run over a resolution range from mesoscale-resolving to submesoscale-permitting. The nu-

merical configuration of this work departs from previous works in a number of ways. Firstly, a seasonally varying surface buoyancy forcing is employed and so the mean mixed layer depth varies by an order of magnitude through the year. Secondly, no temperature-restoring is used and so the model stratification can diverge as the resolution becomes finer. Thirdly, the domain used here is analogous to an open ocean region rather than an eastern boundary current region as in [Capet et al., 2008b,c,d] or a western boundary current region as in [Mensa et al., 2013] or Gula et al. [2014].

The primary aim of the model set-up is to generate a field of geostrophic turbulence that can persist for a number of years without restoring conditions. This demand precludes the use of a channel model approach with an initial horizontal buoyancy gradient, as these gradients either quickly spin-down [e.g. Fox-Kemper et al., 2008] or require buoyancy restoring conditions [e.g. Koszalka et al., 2009; Brüggemann and Eden, 2014] that obscure the difference in stratification as the resolution varies. The numerical set-up should also generate an eddy field that permits submesoscale variability at these resolutions.

2.1.1 Chapter aims and outline

The aim of this Chapter is to set out in detail the numerical configuration used in Chapters 3 and 4. This allows reproducibility of the results and explains the rationale that guided the choice of numerical parameters. The domain configuration is set out in Chapter 2.2, the numerical configuration is described in Chapter 2.3, the physical parameterisations used are considered in Chapter 2.4 and the initial and boundary conditions are in Chapter 2.5. The spin-up and inter-annual variability are discussed in Chapter 2.6. The set-up for additional experiments examined in Chapter 4 are described in Chapter 2.7.

2.2 Model domain

The simulations are integrated using the MITgcm [Marshall et al., 1997] in a hydrostatic configuration. The model set-up is an idealised version of the OSMOSIS observation area at the Porcupine Abyssal Plain site. As such, the configuration is that of an open ocean, abyssal plain location in the mid-latitudes. The model domain is doubly-periodic with side-length of 256 km. The bottom boundary is at 3,700 m depth and the model domain is spanned with 200 vertical levels. The

vertical grid-spacing is refined near the top and bottom boundaries to 3 m to better resolve the boundary layer processes of interest and increases gradually to a maximum of 32.5 m in the interior.

A series of simulations are carried out with horizontal grid resolutions of 4 km, 2 km, 1 km and 0.5 km. The 4 km run acts as the control for our experiment, though comparisons are made with observations to ensure the model state is a reasonable representation of the real ocean. The simulations are run on the UK ARCHER supercomputer, which is a Cray XC30 system. All of the runs are integrated for at least five years with the fifth year used to perform the main analysis in Chapter 3.

2.3 Numerical configuration

A linear equation of state in temperature is employed and so buoyancy gradients are proportional to temperature gradients with a thermal expansion coefficient of 2×10^{-4} K^{-1}. Simulations of geostrophic turbulence generate a downscale cascade of enstrophy that must be dissipated to prevent it accumulating at the grid-scale. In order to do so, diffusion is applied to horizontal gradients in temperature. Enstrophy is also dissipated in the momentum equation using adaptive viscous schemes first developed by Smagorinsky [1963], Leith [1996] and Fox-Kemper and Menemenlis [2013]. Recent results show that adaptive viscous schemes are necessary to allow submesoscale turbulence to develop [Ilicak et al., 2012; Graham and Ringler, 2013; Ramachandran et al., 2013]. For both diffusion and viscosity, biharmonic operators are chosen over Laplacian operators so that explicit diffusion and viscosity are targeted at the highest wavenumbers [e.g. Griffies and Hallberg, 2000; Graham and Ringler, 2013]. At all resolutions the Smagorinsky coefficient is 3, while the Leith and modified Leith coefficients are 1. The biharmonic temperature diffusion coefficient is 4×10^{7} m^{4} s^{-1} at 4 km resolution and reduced by a factor of four for each doubling in resolution. A partial-slip bottom boundary condition is imposed with a quadratic bottom drag [Arbic and Scott, 2008] using a non-dimensional quadratic drag coefficient of 3×10^{-3}.

In addition, vertical mixing of both heat and momentum is carried out with a Laplacian operator with a constant diffusion coefficient of $4\times\ 10^{-5}$ m^{2} s^{-1}. The mixed layer depth is defined throughout as the first depth where the temperature difference from the surface is greater than 0.1° C.

The advection of temperature is carried out using the Prather scheme [Prather, 1986]. This is an upwind scheme that conserves second-order moments in sub-grid tracer distributions and so helps to preserve the sharp frontal structures of interest. No flux limiter is employed for the experiments in Chapter 3. Hill et al. [2012] show that the effective diffusivity of the Prather scheme is similar to the level of diffusion estimated for the real ocean by tracer release studies. The model's default second-order centered advection scheme is employed for momentum. The timestep is 400 s at 4 km resolution and is then reduced by a factor of two with each doubling in resolution.

2.4 Parameterisations

In the vertical, the model is run with the *K*-profile parameterisation (*KPP*, Large et al. [1994]) for the surface boundary layer. This scheme is in practice a suite of parameterisations that aim to represent a number of mixed layer processes. The *KPP* scheme increases the vertical viscous/diffusive coefficients (hereafter 'diffusive coefficients') based on the surface wind stress. It also increases the diffusive coefficients if there is elevated shear at the base of the mixed layer based on a Richardson number criterion. In the event of destabilising surface buoyancy forcing the *KPP* scheme introduces a vertical non-local transport to capture the effect of vertical convective mixing [Marshall and Schott, 1999]. Finally, it also applies higher diffusive coefficients in the event of negative stratification, even if this is not associated with destabilising surface buoyancy forcing as can occur in the presence of down-front winds, as defined in Chapter 1.2.4. In these cases of static instability the *KPP* scheme applies a high (5×10^{-3} m^2 s^{-1}) vertical diffusion coefficient rather than instantaneously mixing buoyancy as done by the default MITgcm convective adjustment scheme or the Price-Weller-Pinkel [Price et al., 1986] scheme.

2.5 Initial and boundary conditions

The model is initialised at rest with a horizontally uniform temperature profile. The initial vertical temperature profile (Figure 2.1, left panel) is derived from an Argo float at the Porcupine Abyssal Plain observation site. This profile was sampled on 23rd March 2012 and is selected as a temperature profile with minimal signs of internal wave heaving or instrument noise. The model is integrated on

an f-plane with a Coriolis frequency $f = 10^{-4}$ s^{-1}. Note that no temperature relaxation conditions are employed and so the model solution can evolve freely. The initial condition is chosen as a representative profile of the observation site that should help produce an eddy field with similar characteristics.

The model is forced at the surface by a heat flux and wind forcing. The prescribed heat flux is uniform across the domain and averages to zero over each 360-day year (Fig. 2.1, right panel) with values based on the sum of the net shortwave, longwave, sensible and latent heat fluxes from the monthly climatology of Berry and Kent [2009] for the Porcupine Abyssal Plain observation region. These heat fluxes are applied to the uppermost model level. As such, heating fluxes result in a more rapid restratification than in the real ocean where shortwave radiative fluxes penetrate in an exponentially decaying manner through the water column. The experiment aims to understand the response of mixed layer dynamics to the seasonal cycle in buoyancy forcing. Higher frequency variability, including diurnal effects, are not included in the main experiments described here. An alternative experiment that does include higher frequency buoyancy forcing is run at 2 km resolution but produced similar results. This is discussed in Chapter 3.

References are made to 'summer' and 'winter' as shorthand for the periods of heating and cooling respectively. The model integration begins with stratification derived from late March conditions – as such the heating period is the first half of every model year and the cooling period is the second half. To aid readability and comparisons with observations from the real ocean, the model outputs are equated with the month they correspond to from the buoyancy forcing.

While the surface heat flux creates an annual cycle in stratification and mixed layer depth, the wind forcing produces a field of geostrophic turbulence and an Ekman transport in the near-surface. The forcing scheme used is based on that of Koszalka et al. [2009] with a streamfunction (ψ) to generate the wind stress that varies in space and time. The consequent curl of the wind stress causes isopycnals to tilt locally through Ekman pumping or suction. The velocity field undergoes Rossby adjustment to the tilt of the isopycnals and the non-linear eddy interactions then induce a turbulent eddy field.

The streamfunction is constructed using zonal and meridional Fourier modes, an example of which can be seen in Figure 2.2. Unlike Koszalka et al. [2009], where a random component to each streamfunction is introduced in Fourier

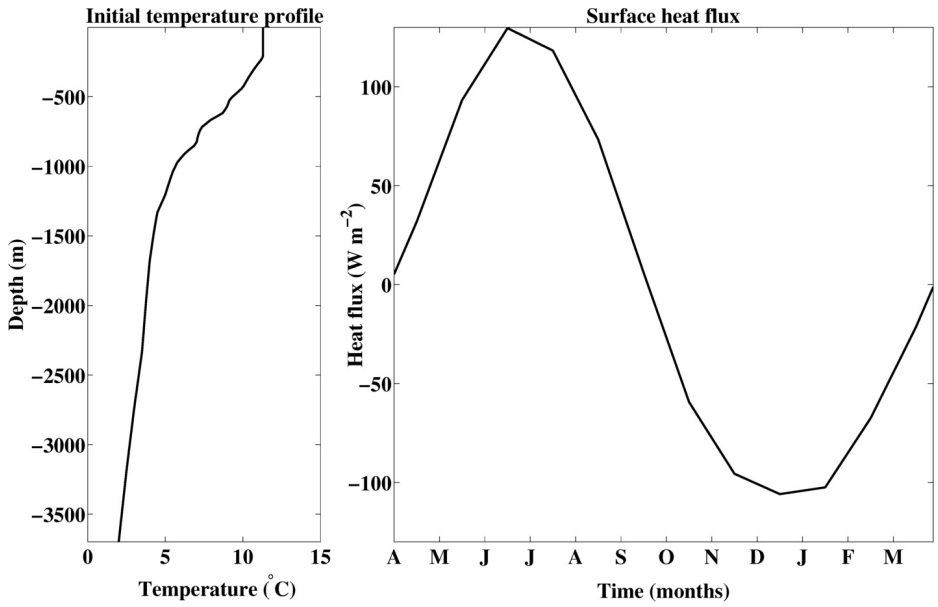

Figure 2.1: (Left panel) The initial temperature profile for all simulations. (Right panel) The heat flux into the domain through the year. The model 'summer' is the first half of the year and the model 'winter' is the second half.

space, a random phase is added onto each streamfunction component-pair in order to randomise the geometric structure of the forcing from month to month:

$$\psi = \psi_0 \sum_{k,l=1}^{3} \sin\left(kx + \phi_1(k,l)\right) \sin\left(ly + \phi_2(k,l)\right), \tag{2.1}$$

where $\psi_0 = 0.02$ N m^{-1}, x and y are the zonal and meridional coordinates respectively, k and l are the zonal and meridional domain wavenumbers respectively, and ϕ_i is a random phase. A new streamfunction is generated each month and the model linearly interpolates between the successive streamfunctions to give a wind field that varies smoothly in time. Inspection of the results show this gives rise to a small amplitude monthly cycle that is not readily apparent in the key model outputs in the presence of the generally turbulent flow. The streamfunction for wind forcing is produced for the 4 km run and then interpolated to the finer resolutions.

In addition, a constant zonal wind of 0.05 N m^{-2} is added to ensure the mixed layer depth extends beyond the uppermost model layer during periods of stabilising heat forcing such that the vector wind stress $\tau = 0.05\mathbf{i} + \mathbf{k} \times \nabla\psi$ where $\mathbf{i}$ is the zonal unit vector and $\mathbf{k}$ is the vertical unit vector. The constant zonal wind is about five times larger than the root-mean-square magnitude of the spatially-varying wind derived from the streamfunction in equation (2.1), and so it is the

main driver of the Ekman transport.

The wind forcing has length scales of 20 - 256 km and so is smaller than the atmospheric length scales with the greatest energy in the mid-latitudes [Nastrom and Gage, 1985]. However, the length scales of the forcing are still larger than the baroclinic deformation radius of approximately 40 km. A test experiment was carried out where a wind streamfunction that was constant in time. Analysis of this run after one year showed no imprint of the wind-forcing in the buoyancy or sea surface height fields. This provides confidence that the non-linear dynamics of the eddy field dominate the solution, rather than the detailed structure of the wind forcing. The wind forcing in this experiment is continuous, but weak, with a magnitude about one-third of the root-mean-square wind forcing estimated from the ERA-interim re-analysis for the region.

2.6 Spin-up and inter-annual variability

At the outset of the runs, the solutions are similar across the range of resolutions as shown in Figure 2.3 (all panels). The solutions begin to diverge between resolutions after about 120 days both in terms of the standard deviation of sea surface temperature (top panel) and mean kinetic energy at the surface (centre panel). From the third year of the simulations the differences between the years at a given resolution are in the range of year-to-year variability (top and centre panels). Particular results with greater inter-annual variability are noted in the results in Chapter 3. The mean energy input from the wind is similar at all resolutions (Fig. 2.3, bottom panel). There is a seasonal cycle in wind energy input with amplitude of just over 10% of the mean value. This reflects stronger surface velocities when the mixed layer is shallow in the summer.

2.7 Interpolation experiments

A set of experiments is conducted in Chapter 4 where the initial state is taken from the 4 km simulation in early December of the fifth model year and interpolated to finer resolution grids. These are referred to as the 'interpolation experiments'. To examine the effect of resolution, an additional interpolation experiment is carried out at 250 m horizontal resolution. Due to computational expense this run at 250 m resolution is limited to 12 days, while the range of resolutions used in Chapter 3 are run for at least 30 days.

The interpolation experiments take the model state in late December (Year 4.66) as their starting point. The temperature, horizontal velocity and free surface fields are then interpolated to finer grids using a 2D spline method. The original 4 km model state is also interpolated in this way onto a 4 km grid to ensure consistency in the comparison between resolutions. The model is then integrated from this initial condition. For these interpolation experiments the surface boundary conditions are simplified to be a constant heat loss of 75 W m^{-2} and a zonal wind of 0.05 N m^{-2} with no spatial structure. The advection scheme in the interpolation experiments is the flux-limited version of the Prather scheme. This is to avoid spurious negative concentrations of the additional tracers used in these experiments. This flux-limited scheme is used for both the active temperature and passive tracers to ensure consistency of fluxes.

Further interpolation experiments with the same initial and boundary conditions are carried out with a passive tracer to track downwelling of particles from the surface layer. The tracer concentration is set to 1 everywhere in the 3 m thick surface level of the model and 0 everywhere else. For the sake of clarity, in this thesis the term 'level' refers to a row in the model grid, whereas the term 'layer' is a qualitative term for vertical regions with similar properties. This tracer release is done in practice using the salt field in the MITgcm with the saline buoyancy coefficient set to 0 to ensure it behaves as a passive tracer.

2.8 Biogeochemical package

2.8.1 Description of biogeochemical package

The simulations employ the biogeochemical package[Dutkiewicz et al., 2005] of the MITgcm. The package employs four biogeochemical tracers: dissolved inorganic carbon (DIC), alkalinity (ALK), phosphate (PO_4) and dissolved organic phosphorous (DOP). The prognostic equation for any of these tracers is

$$\frac{\partial A}{\partial t} = -\nabla \cdot (\mathbf{u}A) + \nabla \cdot (\mathbf{K}A) + S_A \tag{2.2}$$

where A is a tracer, t is time, ∇ is the three dimensional gradient operator, $\mathbf{u}$ is the three dimensional velocity vector, $\mathbf{K}$ is the mixing tensor and S_A is the source or sink due to biogeochemical processes. In these simulations the advective term $\mathbf{u}A$ is calculated using the flux-limited Prather advection scheme. The mixing tensor

K only has terms on the main diagonal due to the *KPP* scheme in the surface mixing layer.

The prognostic equations for the biogeochemical tracers are

$$S_{DIC} = r_{C:P} S_{PO_4} + J_{C_a}, \tag{2.3}$$

$$S_{ALK} = -r_{N:P} S_{PO_4} + 2J_{C_a}, \tag{2.4}$$

$$S_{PO_4} = -J_{prod} - \frac{\partial F_P}{\partial z} + \kappa_{remin}[DOP], \tag{2.5}$$

$$S_{DOP} = f_{DOP} J_{prod} - \kappa_{remin}[DOP], \tag{2.6}$$

where $r_{C:P} = 117$ is the ratio of carbon to phosphorous, $r_{N:P} = 16$ is the ratio of nitrogen to phosphorous, $\kappa_{remin} = 0.95$ yr^{-1} is the remineralization rate. The export of carbon to depth as calcium carbonate is

$$J_{Ca} = -R r_{C:P}(1 - f_{DOP}) J_{prod} + \frac{\partial F_{CaCO3}}{\partial z}, \tag{2.7}$$

where $R = 0.05$ is the rain ratio, $f_{DOP} = 0.67$ is the fraction of new production going to dissolved organic phosphorous. The biological production is

$$J_{prod} = \alpha \frac{I}{I + \kappa_I} \frac{PO_4}{PO_4 + \kappa_{PO_4}} \tag{2.8}$$

where $\alpha = 3$ mmol m^{-3} yr^{-1} is the maximum community production rate, $\kappa_I = 25$ W m^{-2} is the half light saturation, $\kappa_{PO_4} = 5$ mmol m^{-3} is the phosphate half saturation. I is the photosynthetically available radiation at a given depth

$$I = f_{PAR} Q_{sw} e^{-kz}, \tag{2.9}$$

where $f_{PAR} = 0.4$ is the photosynthetically available radiation fraction, Q_{sw} is the downwelling shortwave radiation and $k = 0.02$ is the light attenuation coefficient. Q_{sw} is set based on the latitude implied by the Coriolis frequency of 10^{-4} s^{-1} which is approximately 43°N, as

$$Q_{\mathrm{SW}} = C(1 - a)\cos(\theta_{zen})\mathrm{Df}, \tag{2.10}$$

where $C = 1360$ W m^{-2} is the solar constant, $a = 0.6$ is the planetary albedo, θ_{zen} is the average zenith angle and Df is the daylight fraction at that time of year and latitude. The zenith angle is constant in time and set to reflect early April conditions in the model. This gives $Q_{\mathrm{SW}} \sim 55$ W m^{-2}.

The proportion of the biological production that becomes particulate organic phosphorous (POP) is parameterized as remineralizing to phosphate. This flux is given by

$$F_P = (1 - f_{DOP}) J_{prod} \triangle z (\frac{z}{z_c})^{-a_{remin}} \tag{2.11}$$

where z_c is the depth of the base of each layer, with thickness $\triangle z$, where production occurs and $a_{remin} = 0.9$ is chosen to produce remineralization over distances of a few hundred metres. The flux of CaCO3 is given by

$$F_{CaCO3} = R r_{C:P} (1 - f_{DOP}) J_{prod} \triangle z e^{-(z - z_c)/d_{Ca}} \tag{2.12}$$

where d_{Ca} is the vertical decay scale of the flux of CaCO3.

2.8.2 Initial and boundary conditions

The basis of the experiment is to configure the model so that primary productivity is restricted by the absence of a limiting nutrient from the near-surface euphotic layer. The limiting nutrient is chosen to be phosphate. This limiting nutrient has an initial concentration of 0 in the mixed layer, but is present in the thermocline where it has a similar distribution to potential vorticity. Therefore, the concentration of phosphate is set to 0 mol m^{-3} in the upper 51 m and below this the concentration is set equal to $10^5 q$. The other two fields required for biological productivity are oxygen and dissolved inorganic carbon. The distribution of these are heavily saturated with initial concentrations of 3 mol m^{-3} everywhere in the model domain to ensure dependence of biological productivity on the limiting nutrient.

2.9 Averaging operator

The averaging operator denoted throughout this thesis by an overbar is a horizontal average over a model level:

$$\overline{g(\mathbf{x}, t)} = \frac{1}{A} \int_x \int_y g dx dy, \tag{2.13}$$

where g is an arbitrary function, $\mathbf{x}$ is the position vector, t is time and A is the horizontal area.

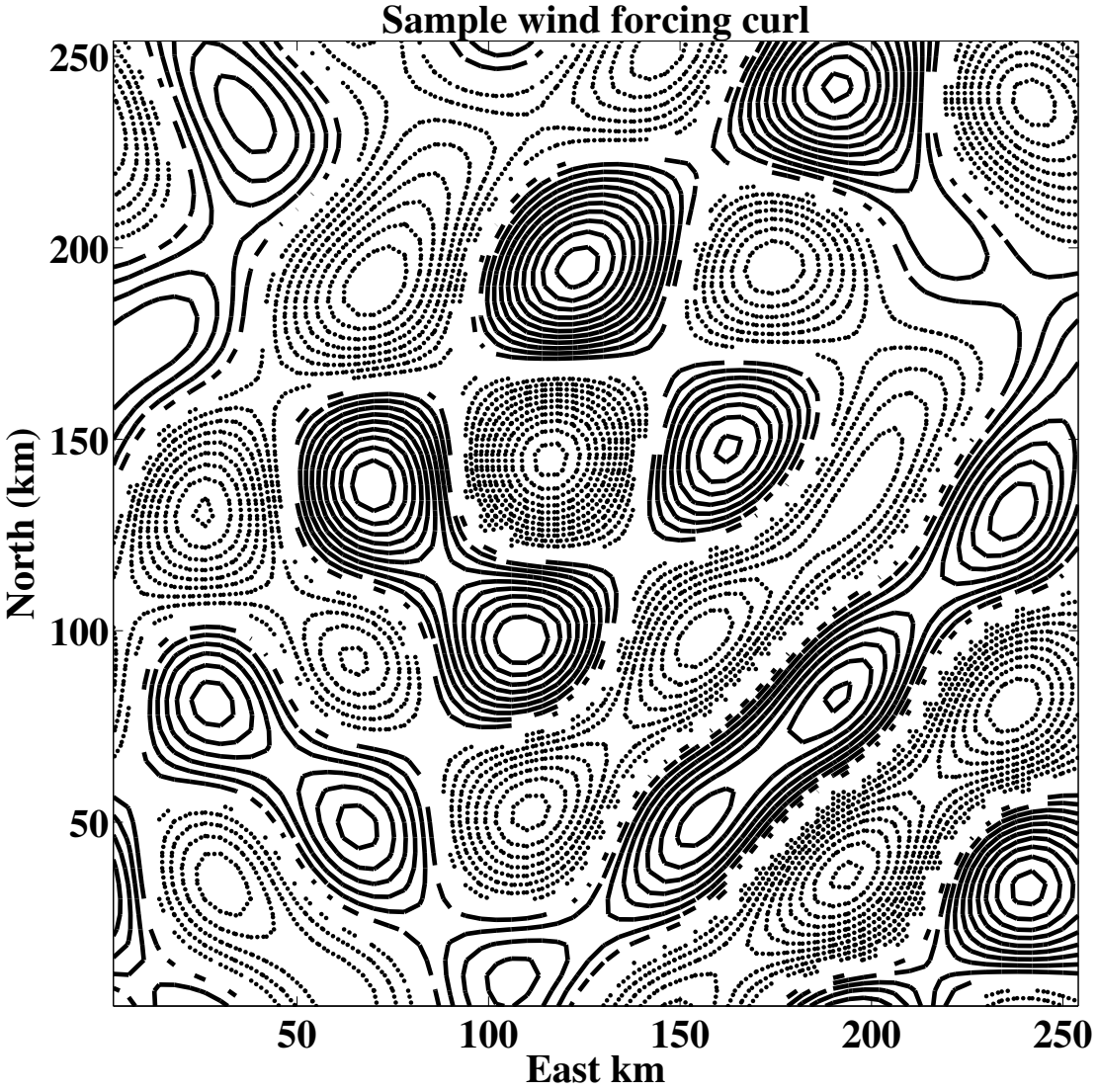

Figure 2.2: A snapshot of the wind-forcing used in the model for one month, presented as the curl of the streamfunction. Solid lines are positive contours and dotted lines are negative contours with intervals of 10^{-7} m s^{-2}.

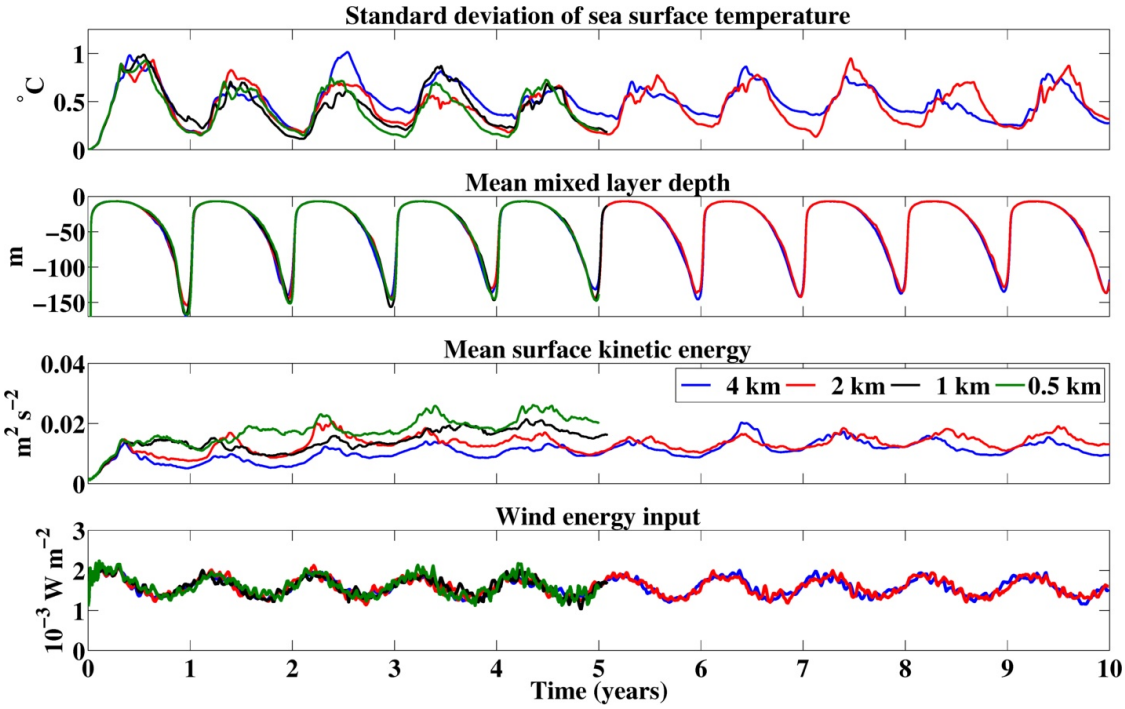

Figure 2.3: Model fields during spin-up. (Top panel) Standard deviation of sea surface temperature. (Centre panel) Mean kinetic energy at the surface. (Bottom panel) The mean input of kinetic energy by the wind stress $\tau \cdot \mathbf{u}$. The two coarser resolution simulations have been run for a further five years to year 10.

CHAPTER 3

Seasonal cycle of submesoscale flows

3.1 Introduction

The upper ocean stratification is an important control on the transfer of momentum and tracers between the atmosphere and ocean interior. The development of upper ocean stratification has historically been viewed as a one-dimensional process driven by surface buoyancy and frictional fluxes, with allowance for shear-driven mixing at the base of the mixed layer. These ideas are encapsulated in a number of one-dimensional parameterisation schemes for the surface boundary layer [e.g. Price et al., 1986; Large et al., 1994]. Attention has since focused on the role other processes may play in setting upper ocean stratification such as geostrophic adjustment [Tandon and Garrett, 1994; Young, 1994; Dale et al., 2008], frontogenesis [Hoskins and Bretherton, 1972; Lapeyre et al., 2006; Shakespeare and Taylor, 2013; Gula et al., 2014], Langmuir turbulence [Grant and Belcher, 2009; Hamlington et al., 2014; Sutherland et al., 2014], Ekman buoyancy fluxes [hereafter EBF, Thomas, 2005; Thomas et al., 2008, 2013], symmetric and inertial instabilities [e.g. Thomas et al., 2013; Thomsen et al., 2013; Bachman and Taylor, 2014], and mixed layer baroclinic instabilities [Samelson, 1993; Boccaletti et al., 2007; Mahadevan et al., 2010; Skyllingstad and Samelson, 2012; Brüggemann and Eden, 2014] amongst others. While there is evidence for each of these processes affecting upper ocean stratification, the interactions between them and their relative strength over the annual cycle remain major outstanding questions [e.g. Capet

et al., 2008b; Lévy et al., 2010; Taylor and Ferrari, 2010; Belcher et al., 2012; Haney et al., 2012; Mensa et al., 2013; Hamlington et al., 2014].

3.1.1 Chapter aims and outline

This Chapter examines the results of the simulations whose numerical configuration is set out in Chapter 2. The results are compared between resolutions and through the seasonal cycle. The distribution of buoyancy is considered in Chapter 3.2, the velocity fields are set out in Chapter 3.3, momentum balances are shown in Chapter 3.4 while individual frontal processes are diagnosed in Chapter 3.5 before concluding with a discussion in Chapter 3.6.

3.2 Buoyancy field

3.2.1 Vertical buoyancy distribution

Level mean vertical temperature profiles ($\overline{T}$) in September at the end of the summer and in March at the end of winter are shown in Figure 3.1. The difference in mean temperature between the runs falls to zero by 350 m depth. This shows that the surface layer is cooler at finer resolution while the upper-thermocline is warmer.

The mixed layer depth over the five years of the simulations are shown in Figure 3.2 (upper panel). The deepest mean mixed layer depth in the simulations is typically in the range of 140-170 m. Mixed layer depths are less than 10 m in summertime at all resolutions, due to the strong stabilising buoyancy forcing and lack of nighttime cooling. There is year-to-year variability in the depth of the maximum mean mixed layer in winter and the resolution dependence is difficult to see in the upper panel of Fig. 3.2. The differences between the resolutions are somewhat clearer in the lower panel of Fig. 3.2, where the mean mixed layer depth is averaged by year-day over years 2 to 5. This shows that the mean mixed layer in the two coarser resolution runs tends to deepen somewhat faster early in the winter than the finer resolution runs (October - February in Fig. 3.2, lower panel). However, the finer resolution runs then continue to deepen until late March in the model, leading to deeper mean mixed layers in the multi-year average at finer resolution. This result perhaps runs counter to an expectation that simulations that can better resolve restratifying mixed layer instabilities [Boccaletti et al., 2007] and frontogenesis [Lapeyre et al., 2006] should have shallower mixed layers.

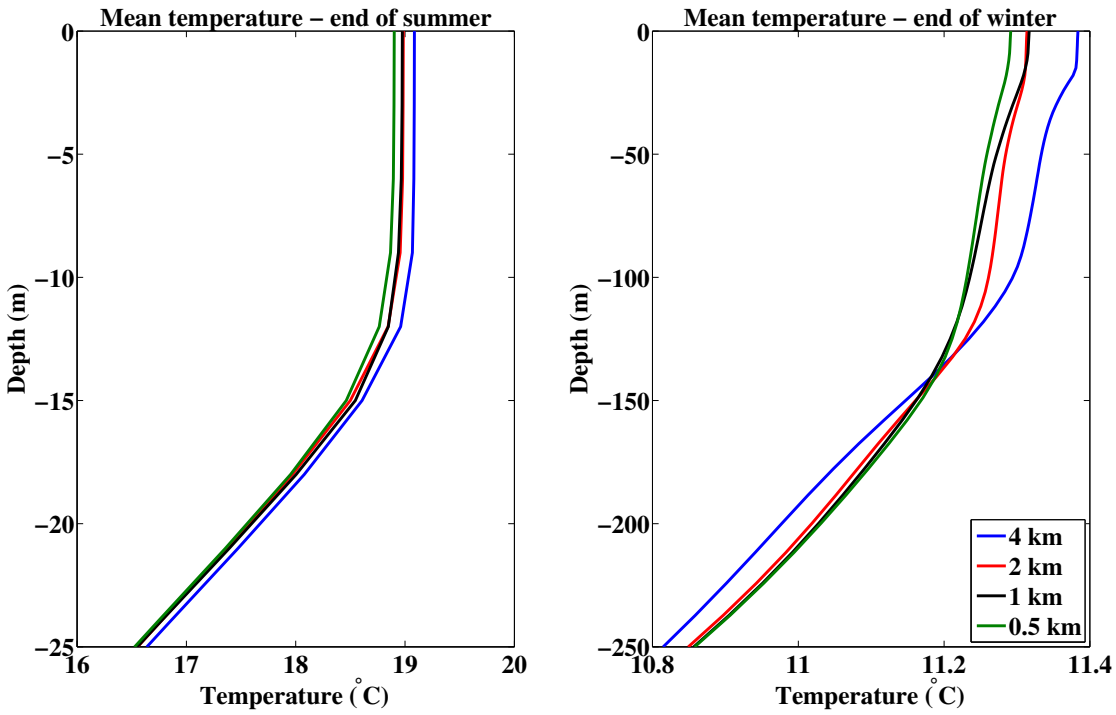

Figure 3.1: Mean temperature profiles. (Left panel) The temperature profile at the end of September in the fifth model year. (Right panel) The temperature profile at the end of March in the fifth model year. Note the different scales on both axes.

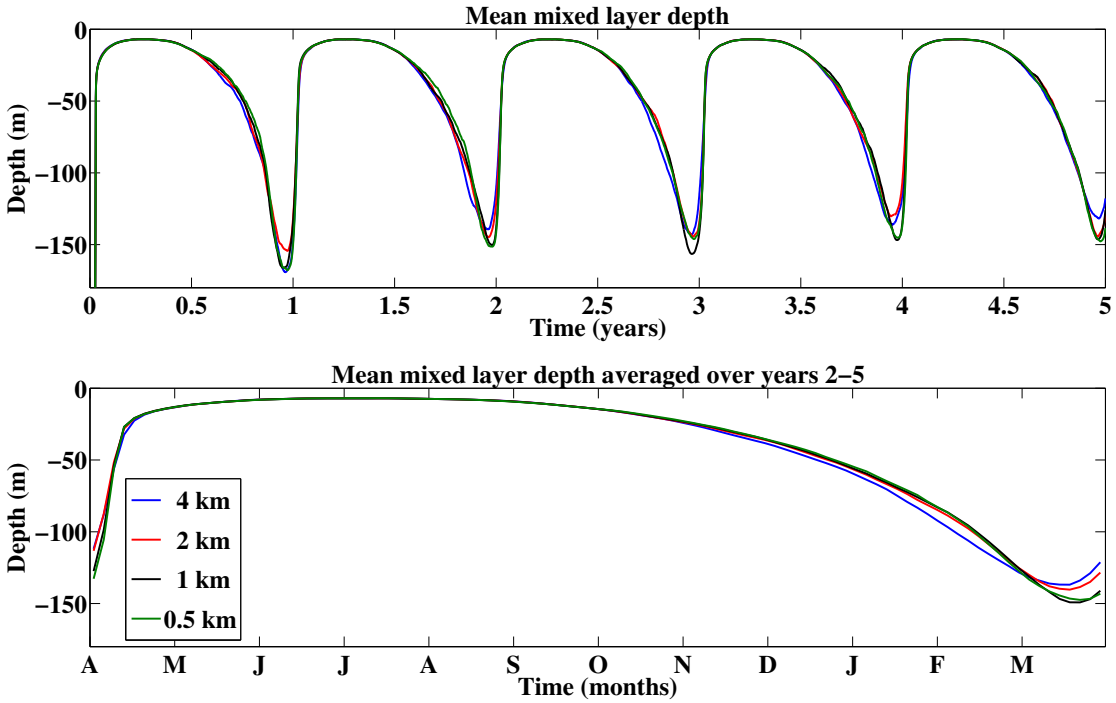

Figure 3.2: The mean mixed layer depth. (Upper panel) The mean mixed layer depth over the first five years of the simulations. (Lower panel) The mean mixed layer depth through the seasonal cycle averaged by year-day over years 2 to 5.

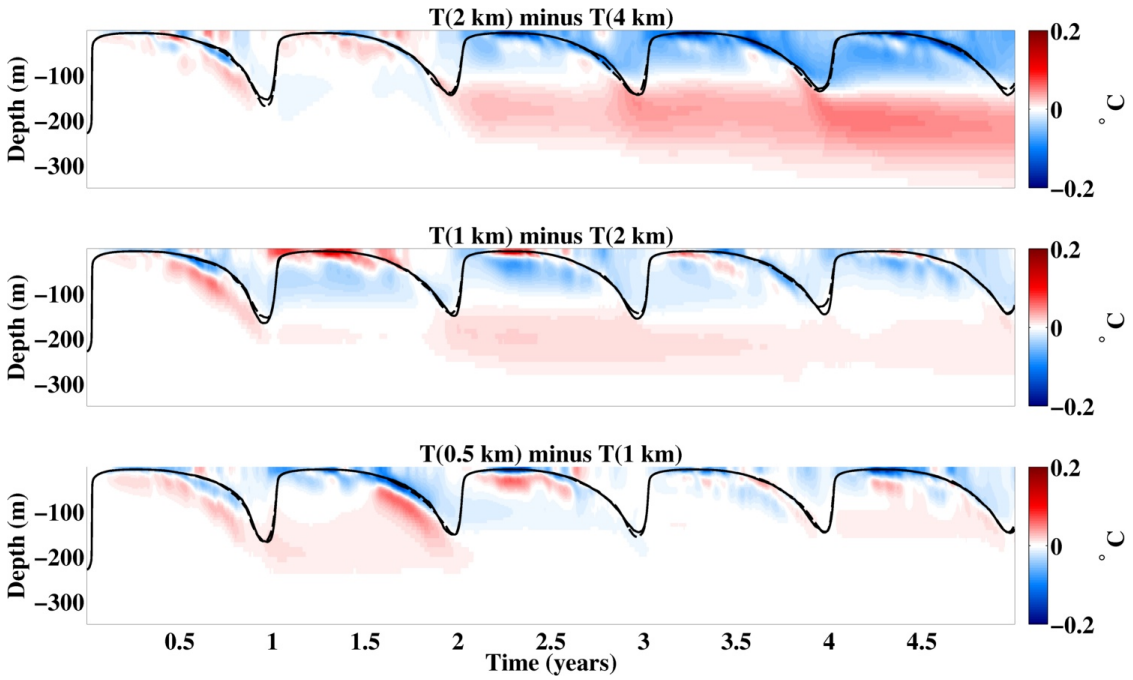

Figure 3.3: Difference in level-mean temperature between resolutions. The upper three panels compare the 2 km, 1 km and 0.5 km runs with the next coarsest resolution. Red colours mean that the finer resolution run is warmer. The solid (dashed) black line is the mean mixed layer depth of the finer (coarser) resolution run.

The mean mixed layer depth provides a one-dimensional view of the vertical distribution of buoyancy in the upper part of the domain. However, it is somewhat sensitive to the definition of mixed layer depth employed. A more comprehensive picture of the relative buoyancy profile is obtained by subtracting the mean temperature of the next coarsest run from each of the 2 km, 1 km and 0.5 km runs over the five years of the simulations. This is shown in Figure 3.3 where red colours correspond to the finer resolution run being warmer. The major feature of the plot is that as the resolution is made finer, the mixed layer becomes cooler and the layer below the deepest mean mixed layer depth becomes warmer.

To examine this vertical structure in relative temperature in more detail, consider how the temperature difference evolves in the first year between the 0.5 km and 4 km resolution simulations in Fig. 3.4 (top panel). From April to September of the first year (year 0 - 0.5) the mixed layer shallows almost to the surface as heating is applied. In this period the mixed layer is cooler at finer resolution, but the highly stratified layer from 10 to 50 m depth is warmer at finer resolution. Therefore, there is an additional transport of heat downwards at finer resolution.

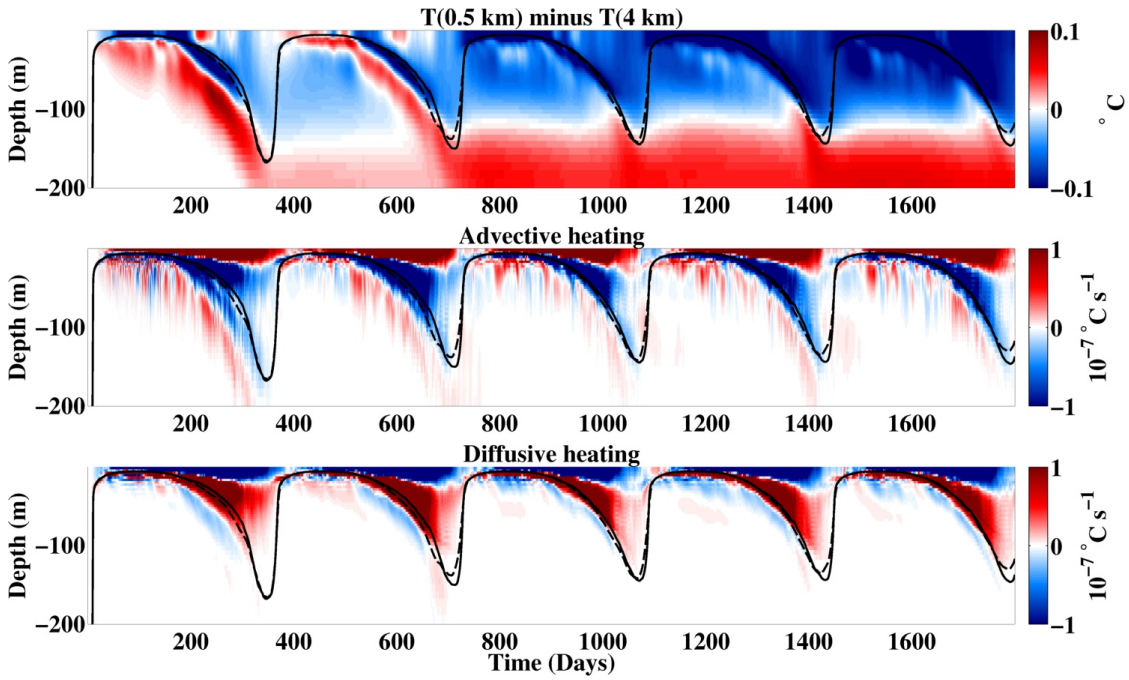

Figure 3.4: Advective and diffusive contributions to temperature differences. (Upper panel) Difference in level-mean temperature ($\overline{T}_{0.5km} - \overline{T}_{4km}$). (Centre panel) Additional heating effect of mean vertical advective fluxes at finer resolution. (Lower panel) Additional heating effect of mean diffusive advective fluxes at finer resolution. Red (blue) colours in the centre and lower panel corresponds to a heating (cooling). The colour scale is saturated by a factor of 10 to show the heating effects in the thermocline. The solid (dashed) black line is the mean mixed layer depth of the 0.5 km (4 km) resolution run.

As the mixed layer begins to deepen from September in the first year (year 0.5 - 1.0 in the top panel of Fig. 3.4), two separate responses are evident. Firstly, the near-surface mixed layer at finer resolution is warmer for a period of about 30 days in early winter. This is shown by the red patch in Fig. 3.4 (top panel) at year 0.6 in the upper 30 m. This near-surface warming is consistent with stronger thermally direct flows such as frontogenesis or overturning instabilities in the winter mixed layer at finer resolution. The second effect is the relative cooling of the mixed layer at finer resolution and the relative warming of the thermocline (year 0.5-1.0). The warming of the thermocline continues throughout the winter. The eventual relative cooling of the mixed layer after the initial relative warming at finer resolution is thus due to the entrainment of cooler waters at the base of the mean mixed layer. Inspection of the upper three panels in Fig. 3.3 shows that the same warming of the thermocline occurs with each increase in resolution. The effect is most pronounced with the grid refinement to 2 km and 1 km. The

main difference between the two finest resolution runs is that the warming occurs earlier in the run at 0.5 km resolution.

Given that frontogenesis and baroclinic instability are both restratifying and become stronger as the resolution is made finer over this range, a first hypothesis is that the relative cooling of the mixed layer and warming of the thermocline is due to stronger diffusive processes at finer resolution. These stronger diffusive fluxes could reflect stronger mixing due to convection triggered by down-front winds [Thomas and Lee, 2005] or lower Richardson numbers at the base of the mixed layer [Large et al., 1994] that lead to shear mixing in the *KPP* scheme [1].

The vertical heat budget for a model level is

$$\frac{d\overline{T}}{dt} + \overline{\frac{d(wT)}{dz}} = \overline{\frac{d}{dz}(\frac{KdT}{dz} - \eta)} \tag{3.1}$$

where the diffusive coefficient K is the sum of the constant vertical diffusive coefficient and the higher diffusive coefficient set by the *KPP* scheme in the mixing layer and η is the heat flux due to the non-local convective adjustment in *KPP* [Large et al., 1994]. The diffusion and convective adjustment terms are combined as the diffusive terms (DF).

The contribution of advective and diffusive terms to the relative heating effect is shown in Fig. 3.4. The divergence of the vertical advective fluxes (centre panel) lead to additional heating of the upper mixed layer and cooling the lower mixed layer, consistent with a stronger thermally direct circulation at finer resolution. The diffusive fluxes offset this by cooling the upper mixed layer and warming the lower mixed layer. Below the mean mixed layer, however, the centre panel shows that excess heating at finer resolution is due to stronger advective heating. Thus, the hypothesis that the relative warming of these depths at finer resolution is diffusive is rejected. Diagnosing the exact physical processes responsible for the relative warming of the thermocline depths at finer resolution is challenging, however, as the model state varies between the different runs due to non-linear eddy interactions. To make progress in understanding the changes in vertical buoyancy distribution between the resolutions, the model state at 4 km resolution is interpolated to to the finer resolution grids when it has been spun-up. This is carried out as part of the experiment in Chapter 4.

[1] A further hypothesis of course is that the thermally-indirect circulation is a consequence of Ekman pumping generated by the artificially small-scales of the wind-forcing. A further experiment discussed in Chapter 4.9.4 with a spatially uniform wind replicates the thermally-indirect circulation and so the structure of the wind-forcing can be rejected as the primary cause.

3.2.2 Horizontal buoyancy distribution

Qualitative differences in the horizontal distribution of buoyancy are illustrated in the snapshots of the magnitude of buoyancy gradients ($|\nabla_h b|$, where ∇ is the gradient operator, h denotes the horizontal components and b is the buoyancy defined in Chapter 1) at the sea surface in Figure 3.5. These snapshots are from January of the fifth year of the simulations, when the mean mixed layer depth is approximately 90 m. Fig. 3.5 shows that fronts become stronger, sharper and more sinuous as the resolution is made finer. In contrast to Capet et al. [2008b], filamentary submesoscale features are also present inside the large vortices in wintertime, for example in the anticyclone at (50 km, 50 km) in the lower-right panel of Fig. 3.5. The properties of these filaments are considered further in Chapter 3.4 and in more detail in Chapter 4.

Values of $\overline{|\nabla_h b|}$, the level-mean magnitude of the horizontal buoyancy gradient through the seasonal cycle are shown in Figure 3.6. The root-mean-square magnitude of these gradients is of order 10^{-7} s^{-2}, with the largest values an order of magnitude stronger (Fig. 3.5, lower-right panel), typical of those observed in the mid-latitude mixed layer [Hosegood et al., 2006].

At the start of the heating period – for example in May in Fig. 3.6 (upper panel) – the mean gradients are low at all resolutions in the mixed layer. As the heating period progresses $\overline{|\nabla_h b|}$ increases more quickly as the resolution is made finer, for example in July in Fig. 3.6 (upper panel). The strength of the buoyancy gradients then decreases more rapidly at finer resolution in the cooling period as the mixed layer begins to deepen (October to March in Fig. 3.6, upper panel). There is significant variation in the values of $\overline{|\nabla_h b|}$ from year-to-year, though the annual cycle persists. The vertical structure of $\overline{|\nabla_h b|}$ in Fig. 3.6 (lower panels) shows that strong gradients in summer are not restricted to the mean mixed layer. As the mixed layer deepens the strength of the horizontal gradients decreases in a similar way with depth in the mixed layer (lower panels). However, a tongue of stronger gradients persists at the base of the deepening mixed layer. This tongue of stronger gradients is increasingly apparent as the resolution is made finer (lower-right panel).

While $\overline{|\nabla_h b|}$ captures variability at smaller scales, the horizontal distribution of buoyancy over the whole surface level can be considered using the power spectral density (PSD) of sea surface temperature (SST). The spectra are calculated in horizontal wavenumber shells after the application of a 2D Hanning window. As for

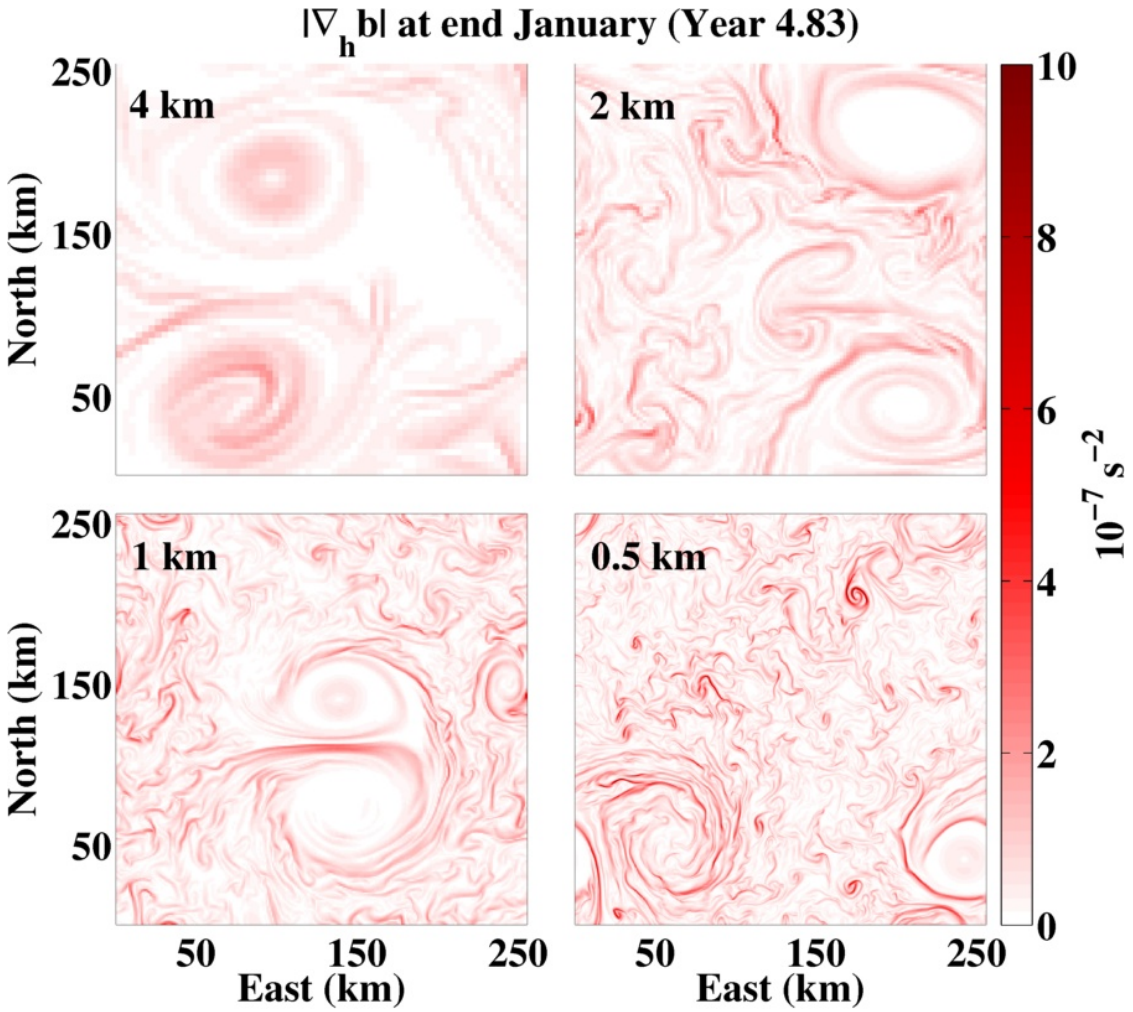

Figure 3.5: A snapshot of the magnitude of the sea surface buoyancy gradients at the indicated grid resolutions. The outputs are derived from the model state in late January at year 4.83 when the mean mixed layer is approximately 90 m deep.

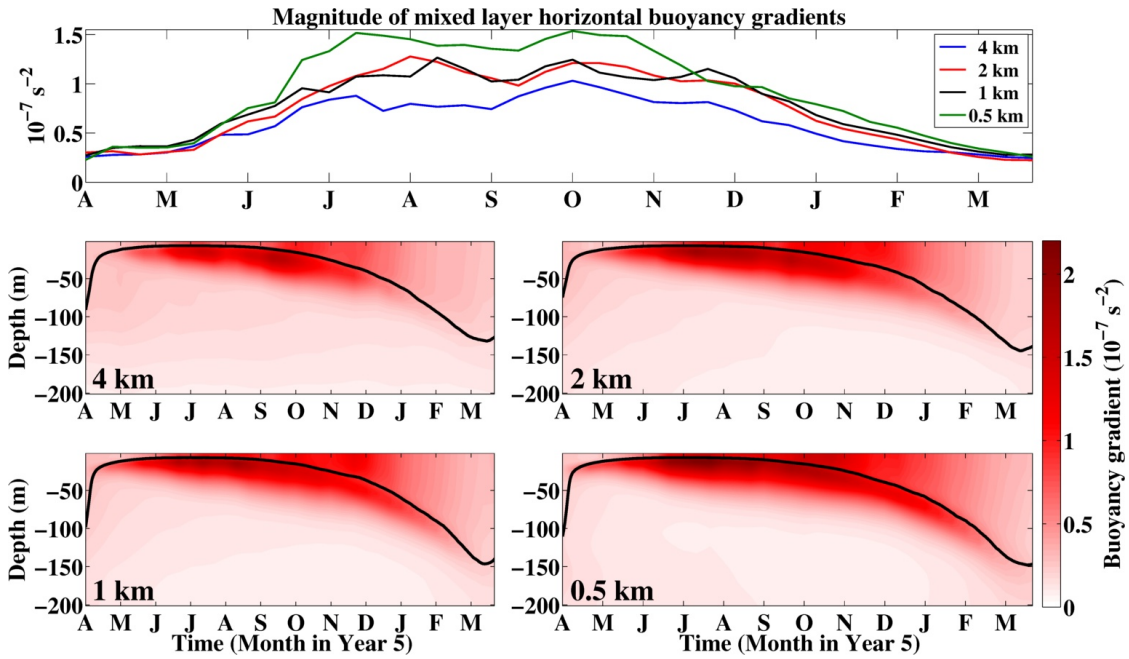

Figure 3.6: The mean horizontal buoyancy gradient $\overline{|\nabla_h b|}$ over the fifth year of the simulations at 10-day intervals. (Upper panel) The mean horizontal buoyancy gradient in the mixed layer. (Lower panels) The vertical profile of $\overline{|\nabla_h b|}$. The black line in the lower panels shows the mean mixed layer depth at that time.

Capet et al. [2008d] the spectra are multiplied by four to recover the variance from before the windowing operation. Figure 3.7 shows the spectra averaged over the summer and winter months. There is an increase in energy at shorter wavelengths as the resolution is made finer, previously found by Capet et al. [2008b]. A comparison of the upper panels in Fig. 3.7 shows that in winter there is less energy in the mesoscale (30-100 km) range than in summer, but similar or greater energy in the submesoscale range (1-10 km). In effect, the spectral slope of SST shallows from summer to winter, suggesting that submesoscale processes are stronger in winter.

3.3 Velocity field

The mean kinetic energy increases as the resolution becomes finer both at the surface and in the model interior (Figure 2.3, centre panel), despite the energy input from wind forcing being of similar magnitude across the range of resolutions (Figure 2.3, bottom panel). The root-mean-square velocities are about 15 cm s^{-1} at fine resolution, which is about 30% less than those observed at the observation

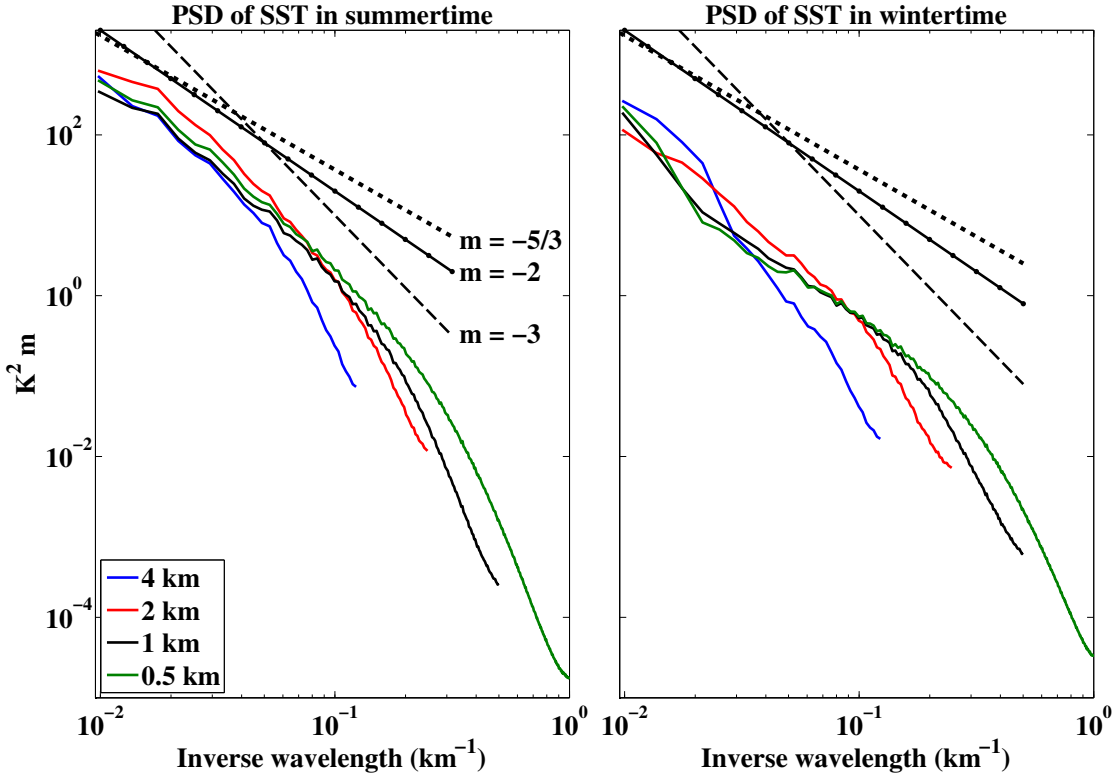

Figure 3.7: The power spectral density of sea surface temperature. (Left panel) The horizontal spectra averaged over the summertime months (April - September). (Right panel) The horizontal spectra averaged over the wintertime months (October - March). The dotted lines show reference slopes m in log-log space.

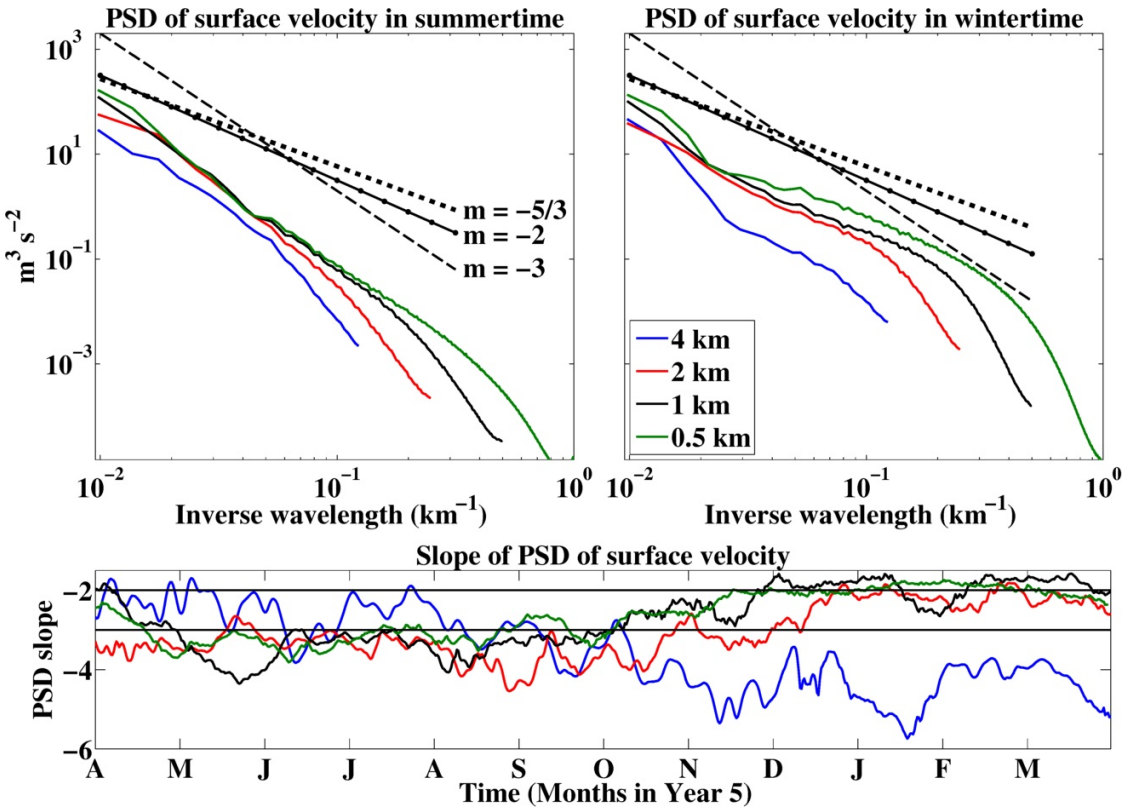

Figure 3.8: The power spectral density for surface velocity. (Upper-left panel) The power spectral density averaged over the summertime months (April - September). (Upper-right panel) The power spectral density averaged over the wintertime months (October - March). The dotted lines show reference slopes m in log-log space. (Lower panel) Time series of the regressed spectral slopes. The reference horizontal lines in the lower panel are at -2 and -3. The upper-limit on the y-axis is a slope of -5/3.

site [Painter et al., 2010]. The mean flow in the model is an Ekman spiral driven by the zonal mean wind stress (not shown).

The slopes of the power spectral density of surface velocity are similar to those for SST anomalies with the slope shallowing from near -3 in summer (Figure 3.8, upper-left panel) to approximately -2 as the winter progresses (Figure 3.8, upper-right panel). The slope is evaluated quantitatively by performing a linear regression on the power spectral density in log-log space at each resolution. To reduce domain-scale and grid-scale effects, this regression is carried out over the range of wavelengths from four times the grid spacing for that simulation to 100 km. The regressed slope remains merely an estimate of the spectral slope due to increasing curvature of the slope in winter. The time series of regressed slopes in Fig. 3.8 (lower panel) shows that the slope steepens to values between -4 and -3 in the restratification period (April to May). It remains in this range

until the cooling begins in September, at which point the slope starts shallowing until reaching a value between -5/3 and -2 in December when the mixed layer has reached approximately 40 m depth. It then stops shallowing even as the mixed layer continues to deepen to 150 m in March. This is broadly consistent with numerical simulations of the North Atlantic that include basin-scale features [Lévy et al., 2010; Mensa et al., 2013]. The seasonal cycle in the slope shown in Fig. 3.8 (lower panel) occurs consistently from year-to-year in the three finer resolution cases. The coarsest resolution case is more variable, but the same overall annual cycle emerges if a multi-year average is taken (not shown).

Figure 3.9 (left panel) shows the vertical profile of the power spectral density of the horizontal velocity in early January of the fifth model year at the finest resolution. The plot is a colour equivalent of the spectra in Fig. 3.8 (upper panels). Shallower spectral slopes are found where the light colours extend to shorter wavelengths. Fig. 3.9 (right panel) shows the same regressed slope values as Fig. 3.8 (lower panel), but applied in the vertical. The regime of shallow spectral slopes is confined to the mixed layer at all resolutions, the mean depth of which is marked by a horizontal line of the same colour. We note that the transition from shallow to steep slopes happens near the mean mixed layer depth of 60 m in Fig. 3.9, and so is not related to the increase in vertical grid spacing that begins from 90 m depth at all resolutions. These vertical profiles of spectral slopes are consistent with the mixed layer being better approximated by quasi-geostrophic dynamics with a vertical scale of the mixed layer depth rather than surface quasi-geostrophy, as in the latter case shallower spectral slopes are also expected below the mixed layer [Callies and Ferrari, 2013].

3.4 Momentum balance

The various balances of momentum give an understanding of how the dynamics differ across resolutions and through the seasonal cycle. The most important of these is geostrophic balance that allows thermal wind balance to be invoked when the hydrostatic approximation is made. Thermal wind balance is of great practical utility if valid, as it allows estimation of potential vorticity from *in-situ* observations such as seaglider transects. Following Capet et al. [2008c], a metric for geostrophic balance is:

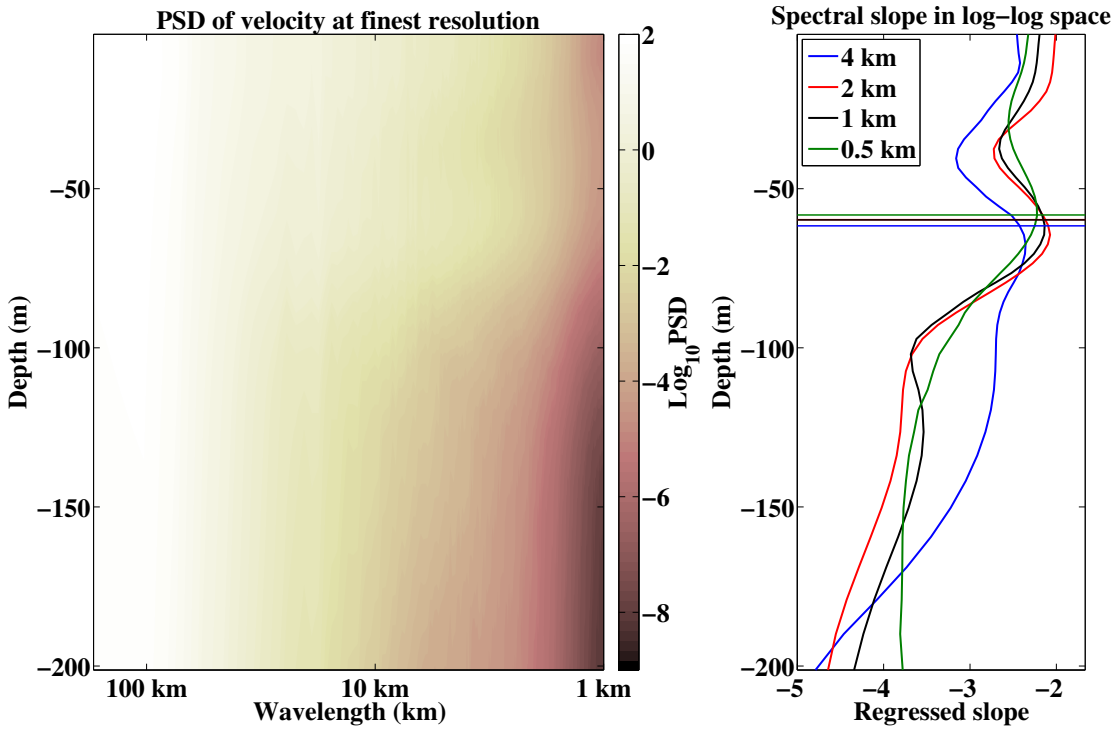

Figure 3.9: The vertical structure of the power spectral density of velocity in early January of the fifth model year. (Left panel) A colour plot of the power spectral density at finest resolution. (Right panel) The spectral slope for all resolutions as estimated from a linear regression in log-log space. The coloured horizontal lines show the mean mixed layer depth at the corresponding resolution.

$$\epsilon_{geo}(\mathbf{x},t) = 1 - \frac{|f\zeta_z - \frac{1}{\rho}\nabla_h^2 p|}{f|\zeta_z| + |\frac{1}{\rho}\nabla_h^2 p| + \mu_{geo}} \tag{3.2}$$

where $\zeta_z = v_x - u_y$ is the vertical component of relative vorticity, p is pressure and $\mu_{geo} = f\zeta_{z,\mathrm{RMS}} + \frac{1}{\rho}\nabla_h^2 p_{\mathrm{RMS}}$ is a small constant that is included to avoid spurious large values in areas of weak force balance. Note that the scale has been reversed from Capet et al. [2008c] such that $\epsilon_{geo} = 1$ means full geostrophic balance.

Capet et al. [2008c] also investigate a generalised cyclostrophic or gradient-wind balance that includes the full non-linear advective terms:

$$\epsilon_{adv}(\mathbf{x},t) = 1 - \frac{|f\zeta_z + \nabla_h \cdot (\mathbf{u}\nabla\mathbf{u}_h) - \frac{1}{\rho}\nabla_h^2 p|}{f|\zeta_z| + |\nabla_h \cdot (\mathbf{u}\nabla\mathbf{u}_h)| + |\frac{1}{\rho}\nabla^2 p| + \mu_{adv}} \tag{3.3}$$

where $\mathbf{u} = (u, v, w)$ is the velocity vector and μ_{adv} is adapted from μ_{geo} to include the contribution of the advective terms. A similar notation is adopted for this term in the balances below. The advection terms include centripetal acceleration and so is expected to better describe the force balance at the centre of vortices and at curved fronts.

The model solution also supports internal waves that lead to more rapid accelerations than those associated with the geostrophic flow. Although the inclusion of the time derivative means the momentum is no longer 'balanced', the inclusion of the time derivative provides useful insight, as discussed below. This 'balance' is called a 'time-advection' by including the divergence of the time derivative of the horizontal velocities:

$$\epsilon_{time-adv}(\mathbf{x},t) = 1 - \frac{|f\zeta_z + \nabla_h \cdot \mathbf{u}_{h,t} + \nabla_h \cdot (\mathbf{u}\nabla\mathbf{u}_h) - \frac{1}{\rho}\nabla_h^2 p|}{f|\zeta_z| + |\nabla_h \cdot \mathbf{u}_{h,t}| + |\nabla_h \cdot (\mathbf{u}\nabla\mathbf{u}_h)| + |\frac{1}{\rho}\nabla_h^2 p| + \mu_{time-adv}} \tag{3.4}$$

where the subscript t denotes differentiation in time.

In a simulation of filamentogenesis in the Gulf Stream Gula et al. [2014] find that the vertical viscous fluxes are of the same order as the vertical shear and horizontal buoyancy gradient in thermal wind balance. They term this 'turbulent thermal wind balance'. This is quantified here as a 'turbulent geostrophic balance' by modifying (3.2) as:

$$\epsilon_{tg}(\mathbf{x},t) = 1 - \frac{|f\zeta_z + \nabla_h \cdot (\tau_z) + \nabla \cdot ((K\mathbf{u}_z)_z) - \frac{1}{\rho}\nabla_h^2 p|}{f|\zeta_z| + |\nabla_h \cdot (\tau_z)| + |\nabla_h \cdot ((K\mathbf{u}_z)_z)| + |\frac{1}{\rho}\nabla_h^2 p| + \mu_{tg}} \tag{3.5}$$

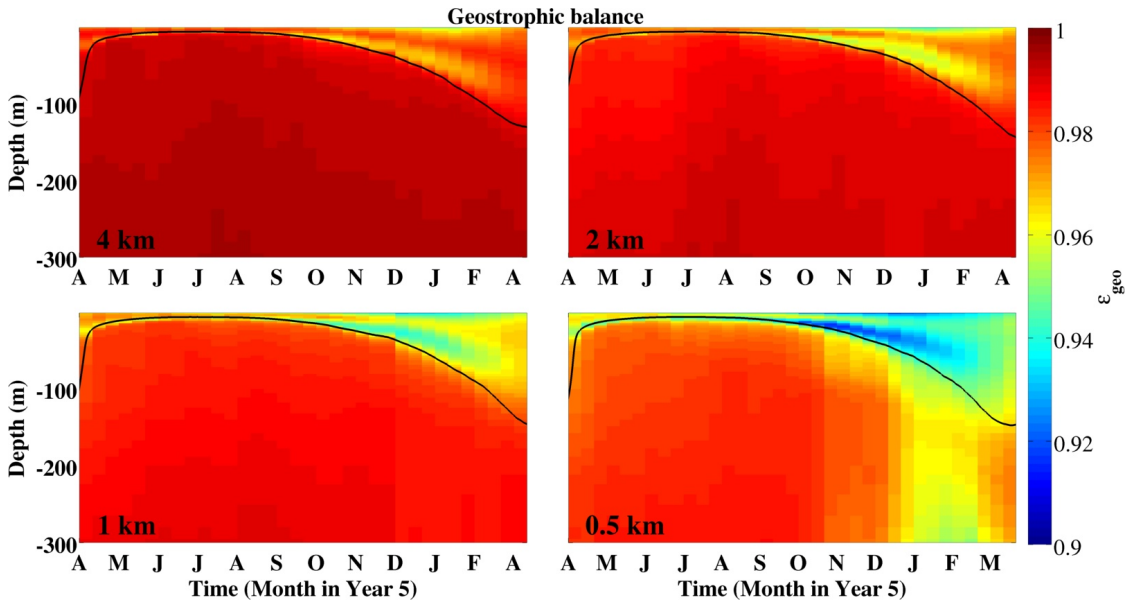

Figure 3.10: The degree of geostrophic balance $\overline{\epsilon_{geo}}$, defined in equation 3.2, calculated from snapshots of model output at 10-day intervals through the seasonal cycle. Values of $\overline{\epsilon_{geo}} \neq 1$ mean a departure from geostrophic balance. The black line is the mean mixed layer depth.

where K is the vertical viscous coefficient that is set by the KPP scheme in the mixing layer but is a constant below and τ_z is the wind stress divergence that accelerates the flow in the uppermost level. This is thus also a generalised version of the 'turbulent Ekman balance' of Taylor and Ferrari [2010].

Finally, to ascertain whether a full description of balance is being approached we can combine all of the terms from the turbulent and time-advection balances as:

$$\epsilon_{tta}(\mathbf{x},t) = 1 - \frac{|f\zeta_z + \nabla_h\cdot(\tau_z) + \nabla_h\cdot((K\mathbf{u}_z)_z) + \nabla_h\cdot\mathbf{u}_t + \nabla_h\cdot(\mathbf{u}\nabla_h\mathbf{u}) - \frac{1}{\rho}\nabla_h^2 p|}{f|\zeta_z| + |\nabla_h\cdot\mathbf{u}_t| + |\nabla_h\cdot((K\mathbf{u}_z)_z)| + |\nabla_h\cdot(\mathbf{u}\nabla_h\mathbf{u})| + |\frac{1}{\rho}\nabla_h^2 p| + \mu_{tta}} \tag{3.6}$$

The annual cycle in $\overline{\epsilon_{geo}}$ is shown in Fig. 3.10. This shows that the degree of balance falls as the resolution is made finer, both in the mixed layer and in the interior. Vertically, the degree of balance is lower in the mixed layer than in the interior, though minima are often found at the base of the deepening mixed layer.

While geostrophic balance is of course the primary balance, there is a change in the residual mean balance across this range of resolutions. Figure 3.11 shows the vertical profiles of horizontal means of the various balances in late January,

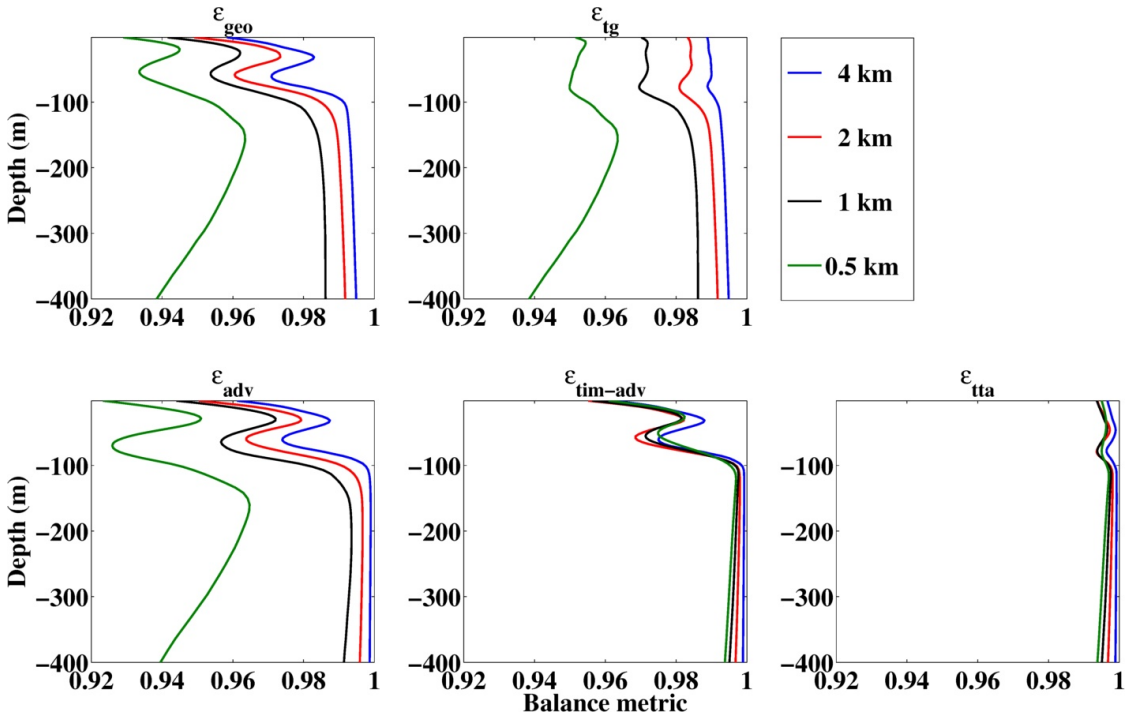

Figure 3.11: Vertical profiles of the balance parameters in late January (year 4.83) during the period of mixed layer deepening. The mean mixed layer is approximately 90 m at all resolutions. The calculation is based on a snapshot of model output. (Top left) Geostrophic balance as measured by $\overline{\epsilon_{geo}}$. (Top centre) Turbulent geostrophic balance as measured by $\overline{\epsilon_{tg}}$. (Bottom left) Advective balance as measured by $\overline{\epsilon_{adv}}$. (Bottom centre) Linear-advective balance as measured by $\overline{\epsilon_{time-adv}}$. (Bottom right) Turbulent-linear-advective balance as measured by $\overline{\epsilon_{tta}}$. The balance values are based on snapshots of model output.

when the mean mixed layer depth is approximately 90 m. This is during the time interval when $\overline{\epsilon_{geo}}$ is low in the thermocline of the finest resolution case (Fig. 3.10, bottom-right panel). Comparing firstly the geostrophic balance, Fig. 3.11 (top-left panel) shows again that the magnitude of $\overline{\epsilon_{geo}}$ falls as the resolution is made finer. Moving to the turbulent geostrophic balance (Fig. 3.11, top-right panel) improves the degree of balance over geostrophy alone. However, this improvement in balance is only present in the mixed layer, as the vertical diffusion of momentum in the interior is much weaker. Now comparing geostrophy and generalised cyclostrophy, Fig. 3.11 (left-hand panels) shows that incorporating advective terms improves the degree of balance by a small amount at coarser resolution. However, for the two finer resolutions $\overline{\epsilon_{adv}} < \overline{\epsilon_{geo}}$ near the base of the mean mixed layer at 85 m and the degree of balance does not materially increase in the thermocline. In order to improve the degree of 'balance' at the finest resolution, the time derivative terms must be included (centre panel, bottom row). In the coarser resolution runs, the addition of the time derivative term again makes little difference and $\overline{\epsilon_{adv}} \approx \overline{\epsilon_{time-adv}}$. Therefore, the time derivative terms become an important part of the residual momentum balance in late winter at fine resolution. The combined balance terms in $\overline{\epsilon_{tta}}$ are shown in Fig. 3.11 (right panel, bottom row), with the residual accounted for by the horizontal diffusion of momentum in the mixed layer and a small factor due to the time-stepping scheme.

The time derivative terms have a distinct spatial structure which can be understood by considering the geostrophic balance ϵ_{geo} at the base of the mixed layer in Figure 3.12. This is taken from the same time as the sea surface buoyancy gradients plot in Fig. 3.5. The time derivative terms account for the departure from balance near (60 km, 60 km) in Fig. 3.12 (bottom-right panel) and are thus associated with the long filamentary streaks that are wrapped into the large anticyclone and visible as buoyancy gradients in Fig. 3.5. The dynamical process that generates these ageostrophic filaments is investigated in Chapter 4 and are found to be associated with strong inertia-gravity wave generation, which is the reason that the time derivative terms are important in the momentum balance at fine resolution. Such filamentation and the accompanying departure from geostrophic balance becomes weaker as the resolution becomes coarser (Fig. 3.12). Lower values of ϵ_{geo} are also found in the centre of the large vortices at all resolutions. It is here that the degree of balance is most improved by moving to advective balance that includes cyclostrophic effects. This shows that the mixed layer portion of the mesoscale vortices becomes more non-linear as the resolution is made finer. The

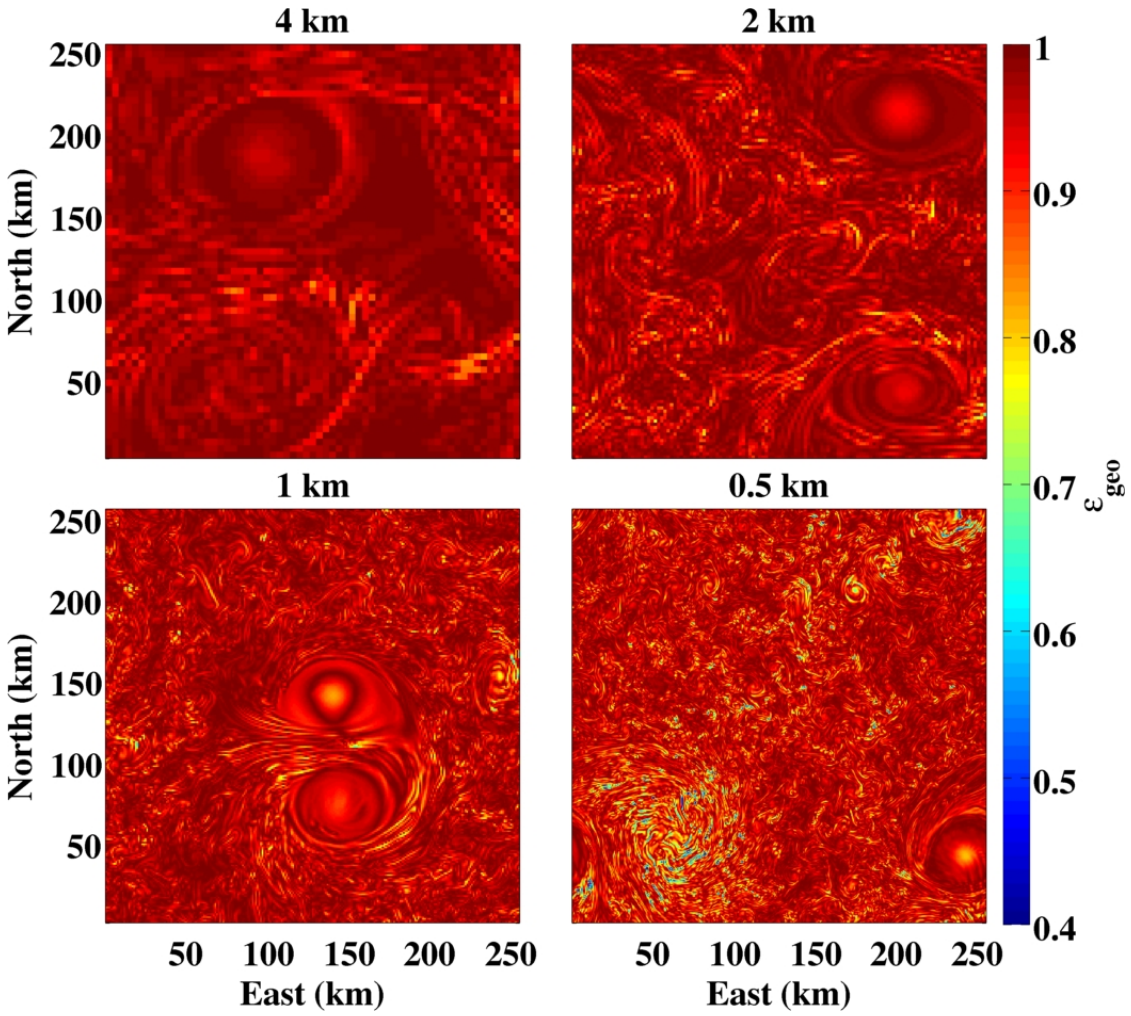

Figure 3.12: Plan views of the geostrophic balance parameter ϵ_{geo} at 74 m depth when the mean mixed layer is approximately 90 m in late January. Dark red values show regions of near-perfect geostrophic balance while blue colours show departures from geostrophic balance. This is taken from the same time as the sea surface buoyancy gradients in Fig. 3.5.

improvement in balance in the mixed layer by the use of turbulent geostrophic balance, measured by ϵ_{tg}, is relatively uniform through the domain.

3.5 Frontal processes

The results presented above show that there are distinct differences across the resolutions in terms of the buoyancy and velocity fields in the upper domain. They also show that as the resolution becomes finer there are growing seasonal differences between the runs. These differences are due to submesoscale processes, that are diagnosed individually here.

3.5.1 Frontogenesis

Although frontogenesis is formally defined to be the development of a discontinuity in buoyancy at a front, it is taken in this thesis to mean the action by the flow field to increase or decrease the variance of horizontal buoyancy gradients. The impact of frontogenesis on horizontal gradients is diagnosed using the frontogenesis function [Hoskins and Bretherton, 1972] modified to include the vertical advective transport:

$$F_s = \mathbf{Q}_s \cdot \nabla_h b \tag{3.7}$$

where:

$$\mathbf{Q}_s = -(u_x b_x + v_x b_y + w_x b_z, u_y b_x + v_y b_y + w_y b_z). \tag{3.8}$$

In agreement with Capet et al. [2008c], the mean magnitude of frontogenesis generally grows as the resolution becomes finer with level-mean values increasing by approximately a factor of two for each doubling in resolution (Figure 3.13, all panels). Of more novelty is the seasonal cycle in the magnitude of frontogenesis as the mixed layer depth varies by an order of magnitude from summer to winter. Figure 3.13 shows that $\overline{F_s}$ is low in the period of mixed layer restratification (April to June, all panels). It then grows in magnitude through the remainder of the summer and into the first part of the winter (August to January) before weakening in the late winter when the mixed layer deepens from 80 m to 150 m. The weakening of $\overline{F_s}$ in winter (all panels) could reflect the ability of mixed layer instabilities to overturn strong buoyancy gradients when the mixed layer is of sufficient depth. The period in the annual cycle when $\overline{\mathbf{Q}_s}$ begins to weaken coincides with the interval when the slope of the surface velocity spectra reaches its shallower values in Fig. 3.8 (bottom panel).

3.5.2 Ekman buoyancy fluxes

The creation or destruction of potential vorticity due to frictional forcing at the boundary has been established observationally and numerically as an important process at ocean fronts [Thomas, 2005; Capet et al., 2008c; Thomas and Taylor, 2010; Mahadevan et al., 2010; D'Asaro et al., 2011; Thomas et al., 2013]. This process is referred to as the Ekman buoyancy flux (EBF) and can be diagnosed as:

$$\text{EBF} = (\frac{\tau}{\rho_o f} \times \mathbf{k}) \cdot \nabla_h b \tag{3.9}$$

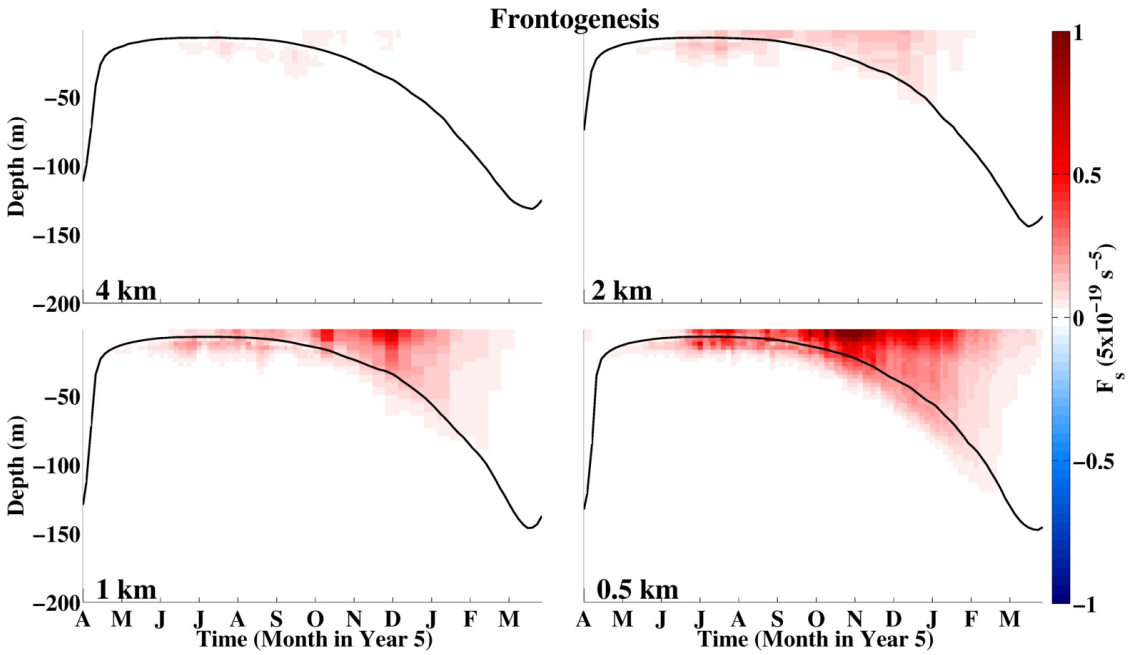

Figure 3.13: The level-mean value of the frontogenesis function, defined in equation (3.7) over the fifth year of the simulations. The calculation is based on snapshots of model output at 10-day intervals. The black line shows the mean mixed layer depth at that time.

where τ is the wind stress, ρ_o is a reference density and $\mathbf{k}$ is the unit vertical vector. The term $\nabla_h b$ is formally the mean buoyancy gradient over the Ekman layer, though we take it to be the surface buoyancy gradient. While the mean value of the EBF is notionally zero when averaged over a periodic domain, there is still a net effect on stratification as the down-front winds induce a vertical diffusive mixing through the whole mixed layer, while the up-front winds induce an advective restratification in the Ekman layer [Thomas and Ferrari, 2008].

Fig. 3.14 shows that the root-mean-square Ekman buoyancy flux has a similar annual cycle to $\overline{F_s}$ in that its peak values occur in summer conditions when $\overline{|\nabla_h b|}$ is largest and it is stronger at finer resolution. The magnitude of the buoyancy fluxes is order 10^{-6} m^{2}s^{-3} at fine resolution. This is some 20 times larger than the buoyancy flux due to the peak surface heating/cooling and emphasises the local importance of the EBF in setting stratification, even in these simulations where the mean wind stress is moderate compared to values achieved in the open ocean. For comparison with other results, note also that the magnitude of the EBF here is an order of magnitude greater than in Hamlington et al. [2014], who focus on the weak wind-wave parameter regime. Although the winds are relatively weak here, the magnitude of the horizontal buoyancy gradients that arise are much stronger.

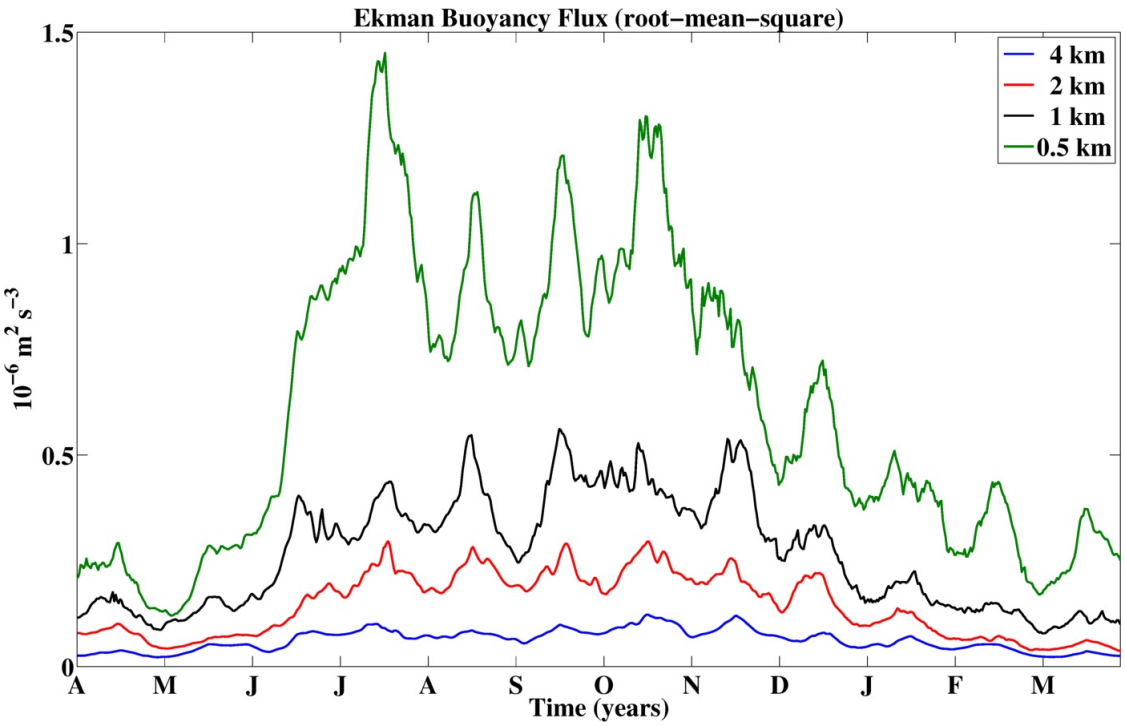

Figure 3.14: The root-mean-square magnitude of the Ekman buoyancy flux, defined in equation (3.9), over the fifth year of the simulations.

The oscillations in the EBF in Fig. 3.14 are the main unfortunate consequence of the monthly cycle in the wind-forcing noted in Chapter 2. The effect of the EBF is investigated further in Chapter 3.5.3 below.

3.5.3 Instabilities of negative potential vorticity

The ocean is subject to a range of instabilities when $fq < 0$, which in these simulations is equivalent to negative potential vorticity. Where negative potential vorticity occurs, the dominant expected response to perturbations can be inferred from the balanced Richardson number $\mathrm{Ri_b}$ (defined in (3.10)). The infinite range of possible $\mathrm{Ri_b}$ can be contracted to an angle ϕ following the approach of Thomas et al. [2013] where a schematic can be found:

$$\phi_{\mathrm{Ri_b}} = \tan^{-1}(-\mathrm{Ri_b^{-1}}) = \tan^{-1}\frac{-|\nabla_h b|^2}{f^2 N^2} \tag{3.10}$$

and

$$\phi_{\mathrm{Ri_b}} < \phi_c = \tan^{-1}(-\zeta_g/f) \tag{3.11}$$

where $\zeta_g = f + \nabla \times \mathbf{u}_g$ where $\mathbf{u}_g$ is the geostrophic velocity. When -180° $< \phi_{Ri_b} < -135°$, the potential vorticity is negative due to unstable stratification and

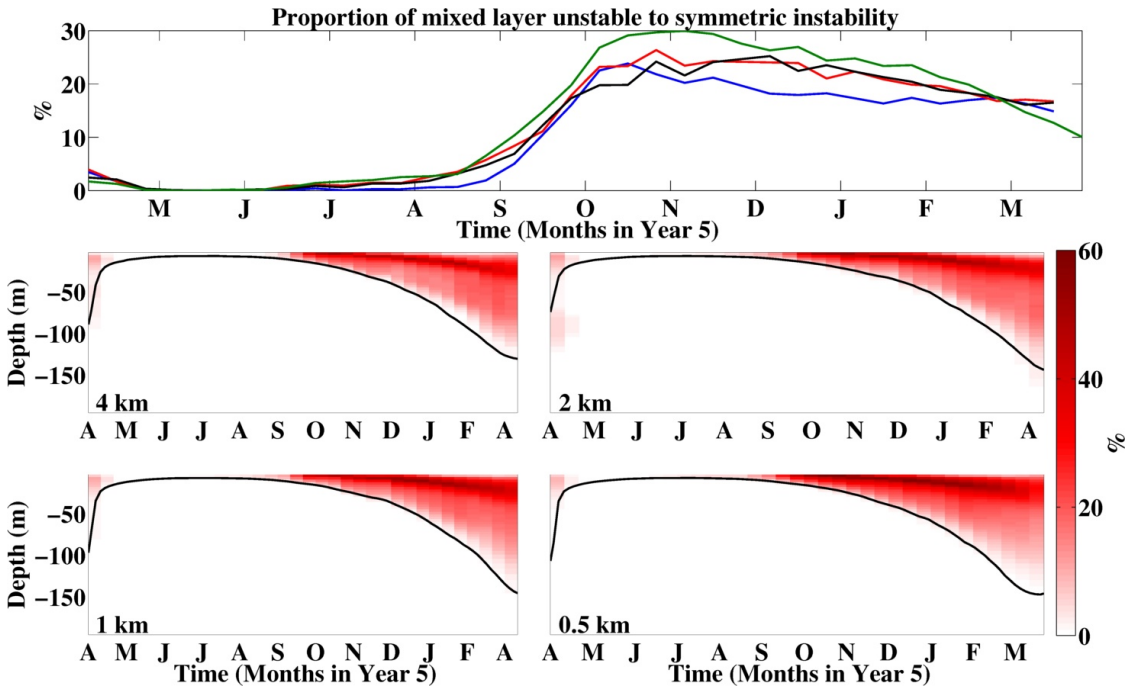

Figure 3.15: The proportion of the domain with negative potential vorticity where a pure or hybrid symmetric instability is predicted. (Top panel) Time series of the mean proportion of the mixed layer volume where symmetric instability is predicted. (Lower panels) The vertical structure of predicted occurrence of symmetric instability. This is calculated based on snapshot model outputs at 10-day intervals during the fifth year of the simulations. The black line in the lower panels is the mean mixed layer depth.

convective instability is expected to dominate. When -135° $< \phi_{\mathrm{Ri_b}} < -90°$, the potential vorticity is negative due to both unstable stratification and horizontal buoyancy gradients and so a hybrid convective/symmetric mode is predicted. For stable stratification and cyclonic vorticity -90° $< \phi_{\mathrm{Ri_b}} < \phi_c$, with $\phi_c < -45°$ implies that a symmetric instability should arise. For anticyclonic vorticity a symmetric mode is expected to dominate where -90° $< \phi_{\mathrm{Ri_b}} < -45°$ and a hybrid symmetric-centrifugal instability is anticipated where $-45° < \phi_{\mathrm{Ri_b}} < \phi_c$.

Figure 3.15 (upper panel) shows that up to 30% of the mixed layer volume is unstable to pure or hybrid symmetric instabilities in winter conditions. The proportion of the mixed layer volume where such a condition holds grows somewhat as the resolution is made finer, though the values are comparable across all resolutions. In the shallow mixed layers early in the restratification period (April - August in Fig. 3.15, upper panel) very little negative potential vorticity is found at any resolution due to the stratifying effect of the surface heating. The proportion of the domain where negative potential vorticity is found then grows in late summer (September - October in Fig. 3.15, upper panel). It reaches its peak

value quite early in the winter by November at all resolutions before gradually decreasing in late winter despite the continual cooling. This reflects the decrease in horizontal buoyancy gradients over the winter in Fig. 3.6.

The vertical distribution of negative potential vorticity is shown in Fig. 3.15 (lower panels) and is similar at all resolutions. The lower panels shows that the occurrence of negative potential vorticity is essentially limited to the mean mixed layer. This implies that the definition of mixed layer depth employed does a reasonable job of capturing the low potential vorticity surface layer. The distribution of negative potential vorticity is not concentrated in the Ekman layer reflecting the tendency for down-front winds to induce vertical mixing and so extract potential vorticity throughout the mixed layer [Thomas and Ferrari, 2008]. The peak proportion of the mixed layer volume that is most unstable to centrifugal instability grows from 1% of the mixed layer volume at the coarsest resolution to 4% at the finest resolution (not shown). In addition, the upper 10 m of the model domain develops a slight negative stratification in the cooling period at all resolutions. This negative stratification in the upper levels is a typical feature of numerical simulations.

As for Capet et al. [2008c], regions of negative potential vorticity are produced by the down-front wind mechanism. Figure 3.16 shows the mean potential vorticity for a given zonal or meridional buoyancy gradient based on a snapshot of model output at the end of December in year 5 at 9 m depth. The top row in Fig. 3.16 shows no systematic relationship between the zonal buoyancy gradient and potential vorticity. However, the bottom row shows that there is a near-linear relationship between the meridional buoyancy gradient and potential vorticity at all resolutions. When $b_y < 0$, colder water lies to the north of warmer water. Given the mean zonal wind, $b_y < 0$ corresponds to a down-front wind scenario where the wind is aligned with the geostrophic shear and fluxes potential vorticity substance out of the ocean [Thomas, 2005]. On the other hand, where $b_y > 0$ the wind is up-front and potential vorticity substance is fluxed into the ocean and so potential vorticity tends to be positive. This effect becomes stronger as the resolution is made finer (Fig. 3.16, lower panels).

A similar analysis can be carried out in Fig. 3.16 where the potential vorticity is compared to the Okubo-Weiss parameter $S^2 - \zeta_z^2$, where $S^2 = (v_x + u_y)^2 + (u_x - v_y)^2$ is the strain rate squared. No systematic relationship between the Okubo-Weiss parameter and potential vorticity is found (not shown). This can be understood by considering the horizontal distribution of negative potential

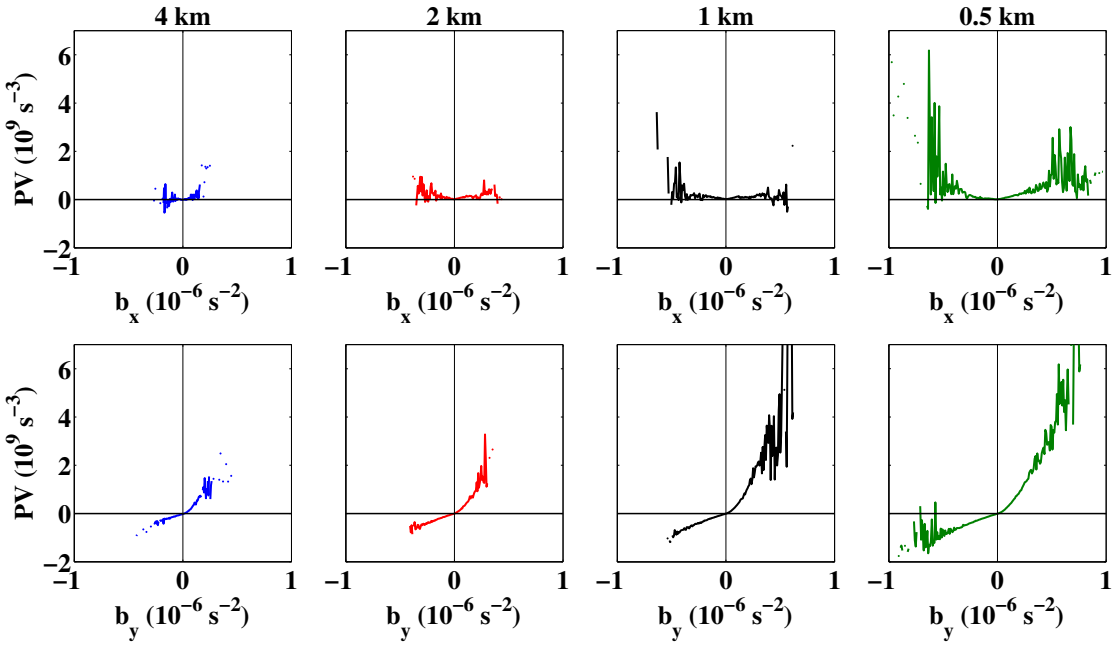

Figure 3.16: Potential vorticity with respect to horizontal buoyancy gradients at 9 m depth at the end of December in year 5. (Top row) The mean potential vorticity for a given zonal buoyancy gradient. (Bottom row) The mean potential vorticity for a given meridional buoyancy gradient. These results are consistent with Fig. 11 of Capet et al. [2008c].

vorticity at the end of December in Figure 3.17. This figure illustrates that negative values of potential vorticity are found both in filaments outside the vortices and also inside the large vortices, for example at (100 km, 80 km) at 4 km resolution in the upper-left panel. Negative potential vorticity in the large vortices correspond to regions of negative meridional buoyancy gradients within the vortices. The detailed structure of potential vorticity in the mixed layer of these wind-forced vortices and the consequences of this negative potential vorticity is examined in detail in Chapter 4.

3.5.4 Vertical advective fluxes

The vertical buoyancy flux is given as $\overline{w'b'}$, where w is the vertical velocity where b is the buoyancy and primes indicate a departure from the level mean. The top panel in Figure 3.18 shows that vertical buoyancy fluxes integrated over the mixed layer become larger as the resolution becomes finer and has its peak value in February and March. This means that the seasonal cycle in vertical advective fluxes differs from the diagnosed seasonal cycle in frontogenesis and Ekman buoyancy fluxes. The lower panels in Fig. 3.18 show the vertical profiles of $\overline{w'b'}$.

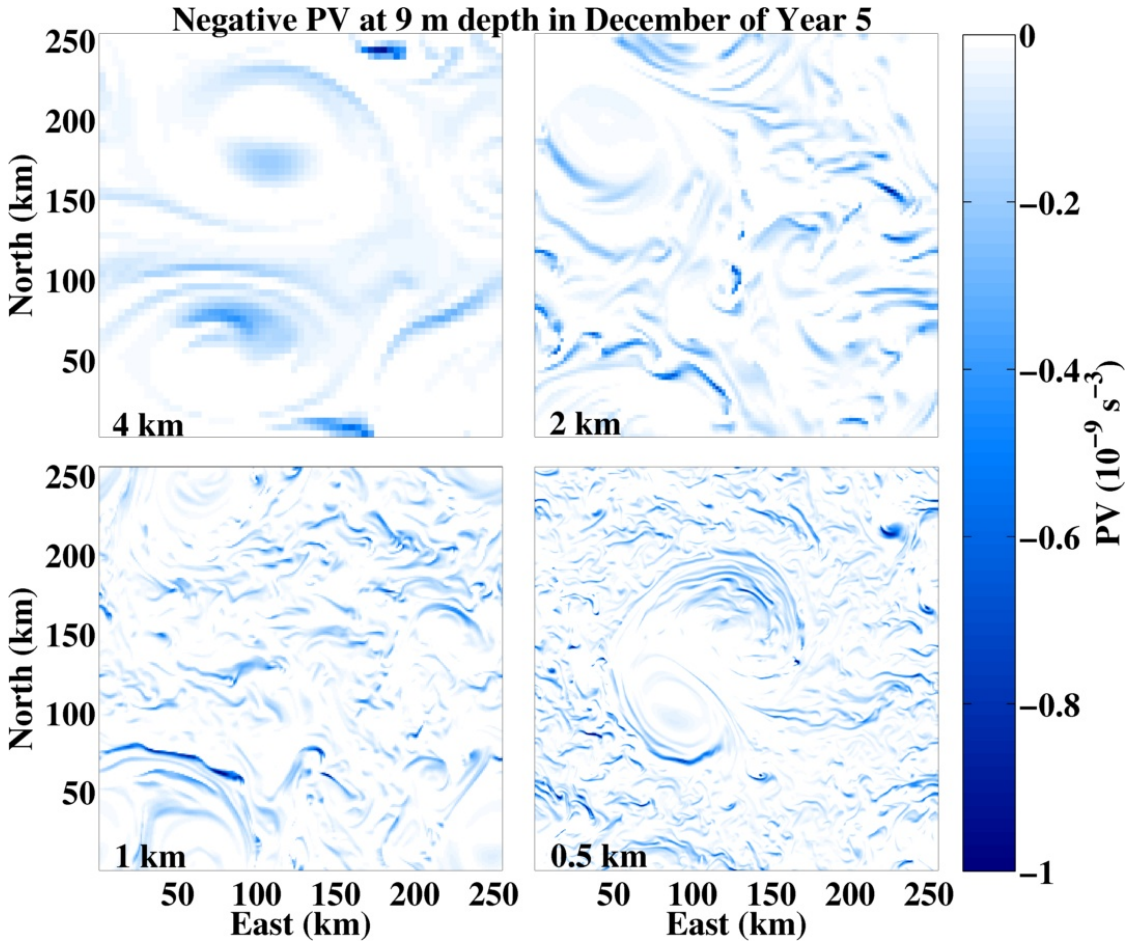

Figure 3.17: Plan views of negative potential vorticity at 9 m depth at the end of December in year 5. The colour scale saturates at $q = 0$ so regions of positive potential vorticity are shown in white.

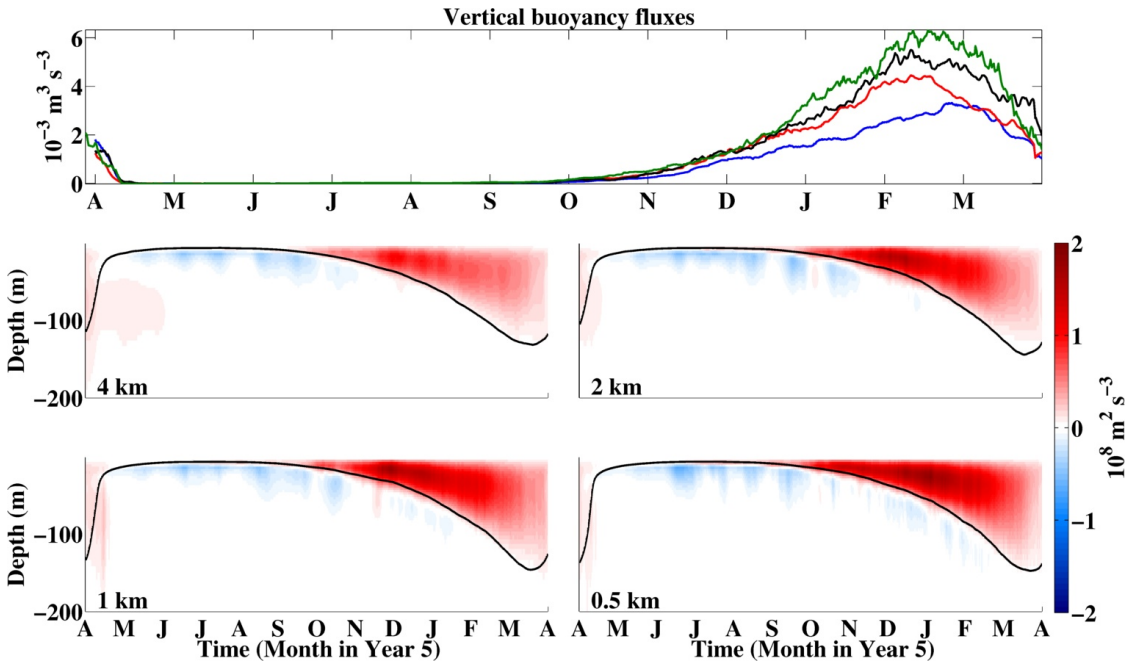

Figure 3.18: The mean vertical advective buoyancy flux $\overline{w'b'}$ over the fifth year of the simulations averaged by model level and in six-hour intervals online. (Upper panel) The flux integrated over the mean mixed layer. (Lower panels) The level-mean profiles of the mean vertical advective fluxes at the resolution indicated. The top panel is a vertically-integrated measure and has different units to the lower panels. The black line in the lower panels shows the mean mixed layer depth.

There are negative vertical buoyancy fluxes below the mean mixed layer throughout the year. It is these negative fluxes that give rise to the heating effect in the thermocline considered in Chapter 3.2.1. The vertical fluxes are uniformly positive in the mean mixed layer, however. While the maximum integrated fluxes occur when the mixed layer is deepest, the largest instantaneous fluxes occur earlier in winter in December and January (lower panels) The seasonal cycle in the vertical buoyancy fluxes is very different from that of the frontogenesis function (Fig. 3.13) and the Ekman buoyancy fluxes (Fig. 3.14), both of which peak in early winter. Therefore, these processes can be ruled out as being the dominant driver of the vertical buoyancy fluxes throughout the winter.

The analysis in Chapter 3.5.3 shows that up to 30% of the mixed layer experiences negative potential vorticity during the winter. Bachman and Taylor [2014] show that symmetric instability can be associated with restratification and positive vertical buoyancy fluxes. In addition, the majority of the mixed layer has positive potential vorticity and so mixed layer baroclinic instabilities, which are exclusively associated with positive vertical buoyancy fluxes, are expected to be

the dominant instability [Stone, 1966b; Molemaker et al., 2005; Boccaletti et al., 2007; Fox-Kemper et al., 2008; Skyllingstad and Samelson, 2012; Brüggemann and Eden, 2014]. The importance of these restratifying instabilities can be estimated through the seasonal cycle by scaling the potential energy available for release. We employ the central concept of the Fox-Kemper et al. [2008] parameterisation by estimating the magnitude of the available potential energy as:

$$\mathrm{APE} = H^2 |\nabla_h b|, \tag{3.12}$$

where H is the mixed layer depth. The magnitude of the available potential energy averaged over the mixed layer is shown in Figure 3.19 where the seasonal cycle agrees with that of the vertical buoyancy fluxes though the buoyancy fluxes. The available potential energy in the mixed layer is much lower in summer, despite increasingly strong buoyancy gradients (May-July in Fig. 3.19). The available potential energy then grows steadily through the cooling period as the mixed layer deepens (September-February in Fig. 3.19). APE reaches its peak in March, 15 days before the mixed layer depth reaches its winter maximum. This offset in time is due to the weakening of horizontal buoyancy gradients by the action of the instabilities up to that point in winter and is consistent with numerical results for the Argentinian Shelf of Capet et al. [2008a].

3.6 Discussion

The results of a series of multi-year simulations in a domain analogous to the mid-latitude open ocean show a seasonal cycle in submesoscale flows. This seasonal cycle becomes more pronounced as the resolution is made finer. The spectral slopes of horizontal wavenumber spectra of SST and surface velocity are steep in summer and then rapidly become shallower as the mixed layer deepens, indicative of stronger submesoscale flows in winter. The shallowing of the velocity spectra evens out when the mixed layer is just 40 m deep, suggesting that the dynamical regime reflected by this shallower slope does not require particularly deep mixed layers.

The effect of frontogenesis on the horizontal buoyancy field is strongest when the mixed layer is shallow. This may mean that frontogenesis acts to increase horizontal buoyancy gradients over the summer but the corresponding increase in available potential energy can not be counteracted by overturning instabilities due to the shallow mixed layer. This balance then changes in winter as the

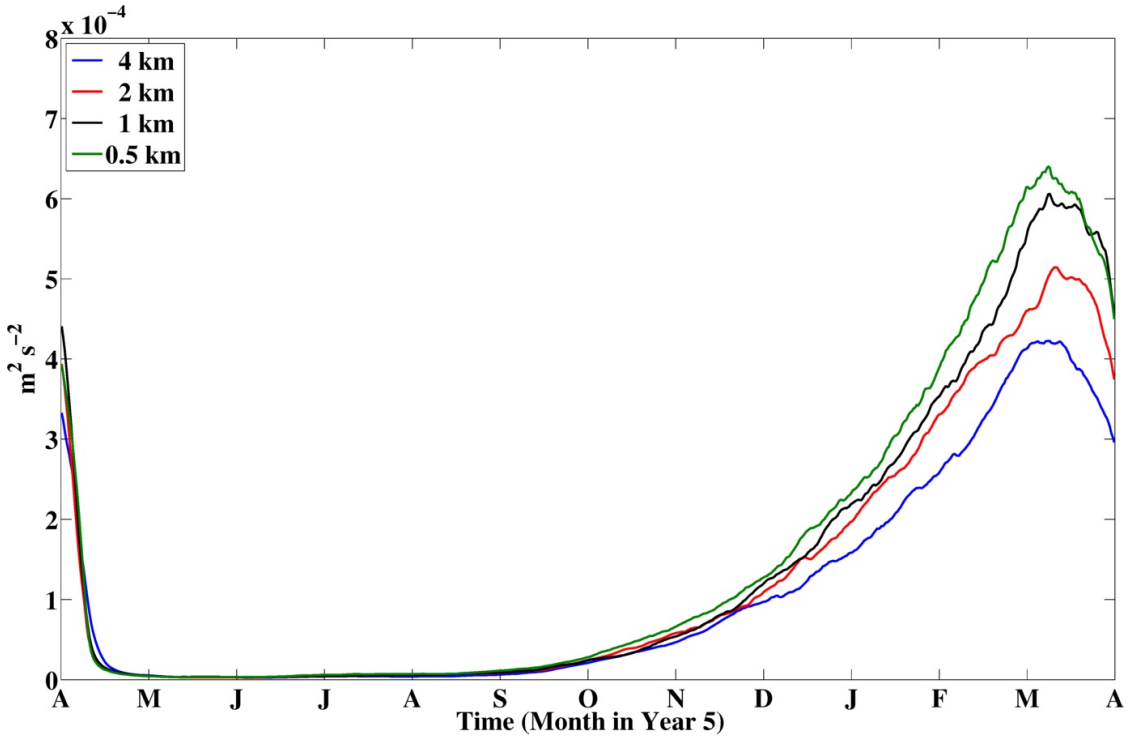

Figure 3.19: A scaling for the domain-average available potential energy in the mixed layer $APE = H^2|\nabla_h b|$, over the fifth year of the simulations.

mixed layer deepens and overturning instabilities grow. This suggests that the balance between frontogenesis and baroclinic instabilities [e.g. McWilliams and Molemaker, 2011] may be sensitive to the vertical length scale, which in this case is the mixed layer depth. The seasonal cycle in available potential energy and vertical buoyancy fluxes is similar, which leads to the conclusion that overturning instabilities are the primary driver of these vertical fluxes, rather than the restratification associated with frontogenesis or Ekman pumping.

Negative potential vorticity is much more prevalent in winter as cooling at the surface and down-front wind forcing act together to locally extract potential vorticity substance from the mixed layer. Symmetric instability is found to be the most likely response to negative potential vorticity with centrifugal instability less important.

The simulations also vary across the range of resolutions. As the resolution is increased, sharper fronts emerge and the residual momentum balance of the flow includes a larger contribution from high-frequency motions. Processes at ocean fronts including frontogenesis and Ekman buoyancy fluxes are found to strengthen as the resolution is made finer. The prevalence of negative potential vorticity does not increase monotonically with resolution, but instead depends

on the flow configuration at a given time. Negative potential vorticity – and submesoscale filaments – are found in the mixed layer of mesoscale vortices, and so the Okubo-Weiss parameter is not a good predictor of the presence of negative potential vorticity.

An open question is the convergence of the simulations over this range of resolutions. The similar seasonal cycle in spectral slopes in the three finer resolution cases can be used to argue for convergence, as per Capet et al. [2008b]. However, the diagnosed submesoscale processes continue to become stronger as the resolution is made finer and the mean stratification profile continues to vary with resolution in Fig. 3.1. Bachman and Taylor [2014] also show that the degree to which symmetric instability is resolved changes markedly over this range of resolutions and so affects the subsequent development of stratification.

A key result is the variation in the surface kinetic energy spectral slope through the annual cycle, and its tendency towards a fixed value towards a value of approximately -2 when the mixed layer deepens beyond about 40 m depth (Fig. 3.8). This slope could be consistent with upper-domain dynamics being approximated by the combination of a shallow quasi-geostrophic regime scaling with the mixed layer depth and a deep quasi-geostrophic regime scaling with the main thermocline depth [Callies and Ferrari, 2013]. The spectral slopes estimated are also close to the -5/3 slopes predicted for surface quasi-geostrophy [Lapeyre et al., 2006; Lapeyre and Klein, 2006]. However, the rapid steepening of the spectral slopes below the mixed layer (Fig. 3.8) is not consistent with predictions of surface quasi-geostrophic theory [Callies and Ferrari, 2013]. Caution is recommended when considering the precise values of the slope calculated. An inspection of the upper panels of Figure 3.8 shows that the spectra have curvature and so changing the wavenumber range over which the slopes are calculated changes the value of the slope from the regression analysis. Furthermore, theoretical predictions of slopes in wavenumber space for various turbulent regimes are based on assumptions that are not strictly valid in this configuration, such as the requirement for energy input to be limited to very large scales.

The results support the notion that submesoscale processes should be observed throughout the open ocean and not just in the vicinity of major boundary currents. The results largely support the use of geostrophic balance to estimate potential vorticity from observations of the density field. However, the improvement in the diagnosed force balance in the mixed layer suggests that increased vertical diffusion of momentum should be taken into account as per Gula et al.

[2014] and advective processes are not negligible in vortices as the resolution becomes finer.

These results highlight the need for further parameterisations of submesoscale processes. A significant proportion of the mixed layer is unstable to symmetric-type modes that re-stratify the mixed layer on faster time scales than baroclinic instability and have energy sources that go beyond available potential energy. To date, only mixed layer baroclinic instability has an explicit parameterisation scheme [Fox-Kemper and Ferrari, 2008]. The frontogenetical and Ekman buoyancy flux processes that generate the strong buoyancy gradients also need to be parameterised.

There are of course a number of limitations to this study in addition to those discussed above such as the artificial structure of the wind forcing. The grid resolutions employed require the use of a vertical mixed layer parameterisation and so important effects like the convective layer depth [Taylor and Ferrari, 2010; Thomas et al., 2013] or interaction with small-scale turbulence [Skyllingstad and Samelson, 2012; Hamlington et al., 2014] could not be explored. The surface boundary conditions are imposed and so do not allow SST anomalies to generate differential air-sea fluxes. In addition, it is often the case that the internal wave field in such model studies is less energetic than in the real ocean [Shcherbina et al., 2013], due to the wind forcing being sub-inertial and the lack of tides and topography [Callies and Ferrari, 2013]. The simulations do allow for the generation of internal waves from unbalanced motions [Shakespeare and Taylor, 2013].

CHAPTER 4

Intense upwelling in anticyclonic vortices

4.1 Introduction

The simulations of an open ocean region described in Chapter 3 show that submesoscale filaments (Figure 3.6) and negative potential vorticity (Figure 3.17) are found in the interior of mesoscale vortices as the grid is refined from 4 km to 0.5 km. This is in contrast to an existing paradigm that submesoscale flows are to be found in the exterior and periphery of mesoscale vortices, a region sometimes referred to as the 'submesoscale soup' [Shcherbina et al., 2013, e.g.]. The properties of these filaments are investigated in this Chapter.

The mesoscale vortex field is the dominant component of the ocean's kinetic energy budget [Ferrari and Wunsch, 2009]. It is composed of large coherent vortices with radius of order 100 km that are clearly visible in observations of sea surface height [e.g. Chelton et al., 2011]. These vortices play an important role in the oceanic circulation as transporters of heat, salt and momentum [e.g. Zhang et al., 2014; Dong et al., 2014] and so an understanding of their dynamics is crucial.

An asymmetry is found with respect to observations of biological productivity in mesoscale cyclones. Anti-cyclones are host to more intense primary productivity than cyclones in oligotrophic regions where the mixed layer is otherwise nutrient depleted [e.g. Yentsch and Phinney, 1985; Strass, 1992; McGillicuddy et al., 1998, 2007; Crawford et al., 2007; Hansen et al., 2010; Gaube et al., 2013]. In the Gulf of Alaska Crawford et al. [2007], for example, show that over half of surface chlorophyll inferred from satellite observations is found inside anticyclonic

vortices that occupy just 10% of the surface area. These observations imply that additional upwelling of nutrient-rich waters occurs in anticyclonic vortices. Upwelling (downwelling) in this thesis is taken to be an upwards (a downwards) vertical displacement of a fluid particle. The velocity vector in a stratified fluid can always be decomposed as $\mathbf{u} = \mathbf{u}_{||} + \mathbf{u}_{\perp}$, where $\mathbf{u}_{||}$ is along-isopycnal motion and $\mathbf{u}_{\perp}$ is the motion of the isopycnal itself. The term upwelling in the literature on fronts and vortices is often applied to the motion of the isopycnal itself. However, the results in this Chapter highlight the importance of vertical motion along isopycnals as well as the motion of isopycnals.

There are two main branches of research to explain this increased productivity in anticyclones. The first branch focuses on the mesoscale dynamics of the vortices to ascertain if, for example, the differential wind stress on each side of an anticyclone can generate a divergence in the vortex core that leads to upwelling of the isopycnal surfaces [e.g. Dewar and Flierl, 1987; Martin and Richards, 2001; McGillicuddy et al., 2007; Gaube et al., 2014b]. However, Mahadevan et al. [2008] show that the upwelling velocities induced by such forcing is relatively weak for typical ocean vortices with a low Rossby number Ro = Vf/L, where V is the azimuthal velocity of the vortex, and L is the vortex radius. The second branch of research considers submesoscale dynamics at the edge of vortices or in the inter-vortex zone. Mahadevan et al. [2008] show that the divergences in Ekman transport and the associated ageostrophic secondary circulations are stronger for anticyclones than cyclones. They propose that this leads to additional upwelling of deeper isopycnal with higher nutrient concentrations around the periphery of anticyclones where gradients in relative vorticity are strong and subsequently there is advection of phytoplankton into the core of the anticyclone. It is not clear, however, if the small-scale upwelling associated with the divergence of the Ekman transport penetrates into the thermocline. This approach also does not take into account the potential vorticity fluxes into and out of the ocean associated with the frictional wind forcing [Thomas and Rhines, 2002; Thomas and Lee, 2005].

4.1.1 Chapter aims and outline

This Chapter investigates the dynamical origin of the submesoscale filaments in mesoscale vortices and the consequences the flow associated with the filaments has for larger-scale properties. The outline of this Chapter is as follows. Chapter 4.2 describes the main properties of the filaments from the model runs used to describe the seasonal cycle in Chapter 3. The interpolation experiments are

then used to illustrate the effect of frictional potential vorticity fluxes on vortices in Chapter 4.3, the growth of the filaments is examined in detail in Chapter 4.4 and their energetics are evaluated in Chapter 4.5. This is followed in Chapter 4.6 by a consideration of the different mechanisms that could give rise to the filaments. Chapter 4.7 then considers the implications of flow curvature for stability to symmetric instability and the inertia-gravity waves generated are examined in Chapter 4.8. The effect of filament generation of exchange of fluid tracers between the mixed layer and thermocline is considered in Chapter 4.9 before concluding with a discussion in Chapter 4.10.

4.2 Properties of filaments

Filaments are apparent in the temperature, the vertical component of relative vorticity and potential vorticity fields in anticyclonic vortices of the simulations used to investigate the seasonal cycle in Chapter 3. The potential vorticity is defined in equation (1.1) in Chapter 1. Figure 4.1 shows the temperature field in a cyclone (upper-left panel) and anticyclone (upper-right panel) from the late winter period at 0.5 km resolution from the simulations described in Chapter 3 when the mean mixed layer depth is 120 m. No filaments are present inside the cyclone (upper-left panel) and the sea surface temperature shows that temperature increases monotonically away from the cold cyclone core. In the anticyclone (upper-right panel), on the other hand, the core of warm temperatures has been strained by the flow and further filaments are developing, for example, in the north of the anticyclone at (100 km, 150 km). The vertical component of relative vorticity at the surface (lower-left panel) shows that the flow field in the cyclone remains well approximated by solid-body rotation, albeit with a core of higher vorticity. However, in the anticyclone filaments of positive ζ_z intrude into the vortex. The bottom-right panel in Fig. 4.1 shows the potential vorticity at 90 m depth, which is about 40 m above the mean mixed layer base. The red colours show the presence of filaments with much higher potential vorticity than the ambient fluid in the mixed layer.

Closer inspection reveals some coherence between the spatial patterns of potential vorticity near the base of the mixed layer (bottom-right panel) and the relative vorticity at the surface (bottom-left panel). In the potential vorticity there is a white area of low values in the centre of the anticyclone around (90 km, 140 km). In the relative vorticity there is a similarly-shaped area of strong negative relative vorticity. On the left hand edge of this patch of low potential vorticity

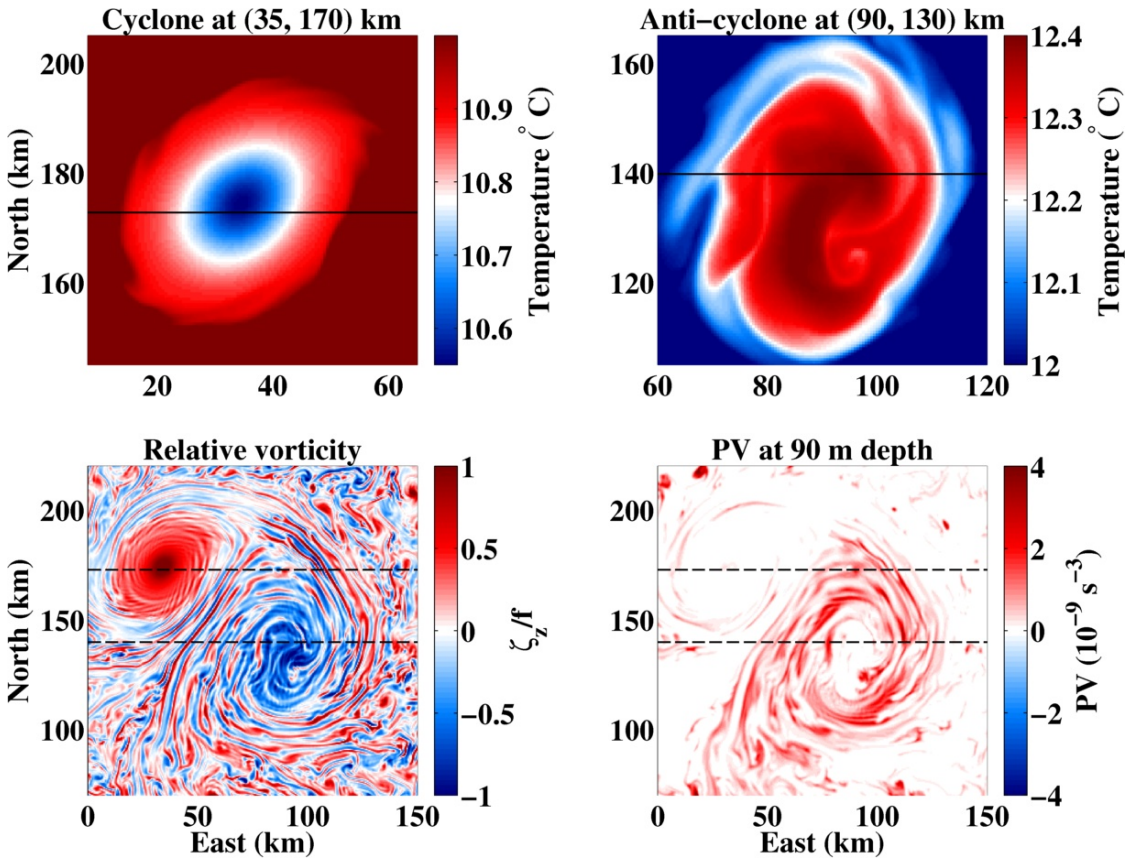

Figure 4.1: Plan view snapshots from the 0.5 km resolution run in early March of year 5. (Upper-left panel) Sea surface temperature in the region of the cyclone. (Upper-right panel) Sea surface temperature in the region of the anticyclone with a different colour scale. (Lower-left panel) ζ_z/f at the surface over both the cyclone and the anticyclone. (Lower-right panel) Potential vorticity at 90 m depth over both the cyclone and anticyclone. The dashed black lines show the locations of the vertical sections in Fig. 4.2.

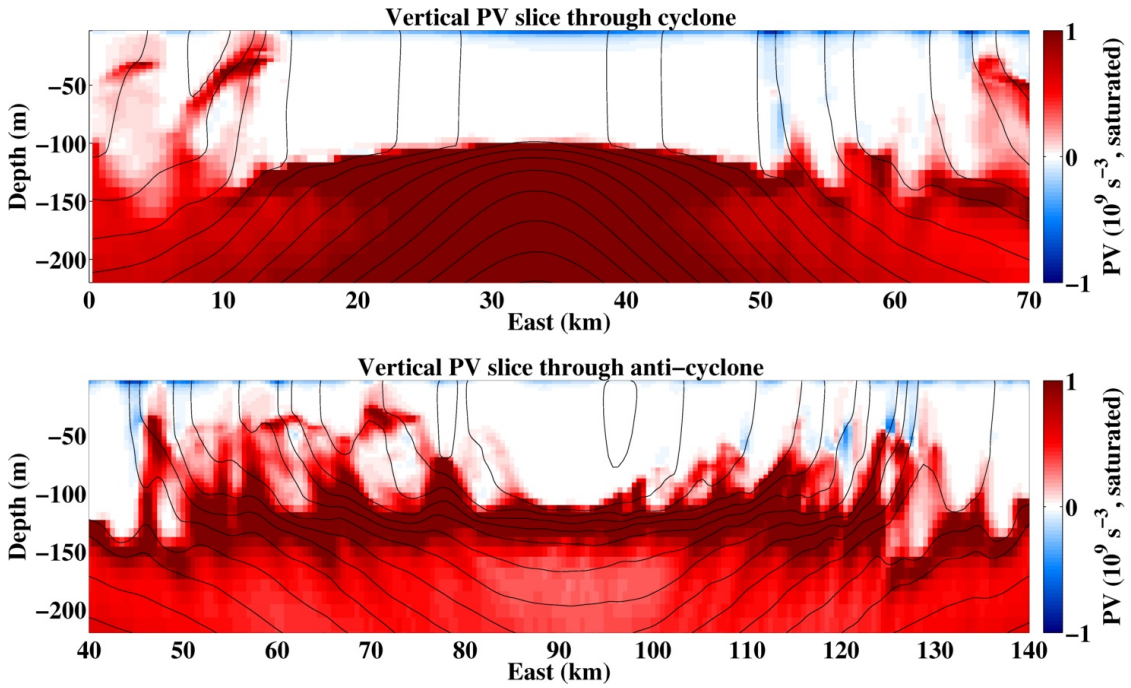

Figure 4.2: Vertical slices of potential vorticity through the vortices in late winter of Year 5. The slices are taken along the dashed black lines shown in Fig. 4.1 (bottom panels). Black lines show temperature contours in intervals of 0.1°C. (Top panel) A vertical slice through the centre of the cyclone. (Bottom panel) A slice through the anticyclone.

(bottom-right panel), there is a positive potential vorticity filament aligned north-south that crosses the bottom dashed black line. Comparison of the same location in the relative vorticity plot shows a filament of positive relative vorticity at the surface. Such comparisons cannot be made for every filament, however, as there is considerable vertical structure in the filamentary features, as is shown below.

The filamentation is thus the result of a process that brings positive potential vorticity anomalies into the mixed layer of the anticyclone. The high potential vorticity values (bottom-right panel) show that the filaments cannot come from the mixed layer outside the vortex. By the impermeability theorem [Haynes and McIntyre, 1987], the potential vorticity cannot cross buoyancy surfaces and so fluid with high potential vorticity in the mixed layer must have gained its high potential vorticity through positive frictional fluxes into the ocean at the surface or entrainment of high potential vorticity fluid from the thermocline.

The vertical structure of potential vorticity can be understood by taking vertical slices through the centre of the vortices along the dashed black lines shown in Fig. 4.1 (lower panels). Figure 4.2 (upper panel) confirms that the cyclone has

little potential vorticity in the mixed layer and there is little deformation of the mixed layer base. In the anticyclone (Fig. 4.2, lower panel) positive potential vorticity anomalies on the eastern (right-hand) side of the anticyclone extend up from the thermocline, for example at (112 km, -80 m) with negative potential vorticity anomalies visible closer to the surface along the same isopycnals. The potential vorticity structure is different on the western (left-hand) side of the anticyclone. On this side there are again positive potential vorticity anomalies that extend up from the thermocline. However, there are also potential vorticity anomalies in the upper mixed layer that are not continuous with the thermocline such as at (72 km, -50 m).

4.3 Effect of Ekman buoyancy fluxes on vortices

The different vertical structure of the potential vorticity anomalies in the near-surface on the east and west side of the anticyclonic vortex in Fig. 4.2 can be found even in the 4 km coarse resolution run. Figure 4.3 shows the temperature and potential vorticity fields at the outset of the 4 km interpolation experiment. The cyclonic vortex centred at (130 km, 200 km) has a cold core (upper-left panel) and positive (negative) potential vorticity (upper-right panel) in its north (south). Given the zonal wind, the vortex is subject to up-front winds on its northern side and down-front winds on its southern side, as defined in Chapter 1.2.4. Therefore, the model potential vorticity structure is consistent with frictional fluxes into and out of the ocean setting the local potential vorticity. The anticyclone centred at (100 km, 75 km) (left panel) has a warm core (upper-left panel) and positive (negative) potential vorticity (upper-right panel) in its south (north). The relative locations are reversed from the cyclone as the sign of the meridional buoyancy gradient is reversed. These results are broadly consistent with those for fronts [Thomas, 2005]. The main difference is that the magnitude of the potential vorticity anomalies are a factor of four larger for the anticyclone than the cyclone, despite similar magnitudes of horizontal buoyancy gradients. This reflects other properties of the vortices, that are considered further in Chapter 4.7 below.

The vertical structure of the regions of positive and negative potential vorticity is different between the up-front and down-front regions. While down-front winds tilt isopycnals to the vertical and thereafter generate convective mixing through the whole mixed layer, up-front winds lead to an advective restratification in the Ekman layer. This is shown in the lower panel of Fig. 4.3 as negative

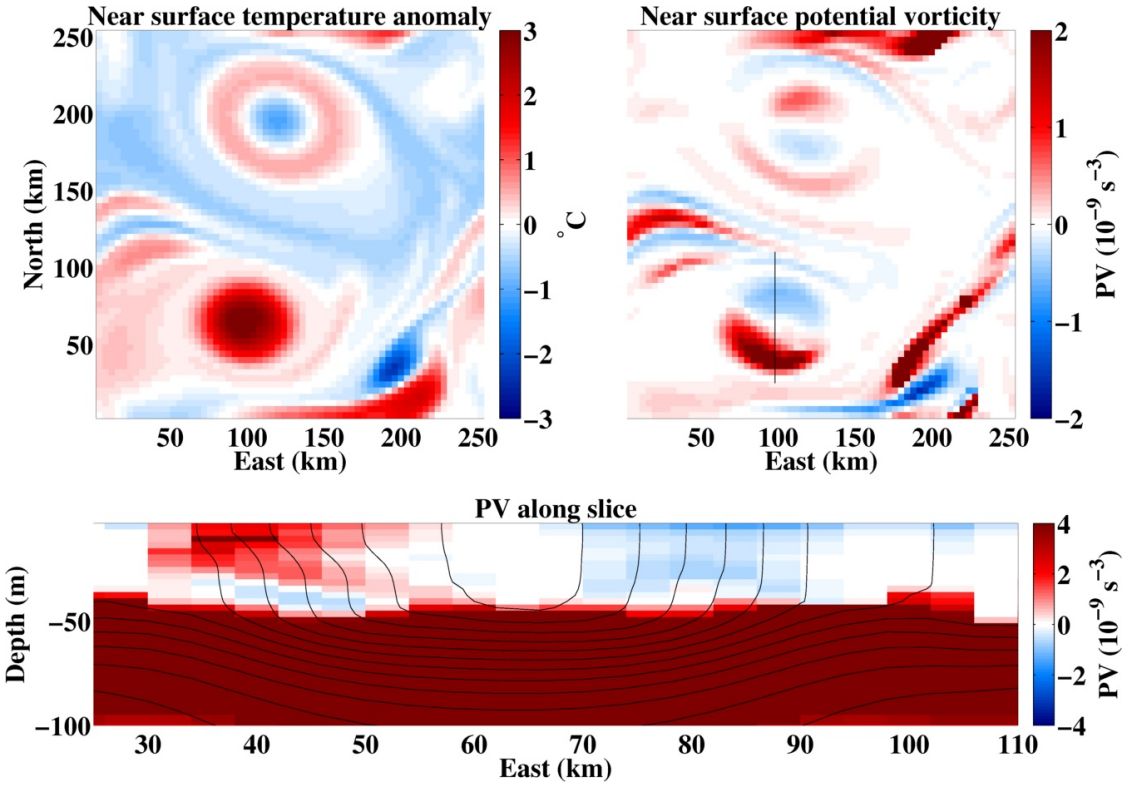

Figure 4.3: Snapshots of temperature and potential vorticity at the outset of the interpolation experiment at 4 km resolution at 9 m depth. (Upper-left panel) Plan view of the temperature anomaly (T - $\overline{T}$) field at the surface. The cyclone is the cold anomaly in the north and the anticyclone is a warm anomaly in the south. (Upper-right panel) Plan view of potential vorticity at the same depth. (Lower panel) Vertical slice of potential vorticity along the black line in the upper-right panel.

potential vorticity extending through the mixed layer in the northern part of the vortex, but positive potential vorticity does not extend through the whole mixed layer in the southern part of the vortex. Instead, there is a thin layer of negative potential vorticity near (45 km, -45 m). This negative potential vorticity arises when the fluid column passes through the down-front wind region in the north of the anticyclone and is maintained as the fluid column is advected around the vortex. This layer of negative potential vorticity below the positive cap layer of potential vorticity is below the layer of active mixing and so is exposed to less vertical diffusivity than the regions of negative potential vorticity elsewhere in the vortex.

These results can thus account for the east-west asymmetry of the potential vorticity in the vertical slice through the anticyclone in Fig. 4.2. The fluid on the right-hand side has just passed through the down-front region and so does not have near-surface stratification. The fluid on the left-hand side has just passed through the up-front region and so has near-surface stratification.

4.4 Filament growth

To track the growth of the filaments described above, the experiment at 4 km resolution, where filamentation in vortices does not occur, is interpolated to finer resolution grids, as described in Chapter 2.7. The initial model state is the 4 km run shown in Fig. 4.3. Figure 4.4 shows the growth of filaments at the end of the first four days of the interpolation experiment at 0.5 km resolution. The left-hand panels are at 26 m, which is at the base of the Ekman layer to which the wind-induced restratification is confined in up-front regions. The positive potential vorticity input by up-front winds in the south of the vortex is not fully eroded at this depth until the fluid column reaches the north of the vortex (upper-left panel). The right-hand panels are at 44 m, close to the base of the mixed layer. The area of positive potential vorticity in the centre of the upper-right panel is a smooth deformation of the mixed layer base that is inherited from the 4 km simulation.

As the interpolation experiment proceeds long filaments of positive potential vorticity begin to appear in the vortex. In the upper two rows on the right-hand side the first filaments appear in the region of negative potential vorticity in the south and west of the vortex, for example at (75 km, 60 km). As noted above, these areas are subject to less vertical diffusion as the stratification in the Ekman

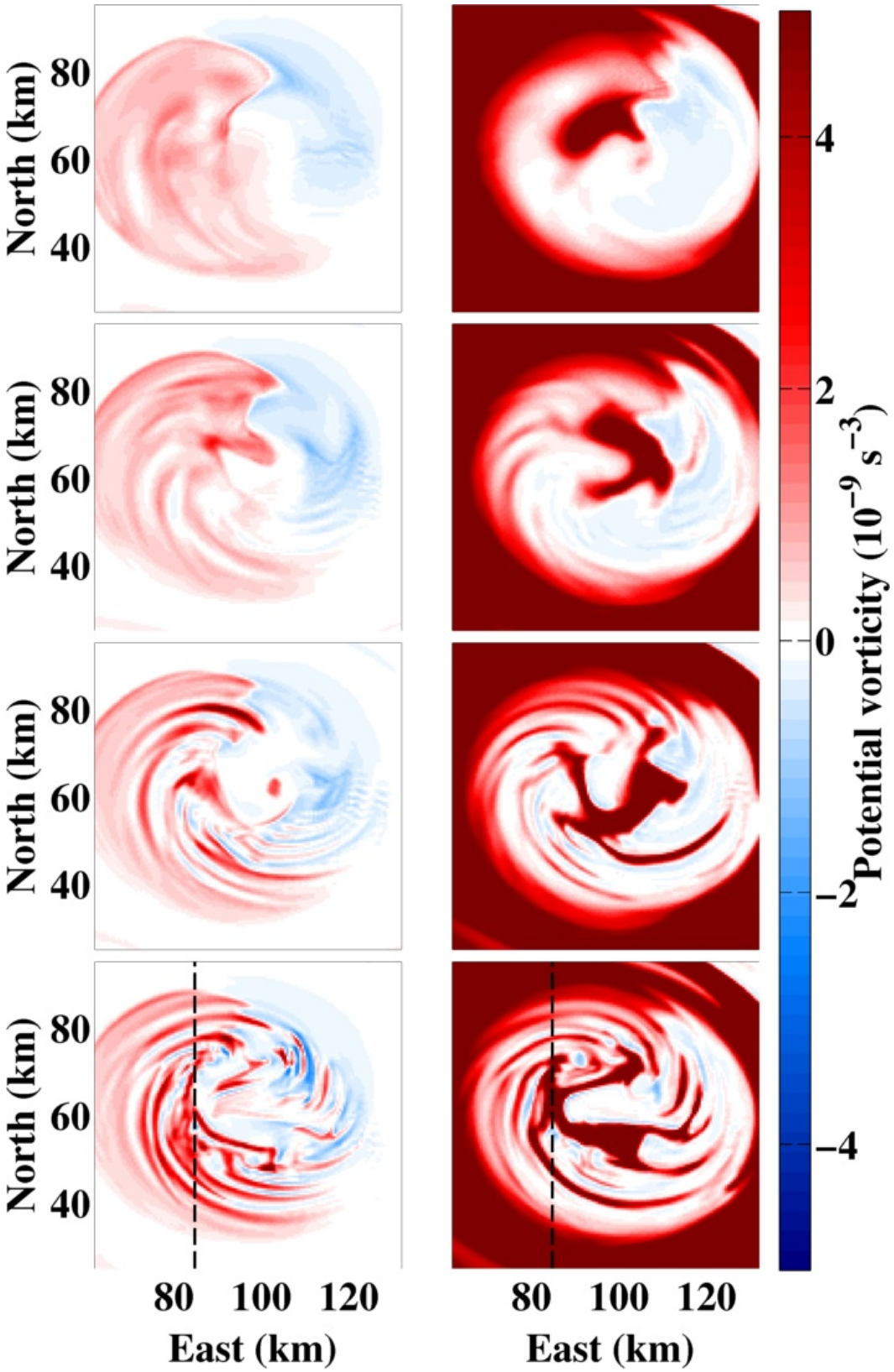

Figure 4.4: Plan views of potential vorticity over the first four days of the interpolation experiments over an anticyclonic vortex at 26 m (left-hand panels) and 44 m (right-hand panels) depth at 0.5 km resolution. The left-hand panels are at the base of the Ekman layer, while the right-hand panels are at the base of the surface layer. (Top row) Hour 24. (Second row) Hour 48. (Third row) Hour 72. (Bottom row) Hour 96.

layer also forms the base of the mixing layer. As the interpolation experiment proceeds, the filaments continue to occupy a larger part of the area of the vortex across these two surfaces.

An example of the vertical profiles of potential vorticity and vertical velocity are shown in Figure 4.5. These slices are along the dashed lines shown in the bottom row of Fig. 4.4. In the north of the vortex there is a series of high potential vorticity filaments extending up from the thermocline (upper panel). The lower panel shows that there are strong vertical velocities of up to 50 m day^{-1}. The vertical velocities are closely-aligned with isopycnal slopes meaning that the upwelling in this case is primarily along the isopycnals such as a displacement of the isopycnals. High potential vorticity filaments are also in evidence in the south of the vortex. The width of the largest filament here is somewhat larger than those in the north of the filament. As the potential vorticity field gives more of a time-integrated sense of flow development, it suggests that the filaments in the north of the vortex, which grew in the low vertical diffusion environment below the Ekman layer to the south and west are shorter wavelength than the filament in the south which grew in the high diffusion environment in the north and east of the vortex.

A similar structure of filamentation in the mixed layer of anticyclonic vortices is found by Koszalka et al. [2009] with vertical velocities of the same magnitude as those found here. They note that the vertical velocities are an order of magnitude larger than predicted by the quasi-geostrophic omega equation.

The effect of varying resolution on the filament growth is shown in Figure 4.6. This figure shows plan views of the potential vorticity above the base of the mixed layer on the fifth day of the simulations. The red blob of positive potential vorticity near the centre of the vortex at all resolutions is a smooth deformation of the mixed layer base present in the 4 km simulation. The filamentation process emerges and strengthens over the entire range of resolutions used here. The differences between the 500 m and 250 m resolution runs are of interest in terms of ascertaining potential convergence of the solutions. It is immediately clear that the finer resolution run has some additional small scale structure, for example the filaments at (115 km, 50 km) in the east of the vortex. The largest positive potential vorticity anomalies, such as the long filament in the west of the vortex near (80 km, 60 km) appear in both of the finer resolution runs. This filament sharpens in width at this depth from a width of about 4 km at 500 m resolution to 3 km at 250 m resolution. The appearance of the finer filaments and the sharpening

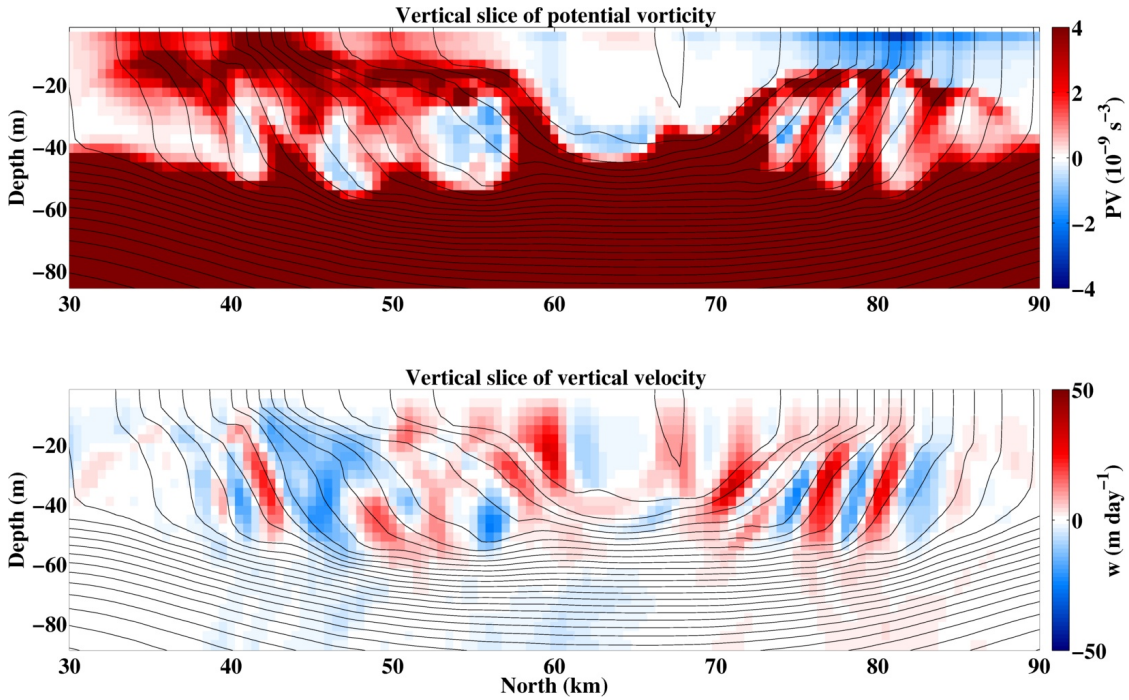

Figure 4.5: Vertical slices of potential vorticity and vertical velocity at Hour 84 of the interpolation experiments at 0.5 km resolution. The slices are taken along the dashed lines in the bottom row of Fig. 4.4. (Upper panel) Potential vorticity. (Lower panel) Vertical velocity. Solid black lines are temperature contours of 0.2°C. The dashed black lines show the depths at which the plan views in the lower row of Figure 4.4 are taken.

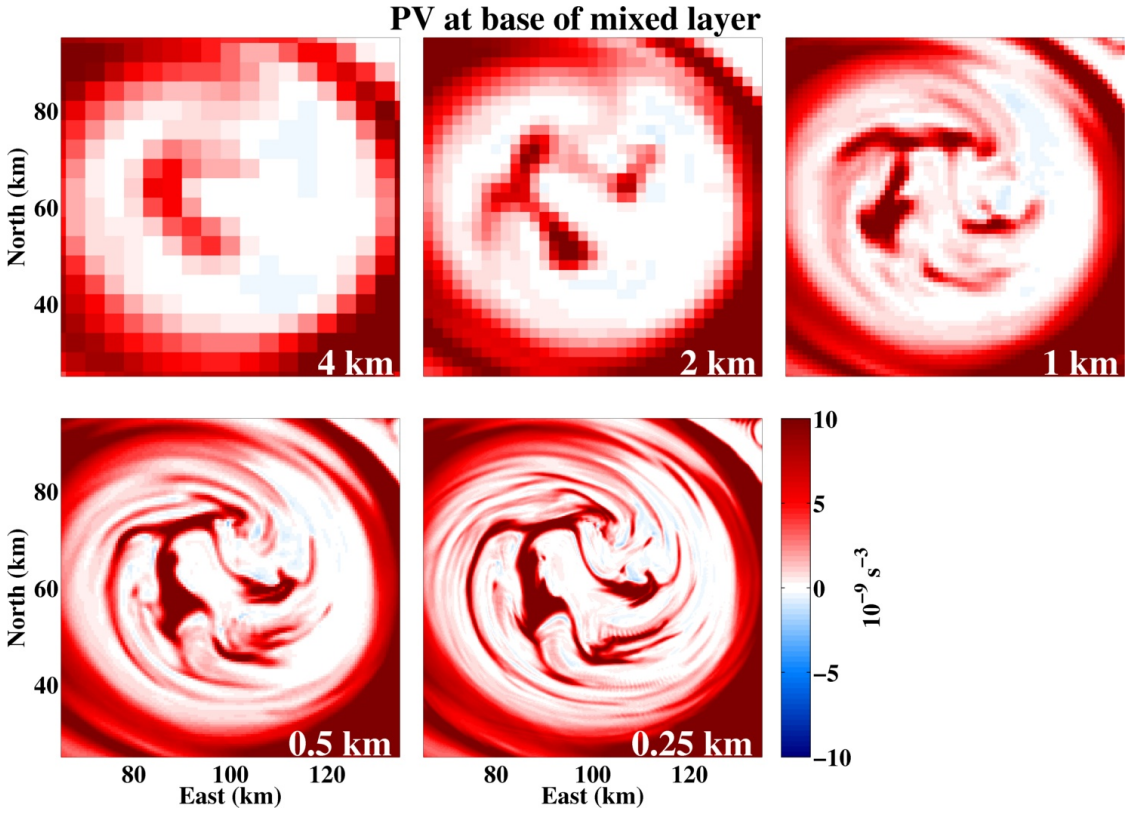

Figure 4.6: Plan views of potential vorticity at 44 m depth over a range of resolutions on the fifth day of the interpolation experiments. Note the larger colour range than in other plots in this Chapter. The red blob of positive potential vorticity near the centre of the vortex at all resolutions is a smooth deformation of the mixed layer base that intersects this depth rather than fluid that has been upwelled from the thermocline into the mixed layer.

of the larger filaments at 250 m resolution show that convergence of this process has certainly not occurred, though it may be that it is starting to be approached. Such convergence does not of course take into account the generation of non-hydrostatic secondary shear instabilities [Taylor and Ferrari, 2009] which require at least an order of magnitude finer resolution and non-hydrostatic dynamics.

4.5 Energetics

The source of the kinetic energy to drive the filamentation process must be from some or all of vertical buoyancy fluxes, vertical shear production or lateral shear production [e.g. Thomas et al., 2013]. The definitions of the fluxes must take into account the curvature of the flow and the presence of shear associated with the Ekman spiral and so the 'geostrophic' shear production term in Thomas et al. [2013] becomes the 'vertical' shear production. The balanced flow for the energy budget is taken to be a cyclogeostrophic flow:

$$\frac{(V_\theta^{bal})^2}{r} + fV_\theta^{bal} = \frac{\partial \pi}{\partial r}, \tag{4.1}$$

where V_θ^{bal} is the balanced azimuthal velocity, r is the radial coordinate of the vortex and π is ρ^{-1} times the pressure. The full azimuthal velocity $V_\theta = -sin(\theta)u + cos(\theta)v$, where $\mathbf{u} = (u, v, w)$ is the Cartesian velocity vector. Perturbations from the balanced azimuthal flow are $V_\theta' = V_\theta - V_\theta^{bal}$. The radial velocity is $V_r' = cos(\theta)u + sin(\theta)v$.

The source terms in the energy budget are the vertical buoyancy flux:

$$BFLUX = w'b', \tag{4.2}$$

where w is the vertical velocity, b is buoyancy and primes denote departures from the vortex mean; the vertical shear production:

$$VSP = -V_\theta' w' \frac{\partial V_\theta^{bal}}{\partial z}, \tag{4.3}$$

and the lateral shear production:

$$LSP = -V_\theta' V_r' \frac{\partial V_\theta^{bal}}{\partial r}. \tag{4.4}$$

It is cautioned that extracting balanced and perturbation quantities remains an on-going challenge, as the vortex is slightly elliptical, as illustrated in Chapter 4.7, and there is an Ekman transport that varies around the vortex.

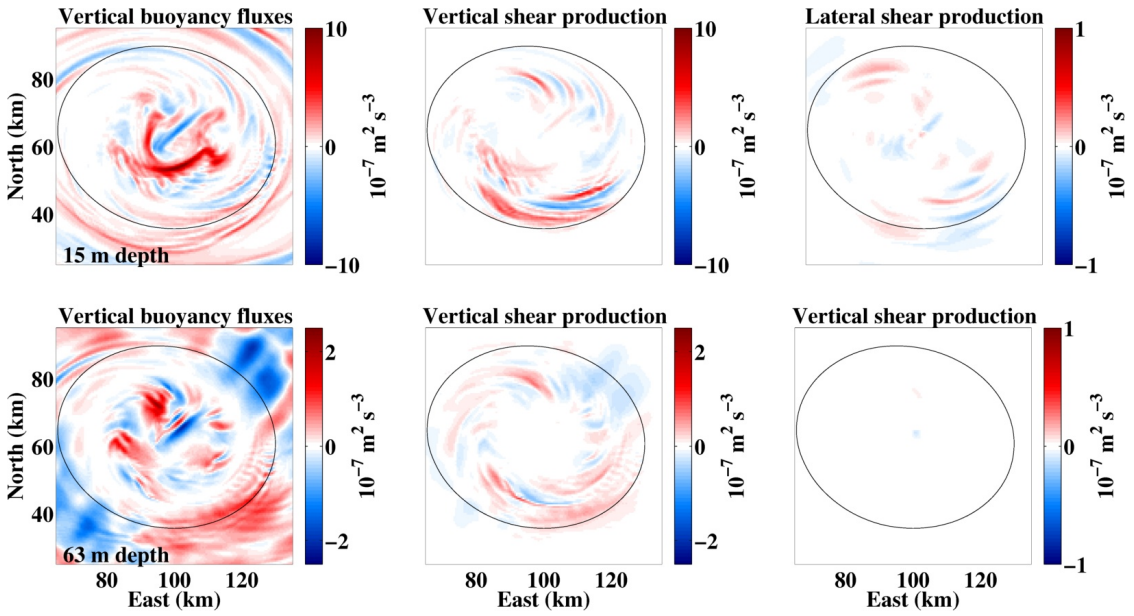

Figure 4.7: Plan views of the energy sources for the perturbations in the mixed layer (top row) and upper thermocline (bottom row) on the fourth day of the interpolation experiments. (Left panels) Vertical buoyancy fluxes (Centre panels) Vertical shear production. (Right panels) Lateral shear production. Different colour scales are used for lateral shear production and in the top and bottom rows. The black contour shows the area over which the energy integrals in Figure 4.8 are calculated.

The shear production terms thus calculated on the fourth day of the interpolation experiments are shown in Figure 4.7. The upper panels show that vertical shear production dominates over lateral shear production in the anticyclone both in the mixed layer (upper panels) and in the upper thermocline (lower panels). Vertical buoyancy fluxes (left panels) are of comparable magnitude to the vertical shear production. The spatial pattern differs between the buoyancy fluxes and vertical shear production, with the largest buoyancy fluxes concentrated in the vortex core, while the vertical shear production is found in the ring around the core of the vortex. This difference in spatial pattern could reflect the filaments being primarily generated by vertical shear production, whereas the vertical buoyancy fluxes are secondary submesoscale baroclinic instabilities.

The black line in Fig. 4.7 shows the boundary within which the mean values in Figure 4.8 are taken. The snapshot plots illustrate the challenge in defining this boundary, which is set to capture the area over which potential vorticity is negative. The mean values in Fig. 4.8 are somewhat noisy due to the challenge of defining the perturbation quantities and the area over which they are taken, but the mean values support the impression given by the snapshots in Fig. 4.7

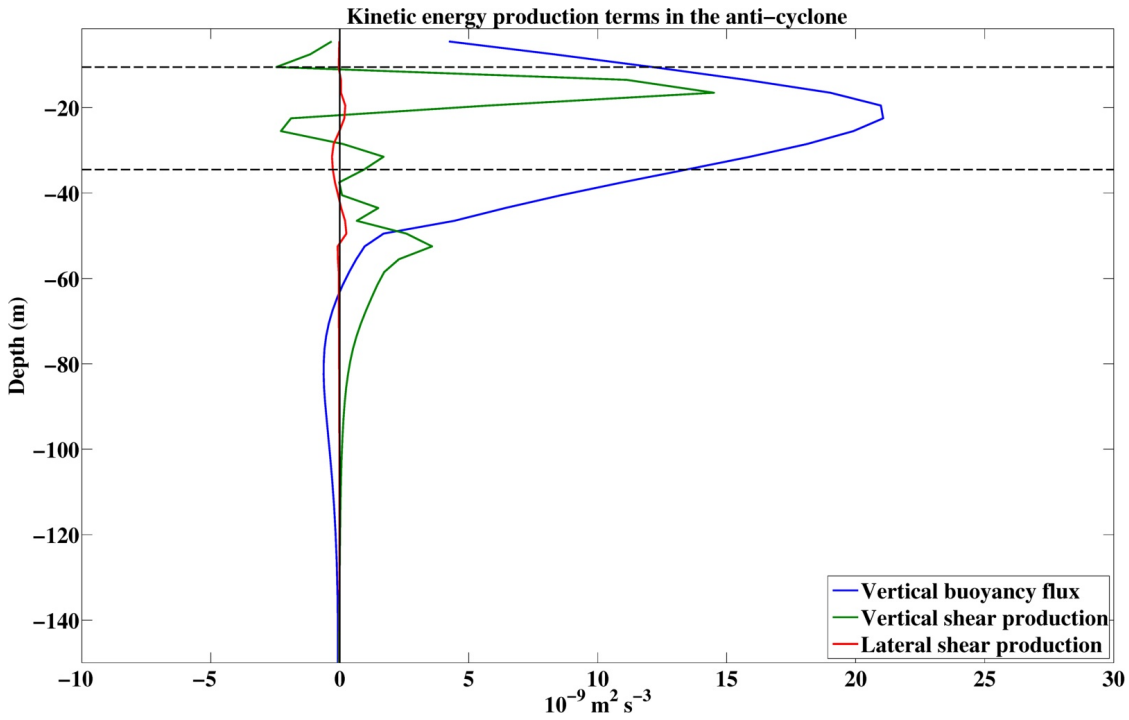

Figure 4.8: Horizontal averages of the source terms in the perturbation kinetic energy budget over the anticyclone on the fourth day of the interpolation experiment. The means have been taken over the area enclosed by the black line in Figure 4.7.

that vertical shear production and vertical buoyancy fluxes are the main sources of perturbation kinetic energy in the mixed layer.

The vertical buoyancy fluxes are negative deeper in the vortex between -120 m and -60 m depth below the mixed layer. This could be an artifact of the area chosen to do the averaging, except that such negative vertical fluxes are found to be a persistent feature of the simulations in Chapter 3.2.1. The energy source terms in Fig. 4.8 suggest that downward kinetic energy fluxes due to vertical shear production could potentially balance the increase in available potential energy implied by the negative buoyancy fluxes, though a full energy budget closure is required.

It is cautioned that Thomas and Taylor [2010] find that the energy budget changes materially for simulations of a symmetrically unstable front when secondary shear instabilities are permitted, rather than parameterised. A numerical configuration that could allow a closure of the energy budget with more confidence is described in Chapter 6.4.

4.6 Mechanisms

If a parameterisation of the filamentation is to be produced for coarse-resolution models, it is imperative that the dynamical causes of the upwelling are understood. By performing the analysis in terms of potential vorticity, the range of possible dynamical causes can be reduced.

A first hypothesis is that the filamentation arises due to mixed layer baroclinic instabilities [Molemaker et al., 2005; Boccaletti et al., 2007]. The positive vertical buoyancy fluxes in the mixed layer (Fig. 4.8) would be consistent with this hypothesis, as the energy source for baroclinic instabilities is the available potential energy of the flow. However, the upwelling has a high radial wavenumber (Fig. 4.5, lower panel), whereas baroclinic instability is associated with a low radial wavenumber that would give rise to a single overturning cell [Stone, 1966b] in the radial direction. The filamentation also has a closer spatial coherence with the vertical shear production in Fig. 4.7, despite the lower mean value of the vertical shear production. Finally, the vertical velocities are primarily-oriented along the isopycnals, (Fig. 4.5, both panels) whereas baroclinic instability induces a vertical displacement of the isopycnals themselves. This leads to the conclusion that baroclinic instability should be rejected as the primary generating mechanism of the filamentation process. The Ekman buoyancy flux leads to regions of positive and negative potential vorticity in the anticyclone. However, the flux of positive potential vorticity is found in the upper 30 m and so cannot account for the positive potential vorticity anomalies that extend up from the base of the mixed layer. The vertical transports associated with down-front winds are primarily diffusive in models run at these resolutions, and so down-front winds cannot account for the advective nature of the upwelling in Fig. 4.5. Therefore Ekman buoyancy fluxes are ruled out as the mechanism that generates the filamentation. The upwelling due to eddy-induced Ekman pumping [Dewar and Flierl, 1987; Martin and Richards, 2001; Mahadevan et al., 2008; Gaube et al., 2014b] has a monopole structure across an vortex, while the simulated upwelling has a higher radial wavenumber. The simulations presented here do not use a relative wind stress or include a parameterisation for the acceleration of the surface wind over a warm core vortex [Gaube et al., 2014b]. Therefore, these vortex-wind interactions are not the cause of the highly filamentation. In addition, the vertical velocities in Fig. 4.5 (b) are also one to two orders of magnitude larger than the vertical velocities predicted from such vortex-wind interactions [Gaube et al., 2014b]. Subsequent

experiments carried out with a relative wind stress show similar results. The interpolation experiments have a constant wind forcing and so the generation of near-inertial motions by high-frequency winds [Lévy et al., 2009] are ruled out as the cause. The entrainment of ambient mixed layer water [Lehahn et al., 2011] is ruled out by the high potential vorticity of the filaments.

Symmetric instability is the dominant instability for flows with positive stratification but negative potential vorticity due to the baroclinic component of potential vorticity [Hoskins, 1974; Haine and Marshall, 1998; Thomas et al., 2013]. Symmetric instability in the mixed layer is thought to grow until it can entrain positive potential vorticity fluid from the thermocline in order to reach a state of zero potential vorticity by mixing the positive and negative potential vorticity fluid [Thorpe and Rotunno, 1989; Taylor and Ferrari, 2009]. Linear stability analyses for symmetrically unstable states predict that the strongest flows are approximately along isopycnals [Haine and Marshall, 1998; Bachman and Taylor, 2014], while the flow itself is ageostrophic [Stone, 1966b]. The main energy sources of the upwelling are vertical buoyancy fluxes and vertical shear production, with the latter most closely linked to the spatial pattern of the filaments.

A further test for the stability of the flow to symmetric instability is the relative alignment of the buoyancy and absolute momentum surfaces. The absolute momentum $M = fr + V_{bal}$, where r is the radial distance from the centre of the vortex and V_{bal} is again the balanced azimuthal velocity. Where the buoyancy surfaces are flat and the absolute momentum surfaces are steep, the flow has positive potential vorticity and is stable to symmetric instability [Hoskins, 1974]. Where the buoyancy surfaces are inclined at a steeper angle than the absolute momentum surfaces, the flow is unstable to symmetric instability. We neglect other scenarios here where the buoyancy surfaces are inverted – which corresponds to a convectively unstable state – and where $M_r < 0$ – which corresponds to a centrifugally unstable state – as the stratification is positive and $\zeta_z > -f$.

The stability is assessed at the outset of the interpolation experiments at 500 m resolution along the section of the anticyclone with negative potential vorticity indicated by the black line in Figure 4.9. The vertical section of potential vorticity is shown in the upper panel of Figure 4.10 with temperature contours in white. The lower panel of Fig. 4.10 shows the absolute momentum fields. Values are negative due to the anticyclonic vorticity of the vortex. In the thermocline, the white temperature contours are relatively flat, while the black absolute momentum contours are close to vertical. In the mixed layer of the vortex between 100

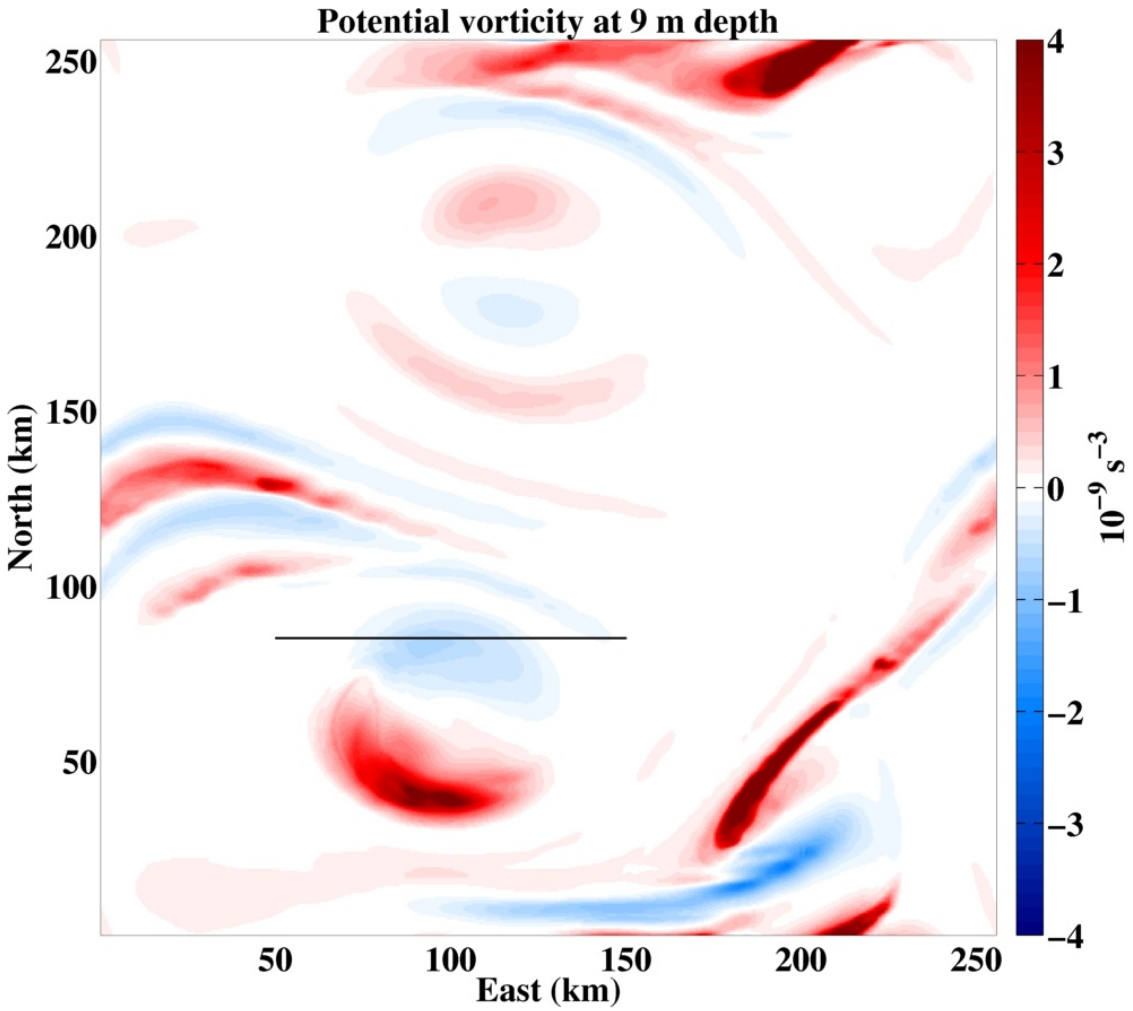

Figure 4.9: The potential vorticity at 9 m depth at day 0.25 of the interpolation experiment at 500 m resolution. The black line shows the section over which the absolute momentum is shown in Figure 4.10.

- 120 km above 40 m depth, on the other hand, the white temperature contours are steep while the absolute momentum contours are flatter. The upper panel shows that this indeed corresponds to the area of negative potential vorticity. On the western side of the vortex, the white temperature contours are clearly steeper than the black absolute momentum contours in the upper 20 m. Below this, the white temperature contours are still slightly steeper than the black momentum contours, though the potential vorticity is slightly positive. This may be due to the cyclogeostrophic balance relationship used to derive the absolute momentum contours breaking down in the far-field of the vortex.

On the basis of the simulation results that the filamentation occurs in regions of negative potential vorticity where the buoyancy surfaces are steeper than the

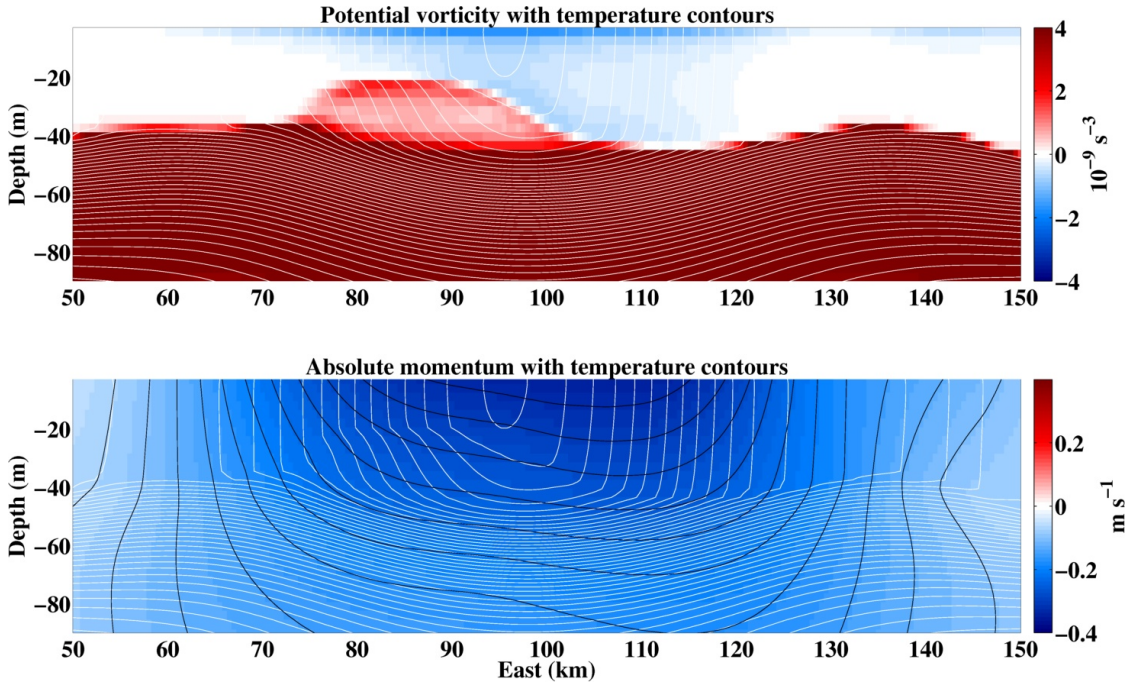

Figure 4.10: The potential vorticity and absolute momentum fields at day 0.25 of the interpolation experiment at 500 m resolution. The section is taken through the region of negative potential vorticity in the north of the anticyclone in Figure 4.9. (Upper panel) The potential vorticity with temperature contours of 0.1°C in white. (Lower panel) The absolute momentum with contours of 0.025 m s^{-1} in black. The white contours are again temperature contours of 0.1°C .

absolute momentum contours, that the upwelling is ageostrophic and entrains positive potential vorticity fluid from the thermocline along isopycnals, the hypothesis that the filamentation is generated by symmetric instability is not rejected. A more detailed examination will require further work. For the remainder of this thesis, however, the assumption is made that the proximate cause of the filamentation is symmetric instability.

Although the classical theory of frontogenesis was developed for states with positive potential vorticity [e.g. Hoskins and Bretherton, 1972], frontogenesis can occur when potential vorticity is negative. However, for the moderate strain rates found in the anticyclone of $\sigma/f \approx 0.2$ (not shown) where $\sigma = ((u_x - v_y)^2 + (v_x + u_y)^2)^{1/2}$, the initial growth rate for symmetric instability is similar to that in the absence of strain [Thomas, 2012]. Frontogenetical effects are, however, expected to extract kinetic energy from the instability over the following days [Thomas, 2012].

4.7 Effect of flow curvature on potential vorticity approximations

The filamentation attributed here to symmetric instability happens within mesoscale anticyclones. This instability happens in a coherent vortex and the stability of such vortices is a classical problem in fluid mechanics [e.g. Kloosterziel and Van Heijst, 1991; Smyth and McWilliams, 1998; Kloosterziel et al., 2007; Lazar et al., 2013] amongst many others. However, this literature concentrates primarily on barotropic vortices vertical stratification but with no initial horizontal buoyancy gradient with no vertical shear due to thermal wind balance. The regions of upwelling in the vortices are mixed barotropic-baroclinic zones, as the isopycnals slope upwards from the base of the thermocline to outcrop at the surface while the gradients in sea surface height associated with the vortex give rise to anticyclonic relative vorticity and angular velocity. In this baroclinic respect the upwelling has dynamic similarity with submesoscale fronts, which are generally taken to be essentially baroclinic in numerical simulations

To illustrate the role of curvature, the thermal wind balance of a flow in cyclogeostrophic and hydrostatic balance is re-derived. Following Smyth and McWilliams [1998], for example, the initial flow is assumed to be cyclogeostrophic and hydrostatic balance with

$$\frac{V_\theta^2}{r} + fV_\theta = \frac{\partial \pi}{\partial r}, \tag{4.5}$$

$$\frac{\partial \pi}{\partial z} - b = 0, \tag{4.6}$$

where V_θ is again the azimuthal velocity, r is the radial coordinate of the vortex and π is ρ^{-1} times the pressure.

In this thesis, the cyclogeostrophic balance should be thought of as reflecting a flow with Rossby number of order one with significant contributions from both centripetal and Coriolis accelerations, as opposed to the high Rossby number cyclostrophic balance without Coriolis acceleration often considered in the atmospheres of slowly rotating bodies such as Venus [e.g. Read, 2013]. These balance equations are then cross-differentiated following the same procedure as for geostrophic thermal wind balance:

$$\frac{\partial}{\partial z}\left(\frac{V_\theta^2}{r} + fV_\theta\right) = \frac{\partial^2 \pi}{\partial z \partial r}, \tag{4.7}$$

$$\frac{\partial^2 \pi}{\partial r \partial z} - \frac{\partial b}{\partial r} = 0, \tag{4.8}$$

before eliminating the pressure term and differentiating the product on the left-hand side of 4.7 giving:

$$\frac{2V_\theta}{r}\frac{\partial V_\theta}{\partial z} + f\frac{\partial V_\theta}{\partial z} = \frac{\partial b}{\partial r}, \tag{4.9}$$

or:

$$\left(f + \frac{2V_\theta}{r}\right)\frac{\partial V_\theta}{\partial z} = \frac{\partial b}{\partial r}. \tag{4.10}$$

In order to understand the effect of replacing $\partial V_\theta / \partial z$ in the baroclinic component of the potential vorticity definition, this is re-written implicitly as:

$$\frac{\partial V_\theta}{\partial z} = \frac{1}{(f + 2V_\theta / r)}\frac{\partial b}{\partial r} \tag{4.11}$$

The effect of the centripetal acceleration is to introduce the quantity $2V_\theta / r$, twice the angular velocity of the vortex, into the thermal wind balance. This is the same term that arises in the stability criterion for barotropic vortices [Kloosterziel et al., 2007]. To get a sense of the relative magnitude of this additional term in the simulated vortices, the pre-factor on the right hand side can be thought of as a scaling factor $\gamma = f(f + 2V_\theta / r)^{-1}$ that multiplies f^{-1} when using horizontal buoyancy gradients to estimate the vertical shear in the baroclinic component of potential vorticity.

A number of cases can be considered to develop an intuitive feel for γ. Firstly, for straight fronts, or equivalently as $r \to \infty$, then $\gamma = 1$ and the geostrophic thermal wind relation is recovered. For cyclonic flows, say $2V_\theta/r \sim 0.5f$, then $\gamma = f/(f + 0.5f) = 2/3$ and so $\partial V_\theta/\partial z = (2/3)f^{-1}\partial b/\partial r$. In this cyclonic case approximating the vertical shear with the horizontal buoyancy gradient leads to overly negative potential vorticity compared to its true value.

For anticyclonic flows, say $2V_\theta/r \sim -0.5f$, then $\gamma = f/(f - 0.5f) = 2$ and so the vertical velocity shear $\partial V_\theta/\partial z \sim 2f^{-1}\partial b/\partial r$. Therefore, in this case approximating the vertical shear with the horizontal buoyancy gradient leads to overly positive potential vorticity compared to its true value. The curvature effect is stronger for anticyclonic flows than cyclonic flows at the same magnitude of angular velocity.

The range of values for γ in practice may be understood by considering the anticyclone in the interpolation experiments at 500 m resolution. The upper panel of Figure 4.11 shows the spatial pattern of γ at the surface in the anticyclone. The vortex centre, where $r = 0$, is taken as the point of maximum pressure anomaly. The scaling factor γ is greater than 1 everywhere due to the anticyclonic flow. The values of γ along the solid and dashed lines are shown in the lower panel of Fig. 4.11. The high values of γ found in the vortex core can be ignored, as the horizontal buoyancy gradients are very weak in the vortex core and there is little effect on potential vorticity. More importantly, γ reaches values between 1.3-1.7 in extensive regions of the vortex. These values of γ are typical of those found throughout the mixed layer. The spatial pattern of γ in Fig. 4.11 is not circular, as the vortex is somewhat elliptic and so higher centripetal accelerations are found along the major axis of the vortex which runs through the regions of higher values of γ. Domain-scale plots suggest that this major axis is on a line that connects the centres of the cyclonic and anticyclonic vortices and so could reflect the remote effect that the vortices have on each other [Bracco et al., 2000].

As a practical consequence, the results show that if an estimate of potential vorticity is being made in the mixed layer of this anticyclonic vortex with buoyancy data alone then $f^{-1}|\nabla_h b|^2$ should be replaced with $\sim \gamma f^{-1}|\nabla_h b|^2$ in the baroclinic component of potential vorticity. The angular velocity profile could be estimated based on altimetry velocities [Douglass and Richman, 2015], though allowance may have to be made for stronger velocities than implied by altimetry in the very baroclinic mixed layer.

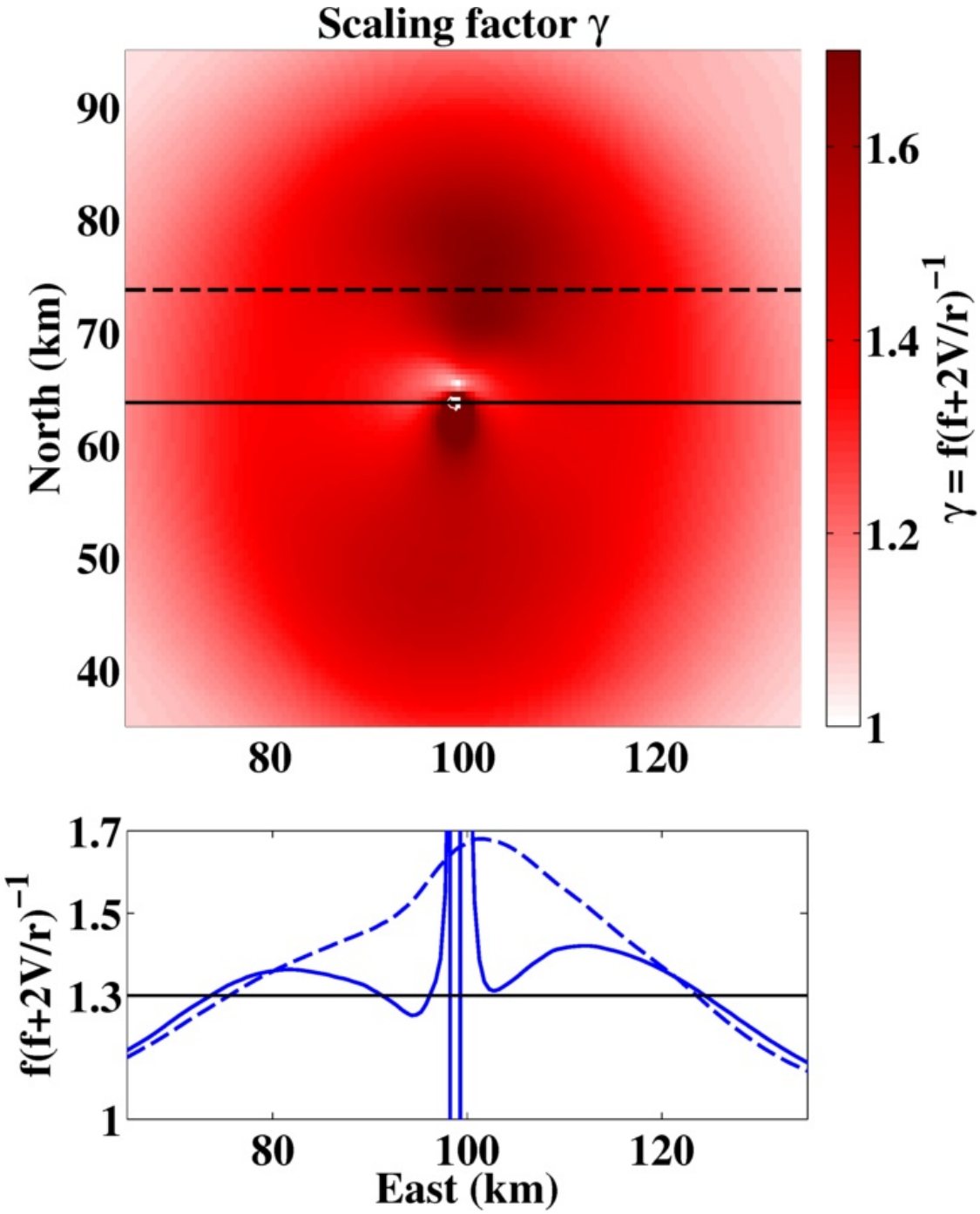

Figure 4.11: Scaling factor γ, defined in the text, for including horizontal buoyancy gradients in an estimate of potential vorticity in an anticyclone. (Upper panel) Plan view of the scaling factor at the surface in the anticyclone. (Lower panel) The scaling factor over the corresponding solid or dashed lines in the upper panel.

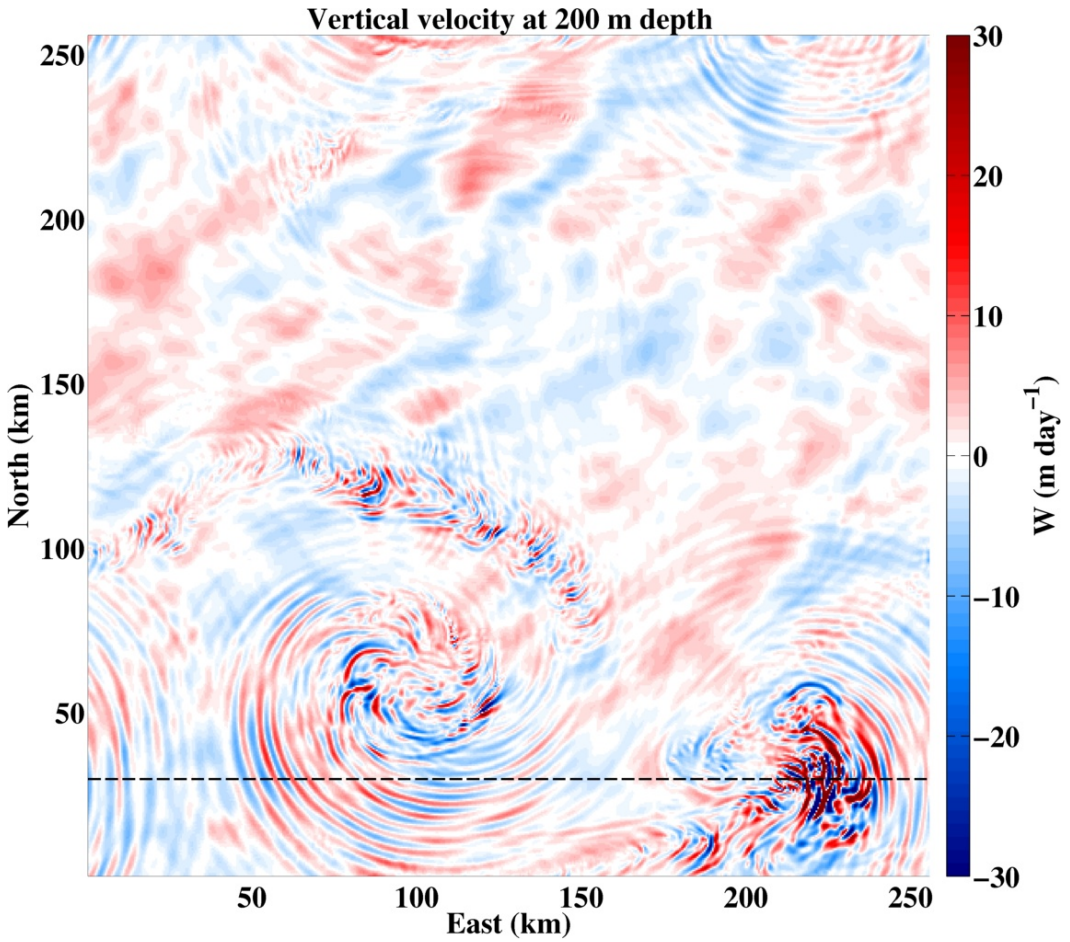

Figure 4.12: Snapshot of the vertical velocity in the thermocline at 100 m depth on day 7 of the interpolation experiments at 0.5 km resolution. The dashed black line shows where the vertical slice in Fig. 4.13 is taken. The anticyclone is centred at (100 km, 60 km) and the cyclone is centred at (145 km, 190 km). The feature at (220 km, 30 km) is a destructive merger between oppositely-signed vortices.

4.8 Inertia-gravity waves

The analysis of momentum balances in Chapter 3 shows that the filaments in the anticyclone have a low degree of geostrophic and cyclogeostrophic balance. If the flow in the filaments does not satisfy a higher degree of balance they may undergo Rossby adjustment to a balanced state while emitting inertia-gravity waves [Rossby, 1938]. Figure 4.12 shows the vertical velocity in the thermocline at 100 m depth in the 0.5 km interpolation experiment. The figure shows the presence of strong vertical velocities with a banded structure. This banding could reflect phase lines of inertia-gravity waves that develop a spiral structure in the same sense of rotation as the anticyclone, for example near (50 km, 60 km). This

structure is suggestive of a wave-capture [Bühler and McIntyre, 2005] whereby the 'mean-flow' – the cyclogeostrophic vortex in this case – is affecting the development of the inertia-gravity waves. The spatial patterns in Fig. 4.12 can be compared to Figure 12 of Viúdez [2008], which shows similar phase banding. For the avoidance of doubt, the wave generation mechanism proposed here is not the spontaneous imbalance considered in [Viúdez, 2008] or [McIntyre, 2009], but rather a consequence of unbalanced instabilities.

The wave-like properties of these bands can be seen in Figure 4.13 by taking a vertical slice of the vertical velocity and potential vorticity fields. The vertical velocity field (upper panel) shows lines of constant phase for waves being emitted from the anticyclone. Taking the phase lines at (125 km, -200 m), the source region in the mixed layer has strong vertical velocities (upper panel) and negative potential vorticity (lower panel). Away from the anticyclone, the plan view in the thermocline in Fig. 4.12 shows that there are also strong wave emissions from the front at (220 km, 30 km). These have a similar vertical phase profile to the waves emitted from the anticyclone and also appear to originate in a region of negative potential vorticity and unbalance motion (not shown). While Fig. 4.13 shows the waves over the upper 400 m, they in fact propagate down through the entire depth of the domain, while remaining within the anticyclone at all depths (not shown).

These inertia-gravity waves are removing energy from the surface layer of the vortex to its deeper layers and to regions outside the vortex. Estimates of the magnitude of energy fluxes associated with spontaneously-generated inertia-gravity waves are typically small compared to the energy of the vortex [Tsang and Dritschel, 2015]. For example, in a simulation of an inertially unstable barotropic vortex Kloosterziel et al. [2007] find that less than 1% of the energy lost due to viscosity in the instability region occurs in a sponge layer where inertial waves are damped. However, this may not be the case here as the waves are being generated by the unbalanced filaments, which may be a stronger process than the spontaneous loss of balance typically considered for large vortices. Direct numerical simulations of the energy flux suggest that the dissipation scales as E^2N^2, where E is the internal wave energy density [Winters and D'Asaro, 1997]. Detailed estimation of the associated energy fluxes will be considered in a follow-on work.

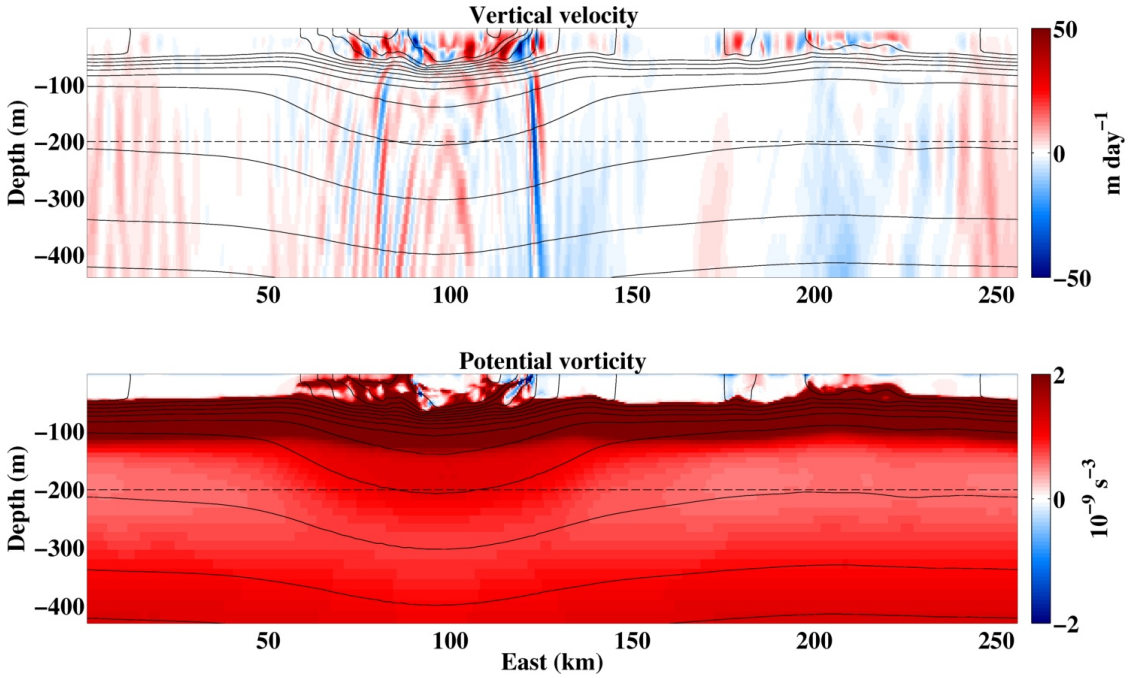

Figure 4.13: Snapshots of the vertical velocity and potential vorticity at day seven of the interpolation experiment at 0.5 km resolution. (Upper panel) The vertical velocity concentration. (Lower panel) Potential vorticity. Black lines are temperature contours with an interval of 0.5° C. The dotted black line shows the depth at which the plan-view in Fig. 4.12 is taken (all panels).

4.9 Subduction

The results presented here show that filaments of high potential vorticity fluid are found in the mixed layer of anticyclonic vortices. This is indicative of a process that can exchange low potential vorticity fluid from the mixed layer for high potential vorticity fluid from the thermocline along buoyancy surfaces that outcrop to the surface. Such exchange between the mixed layer and thermocline is known as 'subduction' [e.g. Marshall and Nurser, 1992] and is considered in more detail here in terms of downwelling of a passive tracer and the upwelling of nutrient-rich water.

The focus here is on subduction occurring within the anticyclonic vortex, rather than frontal subduction [e.g. Pollard and Regier, 1992; Spall, 1995; Thomas, 2008].

4.9.1 Downwelling of a passive tracer

To test whether subduction is indeed occurring, a passive tracer is released in the model at the outset of the interpolation experiments. This indicates the depth to which fluid particles with surface origins can penetrate to. The tracer has an initial concentration of 1 everywhere in the 3 m thick surface level of the model. The tracer is then quickly diffused vertically through the mixed layer in the first hours. The mixed layer is initially about 30 m deep and so 10 times thicker than the surface level of the model. The tracer concentration is thus reduced from 1 to around 0.1 throughout the mixed layer.

Figure 4.14 compares the mean tracer concentration at the 0.5 km and 4 km resolutions. The upper panel shows that the tracer concentration is consistently lower in the mean mixed layer and higher in the mean thermocline at the finer resolution. This is consistent with additional subduction occurring at finer resolution. The lower panel shows the relative mean temperature profiles at these resolutions and is discussed further in Chapter 4.9.4 in terms of fluxes of active tracers.

The tracer distribution and potential vorticity at 60 m depth are shown in Figure 4.15 (upper panels) on day 7. This is in the depth range of higher tracer concentration below the mean mixed layer depth in Fig. 4.14 (upper panel). The colour scale of potential vorticity (top-right panel) is an order of magnitude greater than used previously in this Chapter, as this depth level is in the thermocline through most of the domain.

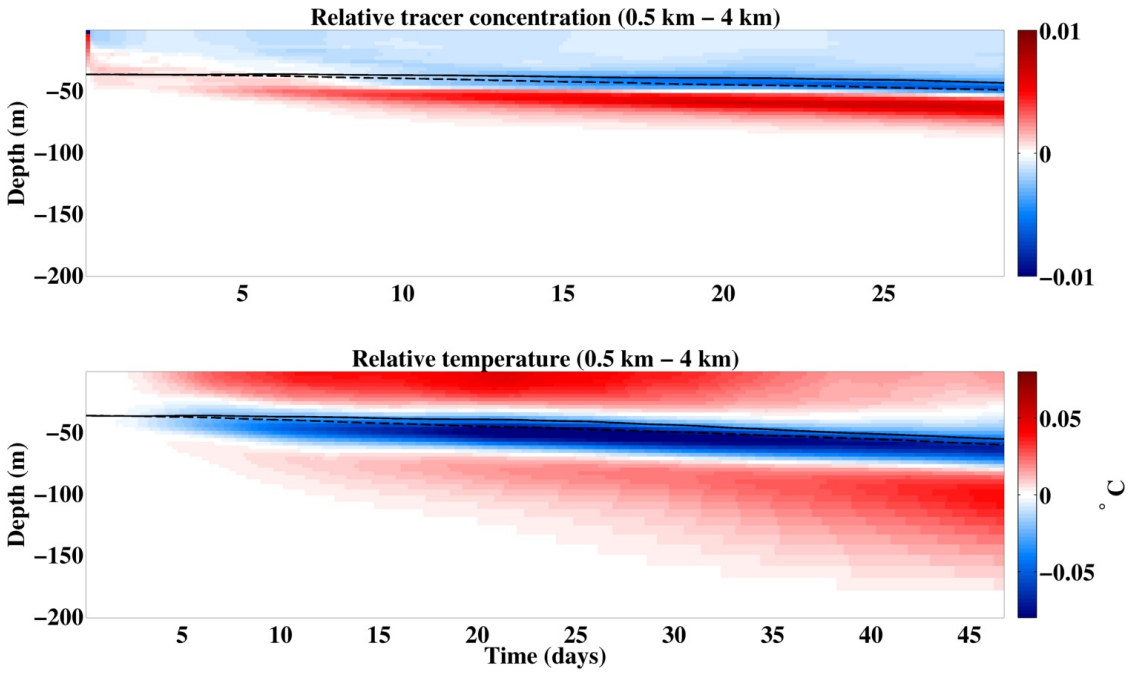

Figure 4.14: Comparison of tracer and temperature profiles between the simulations at 0.5 km and 4 km resolution. (Upper panel) Relative tracer concentration with red colours indicating higher concentrations at finer resolution. (Lower panel) Relative temperature ($\overline{T}_{0.5km} - \overline{T}_{4km}$).

The regions of high tracer concentration at this depth are in the anticyclone and the two fronts to its north and east. In the anticyclone, the lower panel of Fig. 4.15 shows that this depth is at the base of the low potential vorticity surface layer, due to downward doming isopycnals. The fluid at this depth would not considered to be in the mixed layer based on typical mixed layer depth definitions. In this thesis, for example, the mixed layer is taken to be the first depth with temperature 0.1° C less than the surface value. A region with tracer concentration close to 0 can also be seen at (115 km, -50 m). This is a filament with a positive potential vorticity anomaly (not shown). This illustrates the nature of the subduction process outlined here, whereby the downwelling occurs along the shallow trajectories of isopycnals that outcrop at the surface, rather than the more dramatic subduction where a deep mixed layer is restratified by positive buoyancy fluxes at the surface.

The regions of low potential vorticity (upper-right panel) in the anticyclone and at the fronts at 60 m depth all have vertical components of relative vorticity close to -f (not shown). This is in agreement with that the idea of Thomas [2008] whereby frictional destruction of potential vorticity at fronts creates low potential

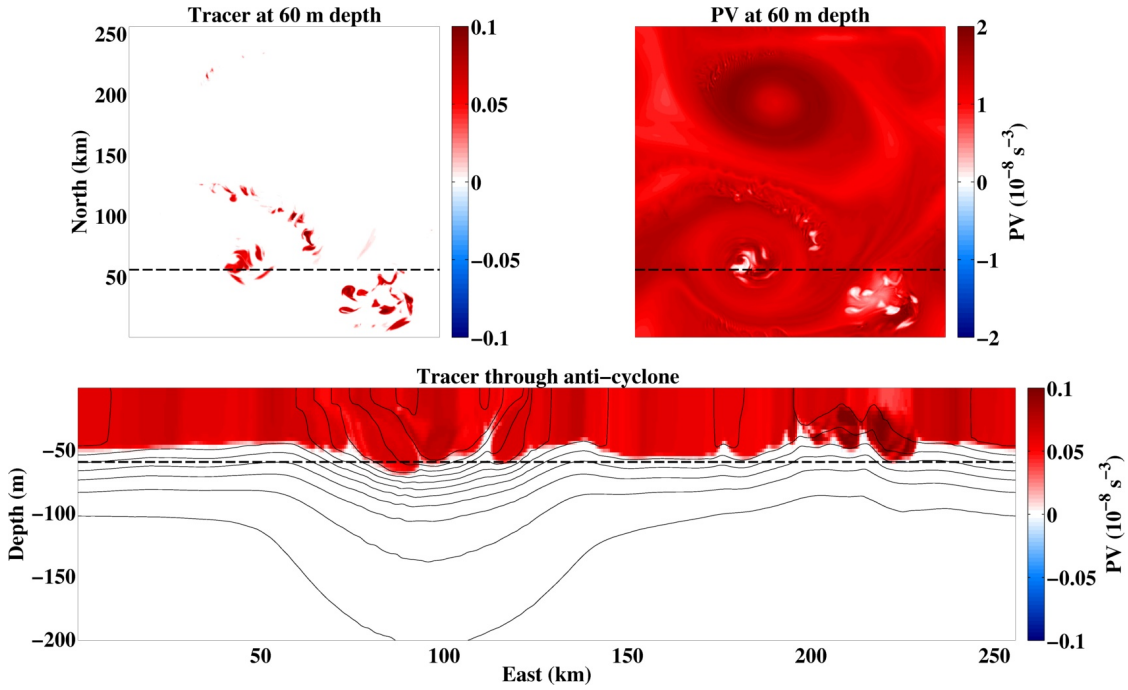

Figure 4.15: Tracer and potential vorticity for the simulation at 0.5 km on day 7. (Upper panels) Plan views of tracer and potential vorticity at 60 m depth. (Lower panel) Vertical slice of tracer concentration through the anticyclone. Solid black lines in the lower panel are temperature contour with interval of 0.5° C. The dashed lines show the relative locations of the plan views and vertical slice.

vorticity fluid that can form lens-like structures in the thermocline where low baroclinic potential vorticity is converted to low vertical potential vorticity. This lens formation occurs during or after any negative potential vorticity has been mixed away to restore stability to symmetric instability.

4.9.2 Limiting nutrient experiment

4.9.3 One dimensional and coarse resolution three dimensional simulations

To control for the response of the model to diffusive and non-submesoscale upwelling from the thermocline, a comparison is made between one-dimensional and coarse resolution three dimensional simulations. The initial conditions for the one-dimensional simulation is the temperature profile inside the anticyclone. The coarse resolution three dimensional simulation is the mesoscale-vortex resolving 4 km run used as the initial condition for the 0.25 km run and horizontal averages are taken over the region of the anticyclone. The boxes in Figure S1 show the region over which averaging is performed.

Figure 4.16 shows that the one-dimensional model has no surface biological productivity as the nutrient remains below the mixing layer depth and so is not transported towards the surface. Biological productivity here refers to the rate of fixation of phosphate. There is higher productivity at depth due to the high nutrient concentrations and the deep penetration of light.

A comparison of the biological productivity at the surface in the 4 km resolution simulation and the 250 m resolution simulation over the first 12 days is presented in Figure 4.17. This shows that there is increased primary productivity in the anticyclone at finer resolution. By day 12 (bottom panels), the mean productivity in the surface level of the anticyclone is five times greater at 250 m resolution compared to 4 km resolution. The anticyclone is not the only high productivity region in the domain at either of these resolutions. There is also a region of high productivity to the north-east of the anticyclone where high productivity is present from day 2 of the experiment. This rapid vertical transport is diffusive, rather than advective (not shown). The diffusive cause of this transport is apparent from the smoothness of the spatial distribution and the rapidity with which it occurs. The diffusive transport occurs in these regions because the mixed layer is sufficiently deep in these regions to extend down to the depths where the limiting nutrient is initially seeded and so the elevated vertical diffusive mixing

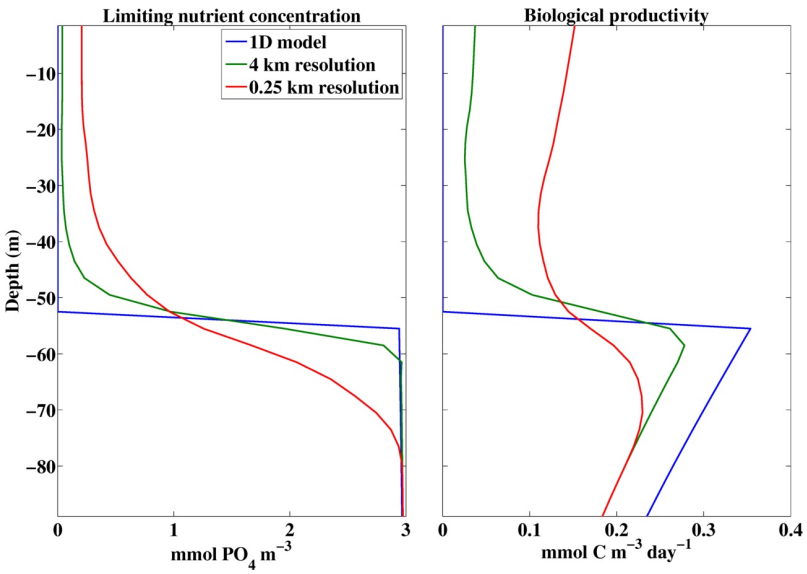

Figure 4.16: Comparison of the biological response in the anticyclone between a one-dimensional simulation, the coarser resolution 4 km simulation and the fine resolution 0.25 km simulation. The left-hand panel shows the concentration of the limiting nutrient. The right hand panel shows the biological productivity.

due to the *KPP* scheme transports the nutrient quickly to the surface. As such, the experimental methodology of a limiting nutrient does not apply in these regions. Higher primary productivity is also found in the south-east corner of the domain, where there is a vortex collision between an anticyclone and a cyclone. This anticyclonic region is similar in many respects to the coherent anticyclonic vortex that is the main focus here.

There is no evidence for higher productivity occurring in the cyclone in the north of the domain at either resolution. Observations do show that cyclones can be regions of higher primary productivity, where the upward-doming isopycnals in cyclones lift nutrient-rich water towards the light [e.g. Benitez-Nelson et al., 2007]. Such a process is related to the initial formation of an vortex and so this behaviour is not captured in this experiment. These results simply highlight the lack of submesoscale upwelling within the cyclone.

While the plots in Fig. 4.17 show the development of biological productivity at the surface, there is also considerable spatial structure in this productivity at depth. Figure 4.18 shows the biological productivity at the surface and at the base of the mixed layer on day 8. The spatial patterns at the surface (left panel) are much more diffused horizontally than the spatial pattern at the base of the mixed layer (right panel). At the base of the mixed layer, the filamentary nature of the

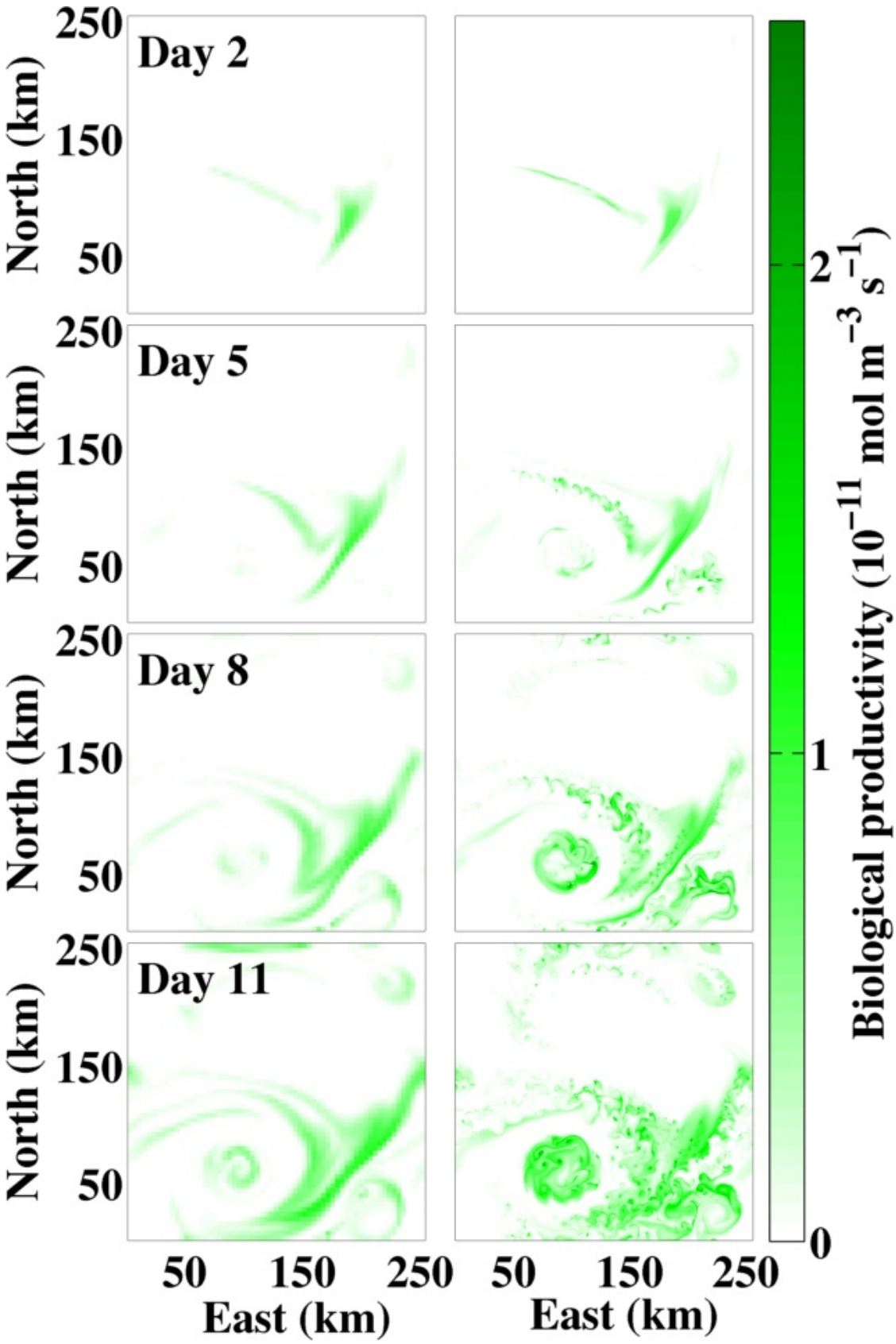

Figure 4.17: Snapshots of biological productivity through time at the surface in the limiting nutrient experiment at 4 km resolution (left panels) and 250 m resolution (right panels).

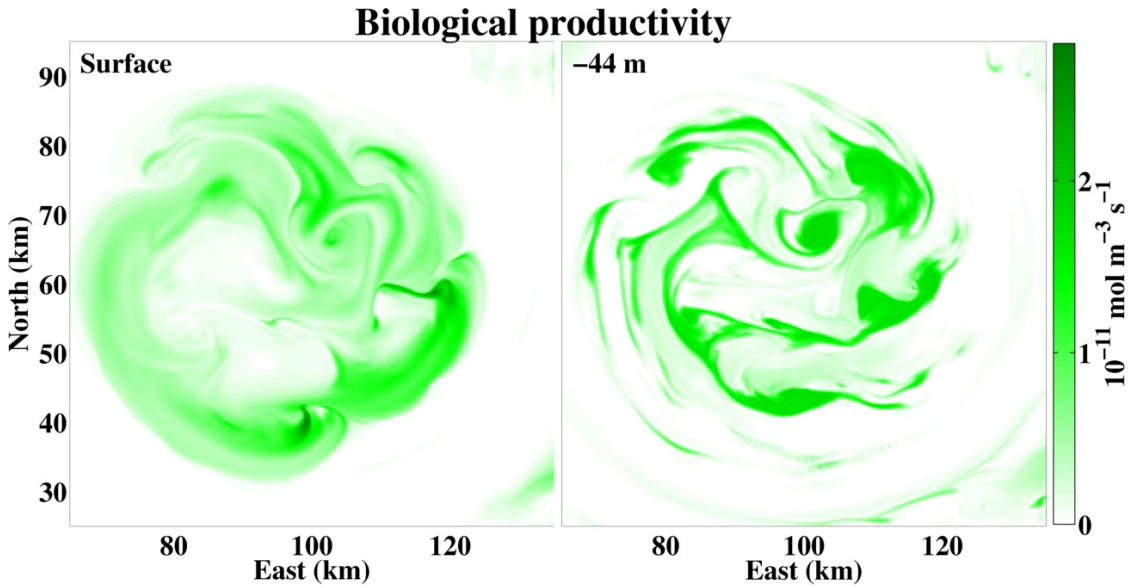

Figure 4.18: Snapshots of biological productivity on day 8 of the limiting nutrient experiment at 250 m resolution at the surface (left panel) and at the base of the mixed layer (right panel).

upwelling is more readily apparent.

The relatively diffuse pattern of productivity at the surface is reminiscent of the satellite image shown in Fig. 1.1. However, this spatial pattern arises in large part due to the *KPP* surface mixing scheme and near-surface patterns should be expected to change if the actual surface turbulent processes such as convection [Taylor and Ferrari, 2010] or Langmuir turbulence [Hamlington et al., 2014] were included.

4.9.4 Vertical buoyancy fluxes

The results in Chapters 4.9.1 and 4.9.2 show that there is strong vertical transport passive tracers. These effects can occur if the upwelling mechanism simply allows exchange of high potential vorticity and low potential vorticity fluid along an isopycnal. Bachman and Taylor [2014], however, show that symmetric instability can also lead to positive or negative vertical buoyancy fluxes where the isopycnals themselves are flattened or steepened, consistent with the fluxes found in Fig. 4.8 and so the effect of the mechanism on the active buoyancy tracer is also of interest. As noted in Chapter 4.5, however, a full closure of the perturbation energy budget is not yet available to provide a complete description. The results here give a sense of how this process may work in the simulations. Before examining the effect of the vertical transport specifically in the anticyclone, the domain-average statistics

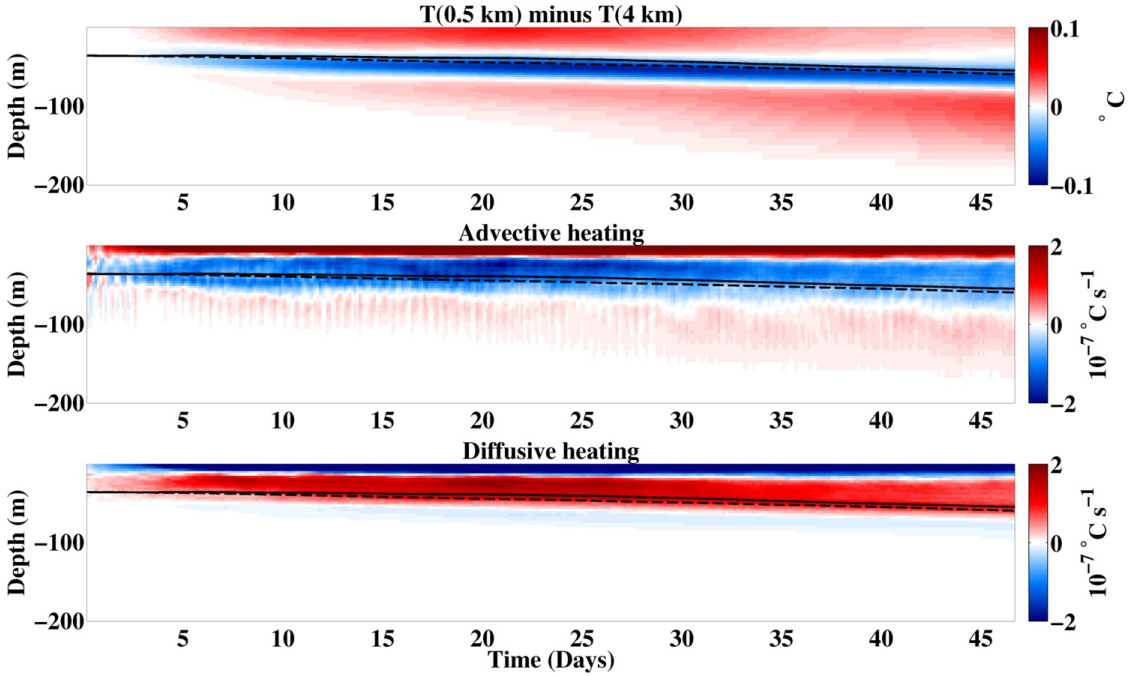

Figure 4.19: Advective and diffusive contributions to temperature differences in the interpolation experiment. (Upper panel) Difference in level-mean temperature ($\overline{T}_{0.5km} - \overline{T}_{4km}$). (Centre panel) Additional heating effect of mean vertical advective fluxes at finer resolution. (Lower panel) Additional heating effect of mean diffusive advective fluxes at finer resolution. See Fig. 3.4 and the accompanying text for a more complete description of the fluxes. Red (blue) colours in the centre and lower panel corresponds to a heating (cooling). The solid (dashed) black line is the mean mixed layer depth of the 0.5 km (4 km) resolution run.

are considered. Figure 4.19 compares the mean temperature between the 0.5 km and 4 km resolutions. The upper panel shows that in the upper mixed layer there is excess heating at finer resolution, a relative cooling of the lower mean mixed layer and a relative warming of the mean thermocline in a layer that steadily thickens below the mean mixed layer depth. This recovers the result in Chapter 3.2.1 that the warming of the mean thermocline is due to vertical advective heating (centre panel) and partially offset by diffusive cooling (lower panel).

The vertical structure of the advective fluxes implies that in the domain-mean there is a thermally-direct cell – where vertical buoyancy fluxes are positive – above a thermally-indirect cell – where vertical buoyancy fluxes are negative – with the boundary between the two cells in Fig. 4.19 given approximately by the mean mixed layer depth.

As the wind forcing is spatially uniform in the interpolation experiments, the circulation associated with the spatial structure of the wind stress used in the full experiments in Chapter 3 can be ruled out as the cause of the thermally indirect circulation.

The use of a common start point for the interpolation experiments allows a direct comparison of the vertical heat fluxes. A plan view of the vertical buoyancy fluxes ($w'b' = wb - w\bar{b}$) at 4 km resolution and 0.5 km resolution on day 3 of the interpolation experiments is given in Figure 4.20. The fluxes are concentrated in two regions of strongly negative potential vorticity (confer with Fig. 4.3, right panel). The stronger advective fluxes at finer resolution have a submesoscale structure both in the mixed layer (upper panels) and thermocline (lower panels). The strongest vertical buoyancy fluxes are about five times greater at finer resolution and are found in the anticyclone and at the front to the east. If the colour range is saturated by a factor of two or more, regions of generally positive vertical buoyancy fluxes appear in frontal regions in a manner consistent with frontogenesis or restratification by extraction of available potential energy by baroclinic instability.

The effect of the vertical buoyancy and potential vorticity fluxes associated with the vertical transport can be estimated on day 7 by comparing the mean temperature and potential vorticity profiles in the anticyclone where the upwelling is resolved compared to the 4 km control run. Figure 4.21 shows that the heating of the upper mixed layer, cooling of the lower mixed layer and heating of the thermocline is stronger inside the cyclone than in the domain outside the anticyclone. In addition, there is a relative heating of the thermocline in the anticyclone

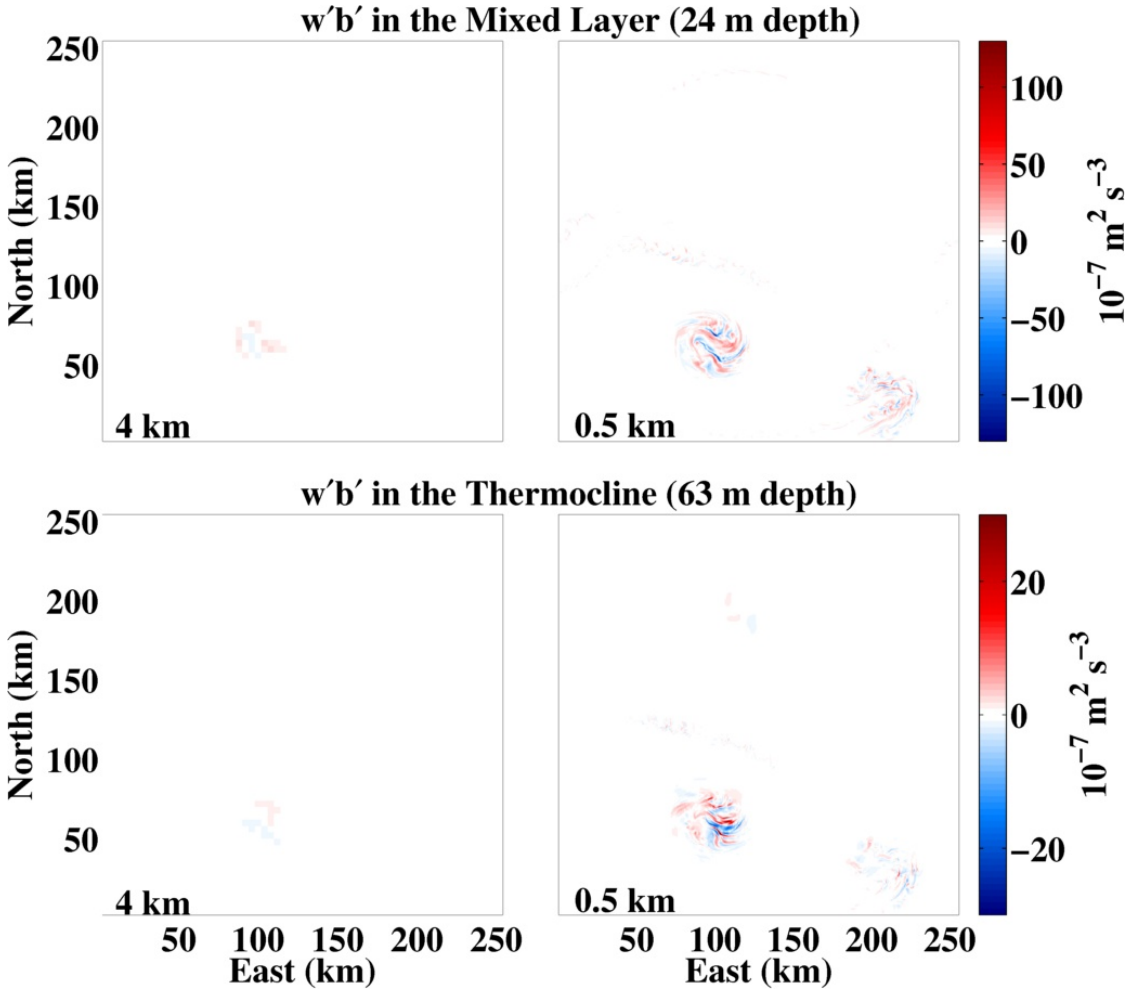

Figure 4.20: Snapshots of the vertical advective buoyancy fluxes ($w'b'$) on the day 5 of the interpolation experiments at 4 km (left-hand panels) and 0.5 km (right-hand panels) resolution. The top row shows the vertical advective buoyancy fluxes at 24 m depth in the middle of the mixed layer. The bottom row shows the vertical advective buoyancy flux at 63 m depth in the thermocline. The mean mixed layer depth is 40 m at this time for both runs.

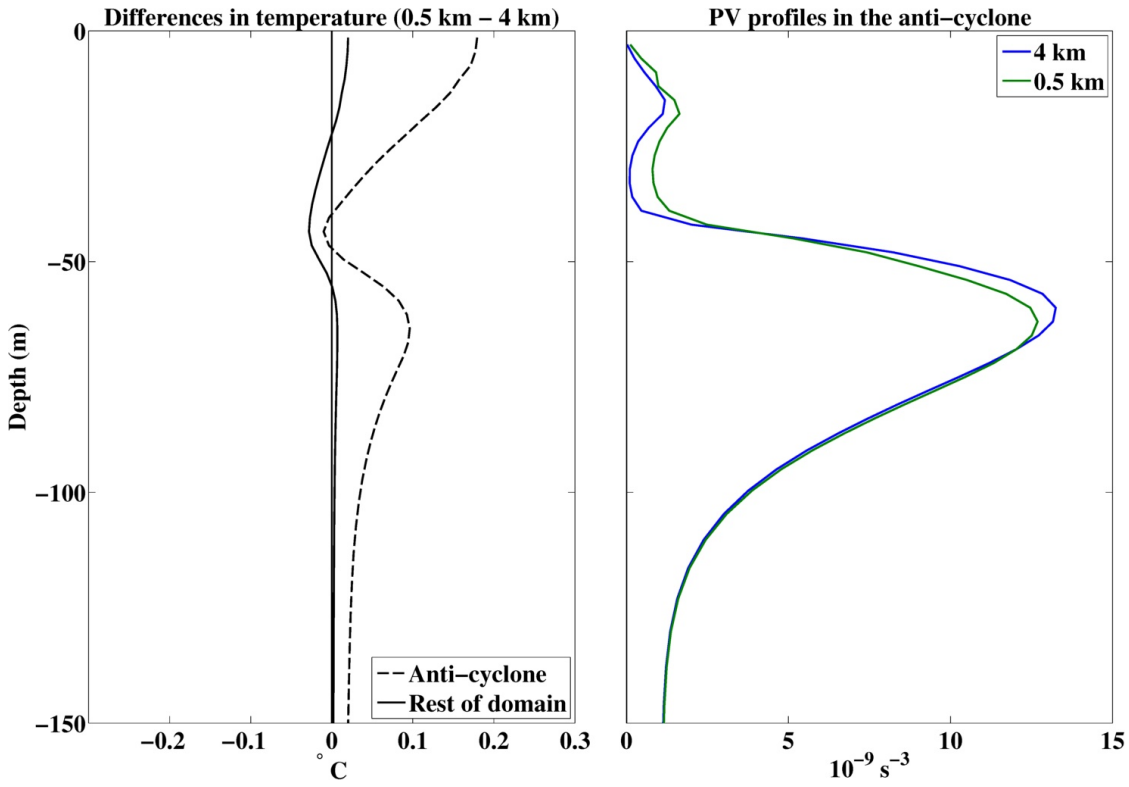

Figure 4.21: Vertical profiles of the temperature differences between the run at 4 km resolution and the run at 500 m resolution inside and outside the anticyclone (left panel) and the mean potential vorticity profiles (right panel).

that is consistent with the negative buoyancy fluxes in the anticyclone at 0.5 km resolution in Fig. 4.8. The potential vorticity profiles (left panel) shows that these changes reflect a stronger upward flux of potential vorticity at finer resolution. The results here illustrate the potential importance of symmetric instability in vertical heat fluxes in anticyclonic vortices.

4.10 Discussion

The numerical results in this Chapter show that intense upwelling of fluid from the thermocline into the mixed layer occurs in anticyclonic vortices. This upwelling is submesoscale in nature and occurs approximately along isopycnal surfaces. The upwelling occurs in regions where the potential vorticity has the opposite sign to f and so is attributed to a form of symmetric instability. Anti-cyclonic vortices are shown to be perhaps the preferred site of symmetric instability in the ocean due to the presence of strong buoyancy gradients, negative relative vorticity and negative angular velocity. The fact that the instability is suppressed in

cyclones in the simulations despite similar wind-forcing suggests that the relative vorticity and angular velocity play a key role in setting the stability of vortices, though further work is required to understand the energetic pathways in more detail.

The filamentation process is associated with a strong flow approximately along isopycnals that outcrop to the surface in the mixed layer of the anticyclone. A simplified biogeochemical experiment shows that this vertical transport can induce strong advective transport of nutrients upwards into the light-rich surface layer. A key conjecture that emerges from this work is that symmetric instability may be of importance for marine ecosystems as an upwelling mechanism. As shown by Taylor and Ferrari [2009], the generation of negative potential vorticity requires mixing with positive potential vorticity fluid to arrive back at a stable state. By the impermeability theorem [Haynes and McIntyre, 1987], this positive potential vorticity must come from diabatic or frictional fluxes of potential vorticity into the ocean from the surface or it must be upwelled along isopycnals from the thermocline. If a symmetrically unstable state is generated, it could be equilibrated by up-front winds as the unstable fluid column moves around the vortex or it could be equilibrated by heating or rain at the surface. These mechanisms would restore stability without inducing transport from the thermocline. Note, however, that both up-front winds and buoyancy fluxes into the ocean may not penetrate down through the full depth of the negative potential vorticity region and so the instability may still occur deeper in the mixed layer. Generating symmetric instability in the real ocean requires that the vortices are sufficiently baroclinic so that the down-front wind region can extract sufficient potential vorticity to lead to negative potential vorticity. This will be a key point of enquiry of observational datasets.

The vertical buoyancy fluxes require further study, but the initial results here show a net restratification in the surface layer, but a destratification in the thermocline.

Theoretical and numerical results show that the shear and vertical transports associated with the surface wave field [McWilliams and Fox-Kemper, 2013; Hamlington et al., 2014] are also of first order importance for frontal instabilities. In particular, Haney et al. [Subm. to JPO] show that the Stokes shear associated with the surface wave field offsets the down-front wind effect when wind and waves are aligned. Furthermore, Colin de Verdière [2012] shows that including the horizontal components of the planetary vorticity vector also destabilises the

flow when relative vorticity is negative. A full analysis will have to take all of these factors into account. A set of steps to make progress in terms of dynamical understanding are set out in Chapter 6.4.

The results highlight the role that both baroclinicity – traditionally considered primarily in relation to fronts – and relative vorticity and angular velocity – traditionally considered primarily in relation to vortices – in setting the stability of the flow. The results suggest that the scalings derived from linear stability analyses such as Stone [1966b] for fronts or Smyth and McWilliams [1998] or Kloosterziel et al. [2007] for vortices have to be modified to take into account the effects of both baroclinicity and curvature. The upwelling of high potential vorticity fluid from the thermocline apparently as part of the equilibration of the instability shows that the presence of a large jump in potential vorticity at the base of the mixed layer must be taken into account. A framework for incorporating these effects in set out in Chapter 6.4.

In the simulation at 0.5 km resolution, the upwelling is associated with vertical velocities of up to 100 m day^{-1}, while vertical velocities of up to 200 m day^{-1} are found at 250 m resolution. These vertical velocities are considerably more intense than other vertical transport mechanisms proposed to account for high primary productivity in mesoscale anticyclones. A differential wind stress [e.g. McGillicuddy et al., 2007; Gaube et al., 2014b] is predicted to generate vertical velocities of up to 0.1 m day^{-1}.

The submesoscale length scale of the upwelling and the lack of a model parameterisation for symmetric instability explains why the associated vertical transport is not captured by mesoscale eddy-resolving models [Oschlies, 2002a; Eden and Dietze, 2009]. Therefore, the symmetric instability in mesoscale anticyclones may provide a new source of nutrient upwelling to assist efforts to close carbon budgets in the ocean. There are of course limitations to the symmetric instability mechanism as a route to higher primary productivity. The source water for the vortex must be nutrient-rich to start with [Crawford et al., 2007; Lehahn et al., 2011; Gaube et al., 2013] and the on-going biogeochemical processes that affect nutrient transports into and out of the mixed layer of the vortex [e.g. Fawcett et al., 2011] must lead to a nutricline with a vertical profile similar to that of potential vorticity. In addition, biological productivity must be nutrient-limited and so the upwelling mechanism would not be effective in light-limited regions in winter or regions of airborne nutrient supply.

The instability of mode water vortices – which are anticyclonic vortices that arise due to a low stratification anomaly in the thermocline and do not have isopycnals that outcrop to the surface – to symmetric instability is also an open question. The symmetric instability mechanism as presented here depends on the vortex having a horizontal buoyancy gradient, a gradient in sea surface height and curvature in sea surface height. Mode water vortices observed in the Sargasso Sea are relatively shallow and have a curved surface signature in altimetry [McGillicuddy et al., 2007], so may be unstable to symmetric instability induced by wind-forcing. Ledwell et al. [2008] find elevated primary productivity in a mode water vortex and infer strong isopycnal mixing of a tracer that they conjecture is due to a submesoscale instability. The symmetric instability mechanism as proposed here is only applicable along isopycnals that outcrop to the surface. It does not appear that the last condition is satisfied with respect to the high productivity observed in that case (Fig. 2 in that paper). It is cautioned that the symmetric instability mechanism is consistent with the presence of elongated filaments of high primary productivity, but such filamentation can also be driven by horizontal shear in an eddying flow [Martin, 2003].

Instabilities resulting from the highly-sheared flow associated with symmetric instability dissipate the kinetic energy of the balanced flow [Taylor and Ferrari, 2009; Thomas and Taylor, 2010]. As such, the symmetric instability mechanism could represent a pathway for dissipating the kinetic energy of mesoscale vortices that account for a significant part of the oceanic kinetic energy budget [Ferrari and Wunsch, 2009]. This local dissipation of kinetic energy in the mixed layer is complemented by the generation of inertia-gravity waves that carry energy downwards away from the mixed layer. The magnitude of the kinetic energy dissipation at fronts is shown to scale with the Ekman buoyancy flux for simulations with no surface waves [Thomas and Taylor, 2010]. This could provide a basis for a parameterisation of the mechanism in vortices. However, this approach may have to be modified to account for non-linear Ekman pumping [Mahadevan et al., 2008] and the role of horizontal shear and curvature in vortex stability. In addition, large-scale estimates of energy dissipation have to take account of the fact that the Ekman buoyancy flux will largely cancel out when averaged over the vortex, due to the opposing up-front fluxes that restratify the Ekman layer. The differential wind stress associated with relative wind effects, that have not been considered here, will also damp the potential vorticity extraction in the down-front region. While, the upwelling in anticyclones occurs over a large portion of the vortex area

and so the possible area for energy dissipation is also high. It is cautioned that these instabilities do not dissipate the entire vortex as they are only found in that part of the vortex's volume that is in the mixed layer.

Finally, of course, observational tests with *in-situ* data are required to ascertain how representative the model results are of the real ocean, where the wind does not always below continuously in the same direction at the same speed. The main test for the symmetric instability mechanism is the presence of thin regions of anomalously high stratification in what would otherwise be the low stratification mixed layer of wind-forced anticyclonic vortices.

CHAPTER 5

Rossby adjustment at open ocean fronts

5.1 Introduction

The presence of sharp fronts in the mixed layer of the open ocean has been a source of interest to oceanographers since the first observations of these fronts [Uda, 1938; Cromwell and Reid, 1956; Knauss, 1957]. The potential role of the surface wind stress in their formation and evolution has been suspected from the start. For example, in the tropical Pacific Knauss [1957] observed a sharp 'wall-front – where the isopycnals are close to vertical – with evidence that the water on the denser side of the front was over-running the lighter water near the surface and then convecting. The wall-front structure was attributed by Knauss [1957] to the Ekman transport given the local alignment of the front and wind. Similar frontal structures were observed in the sub-tropical Pacific by Samelson and Paulson [1988], who again noted that this could be a consequence of the Ekman transport. Samelson and Paulson [1988] conjectured that the front would be subject to Rossby adjustment [Rossby, 1938; Shakespeare and Taylor, 2013] once the wind relaxed as the dynamical balance changed from an Ekman-geostrophic balance to a purely geostrophic balance.

A simple analytical model for the Rossby adjustment of ocean fronts is derived by Tandon and Garrett [1994]. They show that an initially unbalanced front is subject to a vertically-sheared pressure gradient that acts as a torque and generates horizontal vorticity. Tandon and Garrett [1994] show that in the non time-dependant case the front comes into geostrophic balance with a vertically sheared

horizontal velocity with Ri $= 1$ where Ri $= N^2/(u_z^2 + v_z^2)$ is the Richardson number, $N^2 = b_z$ is the stratification, b is the buoyancy which is the negative of the density anomaly $b = -g\rho/\rho_0$, ρ is density and ρ_0 is the reference density, $\mathbf{u} = (u, v, w)$ is the velocity vector and the subscript z denotes differentiation in the vertical. When time dependence is introduced, Tandon and Garrett [1994] show that the Rossby adjustment leads to strong inertial oscillations and the front oscillates around a mean state of Ri $= 1/2$. They note that as the initial state has Ri < 0.25, the transition is expected to be turbulent.

Tandon and Garrett [1994] caution that their model is a simplified set-up. In particular, there is no stratification and so it corresponds to a scenario where the Froude number Fr $= U/NH$, with characteristic velocity U and vertical length scale H, is very large. Shakespeare and Taylor [2013] consider a generalised model of Rossby adjustment that includes variable stratification and rotation. They find that for a front to eventually reach geostrophic balance the near-inertial waves generated during the adjustment must be able to disperse.

While Rossby adjustment has been the subject of numerous laboratory studies [e.g. Ungarish and Huppert, 1998; Cenedese et al., 2012], observations of the process occurring are quite rare. An exception to this is the observational study of Dale et al. [2008] of an upwelling region on the Oregon shelf. Dale et al. [2008] carried out repeated cross-front surveys and dye release during a period when the surface wind changed from a destratifying down-front orientation to a restratifying up-front orientation over a period of 12 hours. The surveys before, during and after the wind reversal show that there was a concomitant change from almost vertical isopycnals to almost horizontal isopycnals. The magnitude of the initial horizontal buoyancy gradients were of order 10^{-7} s^{-2}, which is similar to those estimated for mixed layer fronts. They investigate the potential causes of the change from vertical to horizontal isopycnals and conclude that restratification developed due to Rossby adjustment with an increasingly large contribution from up-front winds.

The dynamics of Rossby adjustment are a classical subject in geophysical fluid dynamics, as outlined in Chapter 1.2.2. One focus here is on the turbulent nature of this adjustment in a so-called 'lock-exchange' configuration with rotation, where the adjustment begins from an initally unbalanced state in the mixed layer. In non-rotating – or very high Rossby number – experiments this is typically a highly-turbulent process [von Karman, 1940; Benjamin, 1968; Simpson, 1982; Kay,

1992; Simpson, 1999; Ungarish and Huppert, 1998; Shin et al., 2004] as the horizontal buoyancy gradient induces a vertical velocity shear that can be strong enough to overcome the stabilising effect of stratification. The effect of this turbulence on the gravity currents in non-rotating environments is a subject of debate. Benjamin [1968] argues that the kinetic energy dissipation and diapycnal mixing associated with the turbulence are an important control on the subsequent development of the gravity currents, while Shin et al. [2004] finds that energy-conserving models of the gravity currents are a good approximation to experimental results. This is of particular relevance for rotating dynamics, as potential vorticity conservation allows prediction of the final adjusted state apart from the energy loss to inertia-gravity waves [Rossby, 1938; Stegner et al., 2004]. A further subject of scrutiny is the nature of the flow at the head of a density current. This part of the current is often where non-hydrostatic effects are particularly acute with subsequent effects on the generation of small-scale overturns that lead to diapycnal mixing [Ungarish and Huppert, 1998]. The rotating case of Rossby adjustment in the ocean and the degree to which it may be turblent in the ocean is a subject of on-going research [Ungarish and Huppert, 1998; Hallworth et al., 2001; Ungarish and Zemach, 2003; Stegner et al., 2004; Holdsworth and Sutherland, 2015]. The rotating case differs as the Rossby deformation radius places a strong constraint on the spatial extent to which adjustment can occur [Ungarish and Huppert, 1998; Hallworth et al., 2001] and the change in velocity also leads to changes in the geometry of the gravity current, which affects in turn the degree of mixing which can occur [Ungarish and Huppert, 1998].

The only parameterisation for submesoscale dynamics that is implemented in global climate models is that due to Fox-Kemper et al. [2008], Fox-Kemper and Ferrari [2008] and Fox-Kemper et al. [2011]. This parameterisation is based on high resolution three dimensional simulations. This parameterisation aims to capture the restratification due to mixed layer instabilities. In the simulations used to develop scalings used for the parameterisation, the magnitude of the initial horizontal buoyancy gradient is $2f^2$ and the geostrophic adjustment phase makes a relatively small contribution to the overall restratification in comparison to the baroclinic instabilities, once the instabilities reach finite amplitude. In addition, the overall restratification process using the Fox-Kemper et al. [2008] parameterisation is relatively adiabatic, though the degree of diapycnal mixing associated with the restratification is the subject of on-going research [Skyllingstad and Samelson, 2012; Bachman and Fox-Kemper, 2013; Brüggemann and Eden,

2014]. Observations of ocean fronts show that horizontal buoyancy gradients may be $10f^2$ or even $100f^2$. The main hypothesis tested in this chapter is that the rapid geostrophic adjustment phase accounts for a significant proportion of the restratification in this case in a manner that is not captured by the Fox-Kemper et al. [2008] parameterisation. A secondary hypothesis is that the turbulent nature of the adjustment becomes increasingly important over the realistic range of horizontal buoyancy gradients. In order for such a geostrophic adjustment to take place, the degree of geostrophic balance at a front must initially be low.

5.1.1 Chapter aims and outline

Observations of an open ocean front made during an OSMOSIS cruise in the North Atlantic are presented. While the observations do not allow definite testing of hypotheses, the way in which they lead to the hypotheses set out above are discussed. Idealised two-dimensional numerical simulations are then carried out to test the main hypotheses set out above.

This Chapter is organised as follows. The dataset is described in Chapter 5.2. The observations are set out and discussed in Chapter 5.3. The configuration used for the numerical model is described in Chapter 5.4, with the model results following in Chapter 5.5 and concluding with a discussion in Chapter 5.6.

5.2 Observational datasets

The data were gathered during the second research cruise of the OSMOSIS project in September 2013 aboard the RRS *James Cook* at the Porcupine Abyssal Plain site. The observation region is shown in Figure 5.1 below with the locations of the closely-spaced observations marked in white. As the name of the region suggests, there is minimal bottom topography in the immediate area. The Coriolis frequency $f = 1.09 \times 10^{-4}$ s^{-1} with a corresponding inertial period of 15.9 hours. Transects of about 20 km length were made during which repeated observations were carried out with a microstructure profiler deployed from a winch on the aft deck and from ship-board systems. The transects were made along a section running north-east to south-west across the site from which the OSMOSIS mooring array had recently been recovered. The ship speed was kept to approximately 1 km h^{-1} to provide an appropriate spatial and temporal sampling frequency and minimise turbulent momentum production by the ship. Given that repeat profiles

can be made every eight minutes, this allows vertical profiles of the upper 200 m to be made at approximately 200 m intervals.

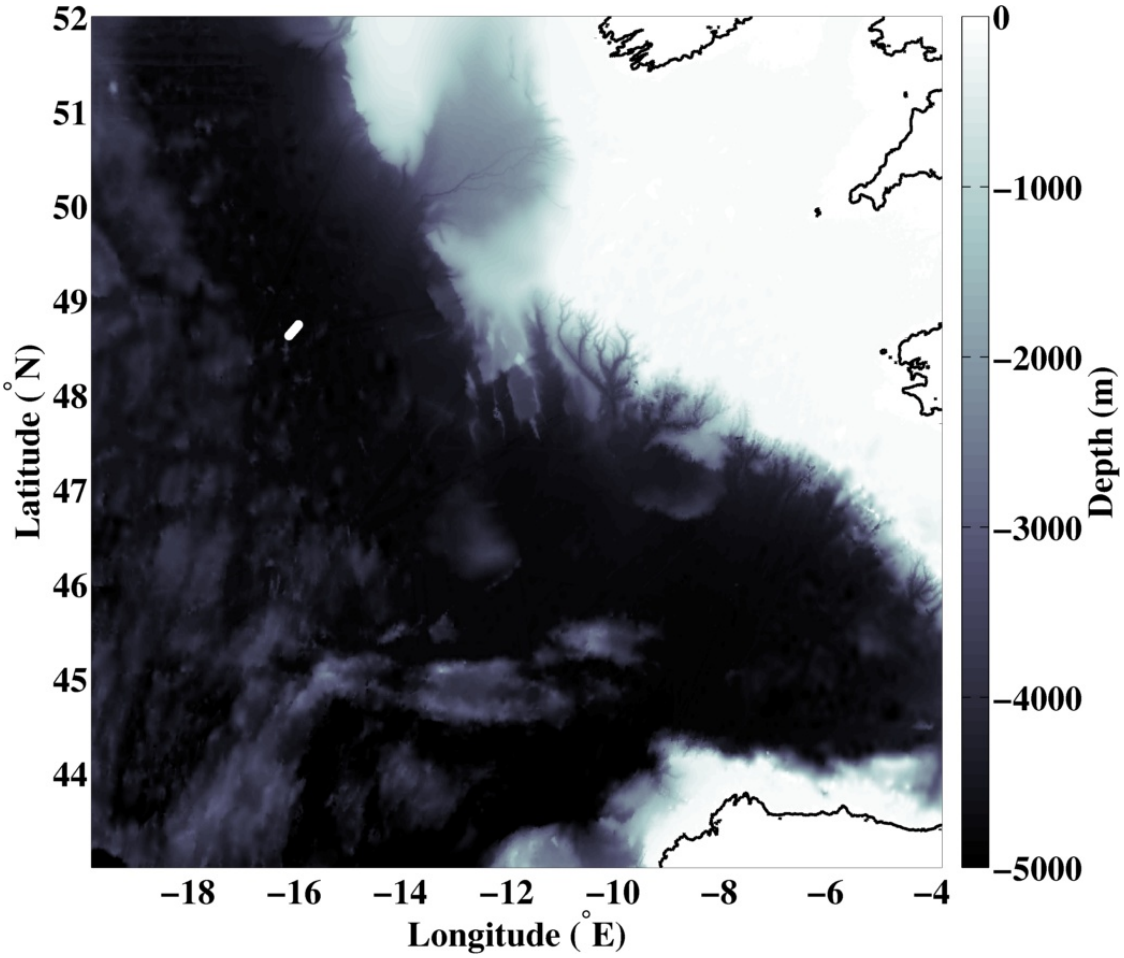

Figure 5.1: A bathymetry map of the observation region. The locations of the densely-spaced observations in the Porcupine Abyssal Plain are shown in white near (-16.2° E, 48.7° N). The coastlines of Ireland, the UK, France and Spain are also visible, going clockwise from the north.

5.2.1 Microstructure profiling

The microstructure vertical profiles were made using the MSS90, a loosely-tethered microstructure profiler produced by Sea and Sun Technology GmbH and ISW Wassermesstechnik. The instrument produces vertical profiles of pressure, temperature, salinity, fluorescence, kinetic energy dissipation and thermal variance dissipation. Microstructure shear probes make direct measurements of cross-axial velocity fluctuations using a piezoceramic beam. Temperature and salinity on the microstructure profiler have been calibrated by comparison with the ship's

conductivity-temperature-depth (CTD) unit. The temperature profiles were in close agreement, but a small vertically uniform adjustment to salinity was required. The seawater package is used to calculate the equation of state. This instrument is referred to as the 'turbulence profiler' below.

5.2.2 Acoustic doppler current profiler

The acoustic doppler current profiler (ADCP) was an RDI broad-band 76.8 kHz (Ocean Surveyor) phased-array ADCP with a 30° beam angle. The ADCP was mounted in the hull 0.25 m to starboard of the keel, 29 m aft of the bow at the waterline, at an approximate depth of 5.3 m. It was configured to sample over 120 second intervals with 96 bins of 8 m length. The 'blank beyond transmit' distance – which is the distance below the unit at which the observations begin – is 8 m.

5.2.3 Wind measurements

Wind measurements were made using a Gill Windsonic anemometer mounted on a bow platform approximately 19 m above the water surface.

5.2.4 Altimetry

The geostrophic velocity field is derived from the AVISO all-satellite delayed time product[1].

5.2.5 Satellite SST

The satellite sea surface temperature data is the GHRSST Level 4 MUR Global Foundation Sea Surface Temperature Analysis. This is a gridded product that combines multiple satellites to produce a 1 km x 1 km map of SST [2]. Conditions during the cruise were generally cloudy, however, and the effective resolution of the sea surface temperature data is much coarser than 1 km.

[1]This was downloaded on 18th July 2014 from:
ftp.aviso.altimetry.fr/global/delayed-time/grids/msla/all-sat-merged.

[2]This was downloaded on 7th May 2014 from:
ftp://podaac-ftp.jpl.nasa.gov/OceanTemperature/ghrsst/ data/L4/GLOB/JPLOUROCEAN/G1SST/2013

5.3 Observations

5.3.1 Remotely-sensed data

Remotely-sensed sea-level anomaly and sea surface temperature (SST) data provide larger scale context for the transect (Figure 5.2). The dark line in each plot shows the closely-spaced locations where the 111 vertical profiles were made while the ship steamed slowly to the south-west. The sea-level anomaly data (left panel) show that the transect took place in a frontal region between a cyclonic eddy to the west and an anticyclonic region to the east. As discussed further below, the geostrophic flow in the frontal region was towards the north-east. The SST data (right panel) shows that these cyclonic and anticyclonic regions correspond to relatively cold and warm regions respectively.

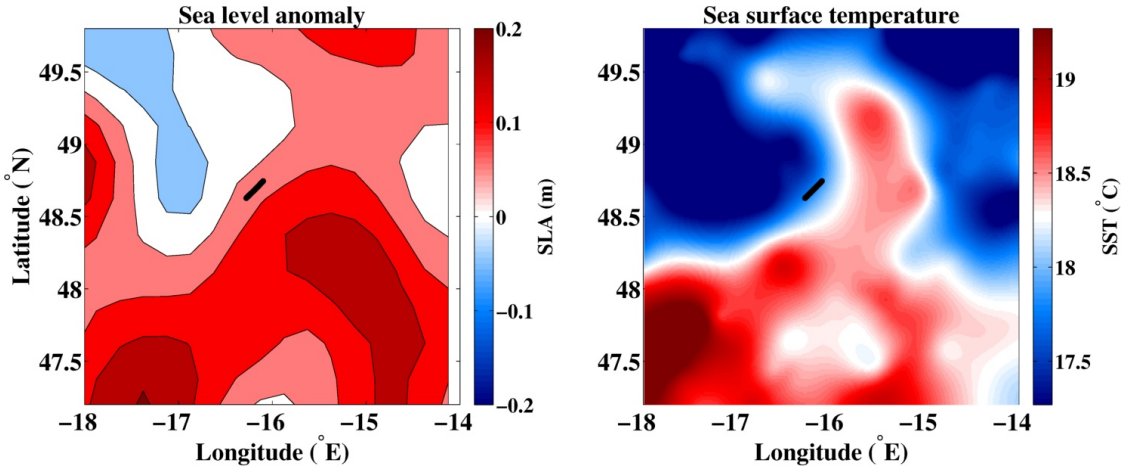

Figure 5.2: Remotely-sensed data at the time of the transect. (Left panel) The sea level anomaly derived from AVISO data. (Right panel) The sea surface temperature. The locations of the microstructure profiles are shown in black. The ship steamed to the south-west during the transects.

5.3.2 Temperature and salinity data

The *in-situ* temperature and salinity data gathered with the microstructure profiler (Figure 5.3) show that a mixed layer front was crossed during the transect. Three different regions can be seen above the thermocline, which has an upper bound between 35-45 m depth throughout. Firstly, in the initial kilometres of the transect there is a region of colder-fresher water (Fig. 5.3, upper and lower panels). Secondly, between km 3 and 9 of the transect this colder-fresher water is overlain in the upper 20 m by a lens of warmer-saltier water (Fig. 5.3, upper and lower

panels). Thirdly, at the end of the transect there is a region of warmer-saltier water (Fig. 5.3, upper and lower panels). The black lines in Figure 5.3 are isopycnals and show that there is a buoyancy difference between the warmer-saltier water and the colder-fresher water with the warmer-saltier water being more buoyant. The front occurs over a vertical scale, H, of about 40 m, a horizontal scale of 4 km and has a stratification, N^2, of approximately $4 \times 10^{-5} s^{-2}$. This gives a mixed layer deformation length of $R_{ML} = NH/f = 2.2$ km, giving a Burger number of 1.5. Given the approximations involved this is taken as a Burger number of order 1. The orientation of the front observed *in-situ* does not agree exactly with the front inferred from the satellite SST in Fig. 5.2 (right panel). This is indicative of local structure to the front at scales too small to be resolved by the remote instruments.

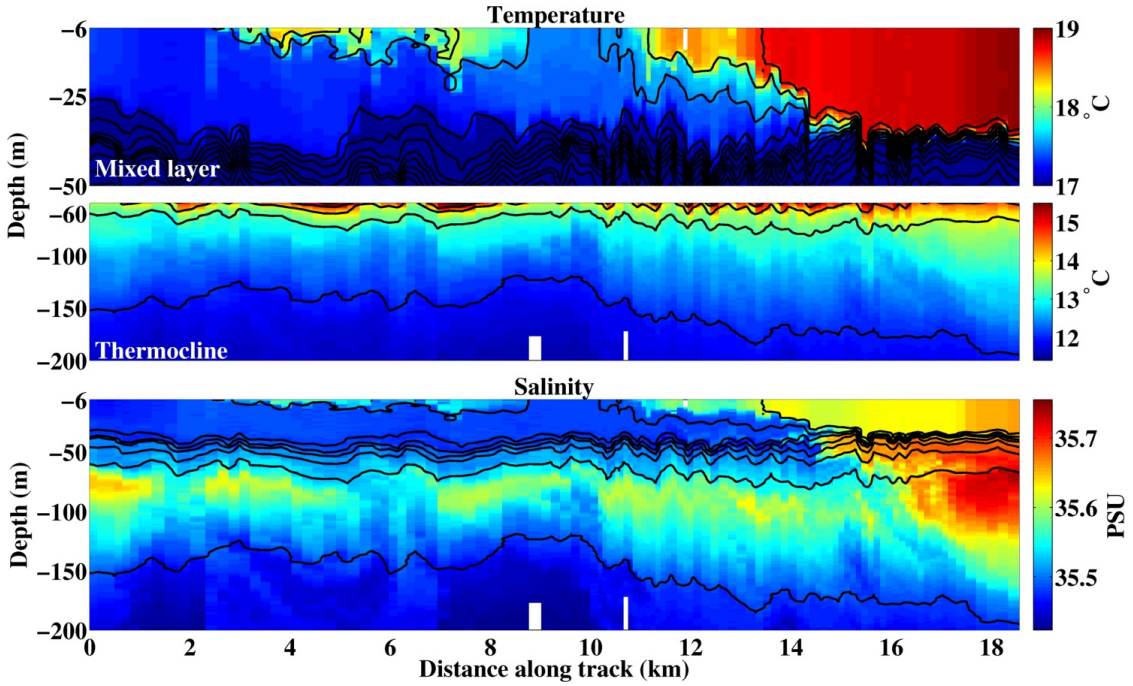

Figure 5.3: The temperature and salinity fields observed during the transect with the microstructure profiler. (Top panel) The temperature field between 6-50 m depth. (Middle panel) The temperature field between 50-200 m depth with a different colour scale. (Lower panel) The salinity field between 6-200 m depth. The black lines are density surfaces with an interval of 0.1 kg m^{-3} in the upper panel and 0.2 kg m^{-3} in the lower panels.

There are vertical displacements in the depth of the mixed layer along the transect with magnitude up to 10 m, such as at km 5 (Fig. 5.3, upper panel). This is presumably due to internal wave heaving that is aliased by this sampling approach. The centre and lower panels in Figure 5.3 show that there are numerous

along-isopycnal salinity gradients. These 'spicy' features – defined to be gradients of temperature or salinity along a constant density surface that are compensated in the equation of state and so do not affect the dynamical processes – have been observed a number of times in the OSMOSIS dataset and are the subject of on-going investigation.

The main front at km 10-14 is relatively broad at the surface in Fig. 5.3, where the region of buoyancy gradients extends over 4 km, but becomes sharper near the base where the change in temperature and salinity becomes a near-discontinuity at -35 m depth (upper and lower panels). Figure 5.4 (left panel) shows vertical profiles of temperature (T) and salinity (S) in the region of the front at km 11. The x-axes limits for temperature and salinity have been set to reflect equivalent contributions to buoyancy. The profiles show that the front is a thermal front that is compensated in salinity by approximately $1/3$. The properties of the water masses observed in the 5-25 m range for the whole transect in T-S space are shown in Fig. 5.4 (right panel). This shows that all of the water above 25 m lies on a near-continuous curve in T-S space. The red dots in Fig. 5.4 (right panel) are from the near-surface lens of warm water and show that the lens also has intermediate T-S properties between the warm and cold side of the front. As both temperature and salinity properties are intermediate between the warmer-saltier and colder-fresher water the lens is unlikely to have formed due to surface fluxes of heat or freshwater. This could imply that the lens is formed of water that has been diapycnally mixed across the front, or advected and mixed laterally. The hypothesised diapycnal mixing could arise due to surface-induced turbulence or internally-generated turbulence [D'Asaro et al., 2011].

The buoyancy data can be used to estimate the potential vorticity at the front. As the vertical shear estimated from the 75 kHz ADCP is noisy, the approach of Thomas et al. [2013] is followed and the flow is assumed to be in thermal wind balance. It is assumed that the front has no curvature or relative vorticity. As such, the potential vorticity is calculated as $q = fN^2 - |b_x|^2/f$ where x is taken to be the along-track direction. This is shown in Figure 5.5. The main point of interest is the negative potential vorticity contribution from the horizontal gradient near the front. The large negative values close to the thermocline in the upper panel primarily reflect horizontal gradients that arise due to internal wave heaving between casts and should be disregarded. When combined with the stratification in the centre panel of Fig. 5.5, the estimated potential vorticity is shown in the lower panel of Fig. 5.5. This shows that there is a region of negative

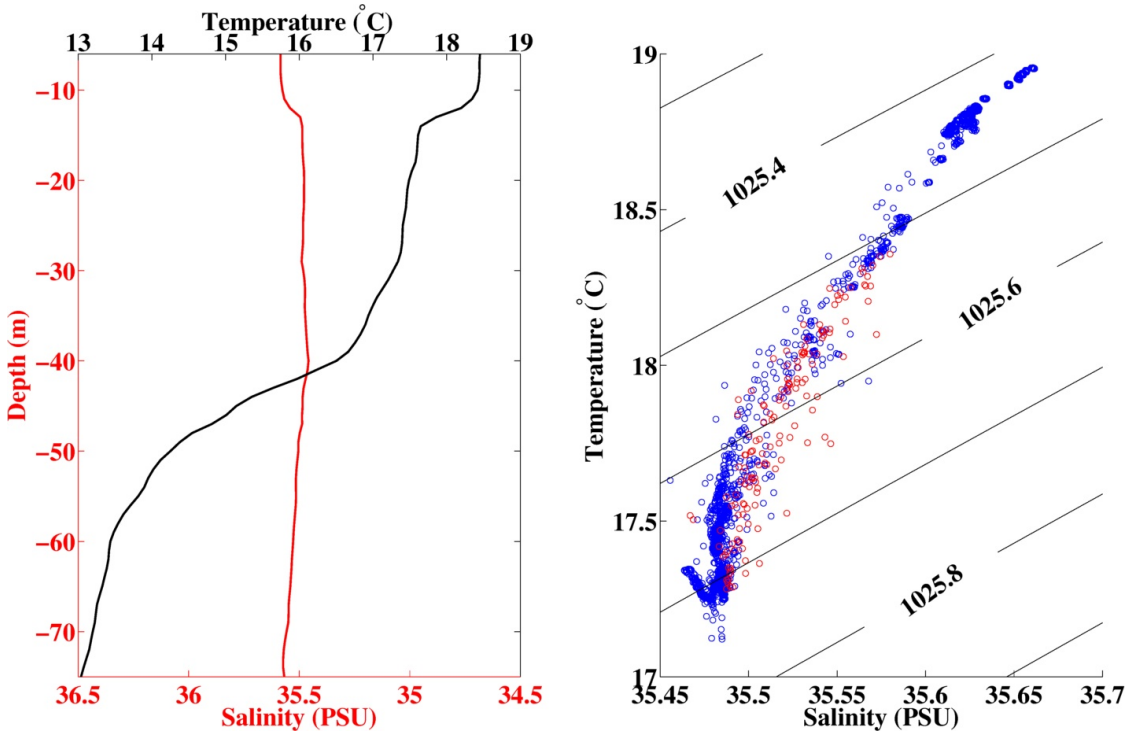

Figure 5.4: Temperature and salinity data from the transect. (Left panel) A vertical profile of temperature and salinity from the slumping front at km 11.7 during the transect. The x-axes have been scaled to give equivalent contributions to buoyancy gradients. (Right panel) The T-S plot of all data gathered from the upper 25 m of the transect showing the relative continuity in T-S properties across the front. The red dots indicate data gathered from the lens of warm water near km 6. The black lines are density surfaces with an interval of 0.1 kg m^{-3}.

potential vorticity in the interface region of the front. Given the averaging and internal wave noise in the data and the exclusion of relative vorticity, this front is best thought of as having low potential vorticity of uncertain sign.

5.3.3 Microstructure data

The microstructure data in Figure 5.6 show that at the start of the transect, from km 0-2, and at the end of the transect, from km 14-18, the dissipation of turbulent kinetic energy (ϵ, upper panel) is high throughout the mixed layer. In these same regions the dissipation of thermal variance (χ^2, lower panel) is very low. This is consistent with these regions being well-mixed vertically.

In the region of the near-surface lens from km 2-8, there is intense dissipation of kinetic energy and thermal variance. This is consistent with the lens being a region of active diapycnal mixing between the warm-salty water and the cool-

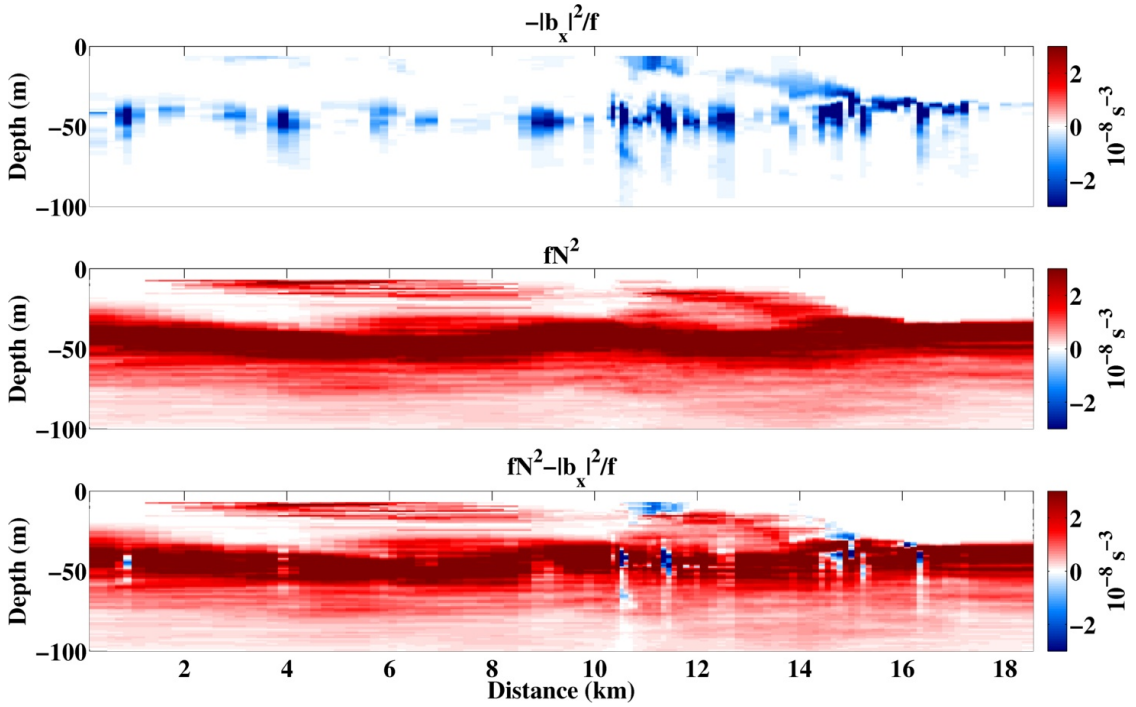

Figure 5.5: The potential vorticity estimated from the turbulence profiler data with an assumption of thermal wind balance. Values have been averaged over two successive casts. (Top panel) The negative-definite tilting contribution to potential vorticity ($|-b_x|^2/f$). (Centre panel) The stratification contribution fN^2 to potential vorticity assuming no horizontal shear. (Lower panel) The sum of the two terms.

fresh water. Below this, however, values of both ϵ and χ^2 are very low. The low values of ϵ suggest that the stratification at the base of the lens is inhibiting downward turbulent transfers while the low values of χ^2 show that this water is well mixed and has recently been exposed to surface forcing. In the frontal region, from km 10-14, there is again a trapping of the active dissipation of turbulent kinetic energy by stratification in the upper 20 m, as for the near-surface lens. This is accompanied by reasonably high values of χ^2, which suggests that the intermediate T-S values seen in the region of the front are due to active mixing processes. In the underflow region below the slumping front between -40 m and -25 m at km 10-14, ϵ and χ^2 are again low. The low values of χ^2 are again consistent with this water already being well-mixed and so only recently removed from exposure to surface forcing.

There is interest in the microstructure data from the transition layer and below [e.g. Sun et al., 2013], though this is not pursued here.

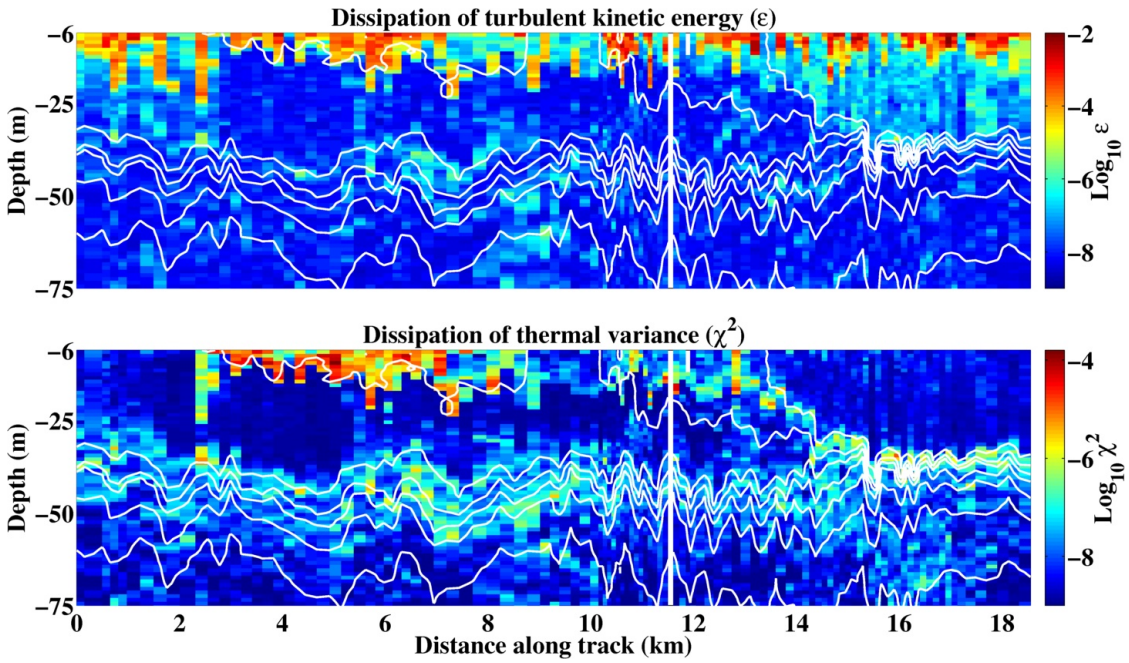

Figure 5.6: The microstructure data from the transect. (Top panel) The dissipation of turbulent kinetic energy (ϵ) on a log scale. (Bottom panel) The dissipation of temperature variance (χ^2) on a log scale. The white lines are density surfaces with an interval of 0.2 kg m^{-3}. White columns indicate profiles removed during quality control.

5.3.4 Velocity data

The vessel-mounted ADCP shows a surprising degree of velocity structure in Figure 5.7, where it is plotted with the isopycnal surfaces derived from the turbulence profiler instrument. Over most of the depth range the flow is close to the along-track direction. This is consistent with the direction of the geostrophic flow implied by altimetry in Figure 5.8 (right panel). However, in the mixed layer of the ADCP data in Fig. 5.7 there is a reversal of the flow at the location where the microstructure data show the presence of a buoyancy front, confined to the shallowest bin of the ADCP data. The along-track gradient of the along-track flow is strongly convergent at the front. To ensure non-divergence this could either reflect a divergence of the cross-track flow or a vertical velocity of order 50 m day^{-1}, where the vertical velocity is assumed to be 0 at the surface and zero cross-track divergence is assumed.

A plan view of the velocity field is given by Figure 5.8. This shows the sea-level anomaly and the geostrophic velocity vectors inferred from altimetry. The magnitude and direction of these is in close agreement with the depth-mean velocity vectors from the ship ADCP.

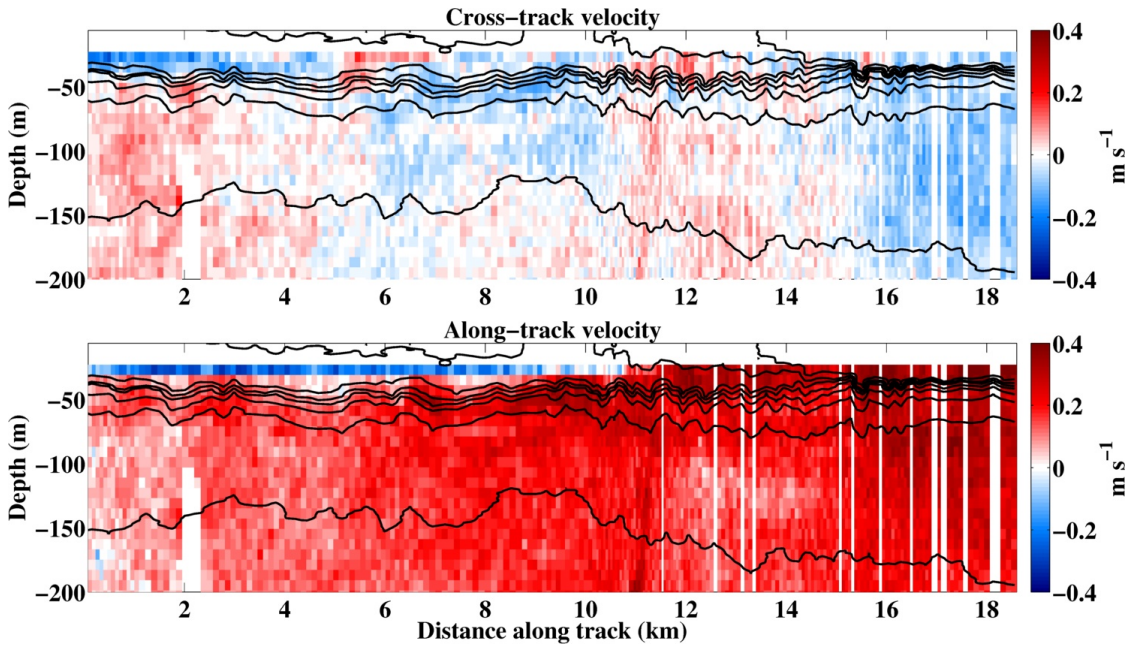

Figure 5.7: The velocity field observed with the vessel-mounted ADCP. The data has been rotated to the transect axis. The black lines are density surfaces with an interval of 0.2 kg m^{-3}. White columns are due to data removed during the quality control process.

5.3.5 Wind forcing

The observed wind stress was generally weak to moderate over the course of the transect with a mean wind stress of 0.04 N m^{-2}. However, the wind stress had been three times stronger in the previous 24 hours Fig. 5.9 (right panel). The wind forcing had a down-front component during the transect, as shown in Figure 5.9 (left panel), which shows that the wind was directed towards the south-east and so induced an Ekman flow from the cold to warm side of the front. Such a destratifying Ekman transport is not reflected in the observed buoyancy structure.

5.3.6 Discussion of observational results

The observations presented here show a mixed layer front located between a cyclonic and an anticyclonic eddy. The *in-situ* data suggests that the front has significant three dimensional submesoscale structure. The generally cloudy conditions means that any submesoscale spatial structure is not visible in the satellite SST data, however. Along the transect, the front has a broader, more diffuse buoyancy gradient near the surface than near the base of the mixed layer. The elevated levels of both turbulent energy dissipation and thermal variance dissipation observed

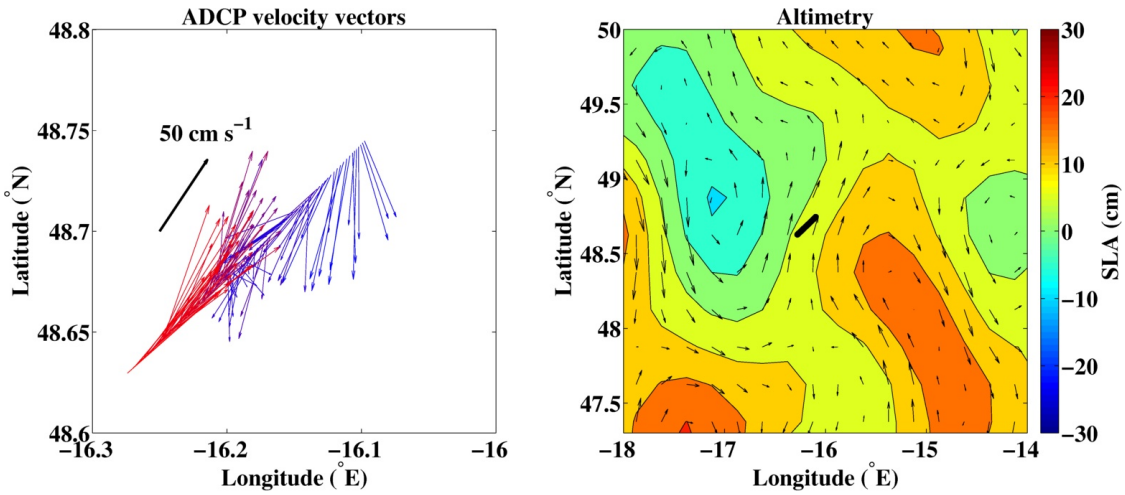

Figure 5.8: Plan views of velocity vectors during the transect. (Left panel) The velocity vectors observed in the ADCP bin centred at 23 m. The velocity vectors have been coloured using the same colour scale as used for the mixed layer temperature plot of Fig. 5.3. A scale vector of 50 cm s^{-1} is included for comparison. (Right panel) A regional view of the velocity field from satellite altimetry on 10th September 2013. Colours show 5 cm contours of sea-level anomalies and the arrows are the inferred geostrophic velocities. The black dots near the centre show the location of the microstructure profiles.

with the microstructure instrument suggest significant diapycnal mixing is ongoing, though the source of the turbulent kinetic energy is not clear. The velocity data from the ship ADCP shows that the velocity field in the mixed layer appears to be somewhat decoupled from the deeper geostrophic flow, as the mixed layer flow is in the opposite sense to the geostrophic flow on the cold side of the front in the mixed layer. It is cautioned that the mixed layer flow likely contains a component due to an inertial oscillation that would alias any calculation of along-track velocity shear. The ship wind data show that there may have been a down-front wind during the transect, which had a weaker magnitude than the wind stress in the hours beforehand.

The limitations of the frontal observations mean that they do not allow for definitive falsification of hypotheses for frontal dynamics. For example, the strong cross-front flow in the mixed layer could represent Rossby adjustment of a front to a decreasing wind-stress, an instability of the geostrophic flow such as symmetric instability given the small region of negative potential vorticity found in Fig. 5.5, a two dimensional slice through a baroclinic instability, or some combination of these. However, the magnitude of the mixed layer flow, the weakening wind stress and the apparently increased diapycnal mixing across the front higher in the mixed layer give rise to the following hypothesis: that the front is undergoing

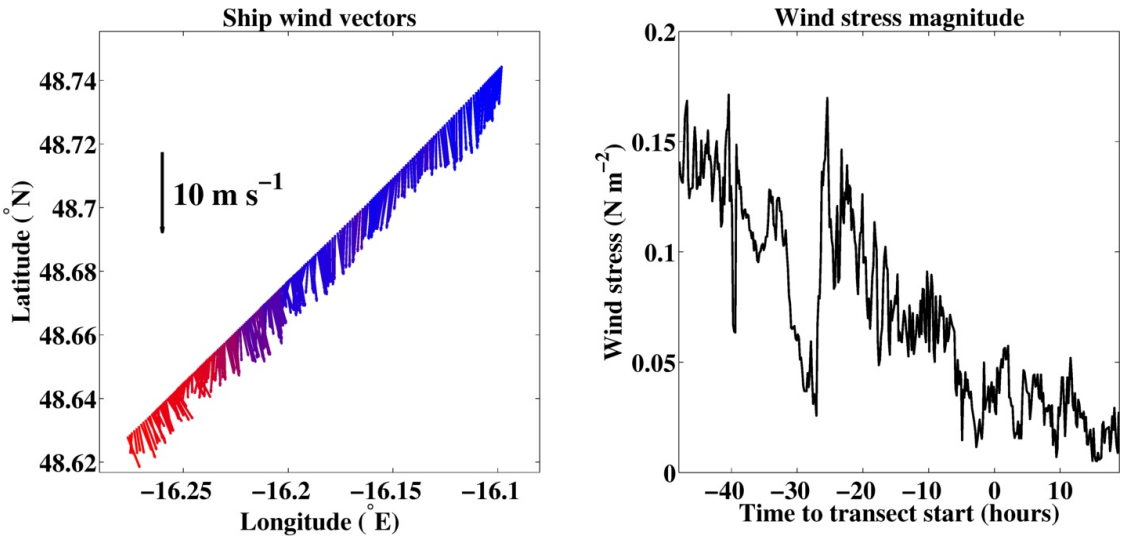

Figure 5.9: The wind field observed from the anemometer mounted on the bow as the ship steamed to the south-west. (Left panel) The wind vectors, coloured according to the sea surface temperature colour scale used in Fig. 5.3 (top panel) to show the location of the front. (Right panel) The magnitude of the wind stress before and during the transect.

Rossby adjustment to a decreased down-front wind stress that leads to a turbulent Rossby adjustment and subsequent diapycnal exchange. This hypothesis can be tested numerically using two-dimensional simulations.

5.4 Numerical set-up

5.4.1 Model overview

The model is run in a 2D configuration. The simulations are integrated using the MITgcm [Marshall et al., 1997] in non-hydrostatic mode. The aim here is to investigate the response of simulated fronts to Rossby adjustment across the range of initial buoyancy gradients commonly observed at mid-latitude mixed layer fronts. Rossby adjustment and the inertia-gravity waves can be thought of as two-dimensional processes and so a two-dimensional domain is used. The major advantage of such a two-dimensional configuration is that is permits much higher horizontal and vertical spatial resolution and so allows small-scale non-hydrostatic effects such as Kelvin-Helmholtz instabilities to be resolved. This two-dimensional domain also permits convection and symmetric instability [Haine and Marshall, 1998], though a positive potential vorticity is used throughout. Three-dimensional processes such as baroclinic instability are excluded, however.

The overall scenario here is where a down-front wind stress is removed. Such a down-front wind stress leads to weak stratification [Thomas et al., 2008] which is approximated in the initial conditions as zero stratification. However, no wind stress is applied at the surface in these simulations to ascertain whether the Fox-Kemper et al. [2008] parameterisation can represent the restratification process adequately in the most 'explosive' case where there is no initial vertical shear to balance the torque of the horizontal buoyancy gradient.

5.4.2 Domain

The domain used for the runs is horizontally periodic with a flat bottom. The flow is two-dimensional in the $x - z$ space, but also supports a time-varying flow in the along-front y dimension. The model is not semi-geostrophic [Hoskins and Bretherton, 1972], as departures from geostrophic balance are allowed in the along-front velocity. The domain is periodic in the x-direction and the initial temperature field contains a warm filament bounded by a colder region which wraps around the domain. This filament domain structure has been used previously [e.g. Hamlington et al., 2014] and avoids issues with lateral boundaries. For the purposes of our investigation, it is imperative that the two fronts are spaced horizontally such that interference between them is kept to a minimum. This is a challenge, as the relatively strong initial horizontal buoyancy gradients used here give rise to a larger deformation radius R_{ML}. On account of this, the domain width in the x-direction is 36 km. The height of the domain is 50 m for the runs with no thermocline and 100 m or 500 m for the runs with a thermocline, with a mixed layer depth of 50 m in the latter cases. The grid resolution is 1 m in the vertical and 5 m in the horizontal.

5.4.3 Numerical configuration

The model is run with a linear equation of state in temperature with a thermal expansion coefficient of 2×10^{-4} K. A 7th-order monoticity-preserving advection scheme [Daru and Tenaud, 2004] is used as it is found to reduce numerical cross-front diffusion of buoyancy compared to other advection schemes available.

Vertical mixing of temperature and momentum is done with a Laplacian operator and viscous and diffusive coefficients of 10^{-5} m^2 s^{-1}. The horizontal viscous coefficient is set by a Smagorinsky scheme [Smagorinsky, 1963] for the Laplacian viscous operator. A constant horizontal diffusion coefficient of 4×10^{-5} m^2

s^{-1} is used for temperature. Note that although the tracer advection scheme is high-order, it is nonetheless implicitly diffusive and is expected to be the primary source of tracer diffusion.

Although the model is run at relatively high resolution, it does not resolve all of the required scales of turbulence in the mixed layer and does not include surface-wave driven processes [e.g. Grant and Belcher, 2009]. The anisotropy of the model grid and dissipation operators may also affect the properties of turbulent flow [Bachman and Taylor, 2014]. The time-step is 2 s. The anisotropy of the model configuration is better suited towards the development of shear-driven turbulence, with concomitant buoyancy overturns rather than representation of convective instabilities that occur when inertial oscillations overturn the whole mixed layer and so these are not the focus of this work. The so-called 'traditional approximation' is made [Colin de Verdière, 2012] and the Coriolis terms are not included in the vertical momentum equation.

The non-dimensional target residual for the conjugate-gradient solver is varied from 10^{-7} to 10^{-9}. There is good agreement between the results with a residual of 10^{-8} and 10^{-9} and so the former value is used as the target residual. The simulation with a target residual of 10^{-7} displayed less fine-scale structure in the most turbulent regions.

5.4.4 Initial and boundary conditions

The initial conditions are for two density fronts of opposite sign with no flow. The runs are carried out both with and without a thermocline to understand the effect of internal wave emission. The runs with a thermocline have a mixed layer with no stratification. As such, these simulations correspond to a zero potential vorticity case in the mixed layer, as considered analytically by Shakespeare and Taylor [2013]. The initial frontal width is set to be 200 m, mimicking the sharp frontal transitions seen in the observations. The buoyancy gradient is constant over the width of the front, which is resolved horizontally over 40 model grid points. The simulations are run with fronts of three different initial gradients of 5×10^{-8} s^{-2}, 5×10^{-7} s^{-2} and 5×10^{-6} s^{-2}. Given the Coriolis frequency employed of 10^{-4} s^{-1} these are referred to as fronts of strength $5f^2$, $50f^2$ and $500f^2$ below. These are typical of the range of buoyancy gradients found in mid-latitude fronts [e.g. Hosegood et al., 2006]. As the stratification and initial flow is zero the initial Richardson number is 0. The initial temperature distribution for the runs with buoyancy gradient of $500f^2$ are shown in Figure 5.10.

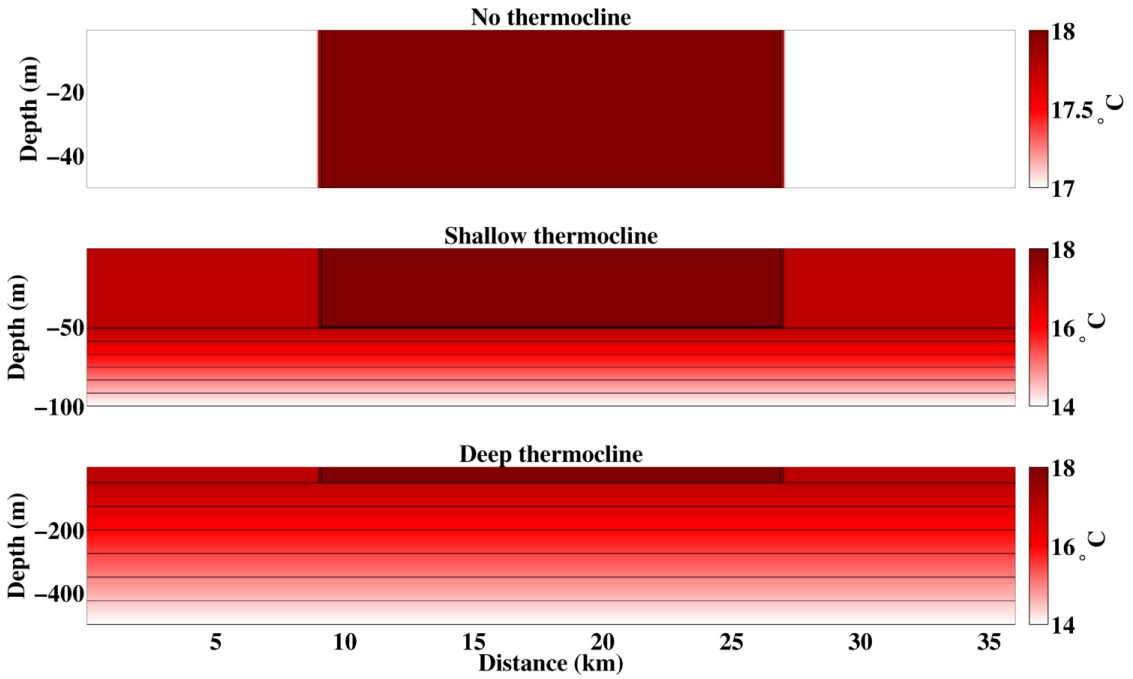

Figure 5.10: Vertical profiles of the initial conditions for the runs with a frontal buoyancy gradient of $500f^2$. (Upper panel) Temperature field for the run with no thermocline. (Centre panel) Temperature field for the run with a shallow thermocline. (Bottom panel) Temperature field for the run with a deeper thermocline Different colour scales are used for each plot. Black lines are temperature contours with an interval of 0.5 ° C.

The upper boundary condition is no stress. The lower boundary condition is a linear drag with drag coefficient of 10^{-6} s^{-1} for runs with no thermocline. For the runs with a thermocline the drag coefficient is increased to 10^{-2} s^{-1} to act as a strong damping to reduce reflection of waves that propagate downwards. The simulations are run without wind in this thesis, the potential effect of including wind forcing is discussed in Chapter 6.4.

5.5 Numerical results

5.5.1 Simulations with no thermocline

In all cases, an ageostrophic cross-front flow develops in which the warmer waters overflow the colder waters in response to the unbalanced torque of the pressure gradient. This across-front flow is accompanied by the development of a vertically sheared along-front geostrophic flow. In addition, the acceleration of the flow and the Coriolis force combine to generate inertial oscillations that cause the front to oscillate around a stable balanced position [Tandon and Garrett, 1994]. These

oscillations can cause the fronts to tilt over into a statically unstable state and generate a convective response after an inertial period (not shown).

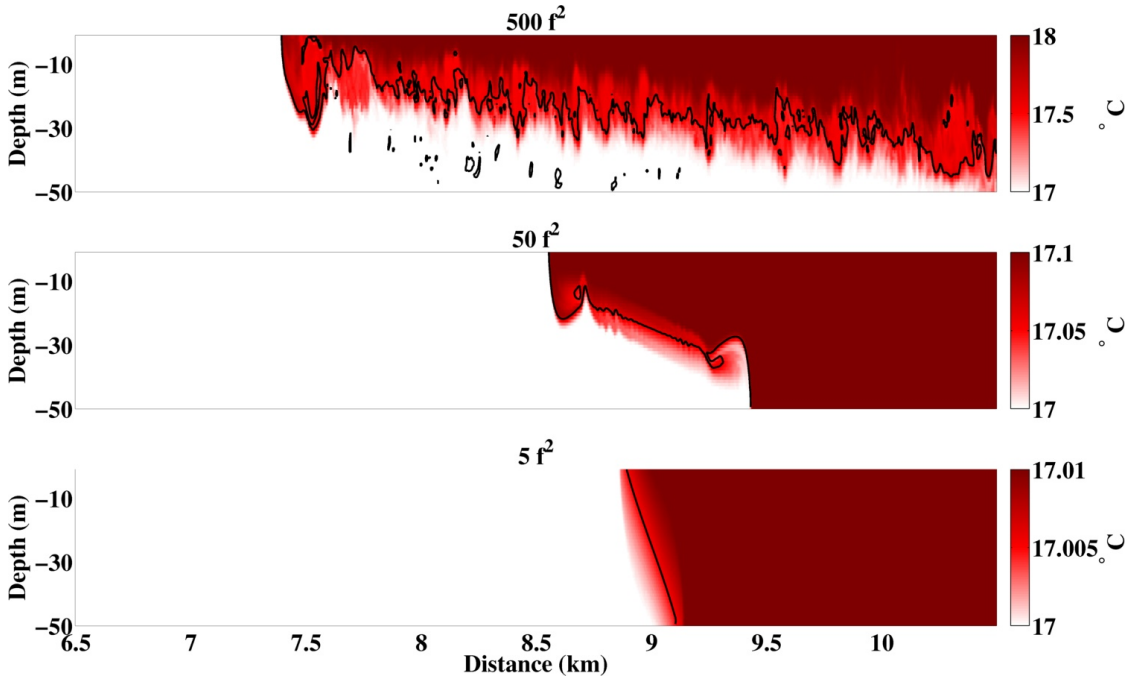

Figure 5.11: The temperature field in simulations with no thermocline at hour 3 at the indicated horizontal buoyancy gradient. Only a portion of the domain is shown due to the symmetry of the two fronts. The black contour shows the mid-point of the colour interval.

The first point of comparison is that as the frontal strength becomes larger the restratification is much more extensive (Figure 5.11, all panels). The Rossby radius R_{ML} approximately increases with the square root of the initial buoyancy gradient. As such the approximate tripling of the frontal width between successive panels in Fig. 5.11 is consistent with an increase in the initial buoyancy gradient by a factor of ten. Equivalently, the adjustment proceeds until the Burger number is of order 1. This is consistent with laboratory studies of Rossby adjustment [Ungarish and Huppert, 1998; Hallworth et al., 2001].

The extent of restratification in each run can be quantified by comparing the available potential energy compared to the available potential energy of the initial state. The potential energy is calculated, following [Winters et al., 1995], as:

$$\mathrm{PE} = g \int_V \rho(z) z dV, \tag{5.1}$$

where g is gravity, $\rho = \rho_0 + \alpha(T - T_{ref})$ with $\rho_0 = 1025$ kg m^{-3} and V is the

volume. The available potential energy is then:

$$\mathrm{APE} = \mathrm{PE} - \mathrm{PE}_{min}, \tag{5.2}$$

where the subscript 'min' means the potential energy of the minimum potential energy state that would result from an adiabatic re-arrangement of the fluid. The degree of restratification is then $\mathrm{APE}/\mathrm{APE}_0$, where the subscript 0 indicates the initial state. A value of 0 would indicate a complete restratification.

Figure 5.12 shows that the restratification in the Rossby adjustment phase is greater as the buoyancy gradient increases. As predicted by the analysis of Tandon and Garrett [1994] and Shakespeare and Taylor [2013], the adjustment is highly oscillatory in this case as the near-inertial waves generated during the adjustment cannot disperse and are only weakly damped by the bottom drag.

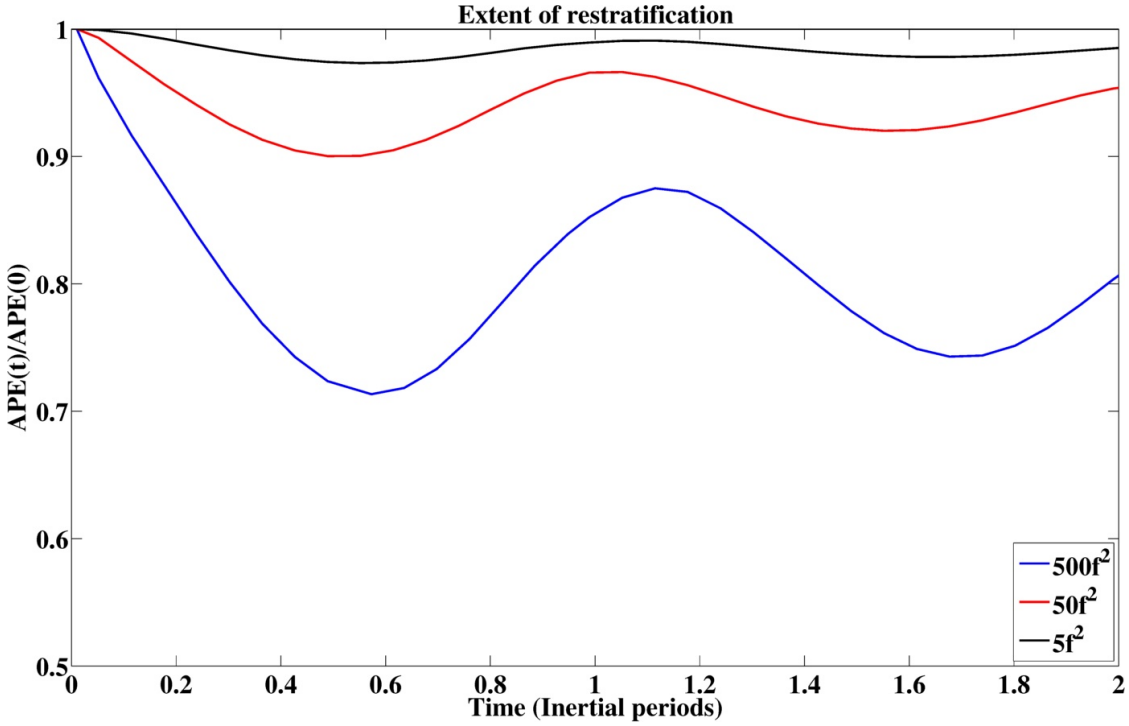

Figure 5.12: The available potential energy compared to the initial available potential energy in the simulations with no thermocline. A complete adiabatic restratification would lead to a value of 0.

The extent to which the adjustment gives rise to diapycnal mixing can be estimated by tracking changes in the minimum available potential energy as the adjustment proceeds, scaled by the initial minimum available potential energy. This calculation is the first stage of the analysis of Winters and D'Asaro [1996] to

derive an effective diffusivity for the turbulent flow. The results of this calculation are shown with a log-scale on the ordinate in Figure 5.13. The proportional change in the minimum available potential energy is, of course, small compared to the magnitude minimum available potential energy. However, the proportional change grows by factor of about 50 with each increase in the initial buoyancy gradient by a factor of 10. This increase is consistent with the snapshots in Fig. 5.11 that show a more turbulent adjustment for stronger initial gradients. The changes in the minimum available potential energy occur sooner for stronger initial gradients and occur before any overturning due to inertial oscillations (Fig. 5.13, all panels).

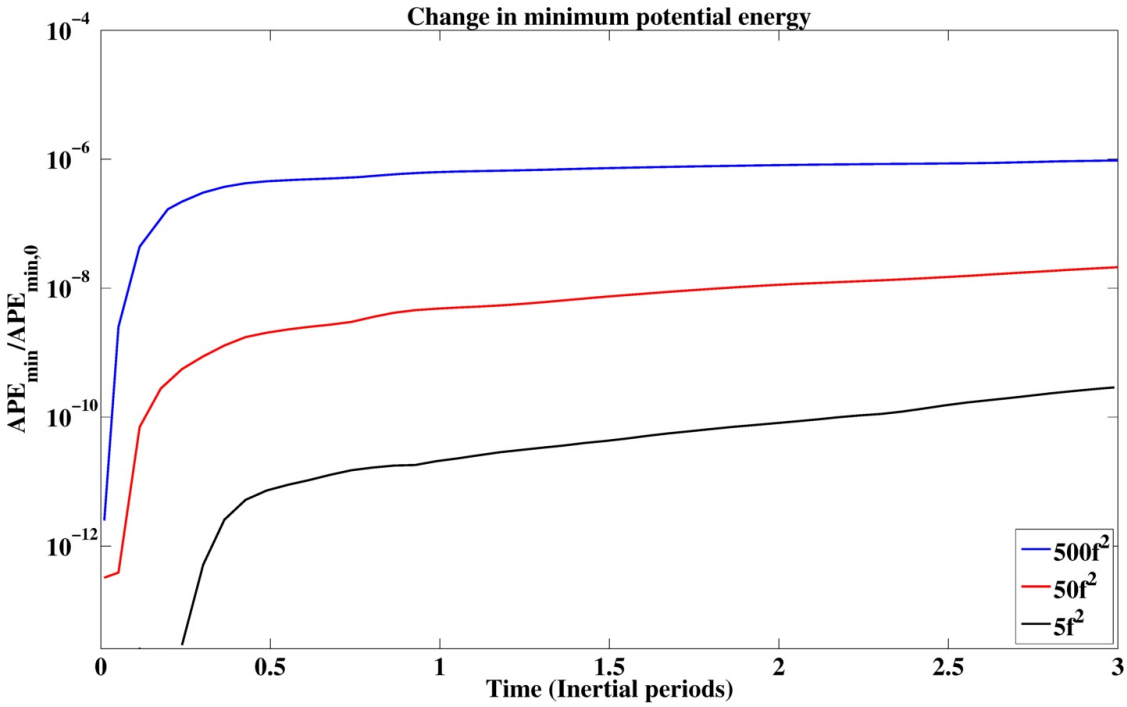

Figure 5.13: The minimum available potential energy in the simulations with no thermocline, non-dimensionalised by the initial minimum available potential energy for each simulation. This is a proxy for cumulative diapycnal mixing in the simulations. The ordinate has a log-scale. Values below 10^{-16} are below the maximum precision available.

The hypothesis for this work is that the rapid Rossby adjustment stage may not be properly represented in the Fox-Kemper et al. [2008] parameterisation, where the initial horizontal buoyancy gradients are much larger than f^2. The restratification velocity is taken to be the rate of displacement of the left-hand front at the surface. The parameterisation velocity is taken from the expression

for the streamfunction in equation 38 of Fox-Kemper et al. [2008]

$$\Psi = C_e \frac{H^2 b_x \times \mathbf{z}}{|f|} \mu(z), \tag{5.3}$$

where $C_e = 0.06$ is the efficiency factor, H is the mixed layer depth, b_x is the horizontal buoyancy gradient, $\mathbf{z}$ is the vertical unit vector,f is the Coriolis frequency and

$$\mu(z) = [1 - (\frac{2z}{H} - 1)^2][1 + \frac{5}{21}(\frac{2z}{H} + 1)^2] \tag{5.4}$$

is the vertical structure function. The horizontal restratification velocity is then $FKetal = d\Psi/dz$. Figure 5.14 shows that the Fox-Kemper et al. [2008] actually describes the initial restratification rate quite accurately for the two weaker frontal configurations (centre and bottom panel). The main departures occur when the inertial oscillations lead to a destratification from hours 10 to 20 of the simulations. The Fox-Kemper et al. [2008] parameterisation, on the other hand, is intended to capture behaviour averaged over many inertial periods. For the stronger frontal set up (upper panel), however, the parameterisation significantly overstates the rate of restratification compared to the actual simulations. This may reflect the buoyancy gradients in the simulations going beyond those for which the parameterisation is designed for. As horizontal buoyancy gradients of $500f6^2$ are relatively extreme, this is perhaps expected. On the basis of this comparison, the hypothesis that the Fox-Kemper et al. [2008] parameterisation cannot capture the restratification associated with stronger geostrophic adjustment events is rejected.

A central point of investigation is that the two dimensional adjustment becomes increasingly turbulent as the initial buoyancy gradient increases over the observationally-motivated range (Fig. 5.11, all panels). Figure 5.15 shows the temperature and Richardson number at the head of the flow for the strongest initial buoyancy gradient of 500 f^2 at Hour 3. The Richardson number here is calculated as Ri $= N^2/(u_z^2 + v_z^2)$ and so is calculated with respect to the shear variance of both the along- and cross-front velocity, rather than the along-front velocity alone as in Tandon and Garrett [1994].

After 50 minutes of the simulation (top-left panel) an overturn has developed from the initial adjustment that gives rise to negative stratification in the region behind the nose of the front near (8.65 km, -20 m) which is the blue area in the top-right panel. Over the following hour, a larger overturn develops that leads to small-scale convection in the region behind the head of the front as it travels to the left (centre-left and bottom-left panels). The thick contours in the right-hand

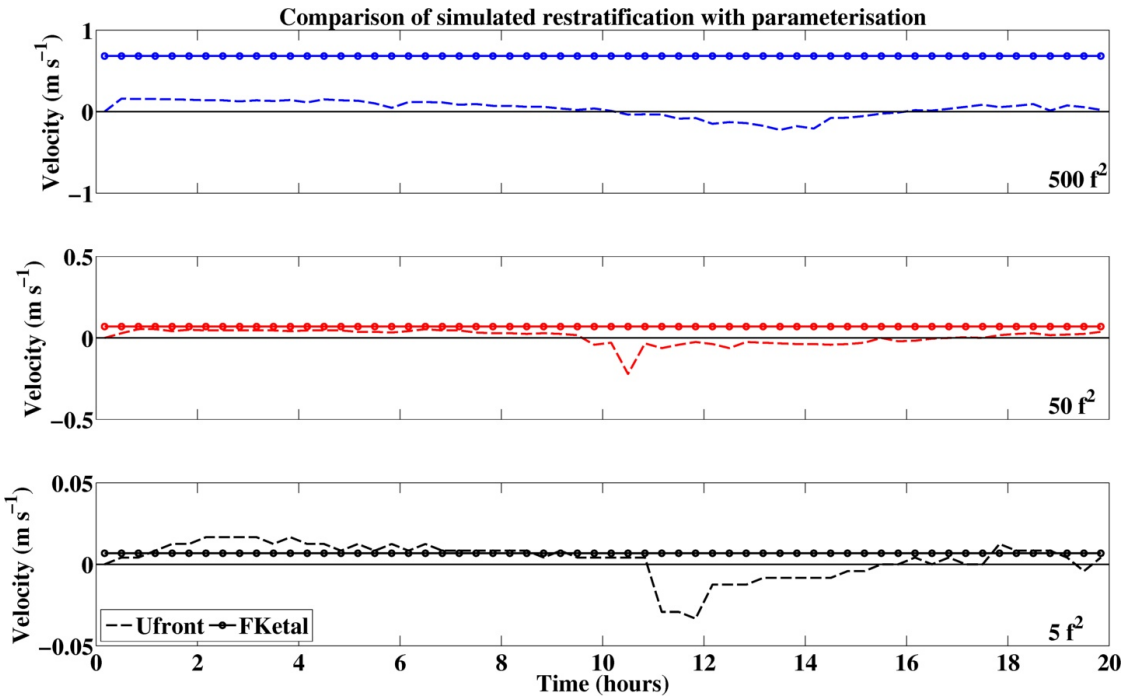

Figure 5.14: A comparison of the restratifying velocity with the restratifying velocity given by the Fox-Kemper et al. [2008] parameterisation. Ufr is calculated as the rate of displacement of the left-hand frontal interface at the surface, while *FKetal* is calculated as per the text.

panels show that the area around the overturn has $0 < \mathrm{Ri} < 0.25$ with $\mathrm{Ri} < 0$ inside the overturn (by definition). Further smaller scale instability waves and overturns are in evidence further along the interface region (bottom panels). For the simulation with initial gradient $50f^2$, turbulent overturns develop after three hours, while the simulation with initial gradient of $5f^2$, small overturns develop near the upper and lower boundaries after 8 hours (not shown). It is perhaps no surprise that turbulence develops in simulations with an initial condition of $\mathrm{Ri} = 0$. It is of more interest to understand why so little turbulence develops for the simulations with weaker fronts that also have an initial condition of $\mathrm{Ri} = 0$.

The Reynolds number for these flows is estimated as $\mathrm{Re} = UL/\nu$ where U is the maximum cross-front velocity, L is the deformation radius and $\nu = 10^{-5}$ m^2 s^{-1}, which is the explicit vertical viscosity used. The use of the deformation radius means that this should be taken as an upper bound for the Reynolds number. Fig. 5.16 shows that the Reynolds number drops by a factor of approximately 15 with each decrease in frontal strength by a factor of 10. The values of the Reynolds number for the weaker fronts in the initial adjustment phase are nonetheless of order 10^5 and so are in the range where turbulence is expected. In addition,

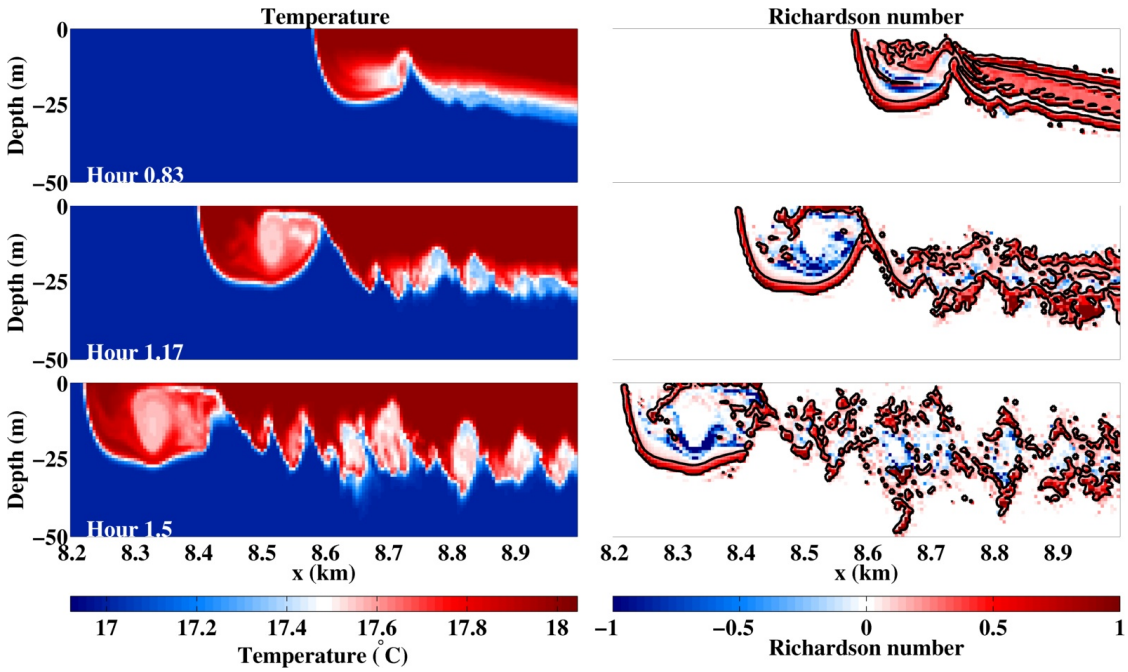

Figure 5.15: The development of buoyancy overturns near the head of the flow for a simulation with no thermocline and initial gradient of $500f^2$. The left hand panels show the temperature field, while the right-hand panels show the Richardson number $\mathrm{Ri} = N^2/(u_z^2 + v_z^2)$ at the same times. The thick black lines are contour lines showing $\mathrm{Ri} = 0.25$. The right hand plots are saturated for $|\mathrm{Ri}| > 1$.

the buoyancy-restoring force is much weaker in the experiments with weaker initial horizontal gradients. There is also an additional, hard-to-quantify, diffusion introduced by the temperature advection scheme used in the simulations, which reduces the Reynolds number below the explicit value shown in Fig. 5.16, which may make the flow more laminar. In any case, the larger Reynolds numbers found in the stronger frontal cases are certainly in the turbulent regime. The stronger fronts here have a horizontal buoyancy gradient that is relatively uniform in the vertical, which does not correspond to the vertical structure found in the observations in Fig. 5.3.

5.5.2 Simulations with a thermocline

The simulations with no thermocline show that Rossby adjustment becomes turbulent for stronger initial gradients. However, the subsequent development of the front is unphysical as the lack of a thermocline restricts the propagation away of inertia-gravity waves generated during the adjustment process. The inclusion of a thermocline leads to a solution with different features.

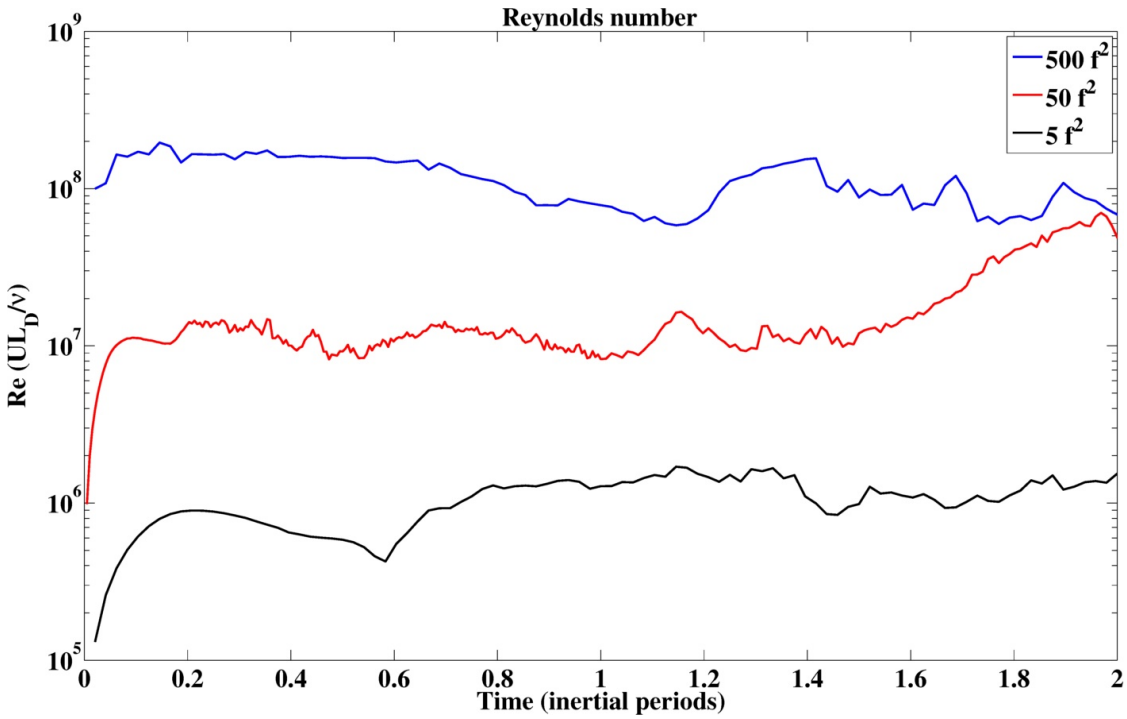

Figure 5.16: Time series of the Reynolds number estimated as Re = UL/ν where U is taken as the maximum cross-front velocity, L is taken as the deformation radius and $\nu = 10^{-5}$ m^2 s^{-1}, which is the explicit vertical viscosity used in the model.

Figure 5.17 shows the temperature field at hour 3 for simulations with the same initial buoyancy gradients in the mixed layer as in Fig. 5.11. Again, there is a larger deformation radius for the stronger initial fronts. However, while the front near the surface extends over two kilometres from the starting point at km 9 (upper panel), the front at the base of the mixed layer extends just one kilometre to the right. A similar effect is found for the runs with a weaker initial buoyancy gradient (centre and lower panels). There is some correspondence between these simulations and the frontal structure found in the observations (Fig. 5.3, upper panel) in that the front is more diffuse in the upper two-thirds of the mixed layer than at the base of the mixed layer, for example at (9.5 km, - 45 m) in the centre panel of Fig. 5.17 though the overall differences are relatively small.

The inertia-gravity waves produced by the adjustment are apparent for the stronger fronts in Fig. 5.17 by the larger displacements of the isotherms. In particular there is a large depression in the isotherms below the nose of the front that extends into the thermocline. The size of this depression becomes larger as the initial buoyancy gradient becomes larger. This depression in the thermocline below the head of the front is similar to that observed by Dale et al. [2008] (Figure

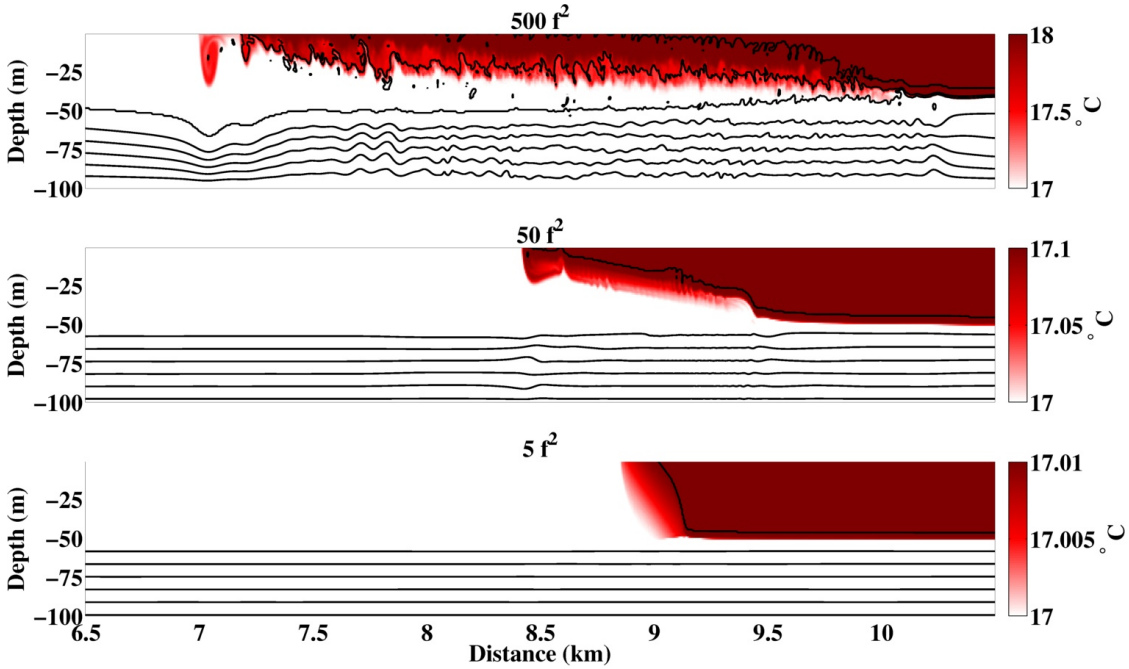

Figure 5.17: The temperature field in the simulations with a thermocline to 100 m at hour 3. The title of each subplot shows the initial horizontal buoyancy gradient. Note the different colour scales. The black lines are temperature contours with an interval of 0.5 ° C.

5b in that paper).

The rate of restratification for the runs with a thermocline (dashed lines) are compared to the runs that have no thermocline but are subject to linear drag (solid lines) in Figure 5.18. The calculations are carried out over the upper 45 m for both sets of simulations to remove the effect of the diffusion of heat across the base of the mixed layer that skews the calculation for the weaker gradients. The figure shows that the results are qualitatively similar, though additional restratification occurs for the runs with a thermocline as the gradients become stronger. The restratification proceeds somewhat faster with a thermocline, despite the very low bottom drag coefficient used for the runs with no thermocline. A comparison of the rate of restratification in these simulations compared to the predicted velocities from the Fox-Kemper et al. [2008] parameterisation shows similar results to those in Figure 5.14.

An additional run is carried out with a deeper thermocline that extends to 500 m with an initial horizontal buoyancy gradient of $500f^2$ and constant stratification below the mixed layer. The temperature field at the third hour of the adjustment (Figure 5.19) shows that inertia-gravity waves generated by the ad-

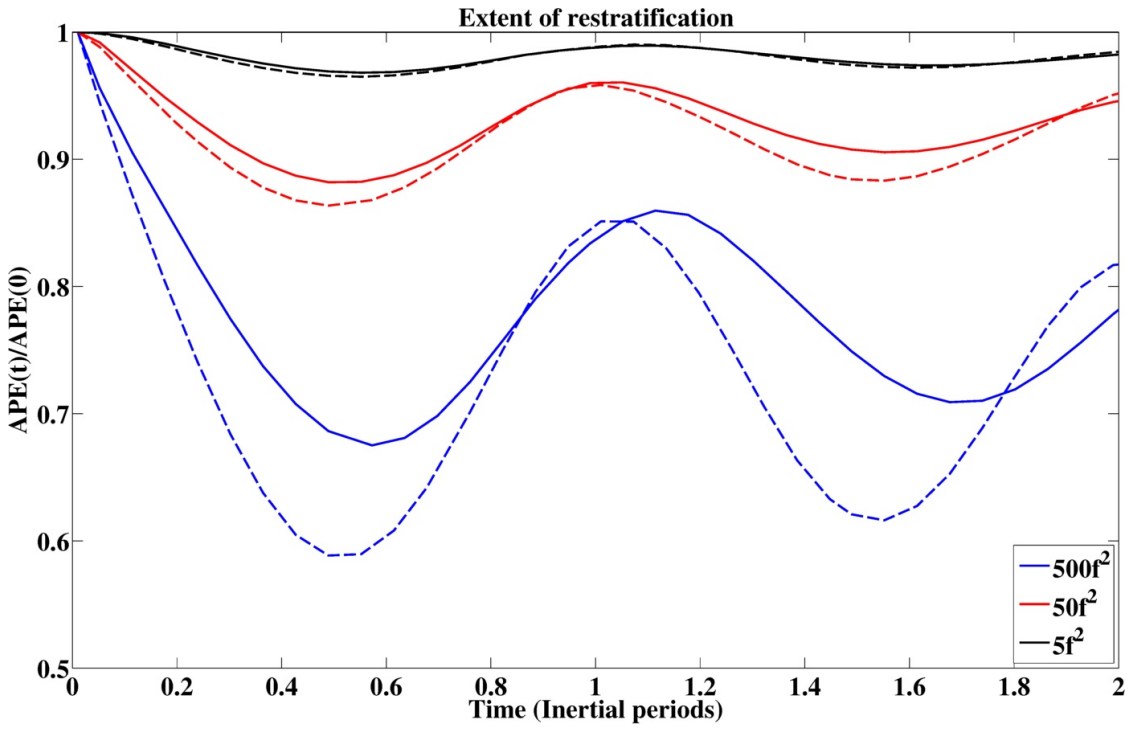

Figure 5.18: The minimum available potential energy in the upper 45 m through time in the simulations without a thermocline (solid lines) and with a thermocline to 100 m (dashed lines), non-dimensionalised by the initial minimum available potential energy for each simulation.

justment quickly propagate downwards through the domain. The magnitude of the displacements below the head of the front is the same throughout the depth range. As the stratification is linear, this cannot be accounted for by weaker buoyancy gradients at depth. There is a slight phase lag at depth.

The across-front velocity field for this deeper thermocline run in Figure 5.20 (left panel) highlights the change in phase of the inertia-gravity waves generated below the head of the front. The vertical velocity field – which is tightly linked to the across-front velocity field in this case by the non-divergence of the cross-front flow – in the right-panel of Fig. 5.20 shows that the inertia-gravity waves generated at the base of the front at (10 km, -50 m) are much weaker than those at the frontal interface near the surface at (7 km, -10 m). The author is not aware of this finding having been reported previously in the literature.

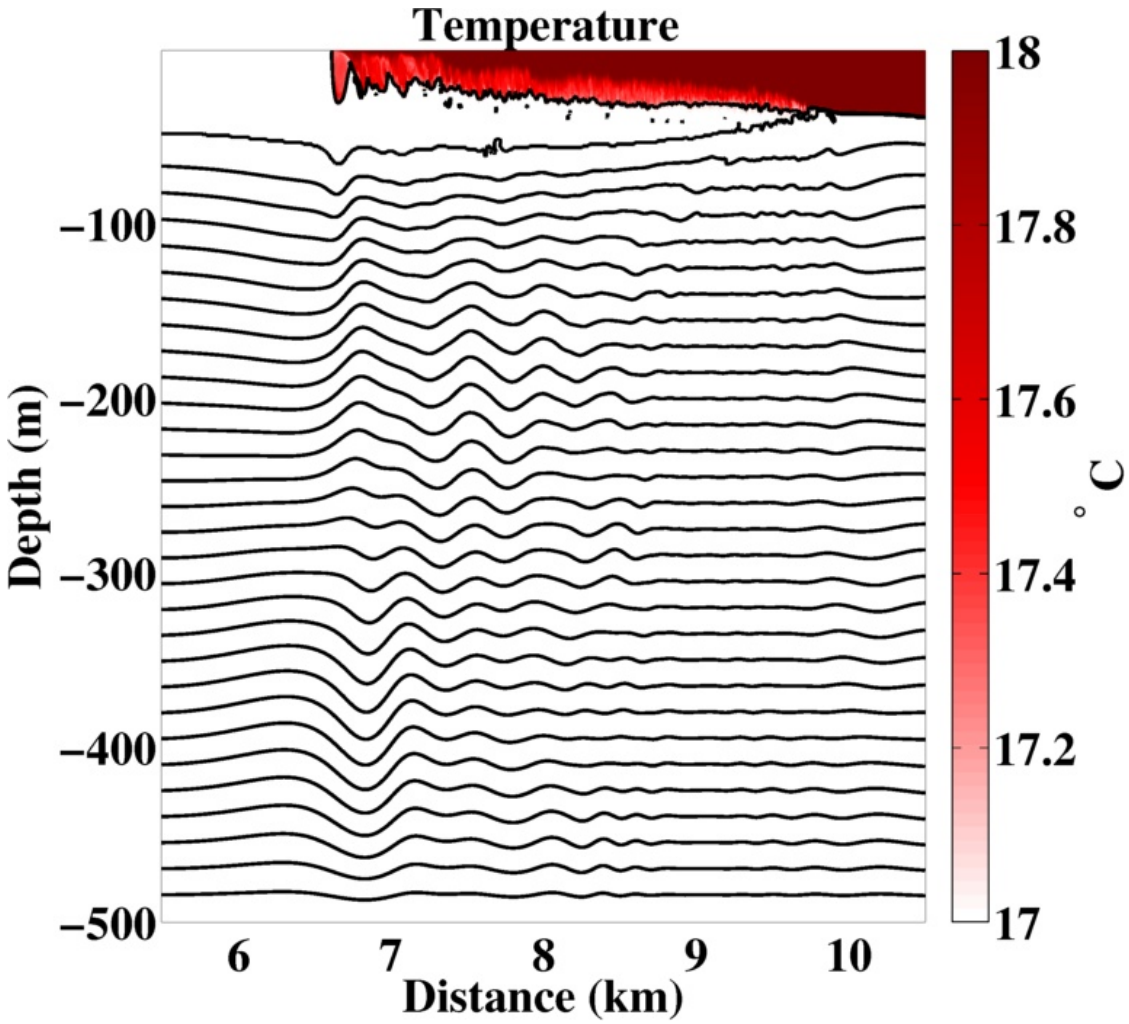

Figure 5.19: The temperature at hour 3 of the run with a deeper thermocline. The colour scale captures gradients in the mixed layer. The black lines are isotherms with a contour interval of 0.5° C. The warmest contour line is at 17° C.

5.6 Discussion

Observations of a mid-latitude front between a cyclonic and anticyclonic eddy show the presence of a submesoscale front. One feature of the observed front is that the front becomes broader and weaker towards the surface while it is sharper towards the base of the mixed layer. The velocity field that is marginally resolved in ADCP observations of the mixed layer show a departure from the geostrophic flow implied by altimetry, which is a good approximation below the base of the mixed layer. These observations took place in the context of a weakening down-front wind and lead to the hypothesis that the flow and buoyancy fields reflect a turbulent Rossby adjustment to the weakening down-front wind. Furthermore,

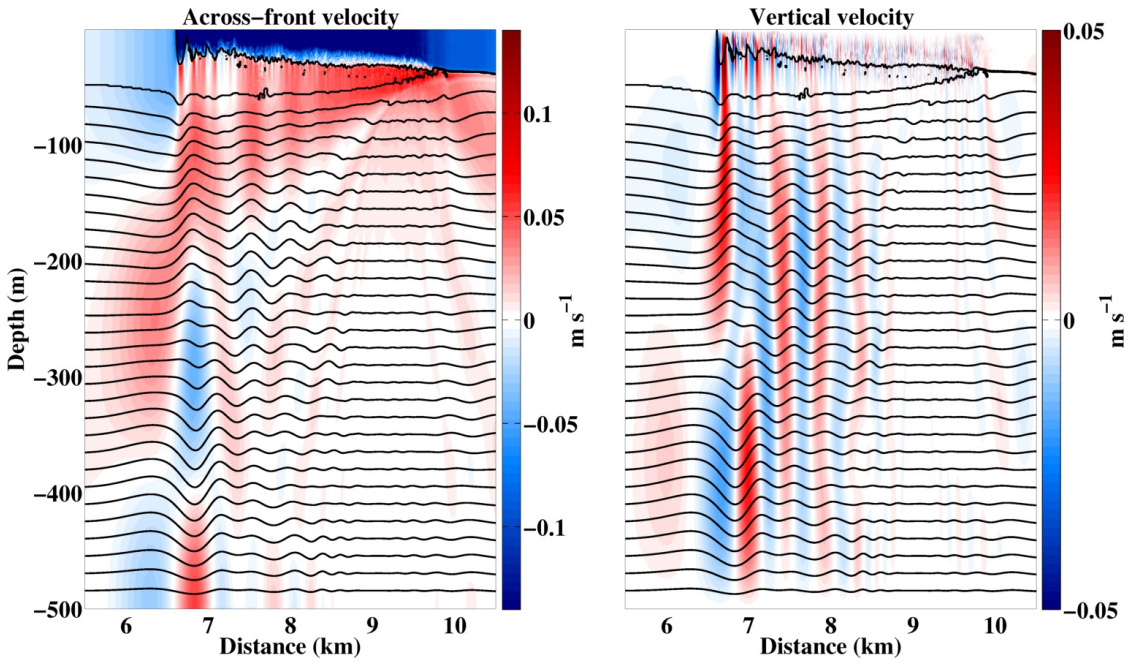

Figure 5.20: Snapshots of the across-front and vertical velocity fields at hour 3 of the run with a deeper thermocline. The black lines are isotherms as in Fig. 5.19. The across-front colour scale is saturated by a factor of 4 at the frontal interface.

an additional hypothesis is that the restratifying effect of such rapid ageostrophic flows are not captured by the Fox-Kemper et al. [2008] parameterisation for mixed layer instabilities.

A set of two-dimensional numerical simulations is carried out as an initial test of these hypotheses. The model set-up allows for Rossby adjustment, inertial oscillations and inertia-gravity waves. The initial condition is for zero potential vorticity, and so it does not allow for symmetric instability. The two-dimensional set-up also precludes baroclinic and barotropic instabilities or Rossby waves. The simulations show that the Rossby adjustment becomes much more turbulent over this range, with greater cross-front diapycnal mixing as Kelvin-Helmholtz instabilities grow in the initial hours of the experiment. It is cautioned that the model set-up in this case is pre-disposed to generate the most turbulent adjustment flow as there is initially no vertical velocity shear to balance the torque of the horizontal buoyancy gradient. While studies of Rossby adjustment in the ocean have primarily focused on the energy loss to inertia-gravity wave generation [Shakespeare and Taylor, 2013, e.g.], these results also suggest that turbulent energy dissipation and diapycnal mixing may also be important. It is noted, however, that recent results in non-rotating lock-exchange experiments downplay the role of such dissipative

processes compared to earlier results [Benjamin, 1968; Shin et al., 2004].

Further work is required to understand the adjustment process where the front is initially in balance between the horizontal buoyancy gradient, the velocity shear, a wind stress at the surface and a vertical turbulent diffusivity. In this case the degree to which the adjustment is turbulent is likely to depend on the degree to which the flow is in an Ekman balance – where the divergence of the wind stress and the Coriolis acceleration are the primary terms in balance – or in a thermal wind balance – where the primary balance is between the Coriolis acceleration and the horizontal pressure gradient. A further important consideration in the case of a relaxation of a down-front wind is the rate at which the down-front wind stress weakens or rotates out of alignment. If this happens at a rate comparable to f^{-1} the adjustment is likely to be stronger and more turbulent. If the decrease in the down-front wind stress occurs over longer time scales, the adjustment is likely to be gentler (M. McIntyre, pers. comm.). In the presence of a thermocline, the simulations also highlight an asymmetry between the upper and lower parts of mixed layer fronts undergoing adjustment. The adjustment is faster near the surface, with more turbulence and stronger inertia-gravity wave emission. This stronger adjustment leads to greater diapycnal mixing across the front.

Approaches where the inclusion of the wind forcing could be pursued are considered in Chapter 6.4. The wind forcing will also extract potential vorticity from one of the fronts and so allow for symmetric instability to emerge in the solutions. A further generalisation would examine the results in a three-dimensional configuration, to allow for the development of baroclinic instabilities.

CHAPTER 6

Conclusions

6.1 Overview

Motivated by recent progress made in understanding submesoscale variability at large ocean fronts this thesis examines submesoscale dynamics in the open ocean. This has included idealised numerical simulations of a wind-forced open ocean domain, high spatial resolution observations of open ocean fronts and submesoscale-resolving simulations of the Rossby adjustment of fronts.

6.2 Contributions

This work has resulted in several new contributions to our understanding of submesoscale dynamics in the eddying open ocean. These are summarised here.

The simulations of an open ocean domain with a seasonal buoyancy forcing illustrate how submesoscale properties change as the mixed layer depth varies by an order of magnitude. While the results are numerical rather than observational, they provide questions that can be asked of observational datasets. The major contributions are listed here.

1. An additional downward heat transport between the mixed layer and thermocline occurs when the resolution becomes submesoscale-permitting and that this heat transport is advective rather than diffusive in nature.

2. The turbulent properties, as reflected in the slope of horizontal wavenumber spectra of surface buoyancy and velocity, are sensitive to the mixed layer depth. The slopes transition from a steep value of -3 in log-log space when the mixed layer is less than 30 m deep to a shallower slope between -2 and -5/3 when the mixed layer deepens beyond about 50 m with a relatively smooth transition from the steep to the shallow slope regime.

3. The residual momentum balance changes as the resolution is made finer with an increased role for advective and high-frequency processes, particularly in vortices and as the mixed layer deepens.

4. Submesoscale processes have different annual cycles whereby frontogenetical processes are stronger when the mixed layer is shallow but overturning instabilities become stronger as the mixed layer deepens.

5. A substantial proportion of the mixed layer volume, including within baroclinic mesoscale vortices, has negative potential vorticity under weak wind forcing and cooling.

These simulations also show the presence of filaments inside mesoscale anticyclones as the resolution becomes submesoscale-permitting. The major contributions are listed here.

1. The three-dimensional potential vorticity structure of the mixed layer of wind-forced cyclonic and anticyclonic vortices is described.

2. A provisional estimate of energy budgets shows the likely importance of vertical shear production and negative vertical buoyancy fluxes.

3. Symmetric instability is identified as the most likely mechanism that gives rise to the filaments.

4. The generation of high potential vorticity filaments gives rise to strong emission of inertia-gravity waves that appear to be trapped in the vortex.

5. It is demonstrated that tracer subduction, nutrient upwelling and vertical buoyancy fluxes of both signs occurs inside the mesoscale anticyclone.

An observational dataset shows the presence of strong ageostrophic flows in the mixed layer around an open ocean front. While no definitive conclusion can be drawn from the available data due to the single clear observation of the front and the limited resolution of the acoustic current profiler, they motivate numerical simulations of Rossby adjustment of fronts in a zero potential vorticity configuration. The major contributions are listed here.

1. It is shown that the Reynolds number for the strong fronts is much larger than for weaker fronts and so the Rossby adjustment is more turbulent with potential for more cross-front mixing.

2. The presence of a thermocline leads to vertical asymmetry in the fronts compared to simulations without a thermocline.

3. It is illustrated that inertia-gravity wave generation in the presence of a thermocline is much stronger at the surface than at the base of adjusting fronts.

6.3 Implications

The results of this work have implications for our understanding of climatic processes and their representation in numerical models. These implications are set out here. Firstly, the results show that the distribution of mass at submesoscales in the mixed layer is a balance between frontogenetical flows that increase the variance of horizontal buoyancy gradients and overturning instabilities that decrease the variance of horizontal buoyancy gradients while leading to a restratification. This may provide an insight into the relationship between frontogenesis and baroclinic instability [Bishop, 1993; Spall, 1997; McWilliams and Molemaker, 2011], namely that the balance is sensitive to the available potential energy with the transition from primarily frontogenesis to primarily baroclinic instability occurring when the mean mixed layer depth is approximately 40 m. At present, only the effect of the overturning instabilities are parameterised in climate models. Frontogenesis is a function of the large-scale strain and so is always partially-resolved. The inclusion of a full overturning parameterisation with partial representation of frontogenesis may bias results.

The concentration of shallow wavenumber spectra in the mixed layer may inform theoretical models used to study mixed layer dynamics. The results are most consistent with models of the open ocean that focus on quasi-geostrophic

rather than surface quasi-geostrophic properties. This represents a conception of the mixed layer as a shallow quasi-geostrophic layer scaling with the mixed layer Rossby radius coupled to a deep quasi-geostrophic regime scaling with the first internal Rossby radius [Boccaletti et al., 2007; Callies and Ferrari, 2013]. Such a model would still only capture the balanced dynamics and neglects unbalanced processes such as symmetric instability. The importance of geostrophic instabilities also emphasises the importance of measuring the oceanic pressure field at finer resolution, particularly the forthcoming wide-swath altimetry mission [Fu and Ubelmann, 2014].

Perhaps the major contribution of this work is the description of submesoscale filaments in mesoscale anticyclones. If observational validation is forthcoming, this process may have important implications for our understanding and modelling of biogeochemical and dynamical processes. The results suggest that the symmetric instability mechanism provides a pathway for nutrients to upwell from the thermocline into the mixed layer along isopycnals that outcrop in mesoscale anticyclones. This could explain the presence of long-lived nutrient blooms visible from satellite in anticyclonic eddies in locations where the mixed layer is expected to be nutrient depleted. The strong nutrient upwelling associated with this mechanism leads to the conjecture that the upwelling associated with symmetric instability may even allow reconciliation of carbon budgets in the mid-latitudes, where estimated primary production from geochemical tracers has long exceeded the estimated upwelling of nutrients required to sustain the productivity.

An identification of the mechanism that drives upwelling in anticyclones would allow it to be parameterised in climate models. Progress towards such a parameterisation has been made in recent years [e.g. Bachman and Taylor, 2014]. The results here emphasise that not only the relative vorticity but also the angular velocity must be taken into account in such a parameterisation. The finding that the negative angular velocity and negative relative vorticity destabilise flow to symmetric instability also substantially increases the area of the ocean where symmetric instability can occur.

The suggestions that the upwelling mechanism is symmetric instability, which is strongly dissipative of kinetic energy, may have implications for eddy lifecycles. The dissipation of energy in the mesoscale eddy field is a major open question in physical oceanography and the presence of symmetric instabilities inside the eddies has not been included in existing budgets [Ferrari and Wunsch, 2009], though Thomas and Taylor [2010] speculate on its potential importance.

The results here suggest that it is indeed important, though only for mesoscale anticyclones. Again, the identification of the mechanism allows further work to establish scalings for kinetic energy dissipation in coarser resolution climate simulations.

There are other, more speculative, implications of the symmetric instability mechanism. The use of a very simplified equation of state in one variable in these simulations means that there are no thermodynamic effects of along-isopycnal exchange. However, in the Arctic, where warm-salty water sits below cold-fresh water [Spielhagen et al., 2011], the upwelling of the warm-salty water along isopycnals would lead to additional heat fluxes out of the ocean. These heat fluxes could then affect climate variables such as the sea ice extent. The down-front wind mechanism cannot happen underneath sea-ice, as a boundary always imparts a stress opposed to the flow and so is intrinsically up-front. The loss of sea-ice thus allows further extraction of potential vorticity in the Arctic as the Arctic becomes more exposed to wind forcing.

The unbalanced filaments also radiate inertia-gravity waves that transfer energy away from the mixed layer of the vortex. The apparent trapping of these waves in the vortex may remove energy from the mixed layer of the vortex. The energy may ultimately end up as a vertical buoyancy flux in the interior if wave-capture ultimately leads to wave-breaking deeper in the vortex.

The simulations of the Rossby adjustment of fronts consider the role of inertia-gravity wave generation in the adjustment flow and illustrate the potential for cross-front diapycnal mixing associated with the flow. This could imply that parameterisations of this process should allow for additional cross-front mixing. The runs with a thermocline also show that the behaviour of the front at the surface and at the base of the mixed layer may be somewhat different, which may also have to be included in parameterisations.

6.4 Future work

There are many outstanding questions remaining at the end of this thesis which I hope to pursue in the future. A selection of these is presented here. The warmer thermocline found in the higher resolution simulations remains a feature of particular interest. The initial hypothesis that it resulted from stronger diffusive mixing at finer resolution has been rejected. The buoyancy fluxes inside the anticyclone in Figure 4.8 show that there are negative mean buoyancy fluxes below the mixed

layer, despite positive mean buoyancy fluxes above the mixed layer. A closer investigation of this is warranted. The current model set-up with a turbulent eddy field limits the extent to which the horizontal resolution can be increased.

Further progress can be made by setting up a new model domain with a single eddy, similar to that used in previous studies of vortex stability [e.g. Smyth and McWilliams, 1998]. While such a configuration could lead to horizontal resolution being increased by an order of magnitude, resolving the small-scale non-hydrostatic secondary instabilities is at the very limits of computational feasibility [e.g. Hamlington et al., 2014] and prohibits a more comprehensive search of the parameter space. One way to address this would be to do a two-dimensional study where the model domain simulates a vertical slice through the vortex. The surface wind would then be rotated to simulate the passage around the vortex. This would require the imposition of a barotropic flow to capture relative vorticity effects [Bachman and Taylor, 2014] and a centripetal acceleration to capture curvature effects. This non-hydrostatic configuration would allow a full investigation of the energy fluxes associated with the instabilities along the lines of [Thomas and Taylor, 2010]. If such an analysis of anticyclones proved successful, it may be possible to extend them to so-called 'mode water' eddies.

Recent results have shown that the Stokes shear may be of first-order importance in setting the Ertel potential vorticity, with the Stokes shear offsetting some of the negative potential vorticity that can result from down-front winds [McWilliams and Fox-Kemper, 2013; Haney et al., Subm. to JPO]. The effect of the Stokes shear could be investigated by imposing a Stokes shear in some simulations, even if Langmuir cells were still parameterised.

Understanding of the vortex instability would be improved by conducting a linear stability analysis. The study of Bachman and Taylor [2014] could be adapted to include curvature effects by including a centripetal acceleration. Indeed, given the adjustment to thermal wind set out in Chapter 4.7, a first guess would be that such an adaption would lead to the first term in Equation (5) in Bachman and Taylor [2014] being multiplied by the factor γ defined in Chapter 4.7. This would result in changes to the growth rate and wavelengths of the most unstable modes. Such a result would also highlight a crucial difference between the angular velocity and relative vorticity effect on stability in that the angular velocity effect is not dependant on the stratification whereas the relative vorticity is. This could be important given the tendency for down-front winds to weaken stratification.

The cyclonic vortices in the numerical simulations received less attention here than the anticyclones due to their relative stability. The mixed layer of cyclones in the simulations does, however, have regions of negative potential vorticity. One question then is whether filament generation can occur in cyclones under a stronger wind stress, with a deeper mixed layer or at higher resolution.

Perhaps the most urgent requirement is an observational test of whether anticyclones are host to high potential vorticity filaments. The potential vorticity anomalies associated with the filaments are characterised by the presence of stratification in the mixed layer where little stratification is expected. The best sampling platform for this may be gliders which can make profiles of temperature and salinity right to the surface, though towed instruments could also be useful. Such an *in-situ* dataset would ideally be accompanied by remote data from altimetry and satellite sea surface temperature to understand the spatial structure of the three-dimensional flow. Upwelling properties could be inferred if there is a degree of spiciness along the isopycnals that outcrop into the mixed layer of the vortex. Fluorescence sensors could also help infer whether any stratification anomalies are host to high primary productivity.

The numerical study of Rossby adjustment illustrates the effect of varying the initial buoyancy gradient over the parameter range found in the mid-latitude open ocean on the degree of restratification and the turbulent nature of the adjustment. However, the analysis here requires significant development. As the study is motivated by the observations of a front in the presence of a weakening wind-forcing, the effect of wind-forcing needs to be included in the simulations. The results here can perhaps be interpreted as the response of a front to an instantaneous weakening of a wind stress. More realistically, the wind stress would decay or rotate out of alignment over a finite time scale. As this time scale grows to be more comparable with the Coriolis timescale f^{-1}, the 'violence' of the adjustment – and thus its turbulent properties – is expected to diminish. In addition, the presence of a wind-forcing will also lead to potential vorticity fluxes and so introduce symmetric instability into the down-front wind scenarios. The analysis itself also needs to be extended to quantify the degree of diapycnal mixing. This will be done using the approach of Winters and D'Asaro [1996] to estimate an effective diffusivity for fronts of different strengths.

Bibliography

Alford, M. H., A. Y. Shcherbina, and M. C. Gregg, 2013: Observations of Near-Inertial Internal Gravity Waves Radiating from a Frontal Jet. *J.Phys.Oceanogr.*, **43 (6)**, 1225–1239.

Andrews, D. G., J. R. Holton, and C. B. Leovy, 1987: *Middle atmosphere dynamics*. 40, Academic press.

Arbic, B. K., and R. B. Scott, 2008: On quadratic bottom drag, geostrophic turbulence, and oceanic mesoscale eddies. *J.Phys.Oceanogr.*, **38 (1)**, 84–103.

Bachman, S., and B. Fox-Kemper, 2013: Eddy parameterization challenge suite I: Eady spindown. *Ocean Modelling*, **64**, 12–28, doi:10.1016/j.ocemod.2012.12.003, URL http://linkinghub.elsevier.com/retrieve/pii/S1463500312001801.

Bachman, S., and J. Taylor, 2014: Modelling of partially-resolved oceanic symmetric instability. *Ocean Modelling*, **82**, 15–27, doi:10.1016/j.ocemod.2014.07.006, URL http://linkinghub.elsevier.com/retrieve/pii/S1463500314000961.

Barth, J. A., 1994: Short-wavelength instabilities on coastal jets and fronts. *Journal of Geophysical Research-Oceans*, **99 (C8)**, 16 095–16 115.

Bates, N. R., a. C. Pequignet, R. J. Johnson, and N. Gruber, 2002: A short-term sink for atmospheric CO2 in subtropical mode water of the North Atlantic Ocean. *Nature*, **420 (6915)**, 489–93, doi:10.1038/nature01253, URL http://www.ncbi.nlm.nih.gov/pubmed/12487116.

Behrenfeld, M. J., 2010: Abandoning Sverdrup's Critical Depth Hypothesis on phytoplankton blooms. *Ecology*, **91 (4)**, 977–989.

Belcher, S. E., and Coauthors, 2012: A global perspective on langmuir turbulence in the ocean surface boundary layer. *Geophys.Res.Lett.*, **39 (18)**.

Benitez-Nelson, C. R., and Coauthors, 2007: Mesoscale eddies drive increased silica export in the subtropical pacific ocean. *Science*, **316 (5827)**, 1017–1021.

Benjamin, T. B., 1968: Gravity currents and related phenomena. *J.Fluid Mech.*, **31 (02)**, 209–248.

Bergeron, 1959: *The atmosphere and the sea in motion: scientific contributions to the Rossby memorial volume*, chap. Methods in Scientific Weather Analysis and Forecasting. An outline in the history of ideas and hints at a program. Oxford University Press.

Bergeron, T., 1928: *Ueber die dreidimensional verkneupfende Wetteranalyse*. Cammermeyer in Komm., – pp.

Berry, D. I., and E. C. Kent, 2009: A new air-sea interaction gridded dataset from icoads with uncertainty estimates. *Bull.Am.Meteorol.Soc.*, **90 (5)**, 645–656.

Bishop, C. H., 1993: On the behaviour of baroclinic waves undergoing horizontal deformation. II: Errorblind amplification and Rossy wave diagnostics. *Q.J.R.Meteorol.Soc.*, **119 (510)**, 241–267.

Bjerknes, J., 1919: On the structure of moving cyclones. *Mon.Weather Rev.*, **47 (2)**, 95–99.

Blumen, W., 1978: Uniform potential vorticity flow .1. theory of wave interactions and 2-dimensional turbulence. *J.Atmos.Sci.*, **35 (5)**, 774–783.

Boccaletti, G., R. Ferrari, and B. Fox-Kemper, 2007: Mixed Layer Instabilities and Restratification. *Journal of Physical Oceanography*, **37 (9)**, 2228–2250, doi:10.1175/JPO3101.1, URL http://journals.ametsoc.org/doi/abs/10.1175/JPO3101.1.

Borchert, S., U. Achatz, and M. D. Fruman, 2014: Gravity wave emission in an atmosphere-like configuration of the differentially heated rotating annulus experiment. *J.Fluid Mech.*, **758**, 287–311.

Bracco, A., J. LaCasce, C. Pasquero, and A. Provenzale, 2000: The velocity distribution of barotropic turbulence. *Physics of Fluids (1994-present)*, **12 (10)**, 2478–2488.

Bretherton, F. P., 1966: Critical layer instability in baroclinic flows. *Quarterly Journal of the Royal Meteorological Society*, **92 (393)**, 325–334, doi:10.1002/qj.49709239302, URL http://doi.wiley.com/10.1002/qj.49709239302.

Brüggemann, N., and C. Eden, 2014: Evaluating different parameterizations for mixed layer eddy fluxes induced by baroclinic instability. *J.Phys.Oceanogr.*, **44 (9)**, 2524–2546.

Bühler, O., and M. E. McIntyre, 2005: Wave capture and wavevortex duality. *Journal of Fluid Mechanics*, **534**, 67–95, doi:10.1017/S0022112005004374, URL http://www.journals.cambridge.org/abstract_S0022112005004374.

Callies, J., and R. Ferrari, 2013: Interpreting energy and tracer spectra of upper-ocean turbulence in the submesoscale range (1200 km). *J.Phys.Oceanogr.*, **43 (11)**, 2456–2474.

Capet, X., E. J. Campos, and a. M. Paiva, 2008a: Submesoscale activity over the Argentinian shelf. *Geophysical Research Letters*, **35 (15)**, L15 605, doi:10.1029/2008GL034736, URL http://doi.wiley.com/10.1029/2008GL034736.

Capet, X., J. McWilliams, M. Molemaker, and A. Shchepetkin, 2008b: Mesoscale to submesoscale transition in the California Current System. Part I: Flow structure, eddy flux, and observational tests. *J.Phys.Oceanogr.*, **38 (1)**, 29–43.

Capet, X., J. McWilliams, M. Molemaker, and A. Shchepetkin, 2008c: Mesoscale to submesoscale transition in the California Current System. Part II: Frontal processes. *J.Phys.Oceanogr.*, **38 (1)**, 44–64.

Capet, X., J. McWilliams, M. Molemaker, and A. Shchepetkin, 2008d: Mesoscale to submesoscale transition in the California current system. Part III: Energy balance and flux. *J.Phys.Oceanogr.*, **38 (10)**, 2256–2269.

Cenedese, C., J. a. Lerczak, and G. Bartone, 2012: A Geostrophic Adjustment Model of Two Buoyant Fluids. *Journal of Physical Oceanography*, **42 (11)**, 1932–1944, doi:10.1175/JPO-D-11-0169.1, URL http://journals.ametsoc.org/doi/abs/10.1175/JPO-D-11-0169.1.

Charney, J. G., 1947: The dynamics of long waves in a baroclinic westerly current. *J.Meteorol.*, **4 (5)**, 136–162.

Charney, J. G., 1971: Geostrophic turbulence. *J.Atmos.Sci.*, **28 (6)**, 1087–&.

Chelton, D. B., P. Gaube, M. G. Schlax, J. J. Early, and R. M. Samelson, 2011: The influence of nonlinear mesoscale eddies on near-surface oceanic chlorophyll. *Science*, **334 (6054)**, 328–332.

Chereskin, T., and D. Roemmich, 1991: A comparison of measured and wind-derived Ekman transport at 11 N in the Atlantic Ocean. *J.Phys.Oceanogr.*, **21 (6)**, 869–878.

Clayton, S., T. Nagai, and M. J. Follows, 2014: Fine scale phytoplankton community structure across the kuroshio front. *J.Plankton Res.*, **36 (4)**, 1017–1030.

Colin de Verdière, Y., 2012: The stability of short symmetric internal waves on sloping fronts: Beyond the traditional approximation. *J.Phys.Oceanogr.*, **42 (3)**, 459–475.

Crawford, W. R., P. J. Brickley, and A. C. Thomas, 2007: Mesoscale eddies dominate surface phytoplankton in northern Gulf of Alaska. *Prog.Oceanogr.*, **75 (2)**, 287–303.

Cromwell, T., and J. L. Reid, 1956: A study of oceanic fronts. *Tellus*, **8 (1)**, 94–101, URL http://dx.doi.org/10.1111/j.2153-3490.1956.tb01198.x.

Cushman-Roisin, B., 1981: Effects of horizontal advection on upper ocean mixing: A case of frontogenesis. *J.Phys.Oceanogr.*, **11 (10)**, 1345–1356.

Cushman-Roisin, B., and J.-M. Beckers, 2011: *Introduction to geophysical fluid dynamics: physical and numerical aspects*, Vol. 101. Academic Press, – pp.

Dale, A. C., J. A. Barth, M. D. Levine, and J. A. Austin, 2008: Observations of mixed layer restratification by onshore surface transport following wind reversal in a coastal upwelling region. *Journal of Geophysical Research*, **113 (C1)**, C01 010, doi:10.1029/2007JC004128, URL http://doi.wiley.com/10.1029/2007JC004128.

Danabasoglu, G., and J. C. McWilliams, 1995: Sensitivity of the global ocean circulation to parameterizations of mesoscale tracer transports. *Journal of Climate*, **8 (12)**, 2967–2987.

Danioux, E., J. Vanneste, P. Klein, and H. Sasaki, 2012: Spontaneous inertia-gravity-wave generation by surface-intensified turbulence. *J.Fluid Mech.*, **699**, 153–173.

Daru, V., and C. Tenaud, 2004: High order one-step monotonicity-preserving schemes for unsteady compressible flow calculations. *Journal of Computational Physics*, **193 (2)**, 563–594.

D'Asaro, E., C. Lee, L. Rainville, R. Harcourt, and L. Thomas, 2011: Enhanced Turbulence and Energy Dissipation at Ocean Fronts. *Science*, **332 (6027)**, 318–322.

Deser, C., M. A. Alexander, and M. S. Timlin, 1996: Upper-ocean thermal variations in the North Pacific during 1970-1991. *Journal of Climate*, **9 (8)**, 1840–1855, pT: J; TC: 256; UT: WOS:A1996VG92100011.

Dewar, W. K., and G. R. Flierl, 1987: Some effects of the wind on rings. *J.Phys.Oceanogr.*, **17 (10)**, 1653–1667.

Dong, C., J. C. McWilliams, Y. Liu, and D. Chen, 2014: Global heat and salt transports by eddy movement. *Nature communications*, **5**, –.

Douglass, E. M., and J. G. Richman, 2015: Analysis of ageostrophy in strong surface eddies in the atlantic ocean. *J. Geophys. Res. Oceans*, **120 (3)**, 1490–1507, URL http://dx.doi.org/10.1002/2014JC010350.

Dritschel, D. G., and M. E. McIntyre, 2008: Multiple jets as PV staircases: The Phillips effect and the resilience of eddy-transport barriers. *J.Atmos.Sci.*, **65 (3)**, 855–874.

Duarte, C. M., A. Regaudie-de Gioux, J. M. Arrieta, A. Delgado-Huertas, and S. Agusti, 2013: The oligotrophic ocean is heterotrophic. *Annual Review of Marine Science, Vol 5*, **5**, 551–569.

Ducklow, H. W., and S. C. Doney, 2013: What is the metabolic state of the oligotrophic ocean? a debate. *Annual Review of Marine Science, Vol 5*, **5**, 525–533.

Dunkerton, T. J., 1995: Horizontal buoyancy flux of internal gravity-waves in vertical shear. *Journal of the Meteorological Society of Japan*, **73 (3)**, 747–755.

Dutkiewicz, S., A. Sokolov, J. Scott, and P. Stone, 2005: A three-dimensional ocean-seaice-carbon cycle model and its coupling to a two-dimensional atmospheric model: uses in climate change studies. –.

Eady, E., 1949: Long waves and cyclone waves. *Tellus*, **1 (3)**, 33–52.

Eden, C., and H. Dietze, 2009: Effects of mesoscale eddy/wind interactions on biological new production and eddy kinetic energy. *Journal of Geophysical Research: Oceans (19782012)*, **114 (C5)**.

Ekman, V. W., 1905: On the influence of the earth's rotation on ocean currents. *Ark.Mat.Astron.Fys.*, **2**, 1–53.

Eliassen, A., 1962: On the vertical circulation in frontal zones. *Geofys.Publ*, **24 (4)**, 147–160.

Emerson, S., P. Quay, D. Karl, C. Winn, L. Tupas, and M. Landry, 1997: Experimental determination of the organic carbon flux from open-ocean surface waters. *Nature*, **389 (6654)**, 951–954.

Eriksen, C. C., R. A. Weller, D. L. Rudnick, and R. T. Pollard, 1991: Ocean Frontal Variability in the Frontal Air-Sea Interaction Experiment. **96 (90)**, 8569–8591.

Ertel, H., 1942: Ein neuer hydrodynamischer Wirbelsatz. *Meteorol.Z.*, **59**, 277–281.

Fawcett, S. E., M. W. Lomas, J. R. Casey, B. B. Ward, and D. M. Sigman, 2011: Assimilation of upwelled nitrate by small eukaryotes in the Sargasso Sea. *Nature Geoscience*, **4 (10)**, 717–722.

Fedorov, K. N., 1986: *The physical nature and structure of oceanic fronts*, Vol. 19. American Geophysical Union, – pp.

Ferrari, R., and M. Nikurashin, 2010: Suppression of eddy diffusivity across jets in the southern ocean. *J.Phys.Oceanogr.*, **40 (7)**, 1501–1519.

Ferrari, R., and C. Wunsch, 2009: Ocean circulation kinetic energy: Reservoirs, sources, and sinks. *Annu.Rev.Fluid Mech.*, **41**, 253–282.

Ferrari, R., and C. Wunsch, 2010: The distribution of eddy kinetic and potential energies in the global ocean. *Tellus Series A-Dynamic Meteorology and Oceanography*, **62 (2)**, 92–108.

Ferrari, R., and W. R. Young, 1997: On the development of thermohaline correlations as a result of nonlinear diffusive parameterizations. *Journal of Marine Research*, **55 (6)**, 1069–1101, doi:10.1357/0022240973224094, URL http://www.ingentaselect.com/rpsv/cgi-bin/cgi?ini=xref&body=linker&reqdoi=10.1357/0022240973224094.

Ford, R., 1994a: Gravity-wave radiation from vortex trains in rotating shallow-water. *J.Fluid Mech.*, **281**, 81–118.

Ford, R., 1994b: The instability of an axisymmetrical vortex with monotonic potential vorticity in rotating shallow-water. *J.Fluid Mech.*, **280**, 303–334.

Ford, R., M. E. McIntyre, and W. A. Norton, 2000: Balance and the slow quasi-manifold: Some explicit results. *J.Atmos.Sci.*, **57 (9)**, 1236–1254.

Fox-Kemper, B., and R. Ferrari, 2008: Parameterization of mixed layer eddies. Part II: Prognosis and impact. *J.Phys.Oceanogr.*, **38 (6)**, 1166–1179.

Fox-Kemper, B., R. Ferrari, and R. Hallberg, 2008: Parameterization of Mixed Layer Eddies. Part I: Theory and Diagnosis. *Journal of Physical Oceanography*, **38 (6)**, 1145–1165, doi:10.1175/2007JPO3792.1, URL http://journals.ametsoc.org/doi/abs/10.1175/2007JPO3792.1.

Fox-Kemper, B., and D. Menemenlis, 2013: Can large eddy simulation techniques improve mesoscale rich ocean models? *Ocean Modeling in an Eddying Regime*, American Geophysical Union, 319–337, URL http://dx.doi.org/10.1029/177GM19.

Fox-Kemper, B., and Coauthors, 2011: Parameterization of mixed layer eddies. III: Implementation and impact in global ocean climate simulations. *Ocean Modelling*, **39 (1-2)**, 61–78, doi:10.1016/j.ocemod.2010.09.002, URL http://linkinghub.elsevier.com/retrieve/pii/S1463500310001290.

Fu, L. L., and G. R. Flierl, 1980: Non-linear energy and enstrophy transfers in a realistically stratified ocean. *Dyn.Atmos.Oceans*, **4 (4)**, 219–246.

Fu, L.-L., and C. Ubelmann, 2014: On the transition from profile altimeter to swath altimeter for observing global ocean surface topography. *J.Atmos.Ocean.Technol.*, **31 (2)**, 560–568.

Fuglister, F., and L. Worthington, 1951: Some Results of a Multiple Ship Survey of the Gulf Stream. *Tellus*, **3 (1)**, 1–14.

Gaube, P., D. B. Chelton, R. M. Samelson, M. G. Schlax, and L. W. ONeill, 2014a: Satellite Observations of Mesoscale Eddy-Induced Ekman Pumping. *J. Phys. Oceanogr.*, **45 (1)**, 104–132, URL http://dx.doi.org/10.1175/JPO-D-14-0032.1.

Gaube, P., D. B. Chelton, P. G. Strutton, and M. J. Behrenfeld, 2013: Satellite observations of chlorophyll, phytoplankton biomass, and Ekman pumping in nonlinear mesoscale eddies. *Journal of Geophysical Research-Oceans*, **118 (12)**, 6349–6370.

Gaube, P., D. J. McGillicuddy, D. B. Chelton, M. J. Behrenfeld, and P. G. Strutton, 2014b: Regional variations in the influence of mesoscale eddies on near-surface chlorophyll. *Journal of Geophysical Research: Oceans*, doi:10.1002/2014JC010111, URL http://doi.wiley.com/10.1002/2014JC010111.

Gent, P. R., and J. C. Mcwilliams, 1990: Isopycnal mixing in ocean circulation models. *J.Phys.Oceanogr.*, **20 (1)**, 150–155.

Graham, J. P., and T. Ringler, 2013: A framework for the evaluation of turbulence closures used in mesoscale ocean large-eddy simulations. *Ocean Modelling*, **65**, 25–39.

Grant, A. L. M., and S. E. Belcher, 2009: Characteristics of Langmuir Turbulence in the Ocean Mixed Layer. *Journal of Physical Oceanography*, **39 (8)**, 1871–1887, doi:10.1175/2009JPO4119.1, URL http://journals.ametsoc.org/doi/abs/10.1175/2009JPO4119.1.

Green, J. S. A., 1970: Transfer properties of large-scale eddies and general circulation of atmosphere. *Q.J.R.Meteorol.Soc.*, **96 (408)**, 157–&.

Griffies, S. M., and R. W. Hallberg, 2000: Biharmonic friction with a Smagorinsky-like viscosity for use in large-scale eddy-permitting ocean models. *Monthly Weather Review*, **128 (8)**, 2935–2946.

Gula, J., M. J. Molemaker, and J. C. McWilliams, 2014: Submesoscale Cold Filaments in the Gulf Stream. *Journal of Physical Oceanography*, **44 (10)**, 2617–2643, doi:10.1175/JPO-D-14-0029.1, URL http://journals.ametsoc.org/doi/abs/10.1175/JPO-D-14-0029.1.

Haine, T. W. N., and J. Marshall, 1998: Gravitational, symmetric, and baroclinic instability of the ocean mixed layer. *J.Phys.Oceanogr.*, **28 (4)**, 634–658.

Haine, T. W. N., and K. J. Richards, 1995: The Influence of the Seasonal Mixed-Layer on Oceanic Uptake of Cfcs. *Journal of Geophysical Research-Oceans*, **100 (C6)**, 10 727–10 744, pT: J; TC: 40; UT: WOS:A1995RD77500009.

Hallworth, M. a., H. E. Huppert, and M. Ungarish, 2001: Axisymmetric gravity currents in a rotating system: experimental and numerical investigations. *Journal of Fluid Mechanics*, **447**, 1–29, doi:10.1017/S0022112001005523, URL http://www.journals.cambridge.org/abstract_S0022112001005523.

Hamlington, P. E., L. P. Van Roekel, B. Fox-Kemper, K. Julien, and G. P. Chini, 2014: LangmuirSubmesoscale Interactions: Descriptive Analysis of Multiscale Frontal Spindown Simulations. *Journal of Physical Oceanography*, **44 (9)**, 2249–2272, doi:10.1175/JPO-D-13-0139.1, URL http://journals.ametsoc.org/doi/abs/10.1175/JPO-D-13-0139.1.

Haney, S., B. Fox-Kemper, K. Julien, and A. Webb, Subm. to JPO: Symmetric and Geostrophic Instabilities in the Wave-Forced Ocean Mixed Layer.

Haney, S., and Coauthors, 2012: Hurricane wake restratification rates of one-, two-and three-dimensional processes. *J.Mar.Res.*, **70 (6)**, 824–850.

Hansen, C., E. Kvaleberg, and A. Samuelsen, 2010: Anticyclonic eddies in the Norwegian Sea; their generation, evolution and impact on primary production. *Deep Sea Research Part I: Oceanographic Research Papers*, **57 (9)**, 1079–1091.

Haynes, P., and M. McIntyre, 1987: On the evolution of vorticity and potential vorticity in the presence of diabatic heating and frictional or other forces. *J.Atmos.Sci.*, **44 (5)**, 828–841.

Held, I. M., R. T. Pierrehumbert, S. T. Garner, and K. L. Swanson, 1995: Surface Quasi-Geostrophic Dynamics. *J.Fluid Mech.*, **282**, 1–20.

Hill, C., D. Ferreira, J.-M. Campin, J. Marshall, R. Abernathey, and N. Barrier, 2012: Controlling spurious diapycnal mixing in eddy-resolving height-coordinate ocean models - Insights from virtual deliberate tracer release experiments. *Ocean Modelling*, **45-46**, 14–26.

Hogg, N. G., and H. M. Stommel, 1985: The Heton, an Elementary Interaction Between Discrete Baroclinic Geostrophic Vortices, and Its Implications Concerning Eddy Heat-Flow. *Proceedings of the Royal Society A: Mathematical, Physical and Engineering Sciences*, **397 (1812)**, 1–20, doi:10.1098/rspa.1985.0001, URL http://rspa.royalsocietypublishing.org/cgi/doi/10.1098/rspa.1985.0001.

Holdsworth, A. M., and B. R. Sutherland, 2015: The axisymmetric collapse of a mixed patch and internal wave generation in uniformly stratified rotating fluid. *Physics of Fluids (1994-present)*, **27 (5)**, 056 602–.

Hosegood, P., M. C. Gregg, and M. H. Alford, 2006: Sub-mesoscale lateral density structure in the oceanic surface mixed layer. *Geophysical Research Letters*, **33 (22)**, L22 604, doi:10.1029/2006GL026797, URL http://doi.wiley.com/10.1029/2006GL026797.

Hoskins, B., 1982: The mathematical theory of frontogenesis. *Annu.Rev.Fluid Mech.*, **14 (1)**, 131–151.

Hoskins, B. J., 1974: Role of potential vorticity in symmetric stability and instability. *Quarterly Journal of the Royal Meteorological Society*, **100 (425)**, 480–482.

Hoskins, B. J., and Bretherton, 1972: Atmospheric Frontogenesis Models - Mathematical Formulation and Solution. *Journal of the Atmospheric Sciences*, **29 (1)**, 11–37.

Hoskins, B. J., and I. Draghici, 1977: Forcing of ageostrophic motion according to semi-geostrophic equations and in an isentropic coordinate model. *J.Atmos.Sci.*, **34 (12)**, 1859–1867.

Hoskins, B. J., I. Draghici, and H. C. Davies, 1978: A new look at the omega-equation. *Q.J.R.Meteorol.Soc.*, **104 (439)**, 31–38.

Hoskins, B. J., M. E. Mcintyre, and A. W. Robertson, 1985: On the use and significance of isentropic potential vorticity maps. *Q.J.R.Meteorol.Soc.*, **111 (470)**, 877–946.

Huang, R. X., 2004: *Encyclopedia of Energy*, chap. Ocean, energy flows in, 497–509.

Huisman, J., P. van Oostveen, and F. J. Weissing, 1999: Critical depth and critical turbulence: Two different mechanisms for the development of phytoplankton blooms. *Limnol.Oceanogr.*, **44 (7)**, 1781–1787.

Ilicak, M., A. J. Adcroft, S. M. Griffies, and R. W. Hallberg, 2012: Spurious dianeutral mixing and the role of momentum closure. *Ocean Modelling*, **45-46**, 37–58.

Iselin, C., and F. C. Fuglister, 1948: Some recent developments in the study of the Gulf Stream. *J.Mar.Res.*, **7 (3)**, 317–329.

Iselin, C. O., 1936: A study of the circulation of the western North Atlantic.

Jenkins, W., 1982: Oxygen utilization rates in North Atlantic subtropical gyre and primary production in oligotrophic systems. *Nature*, **300 (5889)**, 246–248.

Jenkins, W. J., and J. C. Goldman, 1985: Seasonal Oxygen Cycling and Primary Production in the Sargasso Sea. *J.Mar.Res.*, **43 (2)**, 465–491.

Karleskind, P., M. Lévy, and L. Memery, 2011: Subduction of carbon, nitrogen, and oxygen in the northeast Atlantic. *Journal of Geophysical Research*, **116 (C2)**, C02 025, doi:10.1029/2010JC006446, URL http://doi.wiley.com/10.1029/2010JC006446.

Katz, E. J., 1969: Further study of a front in the Sargasso Sea. *Tellus*, **21 (2)**, 259–269.

Kay, A., 1992: Frontogenesis in gravity-driven flows with non-uniform density gradients. *J.Fluid Mech.*, **235**, 529–556.

Klein, P., B. L. Hua, G. Lapeyre, X. Capet, S. Le Gentil, and H. Sasaki, 2008: Upper Ocean Turbulence from High-Resolution 3D Simulations. *Journal of Physical Oceanography*, **38 (8)**, 1748–1763, doi:10.1175/2007JPO3773.1, URL http://journals.ametsoc.org/doi/abs/10.1175/2007JPO3773.1.

Klein, P., and G. Lapeyre, 2009: The oceanic vertical pump induced by mesoscale and submesoscale turbulence. *Annual review of marine science*, **1**, 351–75, doi:10.1146/annurev.marine.010908.163704, URL http://www.ncbi.nlm.nih.gov/pubmed/21141041.

Kloosterziel, R., and G. Van Heijst, 1991: An experimental study of unstable barotropic vortices in a rotating fluid. *J.Fluid Mech.*, **223 (1)**.

Kloosterziel, R. C., G. F. Carnevale, and P. Orlandi, 2007: Inertial instability in rotating and stratified fluids: barotropic vortices. *Journal of Fluid Mechanics*, **583**, 379, doi:10.1017/S0022112007006325, URL http://www.journals.cambridge.org/abstract_S0022112007006325.

Knauss, J. A., 1957: An observation of an oceanic front. *Tellus*, **9 (2)**, 234–237, URL http://dx.doi.org/10.1111/j.2153-3490.1957.tb01878.x.

Koszalka, I., A. Bracco, J. C. McWilliams, and A. Provenzale, 2009: Dynamics of wind-forced coherent anticyclones in the open ocean. *Journal of Geophysical Research*, **114 (C8)**, C08 011, doi:10.1029/2009JC005388, URL http://doi.wiley.com/10.1029/2009JC005388.

LaCasce, J. H., and a. Mahadevan, 2006: Estimating subsurface horizontal and vertical velocities from sea-surface temperature. *Journal of Marine Research*, **64 (5)**, 695–721, doi:10.1357/002224006779367267, URL http://openurl.ingenta.com/content/xref?genre=article&issn=0022-2402&volume=64&issue=5&spage=695.

Lapeyre, G., and P. Klein, 2006: Dynamics of the upper oceanic layers in terms of surface quasigeostrophy theory. *J.Phys.Oceanogr.*, **36 (2)**, 165–176.

Lapeyre, G., P. Klein, and B. L. Hua, 2006: Oceanic restratification forced by surface frontogenesis. *Journal of Physical Oceanography*, **36 (8)**, 1577–1590.

Large, W. G., J. C. McWilliams, and S. C. Doney, 1994: Oceanic Vertical Mixing - a Review and a Model with a Nonlocal Boundary-Layer Parameterization. *Reviews of Geophysics*, **32 (4)**, 363–403.

Lazar, A., a. Stegner, and E. Heifetz, 2013: Inertial instability of intense stratified anticyclones. Part 1. Generalized stability criterion. *Journal of Fluid Mechanics*, **732**, 457–484, doi:10.1017/jfm.2013.412, URL http://www.journals.cambridge.org/abstract_S0022112013004126.

Ledwell, J. R., D. J. McGillicuddy, and L. a. Anderson, 2008: Nutrient flux into an intense deep chlorophyll layer in a mode-water eddy. *Deep Sea Research Part II: Topical Studies in Oceanography*, **55 (10-13)**, 1139–1160, doi:10.1016/j.dsr2.2008.02.005, URL http://linkinghub.elsevier.com/retrieve/pii/S0967064508000672.

Lehahn, Y., F. D'Ovidio, M. Lévy, Y. Amitai, and E. Heifetz, 2011: Long range transport of a quasi isolated chlorophyll patch by an Agulhas ring. *Geophysical Research Letters*, **38 (16)**, doi:10.1029/2011GL048588, URL http://doi.wiley.com/10.1029/2011GL048588.

Lehahn, Y., and Coauthors, 2014: Decoupling physical from biological processes to assess the impact of viruses on a mesoscale algal bloom. *Current Biology*, **24 (17)**, 2041–2046.

Leith, C. E., 1996: Stochastic models of chaotic systems. *Physica D*, **98 (2-4)**, 481–491.

Lenn, Y.-D., and T. K. Chereskin, 2009: Observations of Ekman Currents in the Southern Ocean. *J.Phys.Oceanogr.*, **39 (3)**, 768–779.

Lévy, M., D. Iovino, L. Resplandy, P. Klein, G. Madec, a. M. Tréguier, S. Masson, and K. Takahashi, 2012: Large-scale impacts of submesoscale dynamics on phytoplankton: Local and remote effects. *Ocean Modelling*, **43-44**, 77–93, doi:10.1016/j.ocemod.2011.12.003, URL http://linkinghub.elsevier.com/retrieve/pii/S1463500311002009.

Lévy, M., P. Klein, a. M. Tréguier, D. Iovino, G. Madec, S. Masson, and K. Takahashi, 2010: Modifications of gyre circulation by sub-mesoscale physics. *Ocean Modelling*, **34 (1-2)**, 1–15, doi:10.1016/j.ocemod.2010.04.001, URL http://linkinghub.elsevier.com/retrieve/pii/S1463500310000582.

Lévy, M., P. Klein, and M. Ben Jelloul, 2009: New production stimulated by high frequency winds in a turbulent mesoscale eddy field. *Geophys.Res.Lett.*, **36 (16)**.

Lévy, M., P. Klein, and A. M. Treguier, 2001: Impact of sub-mesoscale physics on production and subduction of phytoplankton in an oligotrophic regime. *Journal of Marine Research*, **59**, 535–565.

Long, M. C., L. N. Thomas, and R. B. Dunbar, 2012: Control of phytoplankton bloom inception in the Ross Sea, Antarctica, by Ekman restratification. *Global Biogeochemical Cycles*, **26 (1)**, GB1006, doi:10.1029/2010GB003982, URL http://doi.wiley.com/10.1029/2010GB003982.

Lorenz, E. N., 1960: Maximum simplification of the dynamic equations. *Tellus*, **12 (3)**, 243–254.

Luyten, J., J. Pedlosky, and H. Stommel, 1983: The ventilated thermocline. *J.Phys.Oceanogr.*, **13 (2)**, 292–309.

Macvean, M. K., and J. D. Woods, 1977: Numerical-model of upper ocean frontogenesis. *Transactions-American Geophysical Union*, **58 (9)**, 892–893.

Macvean, M. K., and J. D. Woods, 1980: Redistribution of scalars during upper ocean frontogenesis - a numerical-model. *Q.J.R.Meteorol.Soc.*, **106 (448)**, 293–311.

Mahadevan, A., 2006: Modeling vertical motion at ocean fronts: Are nonhydrostatic effects relevant at submesoscales? *Ocean Modelling*, **14 (3-4)**, 222–240.

Mahadevan, A., and D. Archer, 2000: Modeling the impact of fronts and mesoscale circulation on the nutrient supply and biogeochemistry of the upper ocean. **105 (Ci)**, 1209–1225.

Mahadevan, A., E. D'Asaro, C. Lee, and M. J. Perry, 2012: Eddy-driven stratification initiates north atlantic spring phytoplankton blooms. *Science*, **337 (6090)**, 54–58.

Mahadevan, A., A. Tandon, and R. Ferrari, 2010: Rapid changes in mixed layer stratification driven by submesoscale instabilities and winds. *Journal of Geophysical Research-Oceans*, **115**, C03 017.

Mahadevan, A., L. N. Thomas, and A. Tandon, 2008: Comment on "Eddy/wind interactions stimulate extraordinary mid-ocean plankton blooms". *Science*, **320 (5875)**, doi:10.1126/science.1152111.

Margalef, R., 1997: Turbulence and marine life. *Scientia Marina*, **61**, 109–123.

Marshall, D. P., and A. C. N. Garabato, 2008: A conjecture on the role of bottom-enhanced diapycnal mixing in the parameterization of geostrophic eddies. *J.Phys.Oceanogr.*, **38 (7)**, 1607–1613.

Marshall, D. P., J. R. Maddison, and P. S. Berloff, 2012: A Framework for Parameterizing Eddy Potential Vorticity Fluxes. *Journal of Physical Oceanography*, **42 (4)**, 539–557, doi:10.1175/JPO-D-11-048.1, URL http://journals.ametsoc.org/doi/abs/10.1175/JPO-D-11-048.1.

Marshall, J., A. Adcroft, C. Hill, L. Perelman, and C. Heisey, 1997: A finite-volume, incompressible Navier Stokes model for studies of the ocean on parallel computers. *Journal of Geophysical Research-Oceans*, **102 (C3)**, 5753–5766.

Marshall, J., and F. Schott, 1999: Open ocean convection: Observations, theory, and models. *Rev.Geophys.*, **37 (1)**, 1–64.

Marshall, J. C., and A. J. G. Nurser, 1992: Fluid-dynamics of oceanic thermocline ventilation. *Journal of Physical Oceanography*, **22 (6)**, 583–595, pT: J; TC: 49; UT: WOS:A1992HX27700002.

Marshall, J. C., A. J. G. Nurser, and R. G. Williams, 1993: Inferring the Subduction Rate and Period Over the North-Atlantic. *Journal of Physical Oceanography*, **23 (7)**, 1315–1329.

Martin, A., 2003: Phytoplankton patchiness: the role of lateral stirring and mixing. *Progress in Oceanography*, **57 (2)**, 125–174, doi:10.1016/S0079-6611(03)00085-5, URL http://linkinghub.elsevier.com/retrieve/pii/S0079661103000855.

Martin, A. P., and K. J. Richards, 2001: Mechanisms for vertical nutrient transport within a North Atlantic mesoscale eddy. *Deep Sea Research Part II: Topical Studies in Oceanography*, **48 (4-5)**, 757–773, doi:10.1016/S0967-0645(00)00096-5, URL http://linkinghub.elsevier.com/retrieve/pii/S0967064500000965.

McGillicuddy, D. J., and Coauthors, 1998: Influence of mesoscale eddies on new production in the Sargasso Sea. *Nature*, **394 (6690)**, 263–266.

McGillicuddy, D. J., and Coauthors, 2007: Eddy/Wind Interactions Stimulate Extraordinary Mid-Ocean Plankton Blooms. *Science*, **316 (5827)**, 1021–1026, URL http://www.sciencemag.org/content/316/5827/1021.abstract.

McIntyre, M., 2015a: *Balanced flow*, chap. Dynamical Meteorology. Elsevier.

McIntyre, M., 2015b: *Potential Vorticity*, chap. Dynamical Meteorology. Elsevier.

McIntyre, M. E., 2009: Spontaneous imbalance and hybrid vortex-gravity structures. *J.Atmos.Sci.*, **66 (5)**, 1315–1326.

McWilliams, J. C., 1985: Submesoscale, coherent vortices in the ocean. *Rev.Geophys.*, **23 (2)**, 165–182.

McWilliams, J. C., and B. Fox-Kemper, 2013: Oceanic wave-balanced surface fronts and filaments. *J.Fluid Mech.*, **730**, 464–490.

McWilliams, J. C., and M. J. Molemaker, 2011: Baroclinic Frontal Arrest: A Sequel to Unstable Frontogenesis. *Journal of Physical Oceanography*, **41 (3)**, 601–619, doi:10.1175/2010JPO4493.1, URL http://journals.ametsoc.org/doi/abs/10.1175/2010JPO4493.1.

McWilliams, J. C., M. J. Molemaker, and E. I. Olafsdottir, 2009: Linear fluctuation growth during frontogenesis. *J.Phys.Oceanogr.*, **39 (12)**, 3111–3129.

McWilliams, J. C., I. Yavneh, M. J. P. Cullen, and P. R. Gent, 1998: The breakdown of large-scale flows in rotating, stratified fluids. *Physics of Fluids*, **10 (12)**, 3178, doi:10.1063/1.869844, URL http://scitation.aip.org/content/aip/journal/pof2/10/12/10.1063/1.869844.

Mensa, J. A., Z. Garraffo, A. Griffa, T. M. Özgökmen, A. Haza, and M. Veneziani, 2013: Seasonality of the submesoscale dynamics in the Gulf Stream region. *Ocean Dynamics*, **63 (8)**, 923–941, doi:10.1007/s10236-013-0633-1, URL http://link.springer.com/10.1007/s10236-013-0633-1.

Michaels, A. F., 2007: Highly active eddies. *Science (New York, N.Y.)*, **316 (5827)**, 992–3, doi:10.1126/science.1140059, URL http://www.ncbi.nlm.nih.gov/pubmed/17510353.

Molemaker, M. J., J. C. Mcwilliams, and X. Capet, 2010: Balanced and unbalanced routes to dissipation in an equilibrated Eady flow. *Journal of Fluid Mechanics*, **654**, 35–63, doi:10.1017/S0022112009993272, URL http://www.journals.cambridge.org/abstract_S0022112009993272.

Molemaker, M. J., J. C. McWilliams, and I. Yavneh, 2005: Baroclinic instability and loss of balance. *Journal of Physical Oceanography*, **35 (9)**, 1505–1517.

Morel, A., H. Claustre, and B. Gentili, 2010: The most oligotrophic subtropical zones of the global ocean: similarities and differences in terms of chlorophyll and yellow substance. *Biogeosciences*, **7 (10)**, 3139–3151.

Munk, W., 1981: Internal waves and small-scale processes. *Evolution of physical oceanography*, 264–291.

Munk, W. H., 1950: On the wind-driven ocean circulation. *J.Meteorol.*, **7 (2)**, 80–93.

Nakamura, M., and R. A. Plumb, 1994: The Effects of Flow Asymmetry on the Direction of Rossby-Wave Breaking. *J.Atmos.Sci.*, **51 (14)**, 2031–2045.

Nastrom, G., and K. S. Gage, 1985: A climatology of atmospheric wavenumber spectra of wind and temperature observed by commercial aircraft. *J.Atmos.Sci.*, **42 (9)**, 950–960.

Nierenberg, W. A., 1996: Harald Ulrik Sverdrup. *Biographical Memoirs, National Academy of Sciences*, **69**, 338–375.

Niiler, P. P., 1969: On the Ekman divergence in an oceanic jet. *Journal of Geophysical Research*, **74 (28)**, 7048–7052.

Nurser, A. J. G., and J. W. Zhang, 2000: Eddy-induced mixed layer shallowing and mixed layer/thermocline exchange. *J. Geophys. Res.*, **105 (C9)**, 21 851–21 868, URL http://dx.doi.org/10.1029/2000JC900018.

Ooyama, K., 1966: On stability of baroclinic circular vortex - a sufficient criterion for instability. *J.Atmos.Sci.*, **23 (1)**, 43–&.

Oschlies, A., 2002a: Can eddies make ocean deserts bloom? *Global Biogeochem.Cycles*, **16 (4)**, 1106–1106.

Oschlies, A., 2002b: Nutrient supply to the surface waters of the North Atlantic: A model study. *Journal of Geophysical Research-Oceans*, **107 (C5)**, 3046–3046.

O'Sullivan, D., and T. J. Dunkerton, 1995: Generation of inertia-gravity waves in a simulated life-cycle of baroclinic instability. *J.Atmos.Sci.*, **52 (21)**, 3695–3716.

Owen, R. W., 1981: Fronts and eddies in the sea: mechanisms, interactions and biological effects. *Analysis of marine ecosystems*, 197–233.

Painter, S. C., R. E. Pidcock, and J. T. Allen, 2010: A mesoscale eddy driving spatial and temporal heterogeneity in the productivity of the euphotic zone of the northeast Atlantic. *Deep Sea Research Part II: Topical Studies in Oceanography*, **57 (15)**, 1281–1292.

Phillips, N. A., 1951: A simple three-dimensional model for the study of large-scale extratropical flow patterns. *J.Meteorol.*, **8 (6)**, 381–394.

Platt, T., and W. G. Harrison, 1985: Biogenic fluxes of carbon and oxygen in the ocean. *Nature*, **318 (6041)**, 55–58.

Pollard, R. T., and L. A. Regier, 1992: Vorticity and vertical circulation at an ocean front. *J.Phys.Oceanogr.*, **22 (6)**, 609–625.

Polton, J. A., Y.-D. Lenn, S. Elipot, T. K. Chereskin, and J. Sprintall, 2013: Can Drake Passage Observations Match Ekman's Classic Theory? *J.Phys.Oceanogr.*, **43 (8)**, 1733–1740.

Polzin, K. L., J. M. Toole, J. R. Ledwell, and R. W. Schmitt, 1997: Spatial variability of turbulent mixing in the abyssal ocean. *Science*, **276 (5309)**, 93–96.

Prather, M. J., 1986: Numerical advection by conservation of second order moments. *Journal of Geophysical Research: Atmospheres (19842012)*, **91 (D6)**, 6671–6681.

Pratt, L. J., J. Earles, P. Cornillon, and J. F. Cayula, 1991: The Nonlinear Behavior of Varicose Disturbances in a Simple-Model of the Gulf-Stream. *Deep-Sea Research Part A-Oceanographic Research Papers*, **38**, S591–S622.

Price, J. F., R. A. Weller, and R. Pinkel, 1986: Diurnal Cycling - Observations and Models of the Upper Ocean Response to Diurnal Heating, Cooling, and Wind Mixing. *Journal of Geophysical Research-Oceans*, **91 (C7)**, 8411–8427.

Price, J. F., R. A. Weller, and R. R. Schudlich, 1987: Wind-Driven Ocean Currents and Ekman Transport. *Science*, **238 (4833)**, 1534–1538.

Ramachandran, S., A. Tandon, and A. Mahadevan, 2013: Effect of subgrid-scale mixing on the evolution of forced submesoscale instabilities. *Ocean Modelling*, **66**, 45–63.

Read, P. L., 2013: The dynamics and circulation of Venus atmosphere. *Towards Understanding the Climate of Venus*, Springer, 73–110.

Redi, M. H., 1982: Oceanic isopycnal mixing by coordinate rotation. *J.Phys.Oceanogr.*, **12 (10)**, 1154–1158.

Rhines, P. B., 1979: Geostrophic turbulence. *Annu.Rev.Fluid Mech.*, **11**, 401–441.

Richardson, P., 1983: Gulf stream rings. *Topics in Atmospheric and Oceanographic Sciences*, A. Robinson, Ed., Springer Berlin Heidelberg, 19–45–, URL http://dx.doi.org/10.1007/978-3-642-69003-7_2.

Rossby, C.-G., 1938: On the mutual adjustment of pressure and velocity distributions in certain simple current systems, ii. *J.Mar.Res.*, **1 (3)**, 239–263.

Rudnick, D. L., and J. R. Luyten, 1996: Intensive surveys of the Azores Front .1. Tracers and dynamics. *Journal of Geophysical Research-Oceans*, **101 (C1)**, 923–939.

Salmon, R., 1980: Baroclinic Instability and Geostrophic Turbulence. *Geophys.Astrophys.Fluid Dyn.*, **15 (3-4)**, 167–211.

Samelson, R. M., 1993: Linear instability of a mixed-layer front. *J. Geophys. Res.*, **98 (C6)**, 10 195–10 204, URL http://dx.doi.org/10.1029/93JC00457.

Samelson, R. M., and D. C. Chapman, 1995: Evolution of the instability of a mixed-layer front. *J. Geophys. Res.*, **100 (C4)**, 6743–6759, URL http://dx.doi.org/10.1029/94JC03216.

Samelson, R. M., and C. A. Paulson, 1988: Towed Thermistor Chain Observations of Fronts in the Sub-Tropical North Pacific. *Journal of Geophysical Research-Oceans*, **93 (C3)**, 2237–2246.

Sawyer, J. S., 1956: The Vertical Circulation at Meteorological Fronts and Its Relation to Frontogenesis. *Proceedings of the Royal Society A: Mathematical, Physical and Engineering Sciences*, **234 (1198)**, 346–362, doi:10.1098/rspa.1956.0039, URL http://rspa.royalsocietypublishing.org/cgi/doi/10.1098/rspa.1956.0039.

Schneider, N., A. J. Miller, M. A. Alexander, and C. Deser, 1999: Subduction of decadal North Pacific temperature anomalies: Observations and dynamics. *Journal of Physical Oceanography*, **29 (5)**, 1056–1070, pT: J; TC: 149; UT: WOS:000080563900011.

Schultz, D., 2015: *Fronts*, chap. SYNOPTIC METEOROLOGY. Elsevier.

Scott, R. B., and F. M. Wang, 2005: Direct evidence of an oceanic inverse kinetic energy cascade from satellite altimetry. *J.Phys.Oceanogr.*, **35 (9)**, 1650–1666.

Shakespeare, C. J., and J. R. Taylor, 2013: A generalised mathematical model of geostrophic adjustment and frontogenesis: uniform potential vorticity. *Journal of Fluid Mechanics*, **736**, 366–413.

Shcherbina, A. Y., E. A. D'Asaro, C. M. Lee, J. M. Klymak, M. J. Molemaker, and J. C. McWilliams, 2013: Statistics of vertical vorticity, divergence, and strain in a developed submesoscale turbulence field. *Geophysical Research Letters*, **40 (17)**, 4706–4711.

Shin, J., S. Dalziel, and P. Linden, 2004: Gravity currents produced by lock exchange. *J.Fluid Mech.*, **521**, 1–34.

Shulenberger, E., and J. L. Reid, 1981: The Pacific shallow oxygen maximum, deep chlorophyll maximum, and primary productivity, reconsidered. *Deep Sea Research Part A.Oceanographic Research Papers*, **28 (9)**, 901–919.

Simpson, J., and J. Hunter, 1974: Fronts in the Irish sea. *Nature*, **250**, 404–406.

Simpson, J. E., 1982: Gravity currents in the laboratory, atmosphere, and ocean. *Annu.Rev.Fluid Mech.*, **14 (1)**, 213–234.

Simpson, J. E., 1999: *Gravity currents: In the environment and the laboratory*. Cambridge University Press, – pp.

Skyllingstad, E. D., and R. Samelson, 2012: Baroclinic frontal instabilities and turbulent mixing in the surface boundary layer. Part I: Unforced simulations. *J.Phys.Oceanogr.*, **42 (10)**, 1701–1716.

Smagorinsky, J., 1963: General circulation experiments with the primitive equations: I. The basic experiment. *Mon.Weather Rev.*, **91 (3)**, 99–164.

Smith, K. S., and J. Vanneste, 2013: A Surface-Aware Projection Basis for Quasi-geostrophic Flow. *J.Phys.Oceanogr.*, **43 (3)**, 548–562.

Smyth, W., and J. McWilliams, 1998: Instability of an Axisymmetric Vortex in a Stably Stratified, Rotating Environment. *Theoretical and Computational Fluid Dynamics*, **11 (3-4)**, 305–322, doi:10.1007/s001620050095, URL http://link.springer.com/10.1007/s001620050095.

Snyder, C., W. C. Skamarock, and R. Rotunno, 1993: Frontal Dynamics Near and Following Frontal Collapse. *J.Atmos.Sci.*, **50 (18)**, 3194–3211.

Sournia, A., 1994: Pelagic biogeography and fronts. *Prog.Oceanogr.*, **34 (2)**, 109–120.

Spall, M. A., 1995: Frontogenesis, subduction, and crossfront exchange at upper ocean fronts. *Journal of Geophysical Research: Oceans (19782012)*, **100 (C2)**, 2543–2557.

Spall, M. A., 1997: Baroclinic jets in confluent flow. *J. Phys. Oceanogr.*, **27 (6)**, 1054–1071.

Spall, M. A., and D. C. Chapman, 1998: On the efficiency of baroclinic eddy heat transport across narrow fronts. *J.Phys.Oceanogr.*, **28 (11)**, 2275–2287.

Spielhagen, R. F., and Coauthors, 2011: Enhanced modern heat transfer to the Arctic by warm Atlantic Water. *Science*, **331 (6016)**, 450–453.

Stegner, A., P. Bouruet-Aubertot, and T. Pichon, 2004: Nonlinear adjustment of density fronts. part 1. the rossby scenario and the experimental reality. *J.Fluid Mech.*, **502**, 335–360.

Stern, M. E., 1965: Interaction of a uniform wind stress with a geostrophic vortex. *Deep Sea Research and Oceanographic Abstracts*, Elsevier, Vol. 12, 355–367.

Stommel, H., 1948: The westward intensification of wind-driven ocean currents. *Trans.Amer.Geophys.Union*, **29 (2)**, 202–206.

Stone, P. H., 1966a: Frontogenesis by Horizontal Wind Deformation Fields. *J.Atmos.Sci.*, **23 (5)**, 455–&.

Stone, P. H., 1966b: On Non-Geostrophic Baroclinic Stability. *Journal of the Atmospheric Sciences*, **23 (4)**, 390–400.

Stone, P. H., 1971: Baroclinic Stability Under Non-Hydrostatic Conditions. *J.Fluid Mech.*, **45 (FEB26)**, 659–&.

Stone, P. H., 1972: Simplified radiative-dynamical model for static stability of rotating atmospheres. *J.Atmos.Sci.*, **29 (3)**, 405–&.

Strass, V. H., 1992: Chlorophyll patchiness caused by mesoscale upwelling at fronts. *Deep Sea Research Part A.Oceanographic Research Papers*, **39 (1)**, 75–96.

Sun, O. M., S. R. Jayne, K. L. Polzin, B. A. Rahter, and L. C. St. Laurent, 2013: Scaling Turbulent Dissipation in the Transition Layer. *J.Phys.Oceanogr.*, **43 (11)**, 2475–2489.

Sutherland, G., K. H. Christensen, and B. Ward, 2014: Evaluating Langmuir turbulence parameterizations in the ocean surface boundary layer. *Journal of Geophysical Research-Oceans*, **119 (3)**, 1899–1910.

Sverdrup, H. U., M. W. Johnson, and R. H. Fleming, 1942: *The Oceans: Their physics, chemistry, and general biology*, Vol. 1087. Prentice-Hall New York.

Tandon, A., and C. Garrett, 1994: Mixed-Layer Restratification due to a Horizontal Density Gradient. *Journal of Physical Oceanography*, **24 (6)**, 1419–1424.

Tandon, A., and C. Garrett, 1995: Geostrophic Adjustment and Restratification of a Mixed-Layer with Horizontal Gradients Above a Stratified Layer. *J.Phys.Oceanogr.*, **25 (10)**, 2229–2241.

Taylor, J. R., and R. Ferrari, 2009: On the equilibration of a symmetrically unstable front via a secondary shear instability. *Journal of Fluid Mechanics*, **622**, 103, doi:10.1017/S0022112008005272, URL http://www.journals.cambridge.org/abstract_S0022112008005272.

Taylor, J. R., and R. Ferrari, 2010: Buoyancy and Wind-Driven Convection at Mixed Layer Density Fronts. *Journal of Physical Oceanography*, **40 (6)**, 1222–1242, doi:10.1175/2010JPO4365.1, URL http://journals.ametsoc.org/doi/abs/10.1175/2010JPO4365.1.

Taylor, J. R., and R. Ferrari, 2011: Ocean fronts trigger high latitude phytoplankton blooms. *Geophysical Research Letters*, **38 (23)**, doi:10.1029/2011GL049312, URL http://doi.wiley.com/10.1029/2011GL049312.

Thomas, L., and R. Ferrari, 2008: Friction, Frontogenesis, and the Stratification of the Surface Mixed Layer. *Journal of Physical Oceanography*, **38 (11)**, 2501–2518, doi:10.1175/2008JPO3797.1, URL http://journals.ametsoc.org/doi/abs/10.1175/2008JPO3797.1.

Thomas, L. N., 2005: Destruction of potential vorticity by winds. *Journal of Physical Oceanography*, **35 (12)**, 2457–2466.

Thomas, L. N., 2008: Formation of intrathermocline eddies at ocean fronts by wind-driven destruction of potential vorticity. *Dyn.Atmos.Oceans*, **45 (3)**, 252–273.

Thomas, L. N., 2012: On the effects of frontogenetic strain on symmetric instability and inertiagravity waves. *Journal of Fluid Mechanics*, **711**, 620–640, doi:10.1017/jfm.2012.416, URL http://www.journals.cambridge.org/abstract_S0022112012004168.

Thomas, L. N., and C. M. Lee, 2005: Intensification of ocean fronts by down-front winds. *Journal of Physical Oceanography*, **35 (6)**, 1086–1102.

Thomas, L. N., and P. B. Rhines, 2002: Nonlinear stratified spin-up. *Journal of Fluid Mechanics*, **473**, 211–244, doi:10.1017/S0022112002002367, URL http://www.journals.cambridge.org/abstract_S0022112002002367.

Thomas, L. N., A. Tandon, and A. Mahadevan, 2008: Submesoscale processes and dynamics. *Ocean Modeling in an Eddying Regime*, M. W. Hecht, and H. Hasumi, Eds., AGU, Washington, D. C, 17–38.

Thomas, L. N., and J. R. Taylor, 2010: Reduction of the usable wind-work on the general circulation by forced symmetric instability. *Geophysical Research Letters*, **37 (18)**, doi:10.1029/2010GL044680, URL http://doi.wiley.com/10.1029/2010GL044680.

Thomas, L. N., and J. R. Taylor, 2014: Damping of inertial motions by parametric subharmonic instability in baroclinic currents. *Journal of Fluid Mechanics*, **743**, 280–294, doi:10.1017/jfm.2014.29, URL http://www.journals.cambridge.org/abstract_S0022112014000299.

Thomas, L. N., J. R. Taylor, R. Ferrari, and T. M. Joyce, 2013: Symmetric instability in the Gulf Stream. *Deep Sea Research Part II: Topical Studies in Oceanography*, **91**, 96–110, doi:10.1016/j.dsr2.2013.02.025, URL http://linkinghub.elsevier.com/retrieve/pii/S0967064513000829.

Thomsen, S., C. Eden, and L. Czeschel, 2013: Stability Analysis of the Labrador Current. *J. Phys. Oceanogr.*, **44 (2)**, 445–463, URL http://dx.doi.org/10.1175/JPO-D-13-0121.1.

Thomsen, S., C. Eden, and L. Czeschel, 2014: Stability Analysis of the Labrador Current. *Journal of Physical Oceanography*, **44 (2)**, 445–463, doi:10.1175/JPO-D-13-0121.1, URL http://journals.ametsoc.org/doi/abs/10.1175/JPO-D-13-0121.1.

Thorpe, A. J., and R. Rotunno, 1989: Nonlinear Aspects of Symmetric Instability. *J.Atmos.Sci.*, **46 (9)**, 1285–1299.

Thorpe, S. A., 2004: Recent developments in the study of ocean turbulence. *Annu.Rev.Earth Planet.Sci.*, **32**, 91–109.

Tsang, Y.-K., and D. G. Dritschel, 2015: Ellipsoidal vortices in rotating stratified fluids: beyond the quasi-geostrophic approximation. *J.Fluid Mech.*, **762**, 196–231.

Uda, M., 1938: Researches on Siome or Current Rip in the Seas and Oceans. *Geophysical Magazine*, **II**, 307–372.

Ungarish, M., and H. E. Huppert, 1998: The effects of rotation on axisymmetric gravity currents. *J.Fluid Mech.*, **362**, 17–51.

Ungarish, M., and T. Zemach, 2003: On axisymmetric rotating gravity currents: two-layer shallow-water and numerical solutions. *J.Fluid Mech.*, **481**, 37–66.

Vanneste, J., 2013: Balance and Spontaneous Wave Generation in Geophysical Flows. *Annual Review of Fluid Mechanics, Vol 45*, **45**, 147–172.

Visbeck, M., J. Marshall, T. Haine, and M. Spall, 1997: Specification of eddy transfer coefficients in coarse-resolution ocean circulation models. *J.Phys.Oceanogr.*, **27 (3)**, 381–402.

Viúdez, A., 2008: The stationary frontal wave packet spontaneously generated in mesoscale dipoles. *J.Phys.Oceanogr.*, **38 (1)**, 243–256.

von Karman, T., 1940: The engineer grapples with nonlinear problems. 615–683, URL http://projecteuclid.org/euclid.bams/1183502816.

Voorhis, A., and J. Hersey, 1964: Oceanic thermal fronts in the Sargasso Sea. *Journal of Geophysical Research*, **69 (18)**, 3809–3814.

Voorhis, A. D., E. H. Schroeder, and A. Leetmaa, 1976: Influence of Deep Mesoscale Eddies on Sea-Surface Temperature in North-Atlantic Subtropical Convergence. *J.Phys.Oceanogr.*, **6 (6)**, 953–961.

Wang, J., G. R. Flierl, J. H. LaCasce, J. L. McClean, and A. Mahadevan, 2013: Reconstructing the Ocean's Interior from Surface Data. *J.Phys.Oceanogr.*, **43 (8)**, 1611–1626.

Weller, R. A., 1991: Overview of the Frontal Air-Sea Interaction Experiment (FASINEX): A Study of Air-Sea Interaction in a Region of Strong Oceanic Gradients. **96**, 8501–8516.

Williams, J., 1793: On the use of the thermometer in discovering Banks, Soundings, etc,. *Trans.Am.Philos.Soc*, **3**, 82–89.

Williams, P. J. l. B., P. D. Quay, T. K. Westberry, and M. J. Behrenfeld, 2013: The Oligotrophic Ocean Is Autotrophic. *Annual Review of Marine Science, Vol 5*, **5**, 535–549.

Williams, R. G., and M. J. Follows, 2003: Physical transport of nutrients and the maintenance of biological production. *Ocean Biogeochemistry*, 19–51.

Williams, R. T., 1968: A Note on Quasi-Geostrophic Frontogenesis. *J.Atmos.Sci.*, **25 (6)**, 1157–&.

Williams, R. T., and J. Plotkin, 1968: Quasi-Geostrophic Frontogenesis. *J.Atmos.Sci.*, **25 (2)**, 201–&.

Winters, K. B., and E. A. D'Asaro, 1996: Diascalar flux and the rate of fluid mixing. *J.Fluid Mech.*, **317**, 179–193.

Winters, K. B., and E. A. D'Asaro, 1997: Direct simulation of internal wave energy transfer. *J.Phys.Oceanogr.*, **27 (9)**, 1937–1945.

Winters, K. B., P. N. Lombard, J. J. Riley, and E. A. D'Asaro, 1995: Available potential energy and mixing in density-stratified fluids. *J.Fluid Mech.*, **289**, 115–128.

Wunsch, C., 1999: Where do ocean eddy heat fluxes matter? *Journal of Geophysical Research-Oceans*, **104 (C6)**, 13 235–13 249.

Wunsch, C., and R. Ferrari, 2004: Vertical mixing, energy and thegeneral circulation of the oceans. *Annu.Rev.Fluid Mech.*, **36**, 281–314.

Wunsch, C., P. Heimbach, R. M. Ponte, I. Fukumori, and E.-G. C. Members, 2009: The Global General Circulation of the Ocean Estimated by the Ecco-Consortium. *Oceanography*, **22 (2)**, 88–103.

Yentsch, C. S., and D. A. Phinney, 1985: Rotary motions and convection as a means of regulating primary production in warm core rings. *Journal of Geophysical Research: Oceans (19782012)*, **90 (C2)**, 3237–3248.

Young, W. R., 1994: The Subinertial Mixed-Layer Approximation. *Journal of Physical Oceanography*, **24 (8)**, 1812–1826.

Zhai, X., H. L. Johnson, and D. P. Marshall, 2010: Significant sink of ocean-eddy energy near western boundaries. *Nature Geoscience*, **3 (9)**, 608–612.

Zhang, X., M. Lewis, and B. Johnson, 1998: Influence of Bubbles on Scattering of Light in the Ocean. *Applied Optics*, **37 (27)**, 6525, doi:10.1364/AO.37.006525, URL http://www.opticsinfobase.org/abstract.cfm?URI=ao-37-27-6525.

Zhang, Z., W. Wang, and B. Qiu, 2014: Oceanic mass transport by mesoscale eddies. *Science*, **345 (6194)**, 322–324, doi:10.1126/science.1252418, URL http://www.sciencemag.org/cgi/doi/10.1126/science.1252418.